

学校代码：10491

研究生学号：1201690057

# 中国地质大学

## 硕士学位论文

### **斑岩顶部岩盖：秘鲁北部Huamachuco-Cajabamba矿带La Arena-Calaorco斑岩型-浅成低温热液型铜金矿床的地质特征和时限**

姓名：Alan H. Santos Polo

学科专业：矿物学、岩石学、矿床学

指导教师：李建威 教授

陈世忠 副导师

培养单位：资源学院

二〇二〇年五月

A Dissertation Submitted to China University of Geosciences  
For Master Degree

**Lithocap on Porphyry Shoulder: Geology  
and lifespan of the La Arena-Calaorco  
porphyry and epithermal deposits,  
Huamachuco-Cajabamba Belt, Northern  
Peru**

MSc Candidate : Alan H. Santos Polo

Major : Mineralogy Petrology and Ore Deposit

Supervisor : Prof. Jian-Wei Li

Dr. Chen Shizhong

China University of Geosciences  
Wuhan 430074 P.R. China

## 中国地质大学（武汉）研究生学位论文原创性声明

本人郑重声明：本人所呈交的博（硕）士学位论文《斑岩顶部岩盖：秘鲁北部 Huamachuco-Cajabamba 矿带 La Arena-Calaorco 斑岩型-浅成低温热液型铜金矿床的地质特征和时限》，是本人在导师的指导下，在中国地质大学（武汉）攻读博（硕）士学位期间独立进行研究工作所取得的成果。论文中除已注明部分外不包含他人已发表或撰写过的研究成果，对论文的完成提供过帮助的有关人员已在文中说明并致以谢意。

本人所呈交的博（硕）士学位论文没有违反学术道德和学术规范，没有侵权行为，并愿意承担由此而产生的法律责任和法律后果。

学位论文作者签名：



日期： 2020年06月05日

## 中国地质大学（武汉）研究生学位论文导师承诺书

本人郑重承诺：本人所指导的硕士学位论文《斑岩顶部岩盖：秘鲁北部 Huamachuco-Cajabamba 矿带 La Arena-Calaorco 斑岩型-浅成低温热液型铜金矿床的地质特征和时限》，是在本人的指导下，研究生在中国地质大学（武汉）攻读硕士学位期间独立进行研究工作所取得的成果，论文由研究生独立完成。

研究生所呈交的硕士学位论文没有违反学术道德和学术规范，没有侵权行为，并愿意承担由此而产生的与导师相关的责任和后果。

指导教师（签字）：\_\_\_\_\_

日期：      年    月    日




## 中国地质大学（武汉）学位论文使用授权书

本人授权中国地质大学（武汉）可采用影印、缩印、数字化或其它复制手段保存本学位论文；学校可向国家有关部门或机构送交本学位论文的电子版全文，编入有关数据库进行检索、下载及文献传递服务；同意在校园网内提供全文浏览和下载服务。

涉密论文解密后适用于本授权书。

学位论文作者签名：



日期： 2020年06月05日

# Resume

## 1. Basic information

Name: Alan H. Santos Polo      Gender : male      Nationality: Peru  
Birth Date: 1985-02-20      Native Place: Cajabamba, Cajamarca  
2003.03—2008.12 Bachelor of Geological Engineering degree of National University of Cajamarca, Peru  
2012.03—2014.12 Master of Economic Geology: mining exploration degree of Catholic University of the North, Chile  
2015-01—2015-07 Internship in the High Resolution Geochronology of the Sao Paulo University, Brasil  
2017-09—2020-07 Studying for master degree in China University of Geosciences (Wuhan), China

## 2. Academic paper

**Santos, A.,** Weimin, G., Rivera, F., Tassinari, C., Cerpa, L., and Kojima, S., 2019, Early Jurassic arc related magmatism associated with porphyry copper mineralization at Zafranal, southern Peru unraveled by zircon U-Pb ages: *Andean Geology*, 46 (3): 445-470

**Santos, A.,** Li, J.W., Chen, S., Chen, N., Cabrera, O., and Perez, J., 2020, Lithocap on Porphyry Shoulder: Geology and lifespan of the La Arena-Calaorco porphyry and epithermal deposits, Huamachuco-Cajabamba Belt, Northern Peru: *Economic Geology*, *in review (manuscript number: SEG-D-20-00074)*.

## 3. Research programs

All research programs were developed and funded by Peru Geological Survey (INGEMMET)

**2009-2011:** “Geology of the border with Ecuador: Peruvian Northwest and its Relationship with Mineral Resources”

- Geological mapping of the Cretaceous volcanic and intrusive rocks linked to VMS and porphyry copper deposits of the Lancones Basin, Northern Peru.

- 1:50K geological mapping of Cenozoic volcanic belt and Miocene porphyry systems, Northern Peru.

**2013-2014:** “Scientific-technical research project within the agreement between the geological survey of China (SGC) and Peru (INGEMMET).

- 1: 25K geological mapping of the Coast Batholith, southern Peru, petrochemical characterization, temporal evolution (U-Pb dating) and relationship with porphyry deposits, IOCGs and gold veins (e.g. Marcona, Acarí)

**2015-2016:** “Petrochemical of the Carabaya Batholith, Southern Peru”

- High resolution geological and structural mapping of the Carabaya Batholith and its relationship with lithium, uranium, tin, and tungsten mineralization.

- Petrographic and geochemical characterization of magmatic units.

## 摘要

La Arena Cu-Au-(Mo) 斑岩型矿床位于秘鲁北部的渐新世-中新世 Huamachuco-Cajabamba 带上，它包括 Calaorco 成矿系统中的高硫型金矿化。La Arena 矿床的探明和控制资源量分别为 262.6 万公吨 (Mt) Cu 和 159.81 吨 (t) Au。Calaorco 高硫型成矿系统包含 16 t Au 的已探明资源量，已生产约 150 万盎司 (Moz) Au。La Arena 位于一复合的、NW 倾向的早期石英闪长岩中心，该岩体大小约 2Km x 1.3Km，侵入到中生代地层中。地层受区域逆掩断层背斜控制，地层褶皱轴向 NW，倾向 NE，Calaorco 高硫型成矿系统则位于该褶皱的西南侧。La Arena 斑岩矿床热液蚀变与富金斑岩带蚀变样式一致，早期钾化带被绢云母-绿泥石化带 (SCC) 改造，它们都被绢云母化带围绕。后者在深部被一个青磐岩化带环状包围，浅部强烈高级泥化蚀变，并形成了 Calaorco 岩盖。斑岩型矿化发育在早期和成矿期安山质斑岩中，从早到晚发育多期次细脉。Calaorco 岩盖位于 La Arena 斑岩西南顶部，受斑岩形态控制。热液蚀变向外和向下，随着 SiO<sub>2</sub> 的减少，Au 含量从石英-叶腊石-明矾石±水铝石向石英-地开石-高岭土±明矾石变化。Calaorco 矿体含有赤铁矿-针铁矿为主体的铁帽，其厚度达到+400 米，下部氧化带中分布有黄铁矿、硫砷铜矿、吕宋铜矿、铜蓝和自然金等。成矿带位于渗透性强的 Chimú 组石英砂岩中，呈层状，脆性断裂发育，并受 NW 和 NE 走向断层控制的多期次角砾岩和硅化蚀变所限定。野外脉体期次和锆石 U-Pb 年龄测定岩浆-热液活动时间持续 2.24±0.79 m.y.，早期侵入岩年龄在 26.64±0.71 和 26.50±0.28 Ma 之间，强矿化早期斑岩年龄在 26.45±0.64 Ma，弱矿化成矿斑岩年龄在 25.58±0.68 和 24.95±0.29 Ma 之间，Calaorco 晚期成矿年龄在 24.81±0.48Ma 和 24.40±0.34 Ma 之间。两个早期含辉钼矿的石英脉体测定 Re-Os 成矿年龄为 26.61±0.41Ma 和 26.51±0.46Ma，三个含辉钼矿细脉的早期斑岩年龄在 26.05±0.39Ma，25.93±0.44Ma，和 25.86±0.44 Ma，时间跨度在 0.75±0.60 m.y.。这意味着辉钼矿在早期安山质斑岩中存在两期辉钼矿矿化。在黑云母、白云母、绢云母和明矾石上测定了 40Ar/39Ar 的冷却年龄，深部钾化带年龄分别为 26.40±0.29 和 26.35±0.14 Ma，SCC 蚀变带黑云母年龄为 25.96±0.16 Ma，绢云母带白云母/绢云母年龄分别为 26.41±0.52、26.38±0.24 和 26.02±0.07 Ma。与 Calaorco 露天矿早期安山质斑岩高级泥化蚀变的明矾石晶体的年龄分别为 25.57±0.16Ma、25.51±0.10Ma、25.51±0.17 Ma，在 Ethel 采场年龄为 25.81±0.16 Ma。Calaorco 和 Ethel 高级泥化蚀变年龄比深部斑岩型热液黑云母蚀变年龄年轻 0.89~0.59 m.y.，但与 SCC 蚀变带的黑云母蚀变范围相近。这支持了以早期安山岩为中心的斑岩到超浅成热液蚀变，存在 0.89±0.34 m.y.的时间跨度，以两个独立的呈脉动式流体热液活动演化。所有的野外特征和同位素数据强烈表明，这两种类型的矿化之间存在密切的时空继承关系，以及在 26.64 Ma 至 24.40 Ma 之间，伴随构造抬升和侵蚀，岩浆热液活动以独立脉动的形式进行。La Arena-Calaorco 矿床的早期斑岩及其热液活动至少演化了 280,000 年时间 (0.94±0.66 m.y.)，其间沉积了约 90%的铜、金和钼等成矿元素。

关键词:La Arena 斑岩，斑岩-浅成热液过渡带，渐新世晚期，Chimú组

## ABSTRACT

The La Arena Cu-Au-(Mo) porphyry deposit is located in the Oligocene-Miocene Huamachuco-Cajabamba belt of northern Peru. It comprises high-sulfidation gold mineralization developed within the Calaorco ore system. La Arena porphyry deposit has the measured and indicated reserves of 2.626 million metric tons (Mt) Cu and 159.81 tons (t) Au, and the Calaorco high-sulfidation system contains proven current resources of 16 t Au, which has produced approximately 1.5 million ounces (Moz) Au. La Arena is centered on a composite, NW-oriented, ~2- x 1.3-km precursor quartz diorite pluton emplaced in Mesozoic sediment rocks, and was focused by the preexisting, regional-scale overthrust anticline folded axis of axial trace NW-orientation and NE-vergent, whereas the Calaorco ore system take place in the southwest flank of the fold.

Hydrothermal alteration of the La Arena porphyry conforms to the gold-rich porphyry zonal pattern, in which early potassic core is widely overprinted by sericite-chlorite (SCC) alteration, and both zones are laterally bordered by an annular sericitic zone. The latter surrounded by a propylitic halo in deeper area, and shallow area is superimposed by an extensive advance argillic alteration forming the Calaorco lithocap. Porphyry-style mineralization is hosted by early and inter-mineral andesite porphyry intrusions, and occurs as multiple veinlets in early, transitional, and late stages. The Calaorco lithocap is superimposed on the La Arena porphyry's southwest shoulder, offset from the causative porphyry suites. The hydrothermal alteration is zoned outward and downward, with decreasing SiO<sub>2</sub> and Au contents through quartz – pyrophyllite – alunite ± diaspore to quartz – dickite – kaolinite ± alunite. The Calaorco orebody contains a dominant hematite-goethite leached capping that attains to ~400 m thick, together with pyrite, enargite, luzonite, covellite and Au in the mixed zones typically underlying oxide gold zone leached of copper. The mineralized zones are hosted in permeable, non-reactive Chimú quartz sandstone, bedding planes, fracture network, and multiple stages of brecciation and silicification controlled by a series of northwest- and northeast-trending faults.

Based on samples that show unambiguous field relationship coupled with zircon U-Pb dating, the magmatic-hydrothermal activity lasted  $2.24 \pm 0.79$  m.y., from emplacement of the precursor pluton between  $26.64 \pm 0.71$  and  $26.50 \pm 0.28$  Ma, followed by an intensely mineralized early porphyry at  $26.45 \pm 0.64$  Ma and weakly mineralized inter-mineral porphyries between  $25.58 \pm 0.68$  and  $24.95 \pm 0.29$  Ma, to intrusions of the late mineral porphyries at Calaorco between  $24.81 \pm 0.48$  and  $24.40 \pm 0.34$  Ma. Re-Os analyses yield ore-formation ages of  $26.61 \pm 0.41$  and  $26.51 \pm 0.46$  for two early molybdenite-bearing quartz veinlets,  $26.05 \pm 0.39$ ,  $25.93 \pm 0.44$ , and  $25.86 \pm 0.44$  Ma for three molybdenite-rich transitional veinlets hosted in early porphyry that are within a time span of  $0.75 \pm 0.60$  m.y. This implies that the molybdenum were deposited in two-separated mineralization stages into the early andesite porphyry. The cooling  $^{40}\text{Ar}/^{39}\text{Ar}$  ages have been determined on biotite, muscovite/sericite, and alunite. The deep potassic biotites have ages of  $26.40 \pm 0.29$  and  $26.35 \pm 0.14$  Ma, biotite in paleo-green SCC alteration zone yielded an age of  $25.96 \pm 0.16$  Ma, muscovite/sericite in sericitic zones dating ages of  $26.41 \pm 0.52$ ,  $26.38 \pm 0.24$ , and  $26.02 \pm 0.07$  Ma. Alunite crystals related to advanced argillic altered roofs of the early andesite porphyry from the Calaorco open-pit yielded ages of  $25.57 \pm 0.16$ ,  $25.51 \pm 0.10$ , and  $25.51 \pm 0.17$  Ma and  $25.81 \pm 0.16$  Ma

from the Ethel area. Advanced argillic alteration at Calaorco and Ethel are ~ 0.89 and ~ 0.59 m.y. younger than the deep porphyry-style hydrothermal biotites, respectively, but similar range as that of the biotite from SCC alteration zone. This supported that the hydrothermal alteration centered in the early andesite from porphyry to epithermal environment evolved along two fluid flow paths as separate pulses of hydrothermal activity within a time span of  $0.89 \pm 0.34$  m.y.

All the field features and combined radiometric data strongly suggests a close spatial-temporal genetic connection between these two styles of mineralization, as well as the tectonic uplift and erosion accompanied of magmatic-hydrothermal activity as separate pulses between 26.64 and 24.40 Ma. The early porphyry and its hydrothermal activity at La Arena-Calaorco deposits formed during at least 280,000 yr. ( $0.94 \pm 0.66$  m.y.), time-interval where about 90 % of copper, gold and molybdenum reserves were deposited.

**Key words:** La Arena porphyry, porphyry-epithermal transition, late Oligocene, Chimú Formation

# Content

## CHAPTER 1

### INTRODUCTION

1.1 Introduction .....	1
1.2 Outline of the thesis.....	2
1.3 An overview of porphyry copper and high-sulfidation epithermal deposits .....	2
1.3.1 Introduction .....	2
1.3.2 Definition.....	3
1.3.3 Tectonic setting.....	4
1.3.4 Global and temporal distribution.....	5
1.3.5 Geological setting .....	6
1.3.5.1 Host rocks.....	6
1.3.5.2 Volcanic connections.....	6
1.3.5.3 Wall-rock influences.....	7
1.3.5.4 Structures.....	7
1.3.5.5 Porphyry to epithermal HS systems transition zones.....	7
1.3.5.6 Alteration-mineralization zoning.....	8
1.3.5.7 Metal zoning .....	13
1.3.5.8 Longevity of porphyry and HS ore formation.....	14
1.4 Porphyry-epithermal deposits in northern Peru.....	15

## CHAPTER 2

### GEOLOGICAL SETTING OF THE LA ARENA DISTRICT

2.1 Introduction .....	17
2.2 Location and access.....	17
2.3 Geological setting.....	17
2.4 Geological of the La Arena District.....	19
2.4.1 Sedimentary rocks basement.....	19
2.4.2 Calipuy Group and its relationship with mineralization.....	20

## CHAPTER 3

### SAMPLING AND ANALYTICAL METHODS

3.1 Introduction.....	22
3.2 Samples collected.....	22
3.3 Analytical methods.....	24
3.3.1 Zircon U-Pb dating.....	24
3.3.2 Hydrothermal biotite and hypogene alunite $^{40}\text{Ar}/^{39}\text{Ar}$ dating.....	24
3.3.3 Molybdenite Re-Os dating.....	25
3.4 Previous geochronological studies at La Arena-Calaorco porphyry and epithermal deposits.....	26

## CHAPTER 4

### GEOLOGY OF THE LA ARENA-CALAORCO PORPHYRY AND EPITHERMAL DEPOSITS

4.1 Introduction .....	28
4.2 Mining overview.....	28
4.3 Geology of the La Arena-Calaorco porphyry and epithermal systems.....	30

4.3.1 Intrusive history of the La Arena porphyry complex.....	30
4.4 Hydrothermal alteration and mineralization.....	35
4.4.1 La Arena porphyry orebody.....	36
4.4.2 Calarco high-sulfidation epithermal orebody.....	44
4.5. Sulfide and metal zoning.....	49
4.6. Supergene alteration and mineralization.....	50
4.7 Other epithermal-porphyry transition in the La Arena district.....	51
4.7.1 Alizar-Vanessa porphyry and epithermal systems.....	51
4.7.2 Agua Blanca porphyry and epithermal systems.....	52

## **CHAPTER 5**

### **PETROCHEMICAL OF THE LA ARENA DISTRICT**

5.1 Introduction .....	53
5.2 Bulk rock geochemistry.....	53

## **CHAPTER 6**

### **GEOCHRONOLOGY**

6.1 Introduction .....	56
6.2 Zircon U-Pb ages of porphyry bodies.....	56
6.3 Re-Os ages of molybdenite-bearing quartz veinlets.....	62
6.4 <sup>40</sup> Ar/ <sup>39</sup> Ar ages for silicate minerals.....	65

## **CHAPTER 7**

### **DISCUSSION**

7.1 District-scale controls and rapid uplift.....	68
7.2 Timing formation of porphyry- and epithermal-style mineralization.....	69
7.3 Exploration implications .....	72

## **CHAPTER 8**

### **CONCLUSION**

7.5 Conclusive remarks.....	74
-----------------------------	----

Acknowledgments.....	76
----------------------	----

References.....	77
-----------------	----

## **APPENDICES.....90**

Appendix 1. Table A1. Chemical Composition of selected rock types related to the La Arena district

Appendix 2. Table A2. LA-ICP-MS Zircon U-Pb Data of Porphyry Intrusions from the La Arena porphyry Cu-Au-(Mo) deposit.

Appendix 3 Method of zircon U-Pb dating (Tahoe Resources, unpub. files), Table A3. U/Pb zircon analytical data obtained using the LA-ICP-MS Method and weighted mean <sup>207</sup>Pb-corrected <sup>206</sup>Pb/<sup>238</sup>U histogram and Concordia diagrams (Fig. A3).

Appendix 4. Table A4. Analytical data for <sup>40</sup>Ar/<sup>39</sup>Ar age determinations.





## Chapter 1

# Introduction

### 1.1 Introduction

Porphyry-type deposits are the source of a major proportion of the world's copper production, therefore they are arguably the most studied and potentially best known ore deposit type (e.g. Titley, 1966; Lowell and Guilbert, 1970; Sillitoe, 1973, 2010; Gustafson and Hunt, 1975; Dilles and Einaudi, 1992; Hedenquist et al., 1998; Hou et al., 2003; Sillitoe and Perelló, 2005; Seedorff et al., 2005; Richards, 2018). These ore deposits are divided into categories depending on whether they carry by-product gold or molybdenum (Kesler, 1973; Sillitoe, 1979, 2000; Kesler et al., 2002), where porphyry deposits with average gold contents of  $\geq 0.4$  g/t (Sillitoe, 1979) or 1:1 ratio (e.g. 1 g/t to 1% Cu) may be defined as gold-rich porphyry deposits (Kirkham and Sinclair, 1995), which have a shallower average depth of formation ( $\sim 2.1$  km; Murakami et al., 2010). Advanced argillic alteration assemblages occur in the shallow parts of many gold-rich porphyry systems (Sillitoe, 1973; Stoffregen, 1987; Hedenquist et al., 1994). These zones are horizontal to subhorizontal blankets of residual quartz, and advanced argillic alteration of hypogene origin, called lithocap (Sillitoe, 1995), which can host high-sulfidation epithermal gold mineralization (Hedenquist et al., 1994; Sillitoe, 1999; 2000; 2010; Chang et al., 2011). The genetic connection between gold-rich porphyry and epithermal gold deposits in the same districts has been documented by many geologist (e.g. Wallace, 1979; Asami and Britten, 1980; Sillitoe, 1983, 1988, 1989; Heald et al., 1987; Rye, 1993; Arribas et al., 1995; Hedenquist et al., 1998; Richards et al., 2006; Hedenquist and Taran, 2013). High sulfidation epithermal gold mineralization is proposed to have occurred at approximately the same time as, or shortly after, subjacent sulfides linked to the potassic alteration (Arribas et al., 1995; Shinohara and Hedenquist, 1997; Chiaradia et al., 2013; Chelle-Michou et al., 2017). In the central and north Andes high-sulfidation epithermal gold deposits occur in proximity to gold-rich porphyry deposits, such as the Maricunga belt of northern Chile (Vila and Sillitoe, 1991; Vila et al., 1991; Mpodozis et al., 1995; Muntean and Einaudi, 2000, 2001; Sillitoe et al., 2013; Valdivia et al., 2014), Cajamarca region (Pinto, 2002; Gustafson et al., 2004; Noble et al., 2004; Davies and Williams, 2005) and Alto Chicama district (Montgomery, 2012; Cerpa et al., 2013) in northern Peru. The Huamachuco-Cajabamba belt, which is also located in northern Peru, has world class high-sulfidation deposits hosted in bedding planes of steeply-dipping quartz sandstone of the Chimú Formation or, less commonly, by overlying rocks of the Goyllarisquizga Group (e.g. Calaorco, La Virgen, El Toro, Ethel, and Santa Rosa; Montoya, 1999; Gauthier et al., 1999; Noble and McKee, 1999; Garay et al., 2012), plus over 5 prospects of gold-rich porphyry (e.g. La Arena, Alizar, Agua Blanca, La Virgen, and Milagros;

Aquino et al., 2006; Montgomery, 2012; Corbett, 2014), although they vary in gold content (average grade 0.24 Au g/t; Tahoe Resources Inc. Annual Report 2018). Some typical features of gold-rich porphyry are described in Cajamarca region (Llosa and Veliz, 2000; Córdova and Hoyos, 2000; Sillitoe, 2000; Davies, 2002; Gustafson et al., 2004). The spatial connection and genetic relations between porphyry-type mineralization and high-sulfidation epithermal gold deposits in the Huamachuco-Cajabamba belt (La Arena-Calaorco porphyry and epithermal deposits) has already been investigated by Aquino et al. (2006), Gauthier et al. (1999), Garay et al. (2012), and Sangay et al. (2017), but no direct evidences are reported in their studies.

As a further investigation of this genetic connection and lifespan of porphyry-epithermal systems, I aim to elucidate the geology and alteration-mineralization features of Calaorco high-sulfidation and La Arena porphyry Cu-Au-(Mo) system, based on optical petrography, mineralogy, U-Pb zircon dating of porphyry bodies,  $^{40}\text{Ar}/^{39}\text{Ar}$  of silicate minerals from lithocap structures and potassic alteration zones and molybdenite Re-Os dating, as well as extensive unpublished in-house data on the mine district.

## 1.2 Outline of the thesis

**Chapter one** begins with an overview of porphyry and high-sulfidation epithermal deposits, as well as description of the genetic connection between porphyry-epithermal deposits of northern Peru and others in the central Andes.

**Chapter two** give a geological setting of the La Arena district.

**Chapter three** presents an overview of the sampling procedure and sample preparation. Also describe the different analytical techniques and procedures utilized during this study.

**Chapter four** description of the geology of the La Arena – Calaorco porphyry and epithermal deposits

**Chapter five** contains whole rock major and trace elements geochemistry for each unit rock outcropping in the mine area.

**Chapter six** explores the lifespan of Calaorco high-sulfidation and La Arena porphyry Cu-Au-(Mo) system. In this chapter U-Pb zircon dating of porphyry bodies, molybdenite Re-Os dating, and  $^{40}\text{Ar}/^{39}\text{Ar}$  isotope is used to date alunite and hydrothermal biotite from lithocap structures and potassic alteration, respectively, which may shed light on the timescale involved in the genesis of the La Arena-Calaorco porphyry and epithermal systems. This approach is possible at La Arena porphyry because the result of drill-core logging, showed that alteration and mineralization are concentric around sequence of intrusive events, from a precursor to late-mineral porphyry bodies. This chapter also presents the discussion of an extensive unpublished in-house U-Pb zircons and  $^{40}\text{Ar}/^{39}\text{Ar}$  silicate minerals files from Tahoe Resources Inc.

**Chapter seven** discussion

**Chapter eight** conclusion

## 1.3 An overview of porphyry copper and high-sulfidation epithermal deposits

### 1.3.1 Introduction

Porphyry Cu±Mo±Au deposits (simply PCDs) and high-sulfidation (HS) epithermal Au-Ag systems represent the most economically important class of these metals and are major exploration and exploitation targets around the world. PCDs and HS deposits have been a principal subject for intensive and extensive scientific research during the last half century. Indeed, the exploration companies and scientific research have generated an enormous collection of geology information and scientific papers, respectively.

Benchmark studies such as: Titley (1966), Lowell and Guilbert (1970), Sillitoe (1973, 1999, 2000, 2010), Gustafson and Hunt (1975), Gustafson and Titley (1978), Einaudi et al. (1977), Gustafson (1978), Titley and Beane (1981), Dilles and Einaudi (1992), Arribas et al. (1995), Hedenquist et al. (1998), Sillitoe and Perelló (2005), Seedorff et al. (2005), Hedenquist and Taran (2013), and Chiaradia et al. (2013) being among the cited papers in the economic geology literature.

The aim of this chapter is to provide a descriptive literature review of porphyry and epithermal deposits, remarking all those features that are relevant to their general understanding.

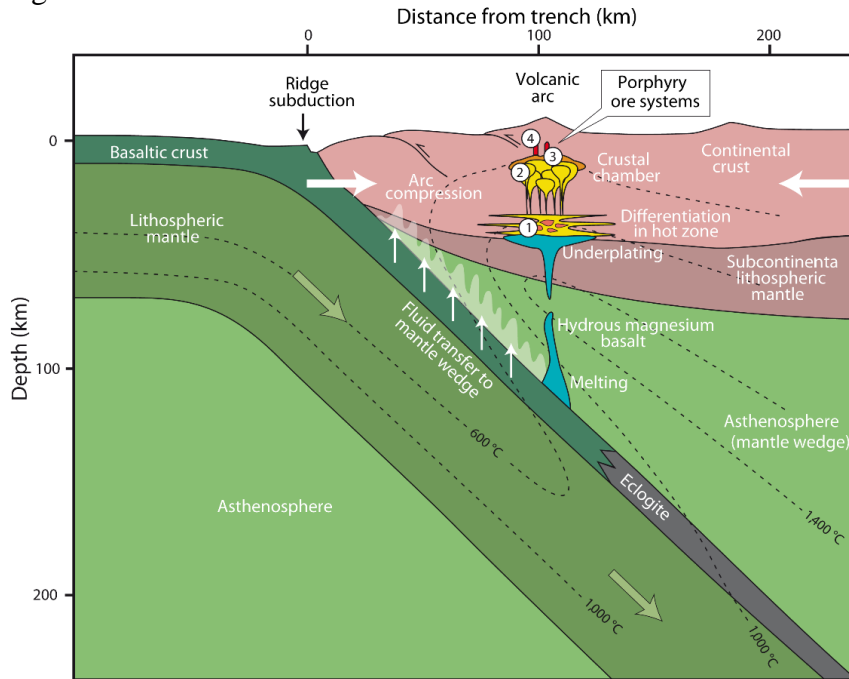


Figure 1.1. Tectonic setting of porphyry copper deposits (Wilkinson, 2013). The four environments where key trigger processes operate that may lead to the formation of large porphyry ore deposits are numbered 1–4: (1) Cyclical enrichment of magmas with metals and water in the deep crust, (2) Saturation of the magma with sulfide facilitates the concentration of metals into smaller volumes of material from which they can later be released, (3) Efficient transfer of metals into hydrothermal fluids that are exsolved from the magmas, and (4) Localized processes trigger the precipitation of ore minerals in the crust.

Otherwise, more than half of the known deposits occur in magmatic arcs, along convergent plate. However, some PCDs and related HS systems can also occurs in postsubduction and collisional tectonic settings expands the range of geological environments and geographical terranes that are prospective for such deposits (Richards, 2009, 2011)

### 1.3.2 Definition

PCDs and related HS deposits are intrusion centered, and are formed by precipitation of ore minerals from hydrothermal fluids (Richards, 2013), typically derived from magmatic arcs formed along convergent plate (Sillitoe, 1972). Porphyry deposits are formed from high-temperature fluids (>500°C; e.g. Wilson et al., 1980; Ulrich et al., 2001). The fluids are exsolved from cooling magmas emplaced in the upper crust (depths of ~5-10 km; Sillitoe and Hedenquist, 2003). They contain Cu, Mo and Au, mainly present as the sulfide minerals pyrite and chalcopyrite, with minor amounts of molybdenite and bornite.

Other elements such as Pb, Zn, Au, and Ag may eventually have economically important concentrations (Sillitoe, 2010). The mineralization is characterized by their large tonnages, relative low ore grades (up to 0.8 wt % Cu), and disseminated ore minerals that occurs within of veinlet stockwork and hydrothermal altered porphyritic intrusions and/or in their immediate wall rocks (Titley, 1966; Lowell and Guilbert, 1970; Seedorff et al., 2005, Sillitoe, 2010). In contrast, the HS deposits are generated in advance argillic lithocaps (Sillitoe, 1995). The HS mineralization contains mainly Au, Ag, and Cu within of pyrite and high sulfidation-state sulfides assemblages typified by enargite, luzonite, digenite chalcocite and covellite (Arribas, 1995). Lithocaps are horizontal to subhorizontal blankets of vuggy residual quartz (extreme base leaching; Stoffregen, 1987) and advanced argillic alteration of hypogene origin (Sillitoe, 1995). These are typically forms at lower temperatures 200°-250°C (Hedenquist and Taran, 2013) and shallow crustal levels (0.2-1 km below the paleowater table: Arribas, 1995; Cooke and Simmons, 2000) over shallow intrusions (Sillitoe, 1995), from highly acidic, oxidized, and sulfur-rich hydrothermal fluids (Arribas et al., 1995; Hedenquist et al., 1998) that may or may not be related to magmatism (Richards, 2013). Lithocaps are spatially (Sillitoe, 1983, 1999), temporally (Arribas et al., 1995), and genetically associated with underlying intrusions (Hedenquist et al., 1998); the latter may be associated with porphyry-style mineralization (Sillitoe, 1999, 2010).

### 1.3.3 Tectonic setting

PCDs and some epithermal Au deposits are formed from hydrothermal fluids exsolved from cooling, water-rich, calc-alkaline magmas emplaced in volcanoplutonic arcs (Hedenquist and Lowestern, 1994; Richards, 2009) at convergent margins (Fig. 1.1), where subduction of an oceanic plate is occurring (such as the circum-Pacific), or has known to have occurred (such as Oyu Tolgoi, Mongolia; Perelló et al., 2001; Fig. 1.2). Large high-sulfidation Au deposits are host at the tops of tectonically thickened crustal section, which were subjected to neutral stress conditions or mild extension (e.g. Yanaocha district; Sillitoe and Hedenquist, 2003; Sillitoe, 2008). In contrast, PCDs are generated mainly in magmatic arcs subjected compressional tectonic regimen (Uyeda and Nishiwaki, 1980; Sillitoe, 1998; Wilkinson, 2013; Fig. 1.1), albeit commonly during stress relaxation (Tosdal and Richards, 2001). Compressional (or transpressive) stresses impedes magma ascent through the upper crust, thus inhibiting volcanism (e.g. Skarmeta et al., 2003; Gow and Walshe, 2005), the resultant shallow magma chambers in these compressional settings are larger (~50 Km<sup>3</sup>; Sillitoe, 2010) than those that form beneath extensional arcs, typified by compositionally bimodal basalt-rhyolite magmatism (Sillitoe 1999, 2003, 2010; Tosdal and Richards, 2001), where chambers at least an order of magnitude larger are needed to produce giant porphyry systems (Dilles, 1987; Cline and Bodnar, 1991; Shinohara and Hedenquist, 1997; Cloos, 2001; Stern and Skewes, 2005). The fractionation of these magma chambers is promoted by their inability to erupt, volatile saturation and generation of large volumes of magmatic-hydrothermal fluids can occur (Sillitoe, 1998). Compression also restricts the number of apophyses that can form on the roof of a large magma chamber (possibly due to the lack of steep extensional faults), providing better, more efficient fluid focusing into a single stock rather than a cluster of intrusions (Sillitoe, 1998). Moreover, compression result in crustal thickening and shorting (Kay and Mpodozis, 2002) with high rates of uplift, exhumation (e.g. Sillitoe, 1998; Cooke et al., 2015; Gow and Walshe, 2005) and erosion promotes efficient extraction and transport of magmatic-hydrothermal fluids due to abrupt decompression

(e.g. Masterman et al., 2005). Worldwide, most deposits tend to occur as clusters or systems uniformly distributed along an arc segment, formed linear belts (Seedorff et al., 2005; Sillitoe, 2010) during very narrow time frames in the life of a magmatic arc (Sillitoe, 1988; Simmons et al., 2013). However, compressive provinces do not seem to host appreciable high-sulfidation mineralization of the same ages as the PCDs despite the presence of extensive advanced argillic lithocaps. The late Eocene-early Oligocene porphyry Cu belt of northern Chile, for example, is characterized by numerous lithocaps, all of them barren (Sillitoe and Hedenquist, 2003).

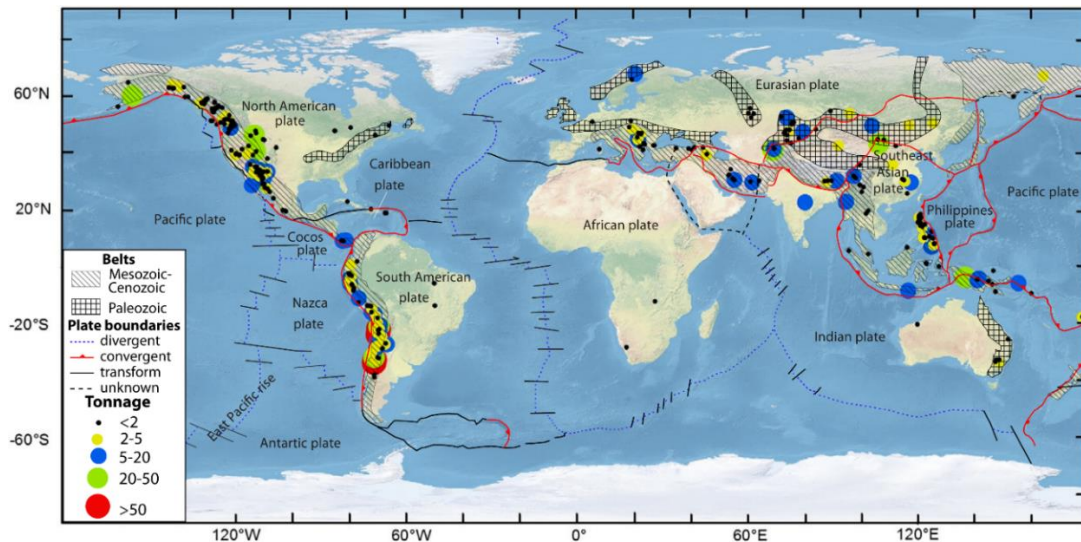


Figure 1.2. Worldwide distribution of porphyry Cu deposits (Sun et al., 2015) and porphyry copper provinces and related mountain belts (Sawkins, 1984), most of the porphyry deposits are distributed along convergent margins. Porphyry Mo deposits are not shown.

#### 1.3.4 Global and temporal distribution

The global spatial distribution of porphyry deposits occur principally within Mesozoic and Cenozoic terrains, less commonly in pre-Mesozoic mountain belts or their eroded roots (Fig. 1.2), becoming increasingly rare with age. The distribution of age of Mesozoic and younger PCDs occur mostly around the Pacific Rim, where is consistent with earlier recognition of the dominance of Cenozoic and Mesozoic deposits (Meyer, 1981; Hunt, 1991). These PCDs display an episodic age, and basically reflects a similar time variation in the intensity of calc-alkaline magmatism along this belt (Sawkins, 1984). An important episode of porphyry copper generation took place, for example, from 74 to 48 Ma ago in the North America Cordillera, but this was followed by a lean period between 48 and 40 Ma ago (Sawkins, 1984). The main episode of such metallization in the Andean Province of South America, the age for most of the deposits ranges from ca. 50 to 3.0 Ma. The youngest episode of PCDs mineralization took place in the southwestern Pacific Island arcs, occurred during Miocene and Pleistocene time (Titley and Beane, 1981; Arribas et al., 1995). More deposits of Paleozoic age (Fig. 1.2), however, are being discovered and developed, for example in the Altaid belt of Eurasia, and the Tasman belt of Australia (Seedorff et al., 2005, and references therein).

The global distribution of porphyry deposits is a complex function of numerous factors, including the uneven distribution of magmatism through time that is related to changes in plate configurations (Burke and Kidd, 1980). The Phanerozoic distribution, however, is

in large part explained in terms of preservation and exposure of deposits (Seedorff et al., 2005).

### 1.3.5 Geological setting

The PCDs and related HS deposits occur in areas displaying a complex geological evolution that includes multiple episodes of faulting, uplifting and erosion, as well as many shallow porphyritic intrusives phases. Despite the complexity of the regions in which these deposits occur, regional studies have revealed that PCDs and related HS deposits in the same districts around the world share many common characteristics, so many geologists have proposed a genetic connection between the two type of deposits.

#### 1.3.5.1 Host rocks

The porphyry copper orebodies are spatially associated with cupolas of high K calc-alkalic stocks (Emmons, 1927; Dilles, 1987; Shinohara and Hedenquist, 1997; Sillitoe, 1997, 1998, 2010; Dilles et al., 2000; Perelló et al., 2003; Seedorff et al., 2005), which represent the supply chambers for the magma and mineralized fluids that formed the vertical elongated (>3 km) stocks, with diameters that range from 0.1 to 1 km (Sillitoe, 2000). The composite stocks span a sequence of intrusive events associated with alteration and mineralization, as well as early porphyries being intruded by inter-mineral and late-mineral phases, a mechanism that causes episodic inflation of the stocks (Sillitoe, 2000). A major problem in determining the primary stock composition in the composite stocks associated with PCDs (e.g. Zentilli et al., 2018), results from the strong and widespread hydrothermal and supergene alterations that mask the composition of these stocks. Moreover, some composite stocks, loci of intrusion may migrate with time so that early, inter-mineral, and late-mineral phases lie alongside one another or are complex intermixed, last one give rise to complex ore distribution patterns (Sillitoe, 2000, and references therein). Nevertheless, Sillitoe (2000) has identified six key criteria to try to effectively subdivide of these composite stocks: (1) veinlets truncated at intrusive contact, where older intrusion will contain more veinlet generations, (2) chilled margins on the margin of the younger intrusions, (3) narrow zones of flow-aligned phenocrysts in the younger intrusion adjacent to the contact, (4) xenoliths in the younger intrusion, either of the older intrusion and/or quartz veinlets xenoliths, (5) better textural preservation and lower vein densities in the younger intrusions, and (6) abrupt changes in metal grades, which are lower in the younger intrusion.

#### 1.3.5.2 Volcanic connections

The batholiths are emplaced chiefly beneath thin covers of their own volcanic ejecta (Hamilton and Myers, 1967; Hamilton, 1969; Thorpe and Francis 1979). Commonly, several discrete porphyry stocks are emplaced in and above the batholith roof zones (Sillitoe, 1972), which are typically of intermediate to felsic composition (Sillitoe, 1973), and generally erupted subaerially ~0.5- 3 m.y. prior to porphyry and mineralization (Sillitoe, 2010). These coeval volcanic rocks may host large HS gold deposits (e.g. Lagunas Norte, Montgomery, 2012; Yanacocha district; Longo et al., 2010; Tantauatay; Gustafson et al., 2004), however, the absence of epithermal mineralization on many PCDs is possibly related to depth of erosion (e.g. Cajamarca region; Gustafson et al., 2004).

#### 1.3.5.3 Wall-rock influences

PCDs are hosted by a wide variety of lithologies, from coeval volcanics, intrusive, sedimentary, and crystalline basement rocks (e.g. Titley, 1993), where wall-rocks with

low permeability, such as marbleized limestone, minimize lateral flow of hydrothermal fluids, thereby focusing rich-metal hydrothermal fluids to the host intrusion and possibly increasing metal concentration (Sillitoe, 2000), or form skarn, carbonate-replacement, and sediment-hosted mineralization types within of reactive carbonates and silty sediment sequences (Sillitoe, 2010). In contrast, large-tonnage HS epithermal deposits are commonly hosted by permeable lithologies, such as: pyroclastic rocks (e.g. Yanaocha district; Longo et al., 2010; Lagunas Norte; Montgomery, 2012). Moreover, bedded tuffs, volcanoclastic sedimentary rocks, and lacustrine mudstone are also able to soak up large volumes of mineralizing fluid to generate major HS deposits (Sillitoe, 1999). However, where volcanic sequences are relatively thin (as in flow-dome complexes as opposed to stratovolcanoes; Sillitoe, 1999) the HS mineralization affected subvolcanic basement, which range from unreactive quartz sandstone (e.g. Montoya et al., 1995; Garay et al., 2012), phillite (e.g. Losada-Calderón and McPhail, 1996), equigranular felsic pluton (e.g. Sillitoe et al., 1996) to receptive calcareous rocks (e.g. Gustafson et al., 2004).

#### *1.3.5.4 Structures*

The preexisting architecture of the basement rocks, the fault systems, and the stratigraphic packages associated with early extensional tectonic settings played a strong role in controlling development of PCDs (Gow and Walshe, 2005). The PCDs are commonly located in the hanging wall of the major thrust faults (Gow and Walshe, 2005), certain structural geometries, such as fault jogs, flexures, step-overs, and fault intersections, offer low-stress extensional volumes during transpressional strain (Richards, 2003; Gow and Walshe, 2005). Such sites represent vertical conduits of relatively high permeability, up which magmas and/or fluid associated will preferentially ascend (Richards, 2003). These dilatant structural settings, evidenced by sheeted (parallel or unidirectional) porphyry-related quartz veinlets that display a strong structural control and may extend considerable distances into the wall rocks (Corbett, 2008)

The formation of characteristic porphyry crackled breccia, radial-concentric veinlets that usually form the stockwork mineralization is evidence of magmatic forces produced especially during second boiling of residual liquids in the largely consolidated igneous rock (Phillips, 1973; Burnham, 1979, 1985; Burnham and Ohmoto, 1980; Sillitoe, 1985; Fournier, 1999).

The shifting location of intrusive centers and major zones of fracture permeability during the evolution of hydrothermal activity is the major factor controlling whether the resultant mineralization-alteration is concentric or asymmetric (Campos, 2002).

In other hand, Many HS deposits commonly contain fault-controlled copper-gold mineralization, such as bodies of vuggy residual quartz, silicification and/or massive pyritic sulfides (Sillitoe, 1999).

#### *1.3.5.5 Porphyry to epithermal HS systems transition zones*

The two deposit types are geologically and mineralogically distinct, but commonly show a close spatial and temporal relationship (Sillitoe, 1983; Arribas et al., 1995; Hedenquist et al., 1998). HS mineralization may be separated from the underlying environment by several hundred vertical meters (Gray and Coolbaugh, 1994), or may be juxtaposed with it or superimposed on it (Sillitoe, 1999). HS mineralization is commonly offset from the surface projection of the causative intrusion (Hedenquist and Taran, 2013). The juxtaposition and superposition of HS on PCDs result from telescoping, generally in response to profound surface degradation by uplift and erosion accompanied

hydrothermal activity (Sillitoe, 1999; Masterman et al., 2005) or, less commonly, volcanic collapse during the hydrothermal lifespans of systems (Sillitoe, 1994). Telescoping of HS over PCDs is controlled by zones of maximum permeability, which was provided by syn-mineral faults (Lindsay et al., 1995; Sillitoe et al., 1996).

The zones of transition between PCDs and HS deposits is recognized in several mineral districts such as: Lepanto-Far Southeast in the Philippines (Arribas et al., 1995; Hedenquist et al., 1998), Maricunga belt in northern Chile (Vila and Sillitoe, 1991; Vila et al., 1991; Mpodozis et al., 1995; Muntean and Einaudi, 2000, 2001; Sillitoe et al., 2013; Valdivia et al., 2014) and Cajamarca region in northern Peru (Pinto, 2002; Gustafson et al., 2004; Noble et al., 2004; Davies and Williams, 2005) (see below).

#### *1.3.5.6 Alteration-mineralization zoning*

Mineral associations are commonly reported as mineral assemblages in the geologic literature (Seedorff et al., 2005). A hydrothermal mineral association is a group of minerals that occurs together, regardless of whether the mineral formed at the same time or in local equilibrium and may have been formed during a variety of overprinting events (Seedorff et al., 2005). A mineral assemblage, however, is a group of minerals that formed contemporaneously in geochemically similar environments and are stable together (Meyer and Hemley, 1967). Thus, a mineral assemblage provides a convenient indicator of the local thermodynamic equilibrium in that system, whereas a mineral association may reflect a paragenetic overprint of two or more mineral assemblages (Longridge, 2016).

The controls on the development of these alteration assemblages can be considered more quantitatively using phase diagrams (Fig. 1.3). Magmatic fluids have a low KCl/HCl ratio and pH which causes K-metasomatism of the rock (Fig. 1.3). This K-metasomatism can manifest itself in various ways, depending on the host rock mineralogy. In more felsic host rocks, plagioclase phenocrysts are altered to orthoclase and hydrothermal biotite may form around, and partly replace, magmatic biotite. The MgO can be added to model mafic wall rocks or minerals (Figs. 1.3 B to F). The advanced argillic environment (low values of  $a_{K^+}/a_{H^+}$ ) is characterized by adalusite, pyrophyllite, and kaolinite together with cordierite (high temperature), chlorite, and biotite (low temperature). Sericitic environment (intermediate values of  $a_{K^+}/a_{H^+}$ ), muscovite can be joined by chlorite and rarely biotite (Seedorff et al., 2005; Figs. 1.3C to E). Potassic environment (high values of  $a_{K^+}/a_{H^+}$  and relatively low values of values of  $a_{Mg^{2+}}/a_{H^+}^2$ ), can contain K-feldspar, K-feldspar and biotite, or biotite only. Cordierite and chlorite could also be part of the potassic alteration assemblages at high and lower temperatures, respectively (Tittley and Beane, 1981). Propylitic alteration plots along the chlorite-K-feldspar phase boundary (Fig. 1.3A), which is characterized by presence of relict K-feldspar, if present in the original rock, with albite, calcite, epidote, and a dusting of sericite or illite as alteration products of plagioclase (Seedorff et al., 2005). Actinolite, epidote, and chlorite with local relict biotite are also present (Fig. 1.3A). Intermediate argillic alteration, a key feature is the presence of relict alkali feldspar in K-rich rocks. Illite (sericite) and chlorite, together with kaolinite, illite-smectite, and smectite are also present, where sericite and/or pyrophyllite are absence the intermediate argillic alteration is restricted to temperatures below to 200°C (Seedorff et al., 2005; Fig 1.3A).

An assemblage that plots in a phase boundary can be defined as transitional between the various types adjacent to the boundary (Seedorff et al., 2005), for example, pyrophyllite



should occur with and outboard of sericitic alteration in the porphyry environment (Hemley and Hunt, 1992; Fig. 1.3).

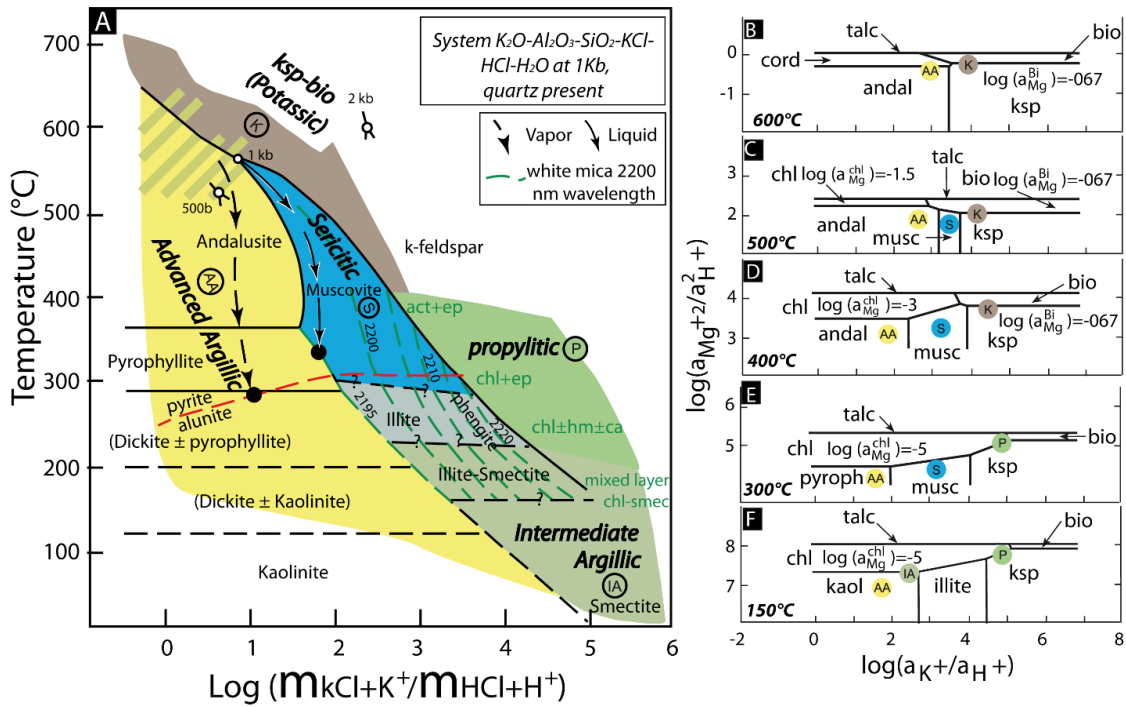


Figure 1.3. **A**. Phase diagram for the system  $K_2O-Al_2O_3-SiO_2-H_2O-KCl-HCl$  at atmospheric pressure. The labelled areas broadly correspond to alteration assemblages (Dilles et al., 2014 from Montoya and Hemley, 1975; Hemley et al., 1980). Dashed green lines represent white mica 2200 nm wavelength (Dilles et al., 2014). The approximate stability of alunite-pyrite coexistence (Hedenquist et al., 1998 from Geggenbach, 1997). Fluid pathway for magmatic liquids (solid arrow) and vapours (dashed arrow) involved in the formation of argillic alteration (Hedenquist et al., 1998). **B** to **F**, note that chlorite, cordierite and biotite stability fields are based on a simple solid solution model for their Mg end members (Seedorff et al., 2005). Abbreviated mineralogy according to Seedorff et al. (2005).

*Porphyry environment*

Porphyry Cu deposits display a consistent, broad-scale alteration-mineralization zoning pattern (Sillitoe, 2010). The zoning comprises, centrally from the bottom upward, several of sodic-calcic, potassic, propylitic, sericitic (or phyllic; Lowell and Guilbert, 1970), intermediate argillic and advance argillic (cf. Meyer and Hemley, 1967, Fig. 1.3). Moreover, chlorite-sericite alteration (Hedenquist et al., 1998, after Sillitoe and Gappe, 1984) or late argillic alteration (Halley et al., 2015) develop between the potassic and sericitic alteration zones (Fig. 1.4). However, advanced argillic alteration are much less well developed in porphyry copper deposits associated with alkaline than with calc-alkaline intrusion (Lang et al., 1995; Sillitoe, 2002, 2010; Holliday and Cooke, 2007), reflecting control of the  $K^+/H^+$  ratio by magma chemistry (Burnham, 1979). Different Cu-Fe sulfide mineral assemblages are associated to each alteration type (Sillitoe, 2010; Fig. 1.4), due to the direct link between sulfidation stage, the principal control on sulfide assemblages, and solution pH, a principal of alteration type (Barton and Skinner, 1967; Meyer and Hemley, 1967; Einaudi et al., 2003).

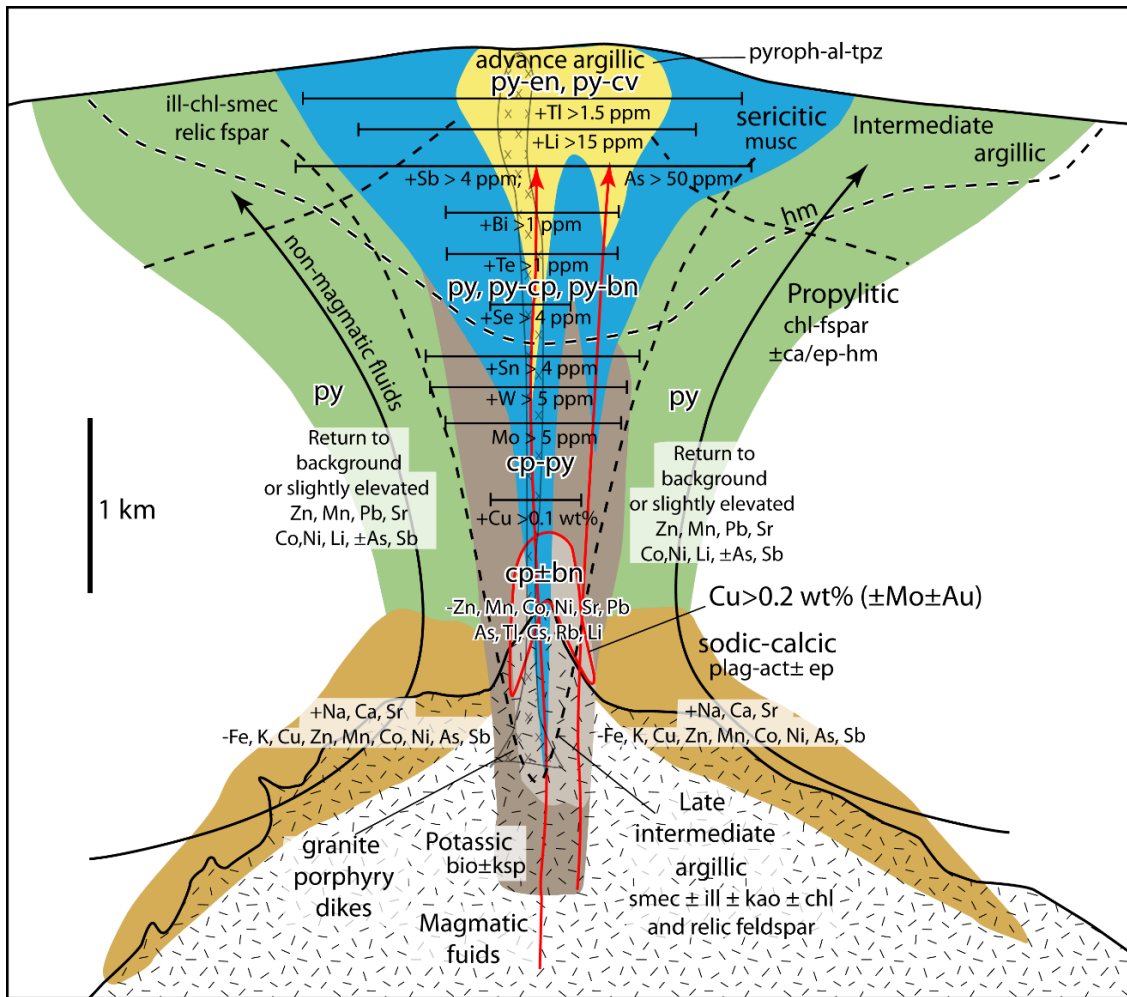


Figure 1.4. Schematic vertical cross section of hydrothermal alteration zoning and metal distribution in porphyry deposits (Halley et al. 2015) for a non-telescoped porphyry copper system. Include representation of generalized alteration-mineralization sequence in porphyry copper systems in relation paleodepth and system life span (Sillitoe, 2010).

The deepest alteration and most proximal to an intrusion is sodic-calcic alteration, commonly magnetite bearing and Cu-Fe sulfides poor. This grades to potassic alteration with biotite and k-feldspar alteration minerals which typically fringes the porphyry intrusion and forms a dome and is often coincident with hypogene ore mineralization (chalcopyrite ± bornite; Fig. 1.4). In some bornite-rich centers, the sulfidation state is low enough to stabilize digenite ± chalcocite (Einaudi et al., 2003). Chlorite-sericite (late intermediate argillic) alteration overprint preexisting potassic assemblages (Sillitoe, 2000; Fig. 1.4). This alteration is characterized by partial to complete transformation of mafic minerals to chlorite, plagioclase to sericite and/or illite, and magnetite and hydrothermal magnetite to specular hematite (Sillitoe, 2000), together with chalcopyrite and pyrite. Potassic and chlorite-sericite alterations typically grades into sericitic alteration which may be structurally controlled. Sericitic alteration may be subdivided into two different types (Sillitoe, 2010): (1) early greenish to greenish-gray sericitic alteration, which is centrally located and hosts a low sulfidation-state chalcopyrite-pyrite assemblage, and (2) late white sericitic alteration has varied distribution patterns in porphyry copper deposits (Sillitoe, 2010), such as may constitute annular zones separating the potassic cores from

propylitic halos (Lowell and Guilbert, 1970). The sericitic alteration is commonly pyrite dominated, where appreciable Cu remains with pyrite and/or chalcopyrite, or as high sulfidation-state assemblages with higher Cu contents (Sillitoe, 2010), such as: pyrite-bornite, pyrite-chalcocite, pyrite-covellite, pyrite-tennantite, and pyrite-energite (Einaudi et al., 2003), resulting in hypogene enrichment (Brimhall, 1979), although any Au may be depleted (Sillitoe, 1999).

Propylitic and advance argillic alteration assemblages occur more distal to the porphyry intrusion and mineralization (Fig. 1.4). The last one, may overprint the upper parts of porphyry copper deposits, where sericitic alteration is transitional upward to quartz-pyrophyllite (Sillitoe, 2010). The final distribution of the alteration assemblages is typically more complicated by changes in hydrology resulting from the emplacement of multiple intrusions, regional uplift and erosion and the development of structures.

#### *Porphyry to epithermal transition zones*

The zones of transition are typically characterized by downward changes from advanced argillic to sericitic alteration, over structurally controlled areas (Sillitoe, 1999; Fig. 1.3A). Advance argillic alteration is commonly dominated by quartz-alunite alteration with variable anhydrite-diaspore-dickite-pyrophyllite (Meyer and Hemley, 1967). In the deepest parts of other HS mineralized zones, sericite may be accompanied by dickite (Corbett and Leach, 1998) or pyrophyllite (Sillitoe et al., 1996). Pyrophyllite can form in two distinct situation (Hedenquist et al., 1998 and references therein): (1) ground-water absorption of volcanic vapor forms very acidic water, producing silicic and quartz-alunite alteration and (2) later situation occurs in fluid-dominated systems and might be expected during retrograde hydrolytic (sericitic) alteration as fluid cools, potentially forming alunite as well (Fig. 1.3A).

At Andes of Peru (Cajamarca region), porphyry-epithermal transition zones are defined by quartz-pyrophyllite alteration rocks with irregular white patches (ovoidal/mottled) of alunite and pyrophyllite that replace the quartz matrix and grade into wormy-shaped clots and discontinuous veinlets (Pinto, 2002), termed patchy (ovoidal; Noble et al., 2011) and wormy (mottled; Noble et al., 2011); texture alteration (also termed gusano; Gustafson et al., 2004). Ovoidal/mottled texture is characterized by ovoids of hydrous aluminum silicate/sulfate minerals such as pyrophyllite and alunite associated with variable amounts of pyrite and energite or covellite set in a typically fine-grained matrix of quartz or chalcedony (Noble et al., 2011). A transition from ovoidal and deeper mottled texture alteration to A-type quartz veinlets occurs in shallow porphyry environment at  $\leq 150$  m depth (e.g. Kufertal porphyry; Gustafson et al., 2004). Moreover, banded quartz veinlets also occur within a narrow vertical range above and overlapping the top of A-quartz veinlets and generally cut A-quartz veinlets (e.g. Yanacocha distric; Gustafson et al., 2004; Maricunga belt; Muntean and Einaudi, 2000). In overall, the mottled quartz-pyrophyllite-alunite overlies sericitic (muscovite) alteration, which in turn overlies deeper biotite-bearing potassic alteration containing pyrite, chalcopyrite and bornite (Longo et al., 2010).

#### *HS epithermal environment*

*Deep HS mineralization:* Contains bodies with silicic alteration in form of brecciated, massive, or residual quartz, which occurs within of advance argillic alteration (Hedenquist et al., 1998; Sillitoe, 1999), and overlying intermediate argillic alteration (Madera and Rohrlach, 1998). Vuggy quartz-pods and -breccia pipes (Stoffregen, 1987) are located by the top of the porphyry stocks (Sillitoe, 1999), such as banded quartz

veinlet are located on the top of a burial porphyry system (Muntean and Einaudi, 2000; Gustafson et al., 2004), both structures contain Cu and Au mineralization. Moreover, at the root of the HS systems, ovoidal- and mottled-textures are found in Andes of Peru characterized by Au and/or Cu mineralization within of enargite in As-rich HS systems and covellite in As-poor HS systems (Noble et al., 2011). These textures spans the interval between root of the HS systems and roof of the PCDs (Gustafson et al., 2004; Noble et al., 2011). The deep parts of the HS environment contains hypogene high-sulfidation state sulfides such as: bornite, digenite, chalcocite, and covellite, and subordinate enargite and chalcopyrite (Sillitoe, 1999). These Cu-rich sulfides are commonly present as partial replacements of dispersed pyrite, with resulting textures that mimic those typical of supergene copper sulfide enrichment (Sillitoe, 1999).

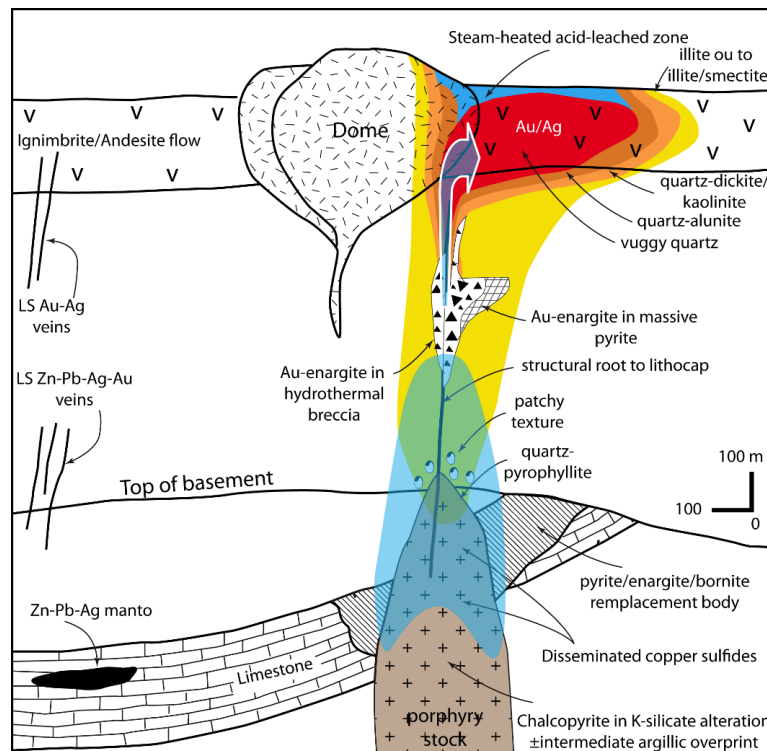


Figure 1.5. Schematic reconstruction of a dome-related HS system separated spatially from the underlying porphyry copper environment (Sillitoe, 1999). Note the upward changes from copper to gold/silver and fault-controlled to disseminated mineralization. The paleosurface is marked by acid-leached rock of steam-heated origin.

*Intermediate-depth HS mineralization:* HS mineralization hosted by bodies of vuggy residual quartz and/or semi-massive to massive pyritic sulfides. They are alteration products of pre-existing rocks, with any space-filling being confined to hydrothermal breccias and cavities, and may be encountered in intermediate depths, in the deep epithermal environment (Sillitoe, 1999). The vuggy quartz occurs as moderately dipping to steep, roughly tabular, fault-, fracture-, or lithologically-controlled ledges (Gray and Coolbaugh, 1994; Sillitoe et al., 1998). HS mineralization typically occur lining voids or in cross-cutting microveinlets and are accompanied by minor kaolinite (Stoffregen, 1987). However, some these are nearly complete supergene oxidation preclude proper determination of the sulfides presents in the cavities (Sillitoe, 1999). The massive sulfides commonly occurs as fault- and fracture-controlled veins (Jannas et al., 1990). Massive

sulfides veins are dominated by Fe sulfides, which include an early massive, fine-grained, locally banded variety (Sillitoe, 1983) as well as latter coarse-grained generation of pyrite. In this deep HS mineralization is dominated by enargite accompanied by subsidiary quantities of luzonite, tennantite and Cu sulfides (covellite, chalcocite, digenite). Cu sulfides predominate at deeper levels (Sillitoe, 1999). Gold and several tellurides minerals are paragenetically late and precipitates during or after partial replacement of enargite by tennantite and chalcocopyrite, indicative of lower sulfidation-state fluid (Sillitoe, 1999).

*Shallow HS mineralization:* HS mineralization in shallow epithermal environment is still structurally controlled, fault- and fractured-fed fluids under relatively low hydrostatic pressure conditions are capable of permeating large volumes of porous or network fractures (Sillitoe, 1999). Lithological permeability and hydrothermal brecciation play much more important roles (Sillitoe, 1999). The mineralized breccias are likely to be generated by self-sealing of upflow conduits by quartz deposition and the consequent overpressuring of ascendant two-phase fluids (Sillitoe, 1999). Such mineralized breccias are therefore inter-mineral in timing, and they commonly contain clasts of vuggy residual quartz, typically a product of early low-pH fluids in HS systems. Hydrothermal breccias with matrices composed of alunite or even intergrown alunite and barite may, however, also be well mineralized (Sillitoe, 1999). Barren flour-cemented breccias are late in HS systems.

Several shallow epithermal HS gold deposits have been show to terminate abruptly downwards, generally as minor quartz pyrite veinlets with low gold contents, which suggests that the bases of these deposits may represent the sites at which acidic fluid was initially generated as the result of meteoric water absorption of ascendant magmatic volatiles (Sillitoe, 1999).

In shallow HS bodies are dominated by enargite and covellite (without Fe sulfides), although luzonite, stibnite-bismuthinite and sphalerite are widely reported (Sillitoe, 1999, and references therein).

Barren acid-leached zones formed in the steam-heated environment above paleo-water tables may be preserved above or alongside shallow HS deposits, and occurs as massive chalcedonic quartz after original opal (Sillitoe, 1999). Mineralized vuggy quartz and massive sulfide seen to be stable during this process, but the argillic haloes to mineralization are readily transformed to fine-grained cristobalite and/or alunite (Sillitoe, 1999).

#### *1.3.5.7 Metal zoning*

The Cu-Mo-Au mineralization of a porphyry deposit is intrinsically linked to igneous processes (Wilkinson, 2013). The process involved in transporting and precipitating metals into ore. The ore mineral may be found completely within the coeval porphyry intrusions (Tsang et al., 2018), partially in the porphyry intrusions and partially within the wall-rock (Berger et al., 2008) or in the wall-rock only. The ore precipitation are principally controlled by fluid chemistry and fluid:rock interactions. This is demonstrated by the concentric zoning surrounding porphyry deposits (Jones, 1992), which viewed in vertical cross section may show gradational zonation (Halley et al. 2015, Fig. 1.4). This zonation of metals can be used as a vector toward the central ore zone, for example: some many porphyry deposits show an increase in Ag/Au outward, and highest Au grades are centrally located and associated with lowest Ag/Au. Thus Ag/Au ratios are useful zonal indicator and can be used as a vector for Au potential (Seedorff et al., 2005). However,

initial gold distribution can be significantly modified by late-stage remobilization and redeposition (Jones, 1992). Other metal ratios, particularly Pb/Cu, Pb+Zn/Cu, and Cu/Au are also useful for clarifying zoning patterns and, in conjunction with structure and stratigraphy, can be used to define and evaluate specific exploration targets (Jones, 1992).

#### *1.3.5.8 Longevity of porphyry and HS ore formation*

Determining the absolute duration of the genetic magmatic-hydrothermal processes occurring in these deposits is fundamental to understanding how they form and instrumental to the development of genetic models to explore a category of mineral deposits (Chiaradia et al., 2013). Accurately measuring the age and duration of these magmatic-hydrothermal events has been the focus during the last decade in the field and analytical studies, using combinations isotopic system (Seedorff et al., 2005; Chiaradia et al., 2013; Richards, 2018). The methods most commonly used have been U-Pb (Dilles and Wright, 1988; Sillitoe and Mortensen, 2010; Li et al., 2017), Re-Os (Stein et al., 1998; Chang et al., 2017),  $^{40}\text{Ar}/^{39}\text{Ar}$  (Marsh et al., 1997), and K-Ar (Arribas et al., 1995). The life span of porphyry deposits and approximate mineralization introduction can be determined by using only traditional U-Pb zircon dating, where the alteration and mineralization are bracketed by a precursor pluton and a late, post-mineralization porphyry body (Sillitoe and Mortensen, 2010). However, limited by the precision (~2%) of in situ U-Pb zircon analysis (Li et al., 2017 and references therein). A high-precision (‰ level) dating technique, such as chemical abrasion-isotope dilution-thermal ionization mass spectrometry (CA-ID-TIMS) zircon U-Pb geochronology, makes it possible to refine the time frame and timescales of porphyry copper systems (von Quadt et al., 2011; Li et al., 2017).

The most uncomplicated approach to constrain the timing and duration of ore-forming events is by dating ore assemblages directly (Li et al., 2017). The ubiquitous distribution of molybdenite in porphyry Cu-Mo deposits and advances in molybdenite Re-Os geochronology permit precise dating of the ore-forming event(s) directly (Deckart et al., 2013; Stein, 2014; Spencer et al., 2015; Li et al., 2017).

High resolution  $^{40}\text{Ar}/^{39}\text{Ar}$  dating, make the isotopic method most precise available for dating magmatic and hydrothermal minerals (K-bearing) from porphyry and epithermal deposits of Cenozoic age (Marsh et al., 1997), with relatively low closure temperatures for argon isotopes (e.g.  $320 \pm 30$  °C for biotite closure temperature; Harrison et al., 1985; McDougall and Harrison, 1999). The method provides high precision, in some case as much as six times greater than the precision of the K-Ar method for similar type of minerals (Marsh et al., 1997). Hence,  $^{40}\text{Ar}/^{39}\text{Ar}$  ages not necessarily measure the crystallization magma ages or early high-temperature hydrothermal alteration events in the porphyry environment (Maksaev et al., 2004; Harris et al., 2008; Deckart et al., 2013). These last precise isotopic methods (Re-Os,  $^{40}\text{Ar}/^{39}\text{Ar}$ , and K-Ar) typically document shorter life spans because it is more difficult, if not impossible, to date the full sequence of events involved in porphyry copper formation (Sillitoe and Mortensen, 2010) and epithermal Au-Ag orebodies, such as: K-Ar dating of the Lepanto-Far Southeast epithermal and porphyry systems, Philippines yielded a hydrothermal duration of 300 ka (Arribas et al., 1995), and  $^{40}\text{Ar}/^{39}\text{Ar}$  dating of the Potrerillos district, Chile (Marsh et al., 1997) and telescoped Yanacocha-Kupfertal systems, Peru (Longo et al., 2010) yielded a hydrothermal duration of 0.8 and 1.5 m.y., respectively.

Therefore, the use of integrated geochronology approached will allow to obtain a more robust age of magmatic-hydrothermal of ore-forming events.



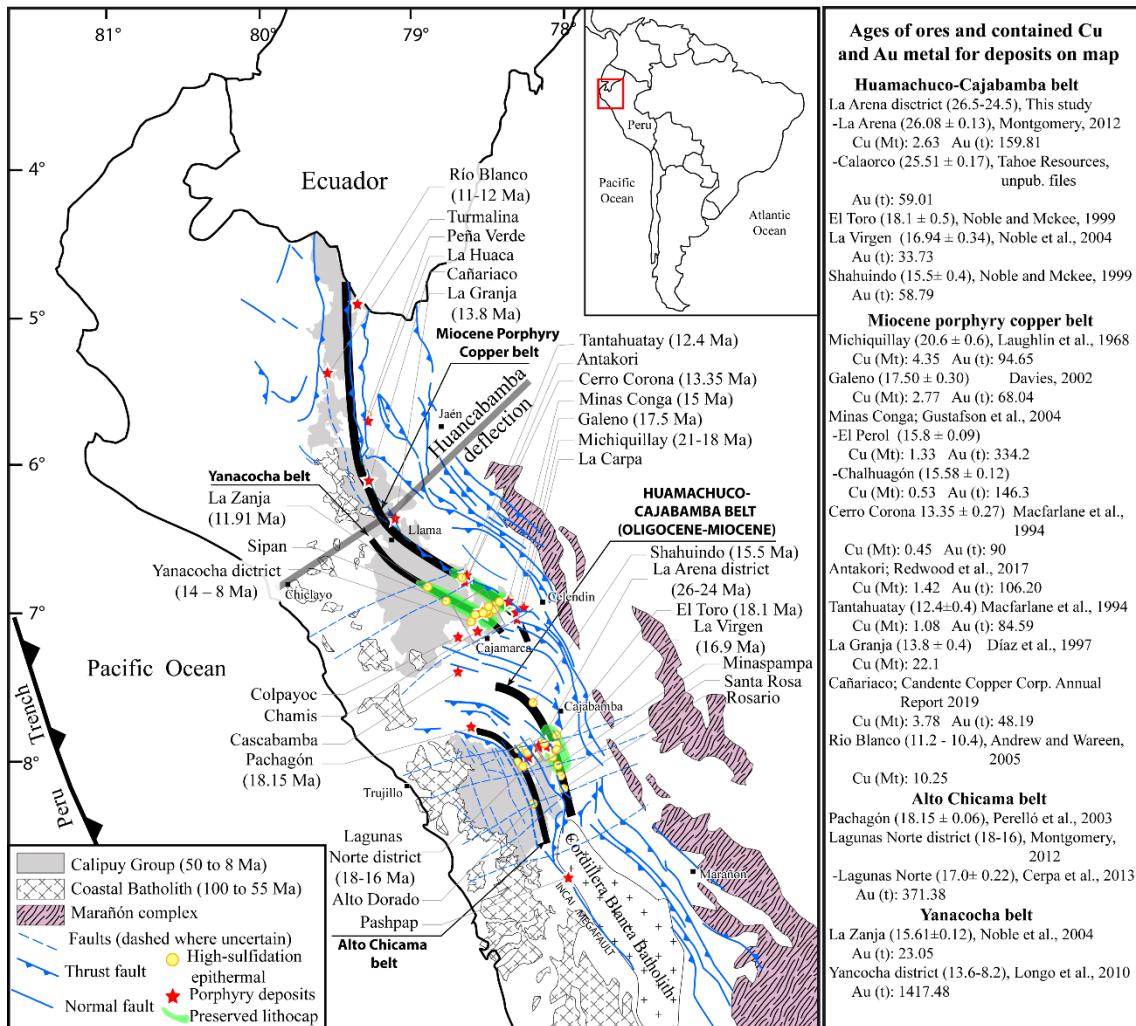


Figure 1.6 Map showing the location of the Huamachuco-Cajabamba belt relative to other regional zones of important high-sulfidation epithermal deposits, porphyry copper systems and preserved lithocaps across Northern Andes of Peru. Also show are the main structures geological together with Marañón Complex, Coastal and Cordillera Blanca batholiths and Calipuy Group belts. Modified from Noble and McKee (1999).

### 1.4 Porphyry-epithermal deposits in northern Peru

In the year 2018, copper production in Peru was at about 2.440 million metric tons (Mt), representing near 11.8 % of the world's total production, on other hand, gold production was reported at 145 metric tons, making up 4.4% of the global production (<https://www.usgs.gov/centers/nmic/gold-statistics-and-information>). This has made Peru the world's second and sixth copper and gold producer, respectively. Nearly 60 % of the copper was recovered from eight porphyry copper in production today, including four (Toquepala, Cuajone, Quellaveco, and Cerro Verde-Santa Rosa) of the world's richest and largest porphyry Cu (Mo-Ag), which was emplaced during the Paleocene (53-58 Ma) in southern Peru (Clark et al., 1990; Simmons et al., 2013). While, more half of gold recovered (~76 tons) came from two Miocene large high-sulfidation epithermal districts of northern Peru (Lagunas Norte and Yanacocha; Fig. 1.6). In addition to the working mines, more than 55 porphyry copper and 36 high-sulfidation epithermal prospects are known, ranking Peru as the third-largest and fifth country of world's copper and gold reserves, respectively (<https://www.andina.pe>). This includes, in particular, the world-class high-sulfidation epithermal and porphyry deposits (Fig. 1.6).

Many of the porphyry occur in Andes of Peru and are genetically and spatially related to Paleocene-Eocene (southern Peru) and late Oligocene-Miocene (northern Peru; Fig. 1.6) porphyry stocks, which range in composition from diorite to monzonite in Paleocene-Eocene porphyry Cu-Mo deposits and from diorite to quartz diorite in Oligocene - Miocene porphyry Cu-Au-(Mo) systems. The porphyries are normally much younger than their host rocks and are emplaced in igneous, Cretaceous sedimentary and/or Pale- and Meso-proterozoic metamorphic rocks. Porphyry stocks emplaced in sedimentary rocks include other varieties of mineralization style such as: polymetallic skarn Zn - Pb - Ag (Au - Cu) mineralization (e.g. El Perol), and/or superjacent high- and intermediate-sulfidation epithermal mineralization (e.g. La Arena, Cerro Corona, Minas Conga, Tantahuatay, Antakori, and others; Fig. 1.6).

Andean evolution seems to be more directly controlled by plate convergence, where Nazca oceanic plate beneath the South American continental plate (Coira et al., 1982; Thorpe, 1984; Allmendinger et al., 1997; Ramos and Aleman, 2000; Fig. 1.2), characterized by: 1) a relatively fast convergence rate shortly followed by 2) a drastic decrease of this rate (Bertrand et al., 2014). This evolution involves the alternation of transtensional regimes characterized by extensional and strike slip faults associated with essentially effusive magmatism, and transpressive regimes (Campos, 2002), dominated by intense fold and thrust development in the Cretaceous sedimentary rocks is the oldest evidence for Andean-type subduction in the Cajamarca region (Davies, 2002).

Basically basaltic to rhyolitic volcanic rocks (Atherton et al. 1985) and coeval plutonic bodies were emplaced in the northern Peruvian magmatic arc (Llosa et al., 1996). This magmatic arc define metallogenetically-distinct lithotectonic belts, each has an associated system of thrust faults parallel to their longitudinal axes, also each emplaced during a discrete time interval and associate to a characteristic metallogenic province such as (Fig. 1.6): Huamachuco-Cajabamba belt (26-15 Ma), Miocene porphyry copper belt (23-12 Ma), Alto Chicana belt (18-16 Ma), and Yanacocha district belt (12.4-8.4 Ma). The magmatic hydrothermal activity development during the late Oligocene (26-23 Ma), gave rise to medium high- sulfidation epithermal deposits (e.g. Calaorco with 59.01 t Au; Tahoe Resources Inc. Annual Report 2018), and very large porphyry copper- gold  $\pm$  molybdenite at La Arena with 2.6 Mt Cu and 159.81 t Au (Tahoe Resources Inc. Annual Report 2018). In contrast, during the early- to late Miocene period (23-9 Ma), represents by far the most important metallogenetic episode along the northern Peruvian arc as a whole (Fig. 1.6). Magmatic-hydrothermal activity at this time was responsible for the emplacement of the world-class high-sulfidation epithermal Au deposit cluster (Lagunas Norte containing 371.38 t Au; Cerpa et al., 2013; Yanacocha with more than 1417.48 Au; Longo et al., 2010). Moreover, mid- to Late Miocene magmatic and hydrothermal activity generated the formation of supergiant porphyry copper-molybdenum (e.g. La Granja with 22.1 Mt Cu; <https://www.riotinto.com/default.aspx>; Rio Blanco with 10.2 Mt Cu; <https://rioblanco.com.pe>), giant to large copper- gold  $\pm$  molybdenite (Michiquillay with 4.35 Mt Cu and 94.65 t Au; Davies, 2002; Cañariaco with 3.78 Mt Cu and 48.19 t Au; Candente Copper Corp. Annual Report 2019; Galeno with 2.77 Mt Cu and 68.04 t Au; Davies, 2002; Cerro Corona with 0.45 Mt Cu and 90 t Au; Longridge, 2016), and very large gold-rich porphyry deposits (Minas Conga with 1.86 Mt Cu and 481.5 t Au; Gustafson et al., 2004), based on the size classification proposed by Clark, 1993 (Fig. 1.6).



## Chapter 2

# Geological setting of the La Arena district

### 2.1 Introduction

The principal aim of this chapter is to outline the geological setting of the La Arena district in the context of the tectonic-magmatic development of the Northern Peruvian margin.

This setting is developed to provide a spatial and temporal distribution of the La Arena and surrounding deposits.

### 2.2 Location and access

The La Arena district is located in the Andes Cordillera of northern Peru ( $7^{\circ}53'31.15''$  Lat. S and  $78^{\circ}07'59.44''$  Long. W), approximately 18 km southwest of the Huamachuco town and 13 km ENE of Lagunas Norte mine in northern Peru (Figs. 1.6, 2.1). The La Arena site is accessible by road from the city of Trujillo to Huamachuco or by road from the city of Cajamarca to Cajabamba and then to Huamachuco.

Geomorphologically, the La Arena-Calaorco deposits is situated in the eastern slope of the Andean Cordillera, close to the continental divide. At the southeastern margin of the La Arena-Calaorco deposits discloses several isolated hills, with a maximum elevation of 4,160 m (a.s.l.) is the Belen porphyry prospect peak, surrounded by Quaternary alluvial plains represent the lowest altitude of about 3,300 m (a.s.l.). Together they make up a geomorphological depression, where was influenced by Andean orientation structure (strike  $\sim 325^{\circ}$ ), which are controlling the spatial distribution of most of the high-sulfidation epithermal deposits and other styles of mineralization, including the La Arena porphyry.

### 2.3 Geological setting

La Arena mineral district is a metallogenic province of Oligocene-Miocene age (Noble and McKee, 1999), and contains copper and gold-bearing mineral deposits, such as porphyry copper-gold, high-, intermediate- and low-sulfidation epithermal and gold-bearing quartz veins, which are hosted within Triassic and Cretaceous marine and continental sedimentary sequences and volcanic rocks (Gauthier et al., 1999). These bedded units undergo thin-skinned movement with compression in a SW-NE orientation during late Cretaceous to Eocene (Mégard, 1984; Benavides-Cáceres, 1999). During the late Middle Eocene (43-42 Ma) fold and thrust was developed in Andes (Benavides-

Cáceres, 1999), where Huamachuco was a deflection zone between Andean- and Chimuanes- trend structures (Steinmann, 1929; Hollister, 1977). Andean structure rotates from NNW to near E-W (Megard, 1984; Fig. 1.6), forming the major echelon structure of the deformed belt, Cajamarca curvature, and the N-S compression (Benavides-Cáceres, 1999), intruded by magmatic phases associated with Calipuy Group (Mégard, 1984; Benavides-Cáceres, 1999; Scherrenberg et al., 2016) during lower Oligocene-to-Middle Miocene (Montgomery, 2012). The first magmatic events are represented by the emplacement of small dacite porphyry Milagros ( $29.54 \pm 0.84$  Ma, Montgomery, 2012) at Lagunas Norte and gabbroic dykes ( $29.4 \pm 1.4$  Ma, Davies 2002) along sub-vertical faults at Cajamarca districts, which may correspond to a period of regional upper crustal relaxation and/or extension (Sébrier and Soler 1991; Davies 2002). These magmatism stages are coincident with break-up of the subducting Farallón Plate between the Cocos and Nazca plate (Lonsdale, 2005) and the ensuing fast convergence ( $\geq 110 \pm 8$  mm/a; Pardo-Casas and Molnar, 1987; Somoza, 1998) of the Nazca and South American Plates, which accelerated the shortening and uplift of the Andes from 28-26 Ma (Aymar regional compression; Sebrer et al., 1988; Sandeman et al., 1995; Jaillard et al., 2000), this age is close to age of the onset of sub-Andean shortening in northern Peru (~30-24 Ma) revealed by low-temperature thermochronology and balanced cross section (Eude et al., 2015). Shortening age is close to magmatic-hydrothermal activity recorded at La Arena and Lagunas Norte districts commenced at ~26 Ma and persisted episodically to 12.4 Ma (Montgomery, 2012) within west-vergent thick-skinned deformation associated with mineral deposits formation such as world's largest zinc, skarn copper, porphyry copper, epithermal gold deposits (~20-0 Ma; Scherrenberg et al., 2016).

At La Arena district, sedimentary sequences are intensely deformed, characterized by moderate, vertical and overturned strata, mesoscale vertical to east-vergent folds of NW-trending, which can be followed for hundreds of kilometers (Fig. 2.1). The shales of the Jurassic Chicama Formation are affected by smaller disharmonic folds, in contrast Chim quartz sandstone and upper strata are affected by regional-scale anticlines. The major antiforms in La Arena district are two NW-SE trending axes that are projected outside the district by more than 70 km in length and 5 km in width (Fig. 2.1), formed as a resulted of NE-SW subduction-related compression stress. This folds are undergone thrust faults that have developed out of the cores of antiforms, then these fold are affected by N-S compression (Benavides-Cáceres, 1999). The north part of La Arena deposit has faults that are oblique to the EES-WWN-striking folds with a sinistral displacement. At the core of the overthrust fold there are shales and quartz sandstone of the Chicama and Chim Formations, respectively. A strongly elliptical porphyry complex with the long axis at Andean orientation (Fig. 2.1), which is inferred to be related to high-sulfidation mineralization, is also present (Gauthier et al., 1999; Bussey y Nelson, 2011; Garay et al., 2012). Although only a few high-sulfidation deposits appear to have formed during compression (Sillitoe and Hedenquist, 2003), the high-sulfidation and porphyry systems located in La Arena district, such as Calaorco, La Arena, Alizar, and Agua Blanca were generated during regional transpressive tectonic regimes (cf. Sillitoe, 1997, 1998; Corbett and Leach, 1998). That must have taken place during stress relaxation in the magmatic arc (cf. Tosdal and Richards, 2001), acted as a trigger for the rapid and forceful emplacement of fluids responsible for copper and gold mineralization in the La Arena district deposits (Corbett, 2014).

## 2.4 Geology of the La Arena District

The geology of the La Arena district has been summarized by Gauthier et al. (1999), Quirita and Gauthier (2000), KMC (2011), Montgomery (2012). There are two main units in the district: (1) a late Jurassic to early Cretaceous basement consisting of sedimentary rocks; and (2) the Oligocene-Miocene Calipuy Group lavas, pyroclastic rocks and coeval hypabyssal intrusive bodies. The last unit is related with introduction of copper, gold and/or molybdenum mineralization at La Arena and Lagunas Norte districts.

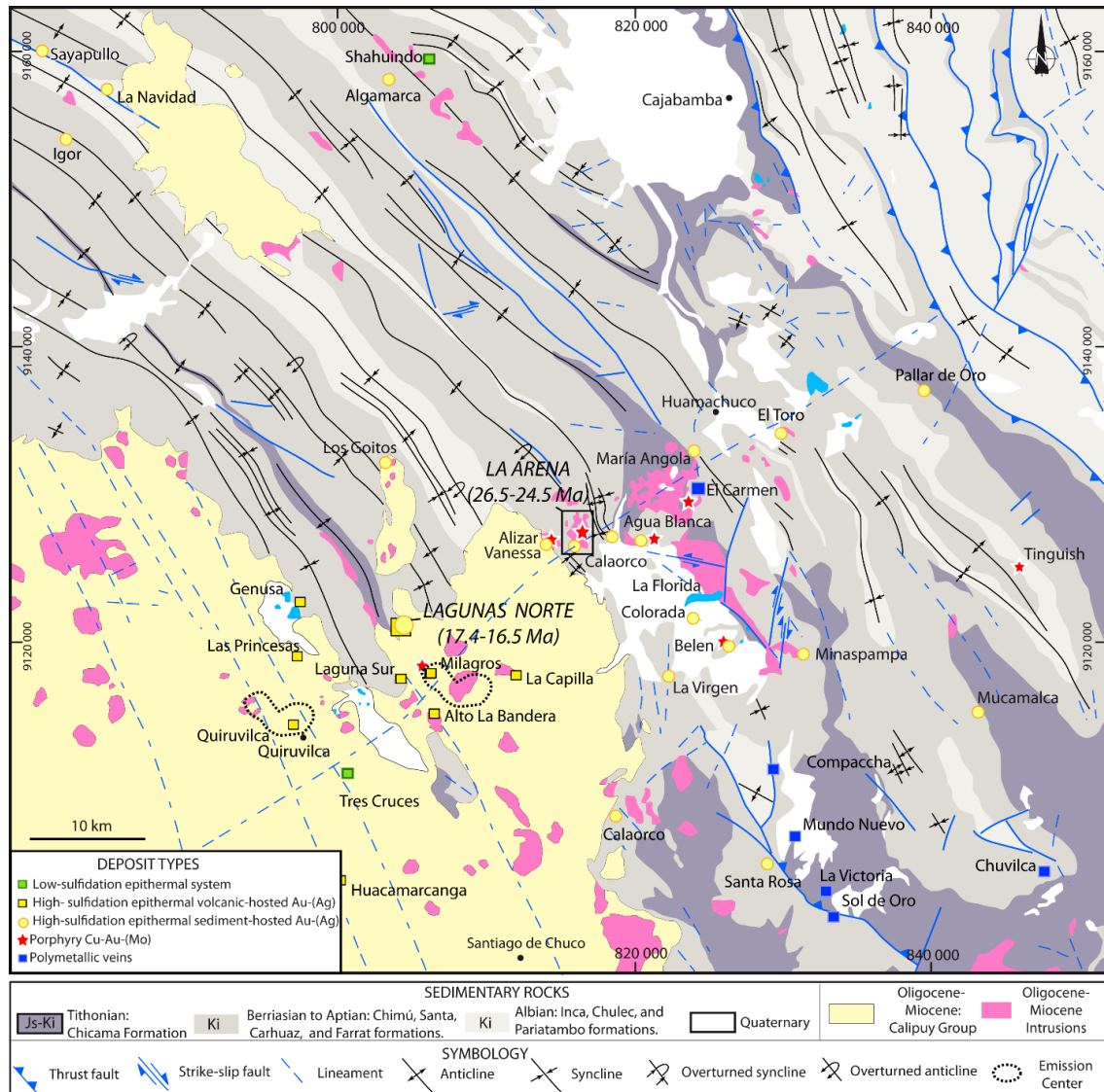


Figure 2.1. Regional geologic map of the La Arena district, showing the simplified geology and location and type of known hydrothermal deposits, based on Reyes (1980) and Montgomery (2012), and more recent mapping by the authors. UTM datum: WGS84, Zone 17 South.

### 2.4.1 Sedimentary rocks basement

The Chicama Formation (Stappenbeck, 1929; Cossío and Jaén 1967) Tithonian age (Jaillard and Soler, 1995) is the lowermost stratigraphic unit of the La Arena district and cropping out largely in the NW and SE of the Florida veins (Fig. 2.1). This unit consists of a succession of dark gray to dark carbonaceous, soft, friable shale and siltstone, with a

few massive thin interbeds of gray to brownish fine-grained sandstone. In the La Arena district, this unit was cut by andesitic dikes and apophysis, which contains anomalous amounts of polymetallic elements (Hg-As-Ag-Pb-Zn-Cu; Gauthier et al., 1999). The late Jurassic to early Cretaceous Chimú Formation (Berriasian; Benavides-Cáceres, 1956) at the base of this unit consists of interbeds of sandstone, quartz sandstone and shale in ascending order. This formation comprises of compositionally mature quartz-sandstone (typically ~95 % SiO<sub>2</sub>) on the top, but contains occasional coal beds, which historically have been exploited, as well as occasionally siltstone and shale intercalations. The boom of exploration has allowed to discover porphyry Cu-Au-(Mo) systems, disseminated high sulfidation-style Au epithermal mineralization, and polymetallic veins as main ore deposits hosted in the sedimentary sequence of the Chimú Formation (Quirita and Gauthier, 2000), such as Calaorco, La Virgen, María Angola, San Rosa, Lagunas Norte, Algamarca, El Toro (Gauthier et al., 1999; Cerpa et al., 2013). The sedimentary sequence continues with the Santa Formation (Valanginian; Benavides-Cáceres, 1956) that overlies and underlies disconformably on the Chimu and Carhuaz Formations, respectively (Benavides-Cáceres, 1956; Reyes, 1980). The Santa Formation is principally composed of dark gray to purplish shale, concretionary limestone which is dolomitic and is interbedded with a few thin beds of dark gray sandstone. The Carhuaz Formation (late Valanginian to early Aptian Benavides-Cáceres, 1956) overlying by the Farrat Formation is dominantly comprised of thin-bedded, soft, friable and brownish shales and silty shales interbedded with a few light gray to brownish, thin-bedded, and cross-bedded quartz-sandstones. The Farrat Formation (late Aptian; Stappenbeck, 1929; Cossio, 1964) consists of a succession of white medium- to coarse-grained, thin-bedded, and cross-bedded sandstone and quartz-sandstone. These sandstones are favorable host rocks, mainly in fractured zone (e.g. Toro mine; Gauthier et al., 1999, Alizar; Barboza, 2017, Shahuindo; Vallance et al., 2018). The sedimentary sequence described above are overlain by Albian transgressive deposits that resulted in shelf deposition (Navarro et al., 2015) of the Inca (Robert and Bulot, 2004; Robert et al., 2009), Chulec (Jaillard, 1987; Robert and Bulot, 2004; Robert et al., 2009), Pariatambo (Benavides-Cáceres, 1956; Robert et al., 2009) Formations, mainly composed of sandstones with marl-limestones, carbonate and black shales, respectively. In the La Arena district no mineralization has been currently registered in association with these last three sedimentary units (Gauthier et al., 1999).

#### 2.4.2 Calipuy Group and its relationship with mineralization

Hypabyssal intrusions and lavas and pyroclastic, medium- to high-K calc-alkaline deposits linked to Calipuy Group (Cossío and Jaén, 1967; Wilson, 1975; Farrar and Noble, 1976; Noble et al., 1990; Rivera et al., 2005; Montgomery, 2012), emitted by various subaerial volcanic centers throughout the Andes of northern Peru during the Eocene-Miocene (54-8 Ma; Navarro, 2007), but in the districts between Lagunas Norte and La Arena the magmatic activity is restricted to the lower Oligocene-to-Middle Miocene (29.54- 12.4 Ma; Montgomery, 2012). The volcanic rocks crop out largely in the southwest of the La Arena porphyry (Fig. 2.1), and cover the Mesozoic strata in an angular unconformity. Andesitic flows and tuffs, andesitic domes, and minor volcanic breccias constitutes the Quiruvilca-Tres Cruces and Los Goitos volcano complexes, which represent the late Oligocene to early Miocene volcanism in Lagunas Norte district (26.1-22.2 Ma, Rivera et al., 2005; Montgomery, 2012). Coeval intrusive activity is recorded at La Arena district (24.6 -26.6 Ma; Gauthier et al., 1999; Montgomery, 2012), where

porphyry stocks cut folded Mesozoic sedimentary strata. Associated hydrothermal activity in this period (26.1 – 25.3 Ma; Montgomery, 2012) gave rise to porphyry Cu-Au-(Mo) deposits (Milagros; Garcia, 2009; La Arena; Aquino et al., 2006), high- (e.g. Calaorco, Garay et al., 2012; Los Goitos, Montgomery, 2012), and low- (e.g. Tres Cruces, Gauthier et al., 1999) sulfidation epithermal Au-(Ag) mineralization. The local magmatism continued the Early Miocene (22.5-18 Ma; Rivera et al., 2005; Rolim, 2005; Navarro, 2007; Gauthier et al., 1999), with the emplacement of andesitic to dacitic domes, andesitic flows and volcanic breccias in both Quiruvilca-Tres Cruces volcano complex and Lagunas Norte domain (Montgomery, 2012). As well as east of the La Arena, barren diorite intrusive body at La Florida mine (~18 Ma, Gauthier et al. 1999) was emplaced in sedimentary rocks of the Chimú and Chicama Formations, although in this epoch weak gold mineralization occurred at the El Toro high-sulfidation system (Noble et al., 2004; Montgomery, 2012). During the late-Early Miocene (18-16.5 Ma) the magmatic-hydrothermal activity increase drastically in the central part of Lagunas Norte district, a well-defined andesitic block-ash and debris flows, volcanic breccias, volcanogenic conglomerates, andesitic to dacitic flows-dome complexes coeval with dacitic hypabyssal bodies constitutes the Saucó volcano complex associated with much of the high-sulfidation hydrothermal activity with at least 7 epithermal gold deposits are known, such as Milagros, Lagunas Norte, La Capilla, Laguna Sur, and Alto la Bandera, (17.7-16.3 Ma, Montgomery, 2012). Moreover, high-sulfidation epithermal mineralization occurs at quartz sandstone-hosted La Virgen deposit (~16.9 Ma, Noble et al., 2004). Part of the Lagunas Norte deposit is also hosted in Chimú quartz sandstone.

During the Early-Middle Miocene (16.1-15.2 Ma, Montgomery, 2012) the locus of magmatism was shifted to the Quiruvilca domain (~5-10 km WSW), which caused minor pyroclastic ash-flow, lava flow coeval scattered dacitic domes of the Las Princesas volcano complex. The Quiruvilca intermediate-sulfidation vein deposits and small Las Princes ore-bearing quartz vein systems occurred in this period (Montgomery, 2012). In the Quiruvilca mine, it is intruded by a barren dacitic Quiruvilca complex at ~12.4 Ma (Montgomery, 2012), with which closes the volcanic activity between Lagunas Norte and La Arena districts.

## Chapter 3

# Sampling and Analytical Methods

### 3.1 Introduction

The sample preparations were carried out at Yuheng Mineral Rock Technology Service Co. Ltd., Langfang, China laboratory included elaboration of thin and polished section, sample crushing and pick minerals, and other case, such as for whole rock geochemistry the samples were crushed and pulverized to -150 mesh. However, the experimental and analytical work were carried out in different laboratories of China Universities (see below).

The present study was focused on documenting the absolute age of the porphyry intrusive bodies related with copper, gold and molybdenum as well as the potassic, sericitic and advance argillic hydrothermal alteration, and molybdenite mineralization of the La Arena-Calaorco porphyry and epithermal systems.

### 3.2 Samples collected

Mapping, drill core logging, assay, and following the criteria suggested by Sillitoe (2000) to have an effective subdivision of porphyry stocks supported a representative sampling of the sequence of porphyry bodies, temporal veinlet relationship, and wall-rock hydrothermal alteration. Three surface samples from Calaorco open-pit and five drill core samples obtained from beneath the leached cap at La Arena porphyry were selected and analyzed by zircon U-Pb geochronologic method. One sample from alunite fracture infillings in the northern part of the Calaorco pit, close to Ethel HS zone and one sample from sericite – clays – chlorite ± biotite hydrothermal alteration were collected and hypogene alunite and hydrothermal biotite minerals were handpicked and analyzed using  $^{40}\text{Ar}/^{39}\text{Ar}$  method. Moreover, five single molybdenite-bearing quartz veinlets were obtained and dated using Re-Os method (Fig. 3.1). Eighteen altered and unaltered whole-rock samples from the La Arena district were selected for major and trace elemental analysis. More than 100 collected samples were examined for mineral identification through standard petrographic analysis of thin and polished sections using both reflected- and transmitted-light microscopy. Approximately 300 hydrothermally-altered samples were obtained and their spectral data were precisely captured by the use of Automatic

Digital Core Logger, of the 300 samples, 18 were selected to obtain their Miniature Imaging Spectrometer (SWIR imaging spectrometer).

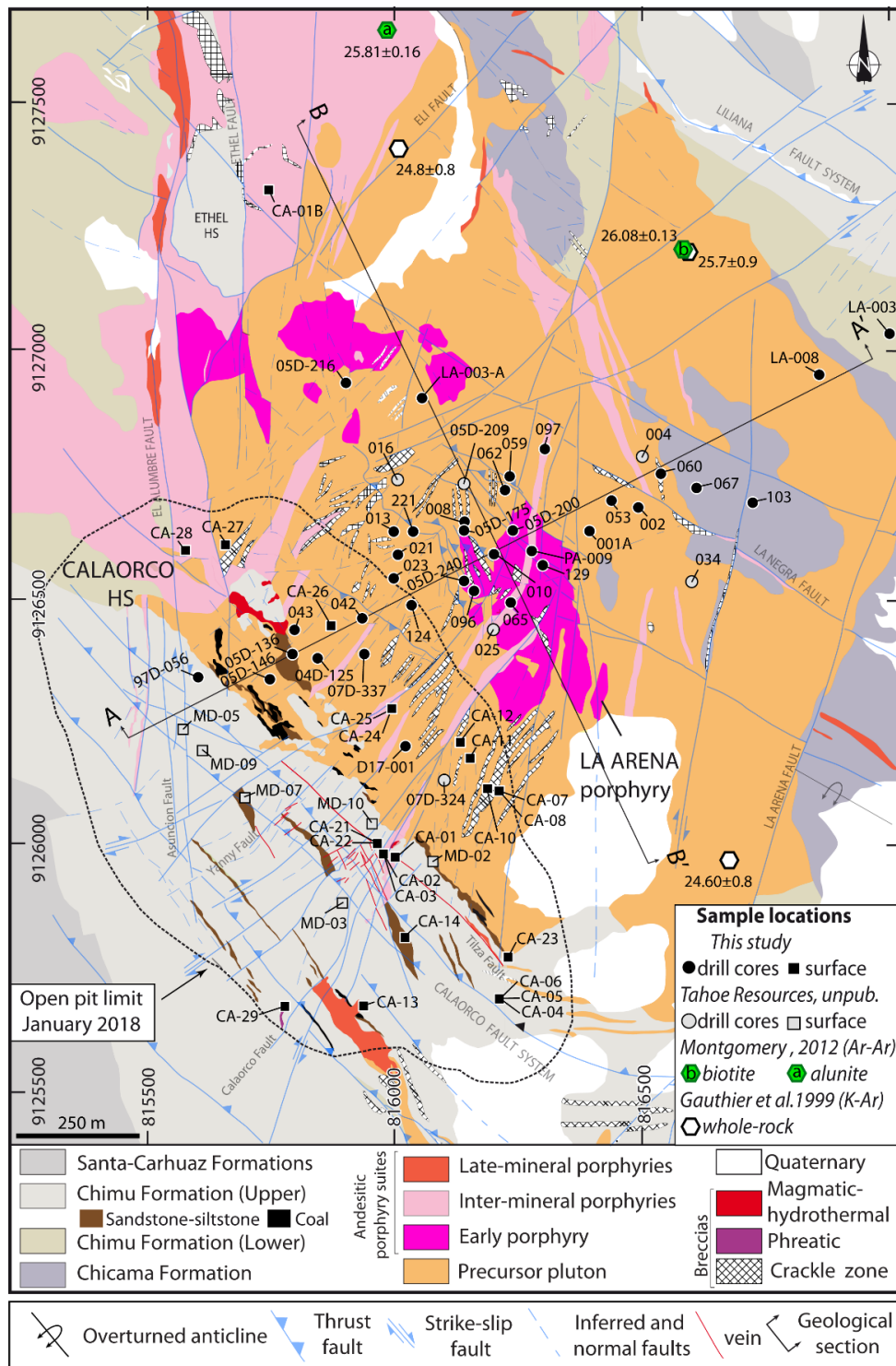


**Figure 3.1** Geological map of the La Arena-Calaorco porphyry and epithermal deposits indicating the surface and drill cores sampling locations. Samples collected for different described in the text. The drill hole labeling was done with a short label (e.g. LA-D15-003-A = LA-003-A, LA-D14-008CD = LA-008, LA-D12-060 = 060, LA-D11-023 = 023, PA-D12-009 = PA-009 and 97D-LA-056 = 97D-056). The map also shows the sample location of previous geochronological studies from Gauthier et al. (1999) and Montgomery (2012).

### 3.3 Analytical methods

#### 3.3.1 Zircon U-Pb dating.

Zircon separation method was done following standard procedures that includes crushing, Wilfley table and a magnetic separation (Frantz), and gravimetric separation by dense liquids (bromoform and methylene iodide) to obtain a zircon concentrate. Finally zircon grains were hand-picked under a binocular microscope. A representative set of 100 zircon grains (zircon grains, including the different morphologies of each zircon population) were arranged in rows in a mounting tablet, and fixed with epoxy resin and were polished to standardize the external surfaces. Cathode-luminescence (CL) SEM images, were used to decipher the internal structures of the sectioned grains and to target specific areas within the zircons.

Zircon U-Pb isotope analytical method was done using a laser ablation inductively coupled plasma spectrometry (LA-ICP-MS) at the Wuhan Sample Solution Analytical Technology Co., Ltd. The detailed analytical method for the laser ablation system and the ICP-MS instrument and data reduction are reported in Liu et al. (2010). Laser sampling was performed using a GeoLas 2005-type instrument. An Agilent 7500a ICP-MS instrument was used to acquire ion-signal intensities.

Zircon 91500 (1065 Ma) was used as an external standard for U-Pb dating, and each measurement was made four times at the beginning of the session, twice every six unknown zircons using the same spot size and conditions as used on the samples, and twice at the end of the session every three samples. Preferred U-Th-Pb isotope ratios used for zircon 91500 standard are from Wiedenbeck et al. (1995). The precision and accuracy of U-Th-Pb dating with this technique have been evaluated by comparison of the ages of zircon standard GJ-1/GJ-2 analyzed thrice at the beginning, once after and before the first and last six unknown zircons, twice at the over every three samples in this study ( $^{206}\text{Pb}/^{238}\text{U}$  ages of  $597.96 \pm 7.14$  to  $619.28 \pm 7.939$  Ma; App 2. Table A2) with that suggested by Jackson et al. (2004) ( $^{206}\text{Pb}/^{238}\text{U}$  age of  $599.8 \pm 1.7$  Ma). Uranium and thorium contents were calibrated against using 3 large spot of glass standard NIST610 with Si for internal standardization analyzed at the beginning and over every three samples. Off-line selection and integration of background and analytical signals, and time-drift corrections were performed using the software ICPMSDataCal (Liu et al., 2010). Uncertainty in the preferred values for the external standard 91500 was propagated to the ultimate results of the samples. Concordia diagrams and weighted mean calculations were generated using the Isoplot/Ex V.2.49 software package by Ludwig (2001).

#### 3.3.2 Hydrothermal biotite and hypogene alunite $^{40}\text{Ar}/^{39}\text{Ar}$ dating.

Hydrothermal biotite and hypogene alunite separated for the selected samples (see above) were first crushed repeatedly and then sieved to obtain mineral grains as uniform as possible in size (0.25-0.42 mm), and biotite concentrate was washed in distilled water in an ultrasound bath for half an hour, and dried. Finally, magnetic separation (Frantz) to obtain a clean biotite concentrate. Medium- to fine grained alunite sample was separated by means crushing in fractions of grains between 0.149-0.125 mm, then magnetic separation (Frantz), and gravimetric separation with dense liquid (iodoform) to obtain an alunite concentration. Finally, hydrothermal biotite and hypogene alunite were hand-picked under a binocular microscope from their respective concentrates.

The argon isotopes of biotite and alunite minerals were analyzed using a thermo multi-collector ARGUS VI noble gas mass spectrometer at the Key Laboratory of



Tectonics and Petroleum Resources, Ministry of Education, China University of Geosciences, Wuhan. The ARGUS VI mass spectrometer is operated using the Qtegra Noble Gas software, which can control the pneumatic valves, CO<sub>2</sub> laser, and crusher through a peripheral controller. Furthermore, the experiments of <sup>40</sup>Ar/<sup>39</sup>Ar laser stepwise heating dating were automatically performed. Detailed descriptions of the automatic <sup>40</sup>Ar/<sup>39</sup>Ar dating technique using Multi-collector ARGUS VI noble gas mass spectrometer are given by Bai et al. (2018).

Samples used in this study were neutron irradiated for 50 h in the 49-2 reactor in Beijing. The laboratory provided production ratios for <sup>36</sup>Ar, <sup>39</sup>Ar, and <sup>40</sup>Ar generated from nuclear reactions involving K and Ca. The correction factors of argon isotopes derived from Ca and K are (<sup>39</sup>Ar/<sup>37</sup>Ar)<sub>Ca</sub>=8.984×10<sup>-4</sup>, (<sup>36</sup>Ar/<sup>37</sup>Ar)<sub>Ca</sub>=2.673×10<sup>-4</sup>, and (<sup>40</sup>Ar/<sup>39</sup>Ar)<sub>K</sub>=5.97×10<sup>-3</sup>, which are determined by measuring the relative production rates of these isotopes in co-irradiated pure calcium salt CaF<sub>2</sub> and potassium salt K<sub>2</sub>SO<sub>4</sub>. The analyses of K-rich biotite and alunite were carried out by <sup>40</sup>Ar/<sup>39</sup>Ar laser stepwise heating. The samples to be dated weighing 1 to 2 mg were individually wrapped in packets of high-purity aluminum foil in thin cylinders (5 – 6 mm in diameter). These samples are packed in quartz tubes. Sealed quartz tubes were loaded into an aluminum capsule packed with Cd-foil of 0.5 mm in thickness for neutron irradiated. Monitor standards were placed in similar packets each containing several milligrams of biotite (sample ZBH25) from the 132.7 Ma Fangshan granodiorite, Beijing (Wang, 1983). Monitor packets were interspersed with packets containing the unknown samples in the quartz tubes, and the position each packet in the tubes was carefully measured before and after irradiation.

For stepwise heating experiments the CO<sub>2</sub> infrared laser is focused to an appropriately small diameter (10.6 μm) to deliver sufficient energy (50 W) to fuse all the sample. Then the sample is exposed to infrared laser emission for 60-second duration (heating time). The internal design minimizes the possibility of ions scattering from the flight tube walls and reaching the collector. A chemical getter pump SAES NP10 positioned at the sample inlet and the ion pump is located on the end of the flight tube close to the ion source. The evolved gas was purified using Zr-Al purification pump and a cryotrap connected with Swagelok pneumatic and manual valves, using a Pfeiffer HiCube 80 Eco turbo pumping station and a Varian StarCell 40 L/s to generating noble gases with sufficient purity for argon isotope analyses in the mass spectrometer.

The argon isotopes of all samples were admitted and analyzed into the ARGUS VI multi-collector mass spectrometer, which comprises a fixed five Faraday detectors equipped with resistors of 10<sup>11</sup> Ω (H2), 10<sup>12</sup> Ω (H1) and 10<sup>13</sup> Ω (Ax, L1 and L2), as well as a low mass CDD (compact discrete dynode) ion counting multiplier (in the L3 position). The collector array allows true simultaneous collection of five argon isotopes of <sup>40</sup>Ar/<sup>36</sup>Ar on H2-L2 (for big signal samples) or H1-L3 (for small signal samples), respectively (Bai et al., 2018, 2019).

The <sup>40</sup>Ar/<sup>39</sup>Ar age spectrum and inverse isochron were generated using the ArArCALC version 2.52 software package by Koppers (2002).

### 3.3.3 Molybdenite Re-Os dating

Fine-grained molybdenite (<300 μm) separation method was done following standard procedures that includes ore crushing, enriching the molybdenite with floatation method, magnetic separation (Frantz), gravimetric separation by dense liquid (iodoform) to obtain

masses of molybdenite concentrates. Finally, pure molybdenite was hand-picked under a binocular microscope.

The determination of rhenium (Re) and osmium (Os) contents and isotopic compositions of molybdenite minerals was performed by inductively coupled plasma-mass spectrometry (TJA PQ ExCell) at the Re-Os Laboratory of the National Research Center of Geoanalysis, Chinese Academy of Geological Sciences, Beijing. The load, digestion, and extraction of the powdered molybdenite mineral samples were carry out using the Carius tube procedure described by Shirey and Walker (1995), and the chemical Re and Os separation procedure followed the method of Du et al. (2004), which is summarized by Xie et al. (2019).

The powdered molybdenite mineral sample was loaded into the Carius tube via glass funnel sized to fit into the sample loading neck and extend into the main portion of the tube. The mixed  $^{190}\text{Os}$  and  $^{185}\text{Re}$  spikes in 6 mol/l HCl solutions (obtained from the Oak Ridge National Laboratory, Tennessee, USA; Xie et al., 2019) were weighed and quantitatively transferred through the funnel into the tube and allowed to freeze in the bottom of the tube. Then 4 ml of 10 mol/l HCl and 2 ml of 16 mol/l  $\text{HNO}_3$  to make aqua regia were introduced through the funnel and allowed to freeze in an ethanol-liquid nitrogen slush between  $-0^\circ$  and  $-50^\circ\text{C}$ .

The next step was sample digestion. Once sealed using an oxygen-propane, the tube is permitted to warm to room temperature and was then placed in a stainless-steel jacket and heated at  $220^\circ$ - $260^\circ\text{C}$  for  $\sim 12$  h. The next stage was sample extraction and Re and Os separation. On cooling, the sample-bearing Carius tube was kept in a frozen state while the neck of the tube was broken and the contents transferred into a distillation flask. The residue was rinsed out with 30-40 ml of 2.5 mol/l  $\text{H}_2\text{SO}_4$ . Separation by distillation for Os and by extraction for Re prior to measurement was done following the method used by Du et al. (2004). Os was separated as  $\text{OsO}_4$  by distillation at  $105^\circ$  to  $110^\circ$  for 50 minutes and trapped in 10 ml of pure water. Inductively coupled plasma-mass spectrometry (TJA PQ ExCell) were used for the determination of Re and  $^{187}\text{Os}$  concentration and isotope ratios.

During this study, the analytical reliability was verified by repeated analyzes of molybdenite standard GBW04435 (HLP) (Du et al., 2004). The average Re-Os age for GBW04435 (HLP) is  $219.9 \pm 3.5$  Ma (95% confidence limit), which is consistent with the age of  $221.4 \pm 5.6$  Ma (Du et al., 2004). Furthermore, the average Re and Os concentrations for GBW04435 (HLP) are  $273.4 \pm 2.9$   $\mu\text{g/g}$  and  $630.7 \pm 4.2$   $\text{ng/g}$ , respectively. These values are in good agreement with certified concentrations of  $283.8 \pm 6.2$   $\mu\text{g/g}$  and  $659.0 \pm 14.4$   $\text{ng/g}$  (Du et al., 2004). The decay constant used for  $^{187}\text{Re}$  of  $1.666 \times 10^{-11}/\text{year}$  has an absolute uncertainty of  $\pm 0.017$  (1.0%) (Smoliar et al., 1996).

### 3.4 Previous geochronological studies at La Arena-Calaorco porphyry and epithermal deposits.

Previous geochronology data for the La Arena-Calaorco orebodies are summarized in Figure 3.2 The temporal hydrothermal alteration of La Arena porphyry deposit was initially examined by Gauthier et al. (1999) in the light of only three whole-rock K-Ar ages ( $2\sigma?$ ) from dacite, andesite and tonalite intrusive bodies yielded dates  $24.60 \pm 0.8$ ,  $24.8 \pm 0.8$  and  $25.7 \pm 0.9$  Ma, respectively (Fig. 3.1). Neither analytical results nor discussion of the validity of the K-Ar ages were given in Gauthier et al. (1999), thus the significance of this date is unclear.

Recent, Montgomery (2012) reports for hydrothermal activity two  $^{40}\text{Ar}/^{39}\text{Ar}$  plateau ages of  $26.08 \pm 0.13$  Ma ( $2\sigma$ ) for hydrothermal biotite from the dacitic? porphyry stock at the margin of the precursor pluton and a poorly defined plateau age  $25.81 \pm 0.16$  Ma ( $2\sigma$ ) for hypogene alunite in quartz-alunite - altered dacitic clasts in hydrothermal breccia at Ethel high-sulfidation deposit, which was already mined by Rio Alto Mining at the time of this study (Fig. 3.1).

Unpublished U-Pb geochronology data (Tahoe Resources, unpub. files), yielded internally reproducible age results for the third intrusive phase (FPA3) of  $25.23 \pm 0.39$ ,  $25.22 \pm 0.54$ ,  $25.13 \pm 0.53$ ,  $24.89 \pm 0.68$ ,  $24.86 \pm 0.58$ ,  $24.85 \pm 0.49$ ,  $24.83 \pm 0.69$ , and  $24.10 \pm 0.55$  Ma ( $1\sigma$ ) and some for fourth intrusive phase (FPA4) of  $24.61 \pm 0.49$  and  $24.51 \pm 0.43$  Ma ( $1\sigma$ ) (App. 3, Table A3). Moreover,  $^{40}\text{Ar}/^{39}\text{Ar}$  dating of hydrothermal biotite from the potassic alteration zone yielded a plateau ages of  $26.40 \pm 0.29$  and  $26.35 \pm 0.14$  Ma ( $2\sigma$ ), sericitic/muscovite from the sericitic alteration zone with results ranging from  $26.41 \pm 0.52$  to  $26.02 \pm 0.07$  Ma ( $2\sigma$ ) at the La Arena ore body, and plateau ages of  $25.57 \pm 0.16$ ,  $25.51 \pm 0.17$ , and  $25.51 \pm 0.10$  Ma ( $2\sigma$ ) for pinkish hydrothermal alunite in quartz – alunite – hematite  $\pm$  goethite andesitic porphyry bodies from advanced argillic zones at Calaorco high- sulfidation system. All unpublished zircon U-Pb data were recalculated ( $2\sigma$ ), considering if individual zircon grain ages do not overlap the weighted mean age within their analytical uncertainty were excluded from final age recalculation (Tables 6.2; App.3, Fig. A3). Then these ages are discussed within the text together with new U-Pb ages reported herein for all intrusive phases identified at La Arena porphyry system.

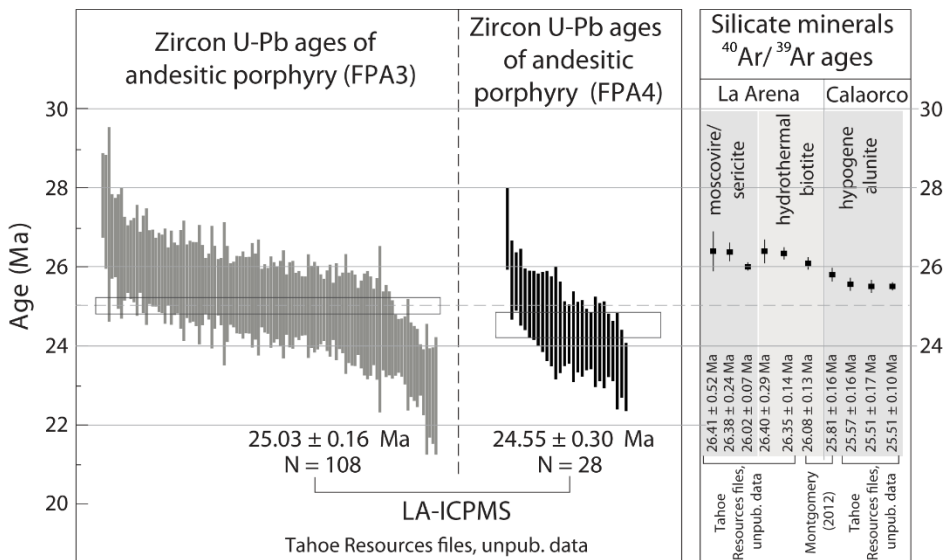


**Figure 3.2.** Summary of unpublished zircon U-Pb and silicate minerals  $^{40}\text{Ar}/^{39}\text{Ar}$  data (Tahoe Resources, unpub. files) and two previously published biotite and alunite  $^{40}\text{Ar}/^{39}\text{Ar}$  data (Montgomery, 2012) for La Arena-Calaorco/Ethel porphyry and epithermal deposits. Unpublished zircon U-Pb ages from Tahoe Resources (unpub. files) are weighted mean of  $^{207}\text{Pb}$ -corrected  $^{206}\text{Pb}/^{238}\text{U}$  dates of several dated FAP3 (called herein inter-mineral porphyry phase) and FAP4 (called herein late-mineral porphyry) samples. The U-Pb and  $^{40}\text{Ar}/^{39}\text{Ar}$  ages corresponding  $2\sigma$  errors for the all dated samples.

## Chapter 4

# Geology of the La Arena-Calaorco porphyry and epithermal deposits

### 4.1 Introduction

The La Arena is a partially explored mineral district, with already identified porphyry Au-Cu (e.g. Alizar), Cu-Au±Mo (e.g. La Arena, Belen), and Cu-Mo (e.g. Agua Blanca) deposits, which are genetically related to a shallow andesite porphyry suite of late Oligocene age with vary in depth of erosion. These porphyry complex are placed in the Chimú quartz sandstone of early Cretaceous age, where quartz sandstone sequences with advance argillic alteration hosted gold (e.g. Calaorco, Vanessa, Agua Blanca, El Toro) deposits. The district provide strong support for interpretation that the quartz sandstone hosted Au deposits are related to magmatically generated hydrothermal systems of high-sulfidation affiliation (e.g. La Virgen, Montoya et al., 1995; Lagunas Norte, Cerpa et al., 2013), many of them are close to subjacent porphyry copper mineralization (e.g. La Arena-Calaorco, Garay et al., 2012).

### 4.2 Mining overview

Extensive and systematic chip and channel sampling of outcrops, project-scale (1:10,000-1:1,000) geologic mapping, magnetic (MAG) and induced polarization (IP) geophysical surveys, and drilling (more than 117 km dilled) within what were to become the La Arena-Calaorco porphyry and epithermal deposits. These works defined the dimension of Cu-Au-(Mo) and Au mineralization at La Arena-Calaorco, which is elliptical in shape with NNW-trending of 2 km in length by 1.5 km wide (Fig. 4.1), and vertical extents of more than 1.2 km (Fig. 4.2). In the surface area, the ore-mineral zone occurs at altitudes between 3,500 and 3,300 m. The Calaorco high-sulfidation system was operated as an open pit in May, 2011 by Rio Alto Mining, in January 2015 it was operated by Tahoe Resources Inc. and since January 2019 by Panamerican Silver. La Arena porphyry is defined by its measured and indicated resources amount of 742.4 Mt, 0.35% Cu, @ 0.24 g/t Au, with a total of 2.626 Mt Cu and 159.81 t Au, and the Calaorco high-sulfidation

system contains proven current resources of 44 Mt, @ 0.4 g/t Au with a total of 16 t Au (Tahoe Resources Inc. Annual Report 2018), attaining a production of approximately 1,520,000 oz Au (J. Perez, pers. Commun., 2019).

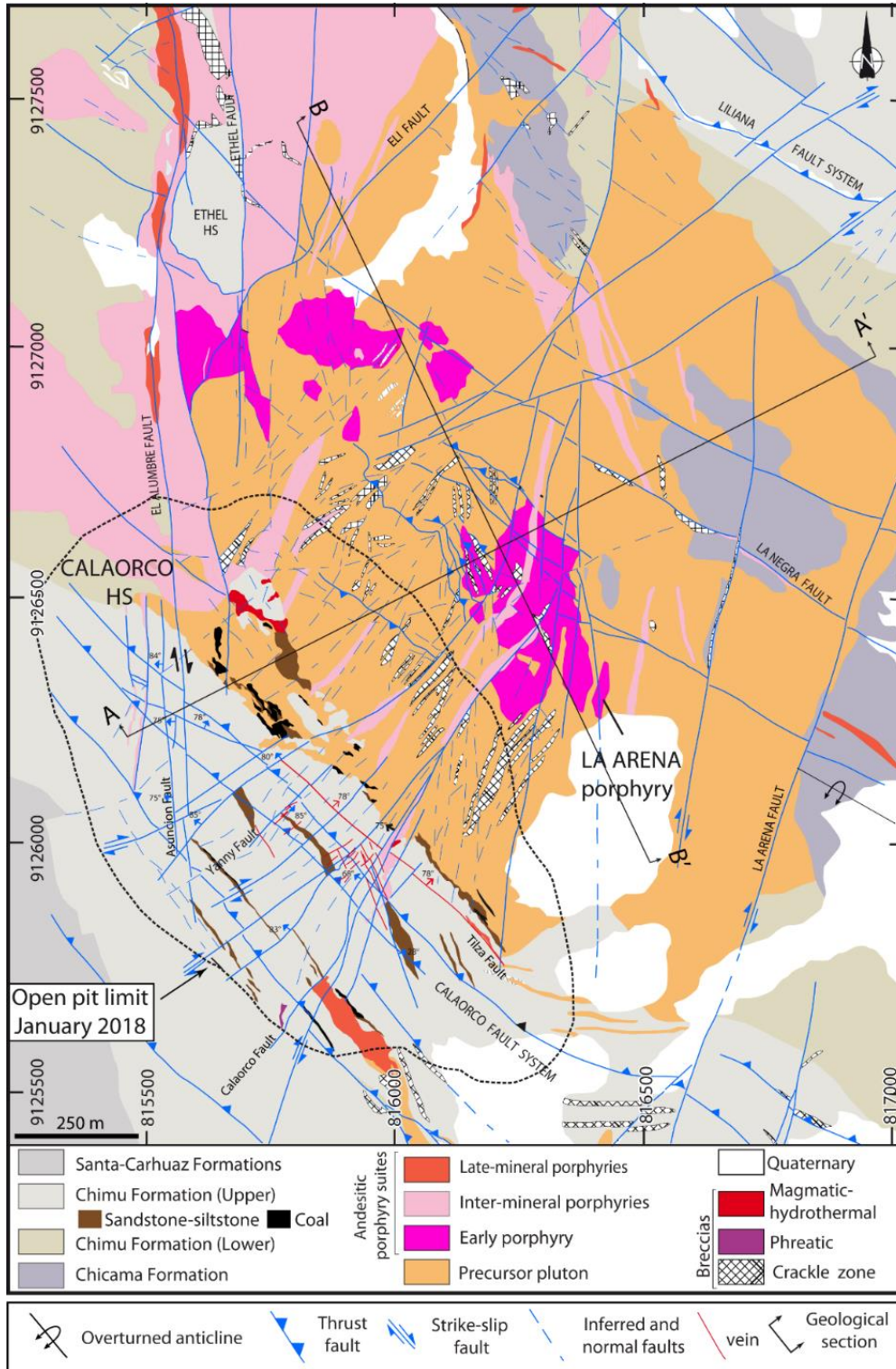


Figure 4.1. Simplified geologic map of La Arena-Calaorco area, based on surface and pit mapping and core logging (based on Tahoe Resources, unpub. files and this study). Positions of sections present in Figures 5.2, 5.4 and 5.10 are also shown. UTM datum: WGS84, Zone 17 South.

### 4.3 Geology of the La Arena-Calaorco porphyry and epithermal systems

The basement rocks at La Arena porphyry system is dominated by Mesozoic pelitic and siliciclastic rocks belonging to the Chicama and Chimú Formations, respectively (Fig. 4.1). The two formations are folded, and the geometry of the antiform is dominated by the orientation of sedimentary bedding ( $S_0$ ) on both flanks of antiform in the Chicama and Chimú Formations. The Chimú Formation at the northeast flank is composed of gently dipping ( $24^{\circ}$ - $40^{\circ}$ NE), quartz sandstone and thin beds of dark fine-grained sandstone (lower part) and quartz sandstone interbedded occasionally with thin beds siltstone and coal (upper part). The upper part of the Chimú Formation at the southwest flank is composed of steeply dipping overturned bedding ( $65^{\circ}$ - $80^{\circ}$  NE), compact medium-to coarse grained quartz sandstones with occasional thin beds siltstone and coal. Due to their brittle nature, the quartz sandstones are fractured and often brecciated. As shown in Figure 2.1, the antiform corresponds to a regional-scale overthrust anticline folded axis of axial trace NW-orientation and NE-vergent. The Calaorco high-sulfidation deposit occurs along the permeable quartz sandstone in the southwest flank of the fold, and is located at La Arena porphyry's southwest shoulder (Fig. 4.1). It has an extent area of approximately  $0.86 \text{ km}^2$  and thickness more than of 0.3 km, which contains NE-trending controlled zones of advance argillic hydrothermal alteration (Calaorco lithocap) and related gold mineralization. Oxidized high sulfidation-style mineralization is characterized by hematite-goethite hosted in the matrix of the magmatic-hydrothermal breccias and crackle breccia zones, that are usually comprised of silicified quartz sandstone of the Chimú Formation (Garay et al., 2012). Several large blocks and roof pendants of pelitic and quartz sandstone rocks, up to ~400 m in vertical extent, are present at the precursor pluton edges, close to contact with the Chimú Formation, defining a NW-trending corridor (Calaorco Fault System; Fig. 4.1) through the southwest margin of the La Arena porphyry system and border northeast of Calaorco lithocap (Fig. 4.2).

#### 4.3.1 Intrusive history of the La Arena porphyry complex

La Arena deposit is concentrically zoned, cylindrical body of quartz with Cu-Fe±Mo sulfide veinlets centered on a multiphase andesitic complex. The multiphase porphyry exhibits rather similar textural features. Distinct differences are recognized in type and degree of hydrothermal alteration, crosscutting relations, xenoliths content and veinlet relationships observed during logging more than 39 diamond drill cores (Fig. 3.1). At least four epizonal intermediate intrusive units are represented in the immediate porphyry prospect (Fig. 4.1), and are denoted by the precursor pluton, early, inter-mineral, and late-mineral andesitic porphyries. The multistage emplacement of the porphyries and their age relationship with respect to alteration-mineralization events are ranged between ~26.64 to 24.40 Ma as listed in Tables 6.1, 6.2, where the IUGS classification of Streckeisen (1974) is used for rock nomenclature.

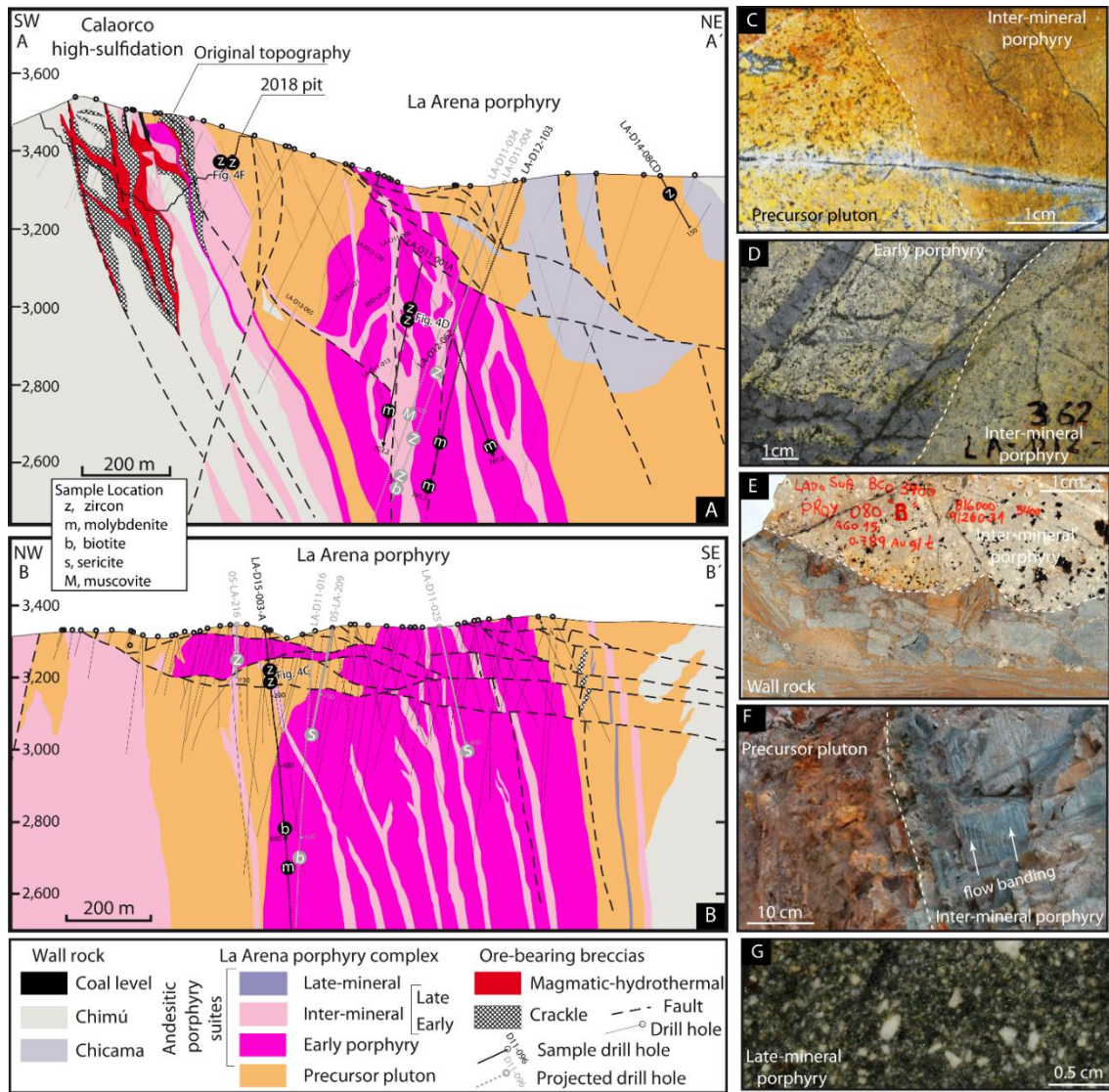
**Precursor pluton:** The late Oligocene precursor intrusive is a rhombus shaped intrusion with diagonals of  $2 \times 1.3 \text{ km}$  (Fig. 4.2). This pluton cropping out largely in the La Arena deposit is the volumetrically largest body of the four recognized phases, cutting subparallel to bedding planes of steep dipping quartz sandstone of the Chimú Formation (Fig. 4.2). The bulk of the oldest intrusive phase is light- to medium-dark greenish, crowded medium- to fine-grained (1-3 mm), semi-porphyrific in texture, and has an overall quartz diorite composition in the northeast of the central part of the main ore porphyry body (Table 4.1). It contains 75 to 65 percent plagioclase phenocrysts (< 3.4



mm) with moderate replacement of carbonates and quartz with absorbed edges over hornblende and biotite, which are mostly replaced by chlorite and sulfide minerals. In contrast, the outcrops between Calaorco HS and La Arena porphyry exhibit light gray to yellowish relict porphyritic texture affected by a hydrothermal alteration with massive sericite-illite and disseminate pyrite (Fig. 4.2C). The strongly hydrothermally altered intrusive body is regarded to have suffered from an early mineralization, because very low-grades metal zones, such as volumetrically minor (2-3% vol) quartz + sulfides veinlets, occur characteristically in the altered body (see Fig. 4.3).

**Early porphyry:** The main principal phase related to the copper-gold-molybdenum mineralization comprises two irregularly-shaped small porphyry bodies (Fig. 4.1). The slightly-elongated large body with <250 m in length at the central area, and other six early satellite porphyry bodies, clustered along the northwest edge of precursor pluton. The latter is commonly medium- to fine- grained (1-4 mm), and slightly yellowish green in color. Early andesitic intrusive typically has a crowded porphyritic texture (45-50% phenocrysts) that comprised of plagioclase, biotite, magnetite and lesser amounts of K-feldspar (< 3%) and hornblende. phenocrysts in a mainly groundmass of plagioclase and quartz (Table 4.1). Plagioclase phenocrysts (0.2- to 0.53-cm long) are diagnostic and typically contain poikilitic inclusion of quartz and/or apatite. Up to 8 percent of the quartz in andesite porphyry occurs as clusters of three or four anhedral grains. The plagioclase phenocrysts mainly converted to carbonates, sericite, illite and kaolinite, biotitization of primary igneous hornblende, and then the hydrothermal biotite is successive chloritized. Early veinlets of quartz + chalcopyrite + pyrite ± molybdenite crosscut early andesite porphyry, which is truncated at the contact with inter-mineral porphyry (Fig. 4D). This andesite porphyry is interpreted to have occurred in a syn-mineral timing, because the high-grade ores (copper, gold, and molybdenum) accompanied by the aforementioned hydrothermal alteration are developed in the most intensely altered zone (Fig. 4.3).

**Inter-mineral porphyry phases:** At least two discrete inter-mineral porphyry phases are present at La Arena porphyry: (1) early inter-mineral porphyry, and (2) late inter-mineral porphyry and for practical reasons during the mapping, were grouped into one main group (Fig. 4.1). Early inter-mineral porphyry typically comprises small bodies of tabular geometry along Calaorco and La Arena, which crop out largely northwest part of the main porphyry body (Fig. 4.1), whereas late inter-mineral intrusive is a volumetrically minor, and usually occurs as dikes within the precursor pluton. Early inter-mineral is a crowded medium-grained porphyritic andesite of medium- to dark- beige in color, being composed of plagioclase, quartz and intensely disseminated fine-grained pyrite (up to 5% vol) together with sericite and/or muscovite (Fig. 4D). Late inter-mineral is commonly fine-grained crowded porphyritic andesite with euhedral plagioclase and rounded quartz phenocrysts with minor pyrite (< 2 vol%). These intrusions host a whole early to late ore mineralization, in which the ore (Cu-Au-Mo) grades decrease markedly from early porphyry (Fig. 4.3). Locally high gold grades also occur in silice parda (cf. Cerpa et al., 2013) formed during the emplacement of inter-mineral porphyry within of quartz sandstone of the Chimú Formation, which is infills fractures with forming cement of small contact breccia bodies (Fig. 4E), and partially replaces silty beds. Inter-mineral porphyry bodies are characterized by the abundant mineralized quartz veinlets fragments and xenoliths derived from early andesite porphyry close to contacts. Zones of flow-aligned phenocrysts occur in inter-mineral bodies along contact with precursor pluton (Fig. 4F).



**Breccia pipe:** magmatic-hydrothermal breccias-type (cf. Sillitoe, 1985) are small bodies (<20 m wide), and well developed on the southwestern into inter-mineral porphyry at shallow levels (200-220 m). The contacts between breccia pipes and their wall rocks are commonly sharp, marked by a sheeted zone and oriented slab-like fragments. This breccias are characterized by monolithic angular to subrounded fragments with a slight vertical displacement. Fragments observed within the hydrothermal breccia include quartz and



quartz-molybdenum veinlets, which range in size from 2-3 mm up to several cm. The matrix of magmatic-hydrothermal breccia is also mineralized, and breccia fragments were separated by 5-15% volume open space and cemented by pyrite and rock flour. These features indicate that the breccia zone occurred in an intra-mineral timing, although the matrix breccia of some small breccias (<2 m) is dominantly rock flour with lesser pyrite. All breccias contain quartz-sericite - altered andesitic clasts with lower copper grade than the adjacent rocks. The breccias pipes were cut by pyrite veinlets, along which the copper and gold grade increase considerably.

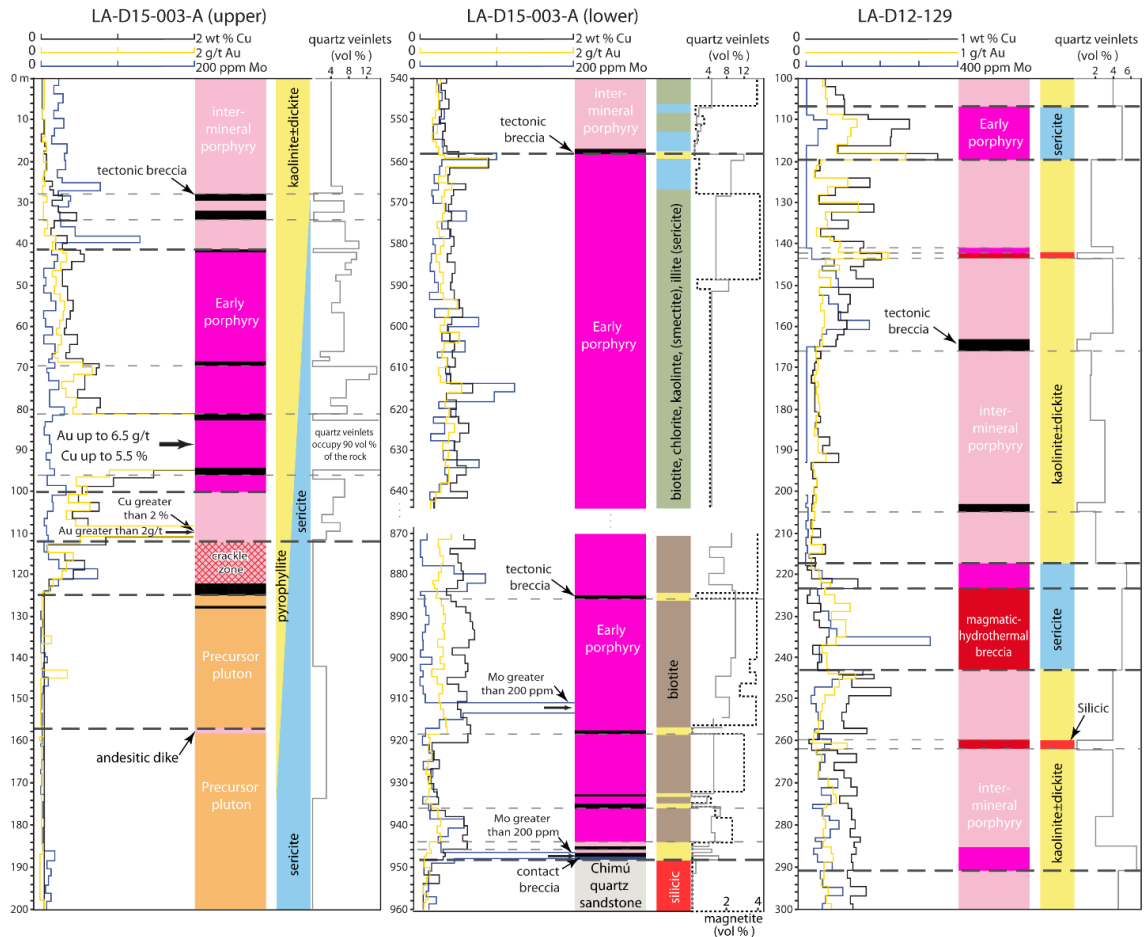


Figure 4.3. Drill hole logs showing lithology, hydrothermal alteration, quartz veinlets and magnetite densities, and copper, gold, and molybdenum grades for two selected diamond drill holes from the La Arena porphyry deposit. High-grade copper generally appears together with elevated gold grades within of early porphyry with high quartz veinlet density (up to 6.5 g/t Au and 5.5% Cu), whereas abrupt drop in copper and gold grades are shows into the inter-mineral and precursor bodies. Molybdenum shows no correlation with copper and gold, molybdenum grades are also higher in early porphyry (up to 327 ppm) than in inter-mineral porphyry (up to 118 ppm). Hydrothermal biotite and sericitic hydrothermal alteration contains similar copper and gold grades.

Table 4.1. Mineralogy characteristics and metal grades of the La Arena-Calaorco porphyry and epithermal deposits intrusive phases

Intrusion phase <sup>1</sup>	Vol % PPX <sup>2</sup>	Dominant phenocryst phase					Vol % GMS <sup>2</sup>	Groundmass Composition	Metal grades		
		quartz	k-feldspar	plagioclase	biotite	Amphibol e <sup>3</sup>			Cu %	Au g/t	Mo ppm
PP	75	4-5% 0.1-0.5 mm	1-3% 0.1-0.5 mm	75-65% 1-3.4 mm (to 0.5 cm)	2-4% 0.2-0.8 mm	2-5% 1-3.5 mm	25	Fine-grained (quartz-plagioclase -K- feldspar)	0.007- 0.05	0.03-0.07	4 -18
EP	80	5-8% 1-2 mm	2-3% 1-1.6 mm	45-50% 2-5.3 mm (to 1 cm)	10-20% 0.1-2 mm	1-2% 0.5-5 mm	20	Aplitic (quartz-plagioclase - biotite - K-feldspar)	≤ 1.2	≤ 0.7	≤ 556
IMP	75	6-8% 0.1-0.5 mm	Minor to absent	40-50% 1-3.5 mm	10-15% 0.3-2.4 mm	10-15% 0.3-2.4 mm	25	Aplitic (quartz-plagioclase -K- feldspar)	0.1- 0.27	0.13- 0.5	50- 180
LM P	65	3-5% 0.5-1 mm	Minor to absent	45-50% 3-5 mm	1-2% 0.5-1.3 mm	20-25% 2-3.3 mm	35	Microaplitic (quartz-plagioclase- amphibole -K-feldspar)	≤ 0.003	-	≤ 0.5

Abbreviations: <sup>1</sup> Porphyritic phase: PP = precursor pluton, EP = early porphyry, IMP = inter-mineral porphyry, and LMP = late-mineral porphyry

<sup>2</sup>PPX = phenocryst, GMS = groundmass

Notes: All phases contain variable amounts of magnetite, apatite, rutile, and zircon as accessories; magnetite and rutile occurs as inclusions in biotite in early porphyry. Magnetite is moderately replaced by hematite

<sup>3</sup>Amphibole (hornblende) and magmatic biotite in EP and IMP are partially to completely altered to hydrothermal biotite. More advance stage of biotite alteration forms chlorite and oxides.

**Late-mineral porphyry:** Volumetrically, the late-mineral intrusive is less abundant in the La Arena porphyry complex, and is exposed in the surface area as dikes, sills and small tabular bodies. The NW- and N-striking, steeply dipping (75-80°NE) dikes occur along the sedimentary rocks (Fig. 4.1). The youngest intrusive phase is dominantly characterized by crowded medium-grained (1-4 mm) porphyritic hornblende-bearing andesite (Fig. 4.2G; Table 4.1). Typically-zoned plagioclase phenocrysts are abundant, and are intergrown as crystal aggregates with a glomeroporphyritic texture. Rounded quartz and euhedral biotite phenocryst rarely occurs in very fine grained matrix, in association with plagioclase crystals. This andesite porphyry is weakly altered and mineralized.

#### 4.4 Hydrothermal alteration and mineralization

The hydrothermal processes in the La Arena and Calaorco deposits are classified from the time-space distribution of different groups of mineral assemblages formed in various stages of mineralization, which were been constrained from detailed field mapping, drill core logging, spectral data analysis, SWIR imaging spectrometer analysis, petrography, and assay data. At least four type of alteration-mineralization assemblages were distinguished at La Arena-Calaorco deposits, where the shallower hydrothermal alteration comprising several sub-type (Table 4.2). The alteration-mineralization was produced by a continuously evolving hydrothermal system associated with pulsating subvolcanic intrusive activity and later concentric around of the early- to late-mineral andesite porphyry phases and adjacent to precursor pluton and permeable Chimú quartz sandstone at the La Arena porphyry's southwest shoulder. The alteration overprint is characterized by the transition from potassic zone to advance argillic lithocap.

Table 4.2. Major alteration-mineralization stages and key minerals

Alteration Type <sup>1</sup>	Key minerals	Coeval alteration type	Key minerals
Potassic	biotite, k-feldspar, carbonates (calcite), magnetite	Propylitic	calcite, epidote, chlorite
Sericite-clay-chlorite	sericite, clay (kaolinite-smectite), chlorite, massive/specular hematite ± biotite		
Sericitic	quartz, sericite, illite, carbonate (ankerite)		
Advance argillic (include Calorco lithocap)	a. quartz, pyrophyllite, alunite, diaspor b. quartz, dickite, kaolinite, alunite c. silicic	Propylitic	calcite, epidote, chlorite, sericite

<sup>1</sup>Alteration type according to Sillitoe (2010)

Early potassic core is widely overprinted by sericite-chlorite alteration, and both zones are laterally bordered by an annular sericitic zone. The sericitic zone is surrounded by a propylitic halo in the deeper area, and the shallow are is superimposed by an extensive advance argillic alteration (Garay et al., 2012, Fig. 4.4). The advance argillic alteration is regarded as the Calaorco lithocap (cf. Bodnar and Beane, 1980; Sillitoe, 2000; Hedenquist and Taran, 2013).

#### 4.4.1 La Arena porphyry orebody

Intense hydrothermal alteration with different types of veinlets occurs in the andesitic porphyries suits and at the contact zone with wall rocks (see below). The hydrothermal zonation is schematically illustrated in the two cross sections in Figure 4.4.

Early potassic alteration is associated with the main-stage copper-gold mineralization, and is identified by drilling to a depth of ~800 m below the current-day surface (Fig. 4.4). The dominant assemblage consists of quartz aggregates, extensive hydrothermal biotite, chlorite, and lesser K-feldspar and carbonates. Chalcopyrite, lesser pyrite, and trace bornite are disseminated within moderate to pervasive biotitized and silicified matrix of the early andesitic porphyry. Mafic minerals (biotite and hornblende) are almost totally replaced by brownish randomly-oriented aggregates of fine-grained hydrothermal biotite intergrown with rutile and magnetite. Subhedral plagioclase phenocrysts contain poikilitic inclusions of hydrothermal biotite, rutile, and zircon, and are partially replaced by carbonates and lesser amounts of K-feldspar, although locally K-feldspar up to 30 percent in samples from drill hole LA-D15-003-A at 848 m of the current surface. Hydrothermal magnetite is also present in the type of hydrothermal alteration, and is more abundant ( $\leq 4$  vol %; Fig. 4.3) in the biotitized zone. The development of propylitic alteration is associated wall-rock alteration occurred locally coeval with the potassic alteration, and even after the advance argillic alteration. The propylitic alteration is characterized by a weak propylitic alteration (calcite-epidote-chlorite) and minor silicification in localized zones of the precursor porphyry, close to the contact margins with sedimentary host rocks. Calcite and epidote appear with replacing plagioclase phenocrysts, while chlorite replaces igneous biotite and hornblende. This weak hydrothermal alteration is also an evident along the barren late-mineral hornblende andesite porphyry.

Sericite-chlorite (SCC; Sillitoe and Gappe, 1984) alteration is a transitional zone between early potassic and hydrolytic sericitic alteration, because as a paleo-green appearance clearly overprints and partially affected considerable volumes of the upper potassic zone and central section of the porphyry system (Fig. 4.4). This hydrothermal alteration is defined by partial to whole transformation of igneous biotite crystals and hydrothermal biotite to chlorite - calcite  $\pm$  epidote  $\pm$  anatase  $\pm$  clays (i.e. kaolinite, smectite, and irregular intergrowth with illite), whereas K-feldspar and plagioclase with magnetite - zircon inclusions were replaced by muscovite-sericite together with clays and calcite. The SCC alteration typically yields chalcopyrite and trace amounts of pyrite, bornite, and igneous - hydrothermal magnetite, which are contained in early quartz veinlets and as disseminated grains in the quartz + sericite + biotite + chlorite + carbonate + clays matrix in the early andesitic porphyry (Fig. 4.5A). Hydrothermal magnetite volume increases considerably within early veinlets, but both magnetite-types are variably replaced by hematite and/or specular hematite (martitization). This phenomenon indicates a progressive oxidization during the transition from potassic to the SCC alteration (Fig. 4.5B). The magmatic-hydrothermal breccias described earlier contain fragments with A- and B-type veinlets with kaolinite, illite - smectite  $\pm$  chlorite assemblages. These relationships indicate this ore-related breccias bodies occurred coeval or immediately after the SCC alteration.

The annular sericitic zone is common in the upper parts and lateral zones separating the potassic core from propylitic halo (Fig. 4.4), and showing a close relationship to the early and inter-mineral andesite porphyries. Early greenish-gray to greenish sericitic alteration overprints totally or partially destroys the potassic and SCC assemblages, while

late white sericite alteration is mainly distributed in quartz veinlet halos (Fig. 4.5C), where white sericitic overprints of the SCC alteration veinlet halos are zoned outward to kaolinite-smectite-chlorite alteration (Fig. 4.5A). The degree of sericitization falls away quite rapidly around a few veinlets. However, within quartz veinlet stockwork zone it can be pervasive across widths of tens of meters in the central parts of the porphyry system where veinlet density is high (Fig. 4.5D).

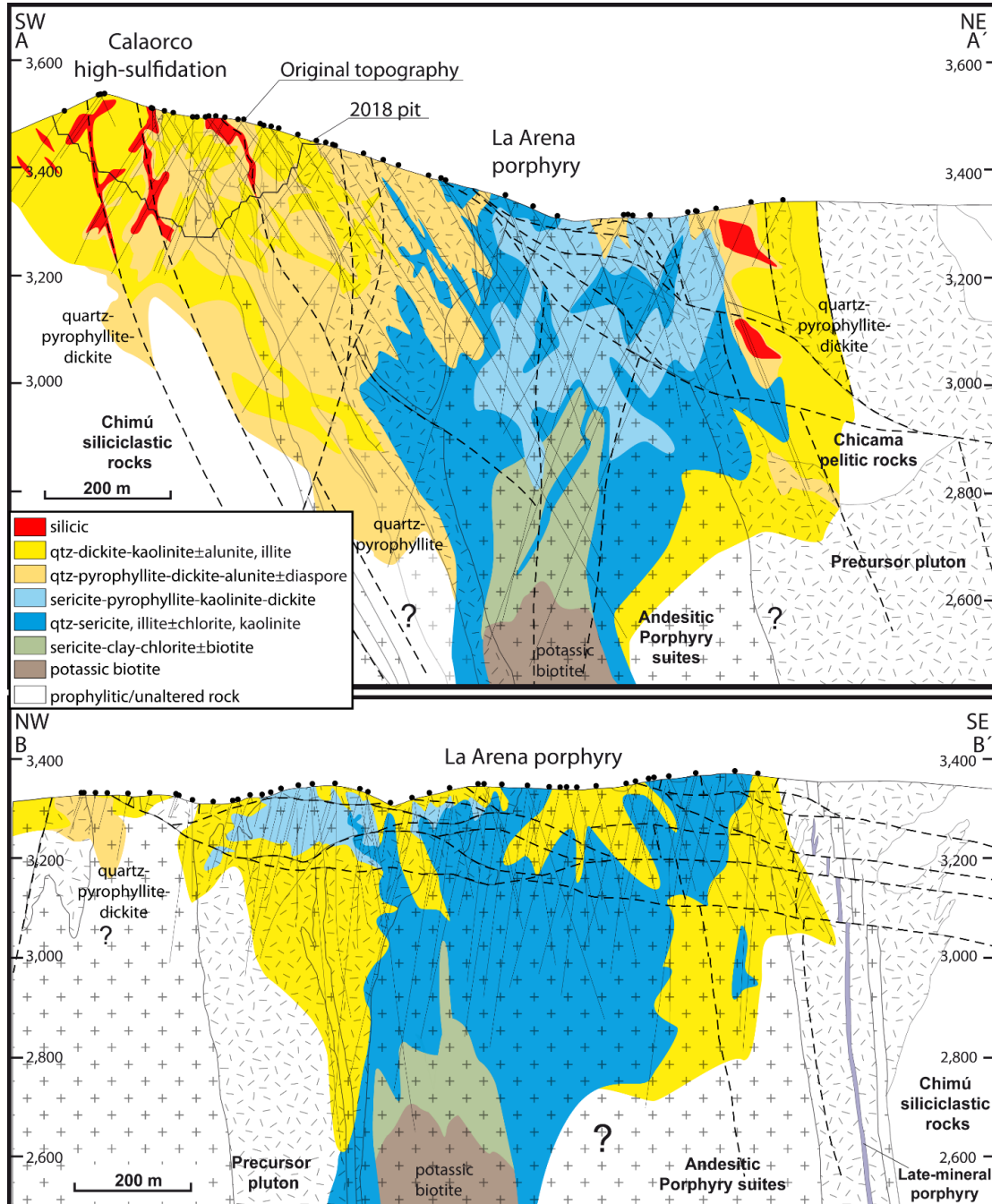


Figure 4.4. Distribution and hydrothermal alteration based on drill core logging and more than 6200 spectral analysis from at least 500 drill holes (thin black line) were interpreted from Tahoe Resources, unpub. files and this study. Alteration type and distribution are shown along two schematic cross sections of the La Arena and Calaorco deposits. Geological units are shown in different frames. Position of cross sections presented in figure 4.1.



Sericitic hydrothermal alteration is typified by complete transformation of the matrix and subhedral plagioclase (up to 40 vol %) to sericite ( $\leq 0.05$  mm) - muscovite ( $\leq 0.15$  mm) at deep level, while sericite-illite, lesser chlorite, kaolinite and carbonate in the shallow ore zone (~390 m deep; Figs. 5.5D, E). Infrared absorption spectra (using Terra-Spec) indicate that the carbonate is ankerite (i.e., enriched in Fe and Mn) together with sericite-

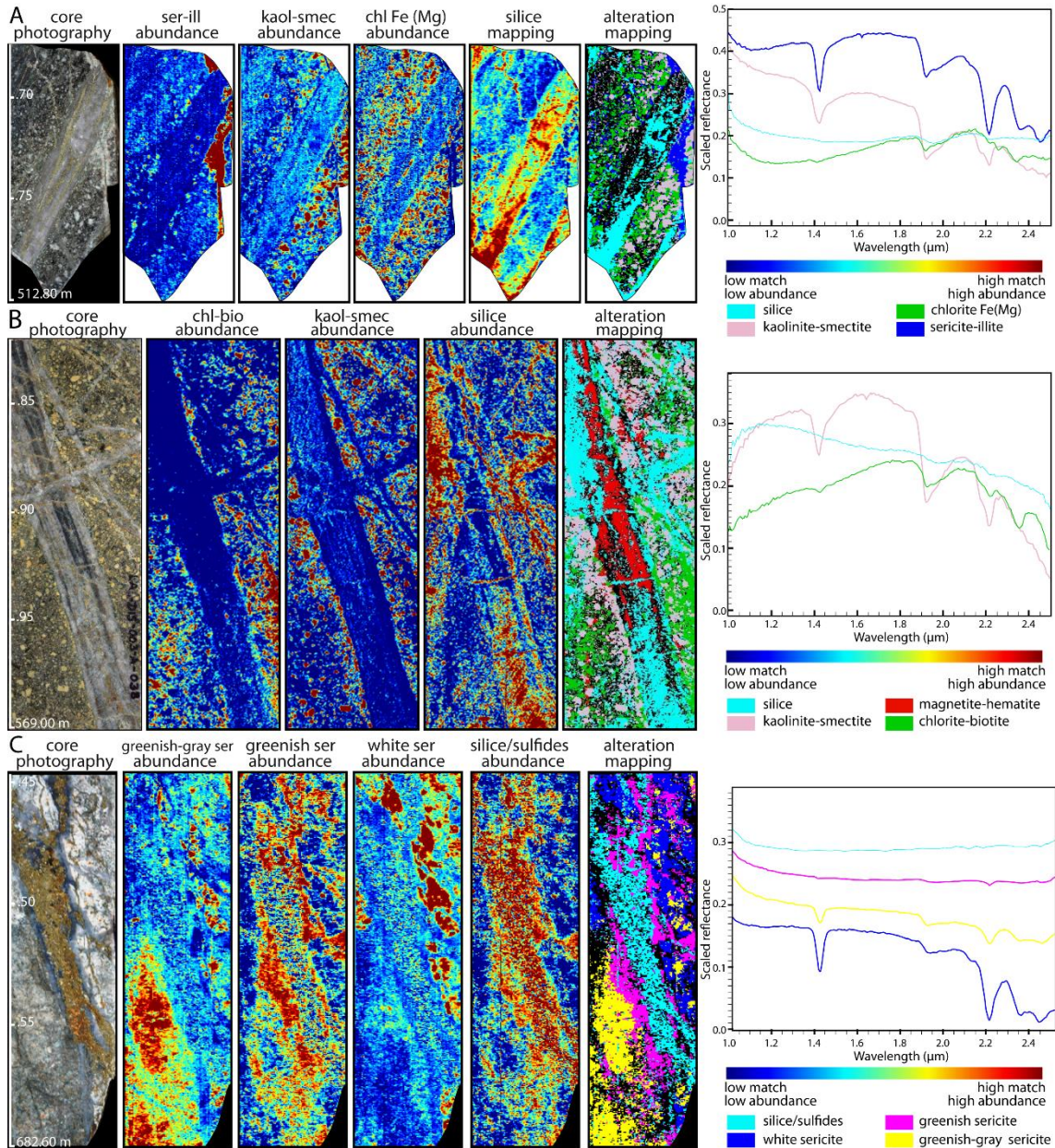


Figure 4.5. CoreScan image. Abundance and mapping of different hydrothermal alteration minerals at the La Arena Cu-Au-(Mo). **A.** Early andesite porphyry whit chlorite-sericite-clays (kaolinite-smectite) alteration cut by anhedronal quartz-pyrite ± chalcopyrite ± magnetite ± bornite AB<sub>E</sub> veinlet. SCC is overprinted by pyrite-dominated D<sub>L</sub> veinlet halos, which are zoning inward from kaolinite-smectite ± chlorite to white sericite. **B.** Green to yellowish green SCC alteration with chlorite-biotite dominating over kaolinite-smectite **C.** Greenish-gray to greenish sericitic alteration overprinted by white sericitic halos of a pyrite-molybdenite B<sub>E</sub> veinlet. **D.** Pervasive yellowish sericitic-illite alteration that overprints quartz veinlet stockwork zone within early andesite porphyry. **E.** Yellowish sericitic-illite alteration overprinted by white illite and illite-kaolinite alteration in inter-mineral andesite porphyry with quartz veinlets fragments.



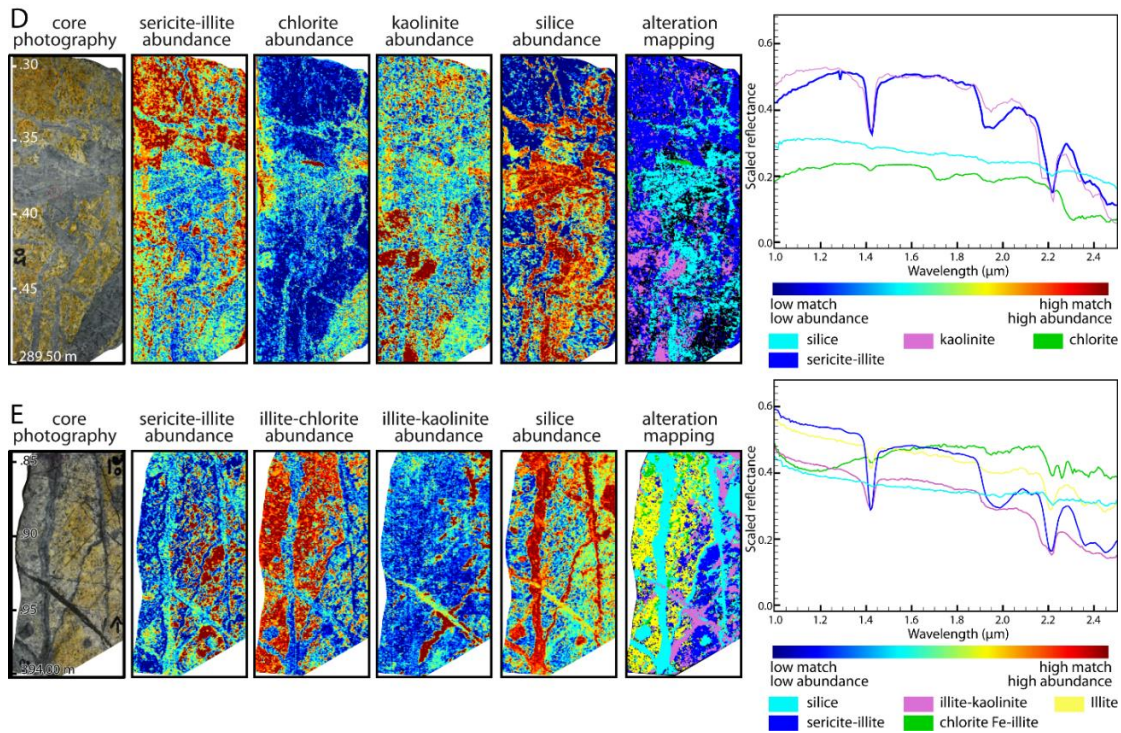


Fig. 4.5. (Cont.)

illite. This alteration in the surface area is yellowish to dark brown in appearance (Fig. 4.5D). Transition between sericitic to advance argillic alteration is also registered in the La Arena porphyry system. Relicts of the sericite – quartz – carbonate or sericite – clays – chlorite alterations are overprinted by advance argillic phyllosilicate + kaolinite – dickite alteration (Fig. 4.4), and rarely diasporite and alunite.

Following the sericitic alteration, extremely acidic fluids generated the advanced argillic alteration assemblage, which is the most extensive hydrothermal alteration in the surface at La Arena porphyry, and is projected to deep as a halo to sericitic alteration, characterized by overprints partial to total destroys the earlier formed sericitic assemblage. This stage is defined by the presence of two mineral assemblages from moderate ( $\sim 360^\circ$  -  $280^\circ\text{C}$ ) to low ( $< 280^\circ\text{C}$ ) temperature (Seedorff et al., 2005): quartz – pyrophyllite + dickite – alunite  $\pm$  diasporite and quartz – alunite, diasporite, and trace pyrite alteration assemblages. The former formed prior and shows a close relationship to crackle breccia zones, which are commonly located in the upper parts and immediately above La Arena porphyry bodies (reach 200 m under the currently surface) marks the transition to the style of advance argillic alteration that host the high-sulfidation epithermal mineralization of Calaorco. The latter is present in the fracture network filling, anhedral pyrite is present as isolate grains within of alunite that is partially replaced by diasporite. The wall rock is pervasively altered into quartz-alunite-pyrophyllite plus massive and/or botryoidal goethite, and rutile. This crackle breccia alteration zones in the surface are variably superimposed by a second advance argillic alteration assemblage of quartz – dickite – kaolinite  $\pm$  alunite together with illite and hematite-goethite. Silicic alteration appears to have intensely developed with increasing distance from La Arena porphyry in magmatic-hydrothermal breccia bodies and fault structures located at Calaorco orebody, probably as a result of cooling and pH increase of the hydrothermal fluids (cf. Sillitoe, 1999).



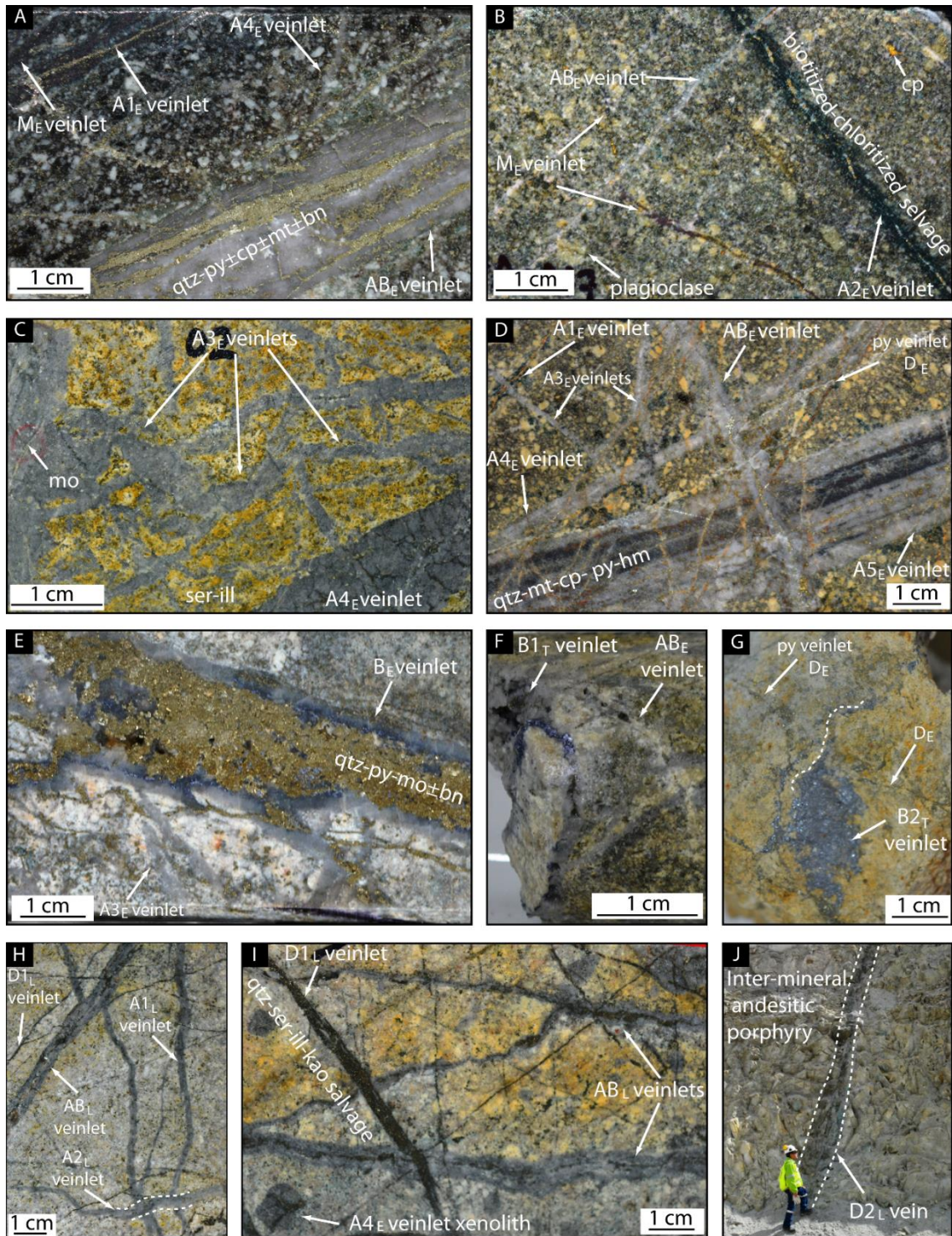


Figure 4.6. Photographs of veinlet types and wall-rock alteration. **A.** Magnetite-rich veinlets ( $M_E$ ),  $A1_E$ -style quartz veinlet with 50 vol % disseminated magnetite and chalcopyrite, lesser pyrite and hematite.  $A4_E$ -quartz veinlet is cut by  $AB_E$ -style quartz veinlet with pyrite and trace chalcopyrite filling the center-line. All type veinlets are cutting early andesite porphyry; wall rock assemblage is plagioclase-hydrothermal biotite with later chlorite **B.**  $A2_E$ -quartz veinlet with 15 vol % of magnetite and a well-developed biotitized-chloritized halo, which is cut by  $AB_E$  veinlet in early andesite porphyry. **C.** Granular  $A3_E$ - and  $A4_E$ -style quartz veinlet cutting early andesite porphyry with quartz-sericite-pyrite and ankerite alteration. **D.** Early andesite porphyry with intermediate argillic alteration is cut by multiple generation of  $A1$ - $5_E$ -quartz veinlets.  $A1_E$ - and  $A2_E$ -quartz veinlets are cut by  $A4_E$ -banded quartz-magnetite-chalcopyrite±pyrite and specular



hematite veinlet. Both are cut by AB<sub>E</sub>-type and early generation of pyrite veinlets (D<sub>E</sub>-type). **E.** Early andesite porphyry with greenish-gray sericite alteration cut by B<sub>E</sub>-type veinlet containing chalcopyrite, pyrite and molybdenite exhibit white sericitic alteration halo. **F.** AB<sub>E</sub> veinlet cut by quartz – molybdenite ± pyrite B1<sub>T</sub>-type veinlet white sericite selvage. **G.** Molybdenite-rich B2<sub>T</sub> veinlet cut pyrite-dominated D<sub>E</sub> veinlets within early andesite porphyry with pervasive sericitic alteration. **H.** Wavy A1<sub>L</sub> veinlet cut by a thin discontinuous A2<sub>L</sub>-type and AB<sub>L</sub> veinlet in inter-mineral andesite. **I.** AB<sub>L</sub> veinlets cut by D1<sub>L</sub>-type veinlets, both type of veinlets cut the intra-mineral andesite porphyry, which contained refractory quartz-bearing A4<sub>E</sub> veinlets with sericitic alteration. **J.** Massive pyrite vein (D2<sub>L</sub>) within inter-mineral porphyry with quartz-kaolinite hydrothermal alteration, emplaced on the La Arena porphyry shoulder close to Calarco orebody. Abbreviated mineralogy according to Seedorff et al. (2005).

## Veinlet types, metal correlation and distribution

Many veinlets contain variable amounts of Fe oxides, gold, and Cu-Fe-Mo sulfides in the La Arena deposits. The veinlets and their sequences of emplacement are defined into following groups, based on descriptive criteria including structure, texture, mineralogy of veinlets filling and alteration enveloped, orientation and crosscutting relationships: (1) M- (cf. Clark, 1993), (2) A- (cf. Gustafson and Hunt, 1975), (3) AB- (cf. Clode et al., 1999), (4) B- and, (5) D-veinlets (cf. Gustafson and Hunt, 1975), in chronological order in emplacement. However, at least two (early and late) veinlet sequences were generated episodically following the early andesite porphyry and inter-mineral porphyry, also some of these veinlets (transitional) were generated without the identification of a contemporaneous porphyry stock. Early-, transitional- and, late-stage veinlets (Fig. 4.6), which are widely recognized in porphyry copper deposits worldwide (e.g. Seedorff et al., 2005), and are summarized in Table 4.3

*The early stage:* This stage predates the inter-mineral andesite porphyry. Magnetite-rich (M<sub>E</sub>-type) veinlets are the earliest and deepest type at La Arena. They occur throughout of the potassic zone in the early andesite porphyry, but are also found in low abundance in the SCC alteration zone. These veinlets are typically a few centimeters long, <0.3 mm wide, crudely planar (Fig. 4.6A). M<sub>E</sub>-type arrays of individual magnetite grains without Cu-Fe sulfides mineralization. However, M<sub>E</sub> veinlets that occur in the SCC alteration contain variable amounts of magnetite, lesser chalcopyrite, and trace pyrite. Magnetite grains are partially oxidized to massive hematite and/or specular hematite. A-quartz veinlets are the most abundant veinlets type at La Arena porphyry system (Fig. 4.6). These veinlets run in a NW, N and NE direction, which is reflected by the structurally-controlled the emplacement of the orebodies, such as concentric distribution in the central part of the early and intra-mineral andesite porphyries. For the A-type quartz veinlet, at least five subtypes can be macroscopically recognized, based on their structure, composition and crosscutting relationship. These 5 subtypes, locally forming a dense stockwork, and are called A1<sub>E</sub> to A5<sub>E</sub> in relative age sequence. A1<sub>E</sub>- and A2<sub>E</sub>-type veinlets are generally less than 3 mm wide of irregular distribution, and are present within deeper parts of the early porphyry with SCC alteration. They contain gray quartz, magnetite-hematite, carbonate, lesser chalcopyrite, and trace pyrite. In contrast A2<sub>E</sub> veinlets have well-developed quartz-chlorite-biotite alteration envelopes (Fig. 4.6B). A3<sub>E</sub>-type veinlet is a highly irregular subtype, and lacks internal symmetry and pinching along their length. A4<sub>E</sub>-type veinlets are the most abundant subtype with a relative straight form, but have no center line. Both A3<sub>E</sub>- and A4<sub>E</sub>-types (Fig. 4.6C) occur mostly above A1<sub>E</sub> and A2<sub>E</sub> veinlets, contains quartz, with variable amounts of chalcopyrite, pyrite, and hematite in fracture network within veinlets. This textural relationship could suggest that the Cu-Fe sulfides were deposited slightly later than quartz-dominated A3<sub>E</sub>- and A4<sub>E</sub>-type

veinlets. In addition, molybdenite occurs locally as disseminates in A3<sub>E</sub>, which may or may not also have deposited at the same time as B<sub>E</sub> veinlets. A3<sub>E</sub> and A4<sub>E</sub> veinlets are the earliest significant contributor of Cu, Au and Mo of the early stage. A5<sub>E</sub>-type cut to all A1<sub>E</sub>- to A4<sub>E</sub>-type veinlets (Fig. 4.6D), and are irregularly distributed in early andesite porphyry. They are generally less than 1 cm, but some attain widths of 3 cm with sharp boundaries, and alteration salvages are absent. Near the center of the veinlets contains one or more thin (< 6 mm) bands enriched in magnetite subparallel to the veinlet walls; symmetrical banding is common, and these veinlets display a banded structure, such as banded quartz veinlets (Muntean and Einaudi, 2000, 2001; Gustafson et al., 2004). More thin (< 1 mm) and dashed magnetite bands are concentrated near the veinlet walls. Magnetite occurs as micrometer-sized (~ 0.1 mm) anhedral grains, together with massive/specular hematite, chalcopyrite and traces to minor amounts of pyrite. Veinlets exhibit sharp boundaries and alteration salvages are absent. AB<sub>E</sub>-type veinlets occur mostly distributed throughout the upper part of the porphyry system (SCC and sericitic zones), and cut all the earlier-stages of A-veinlets (Fig. 4.6D). AB<sub>E</sub>-type veinlets are thicker veinlets (up to 2.5 cm), generally continuous planar to sub-planar structures with sharp edges, and there are no detectable alteration envelopes. The key characteristic of this type is the presence of a poorly defined center-line fill of pyrite, less chalcopyrite, magnetite and trace bornite. Locally AB<sub>E</sub>-type veinlets were reopened later, and carbonates were deposited with filling >20 vol%. Pyrite-molybdenite predominated in the B<sub>E</sub> veinlets (Fig. 4.6E); molybdenite is < 0.3 mm in diameter, and appears to replace chalcopyrite – pyrite. Many veinlets of this type tend to cut towards A3<sub>E</sub>- and AB<sub>E</sub>-type veinlet edges with irregular veinlet walls, and lack internal symmetry with continuous central fill. Those are generally bordered by envelopes of quartz, white sericite, pyrite, and minor carbonates. Pyrite, lesser quartz, chalcopyrite, molybdenite, carbonates, and trace quantities of bornite frequently occur in the B<sub>E</sub>-type veinlet filling, nevertheless molybdenite increases towards the inner edges of veinlets that constitute less than 4 % of the veinlet volume. All early generation of A-quartz and AB<sub>E</sub> veinlets are cut by early-stage, millimetric-scale pyrite veinlets (D<sub>L</sub>-type), which lack alteration envelopes (Fig. 4.6D).

*The transitional stage:* The transitional stage postdates the early andesite porphyry, but predates the emplacement of inter-mineral andesite porphyry. The crosscutting relationships between D<sub>L</sub>, B1<sub>T</sub>, and B2<sub>T</sub> veinlets indicate that a late Mo-rich mineralization formed B1<sub>T</sub> and B2<sub>T</sub> veinlets (Figs. 5.6F, G) after of preferential extraction of Cu and Au from the parental chamber. These type of veinlets provide the major contribution of Mo mineralization at La Arena (<556 ppm Mo). The B1<sub>T</sub> veinlets range in thickness from 0.5 cm to about 3 cm, in contrast molybdenite-rich B2<sub>T</sub> veinlets range from hairline streaks to 5 mm. Both types of veinlets are widely found in the exposed parts (up to 4 vol%), but are irregularly distributed, and located north of the early porphyry. They are mostly concentrated (5 to 8 %), close to the contact with quartz diorite precursor pluton as a discontinuous B1<sub>T</sub> veinlets shell that largely coincides with pervasive sericitic alteration zones. Molybdenite mineralization occurs as medium-grained (< 1.5 mm) short fracture coating in B2<sub>T</sub>-type, and dissemination and/or isolated fine-grained (< 1 mm), together with pyrite within B1<sub>T</sub> veinlets and early andesite porphyry.

Table 4.3. Principal veinlet types at the La Arena Cu-Au-(Mo)

Veinlet type*	Dimensions	Habit	Veinlet fill		Veinlet halo		Distribution and comments
			Gangue	Sulfides	Gangue	Sulfides	
<u>Early-stage veinlets (Early andesite porphyry)</u>							
M <sub>E</sub> -type (M <sub>E</sub> )	Few cm long and <0.3 mm wide	Planar to sub-planar	mt, hm	trace cp, py			The earliest and barren veinlet event of irregular distribution within potassic and SCC alteration.
A-type (A1 <sub>E</sub> )	Few cm long and <0.25-3 mm wide	Planar to sub-planar but sharp defined walls	Gray qtz, mt, minor hm	trace cp, py			Irregular distribution into SCC alteration with elevated magnetite contents.
A-type (A2 <sub>E</sub> )	Few cm long and <3 mm wide	Slightly wavy to planar but sharp defined walls; veinlets have a center-line not well-defined	Gray qtz, mt, hm, chl, ca	Minor cp, py	Important; 0.1 cm to 0.25 cm bio-chl alteration salvage	Minor cp, py	Rarely observed and never in countable amounts
A-type (A3 <sub>E</sub> )	Few cm long and <2.5 cm wide	Wavy and discontinuous in form but sharply defined walls.	Granular qtz, hm	Important: cp, py, locally mo			Dominant veinlet type in the shallow ore zone with significant contributor of Cu-Au and Mo into sericitic alteration
A-type (A4 <sub>E</sub> )	Strike continuity from <1 cm to more than 1 m and <0.1 mm to ~3 cm wide	Planar to sub-planar. Occur as multidirectional stock-works and sheeted arrays	Anhedral granular qtz, mt	Important: mainly cp, py	Commonly lack prominent alteration envelopes	Minor cp	Widely distribution within the EAP, within of potassic, SCC, and sericitic alteration zones. These veinlets are truncated by IAP.
Banded qzt (A5 <sub>E</sub> )	Strike continuity from millimeters to more than 50 cm and <1.5 cm wide	Planar to slightly wavy; show bands of dark to black quartz	qtz, mt, hm. Micron-sized grains of mt form the dark bands qtz	Important: mainly cp, py	Lack alteration halos, although kao-smec halos developed to 680 m depth	Minor cp and py	Irregularly distribution in early porphyry, where appear at 570 m and continue to depth
AB <sub>E</sub> -type (AB <sub>E</sub> )	several cm long and 0.5-1.5 cm wide	Planar to slightly wavy, with sharp edges; with center-line development	Vitreous qtz, mt	Important; mainly py, cp, trace bn	Normally without halos	Uncommon	Later veinlet events transitional to B. Widely distribution throughout the orebody.
B <sub>E</sub> -type (B <sub>E</sub> )	strike continuity from <2 cm to more than 0.3 m and 0.5 to 2 cm wide	sharp planar wall-rock contact with vuggy centerlines	Coarse granular qtz	Important: mainly py, mo, trace bn	Generally lack alteration envelopes but locally with white qtz-sericite, ca halos	Minor py	Significant contributor of Mo. Commonly occurring in the deep Mo-rich zone
Pyrite veinlet (D <sub>E</sub> )	Few cm long and <2 mm wide	Discontinues and planar	minor qtz	mainly py	Normally without halos		Dominant veinlet type in the depth to shallow ore zone
<u>Transitional-stage veinlets (Early andesite porphyry → Inter-mineral andesite porphyry)</u>							
B1 <sub>T</sub> -type (B2 <sub>T</sub> )	several cm long and <3 cm wide	sharp planar to slightly wavy wall-rock contact	Coarse granular qtz	Important: mainly mo, py	Important; up to 1 cm white sericite alteration salvage	Mainly py	Principal contributor of Mo. Commonly occurring in the deep Mo-rich zone with sericitic alteration
B2 <sub>T</sub> -type (B2 <sub>T</sub> )	few cm long and <5 mm wide	sharp planar		Mainly mo			Occurring as short fracture coating in the EAP close to the contact zone with the precursor pluton
<u>Late-stage veinlets (Inter-mineral andesite porphyry → Late-mineral porphyry)</u>							
A-type (A1 <sub>L</sub> )	few cm long and <0.25 cm wide	wavy wall-rock contact	Granular qtz	Minor cp, py			Occurring in the shallow ore zone with sericitic alteration
A-type (A2 <sub>L</sub> )	several cm long and <0.35 cm wide	Slightly wavy and discontinuous	qtz	Minor py, cp			Occurring in the shallow ore zone within IAP.
AB <sub>L</sub> -type (AB <sub>L</sub> )	several cm long and <0.8 cm wide	Slightly wavy to planar and center-line discontinues	qtz	Important; mainly py, cp			Few but common throughout the deposit.
B <sub>L</sub> -type (B <sub>L</sub> )	several cm long and <0.7 cm wide	Planar to slightly sinuous with vuggy centerlines	qtz	Important: py, mo			Rarely observed at 250 m depth
D-type (D1 <sub>L</sub> )	several tens of cm long and a few mm to 3 cm wide	Planar and continuous	Minor qtz, and patches of ca	Important: mainly py, trace cp	Important; 0.5 cm to 2 cm qtz-ser alteration salvage	Important; dominantly py	Widely distribution in the upper levels of the ore body, decreasing in abundance with depth
Massive pyrite (D2 <sub>L</sub> )	Tens of m long and <35 cm wide	Planar and continuous, with sharp edges	Minor qtz	Important: py			Dominant vein type on the La Arena porphyry shoulder close to Calaorco orebody

\* Classification according to Gustafson and Hunt (1975; A-, B-, D-types), Muntean and Einaudi (2000; banded quartz), Sillitoe (2000; quartz-magnetite-chalcopyrite), Clode et al. (1999; AB-type) Abbreviated mineralogy according to Seedorff et al. (2005)

*The Late stage:* The late stage postdates the inter-mineral, but predates the emplacement of the late-mineral porphyry. This stage is characterized by a repetition of veinlet generation of the early-stage veinlets but with a decrease in density and sulfide contents. The wavy granular quartz-rich A<sub>1L</sub> veinlets are cut by quartz-dominated A<sub>2L</sub> veinlets and in turn both cut by AB<sub>L</sub> (Fig. 4.6H). Chalcopyrite predominantly occurs as disseminations in A<sub>1L</sub> veinlets, whereas pyrite occurs in three types (A<sub>1L</sub>, A<sub>2L</sub>, and AB<sub>L</sub>) of veinlets. Molybdenite-pyrite bearing B<sub>L</sub> veinlets are planar to slightly sinuous in form of <0.7 cm wide, and are rarely observed within the inter-mineral porphyry with strong to moderate sericitic alteration zones nearby early porphyry contact. They are regarded as the significant contributor of Mo, with high grades up to 180 ppm. D<sub>1L</sub> and D<sub>2L</sub> veinlets are predominantly associated with all of the andesite porphyries. The first type of veinlets tends to be thin (<3 cm), and is located in the central part of porphyry system. D<sub>1L</sub>-type consists of pyrite and trace chalcopyrite in the veinlet filling, with coarse-(muscovite) to fine-grained sericite, illite, kaolinite, quartz, and pyrite in the envelope (Fig. 6I). The D<sub>1L</sub> veinlets with pervasive sericitic envelopes overprinted the SCC alteration in the early porphyry at 515 m below the surface, white sericitic veinlet halos are zoned outward to kaolinite – smectite – chlorite assemblage alteration for few tens of millimeters from the fracture or fault planes (Fig. 4.5A). The second comprises a generation of massive sulfide veins spanning at the southwest shoulder of the La Arena porphyry system, where Calaorco high-sulfidation epithermal orebody is emplaced. These pyrite veins are structurally controlled by transandean orientation structures of strike ~220°, which have several tens of meters long and up to 35 cm wide (Fig. 6J) within of pervasive kaolinite – dickite ± alunite alteration zone. D<sub>2L</sub>-vein cut magmatic-hydrothermal breccias with high-hydrothermal mineralization of the Calaorco orebody, and late inter-mineral porphyry. Pyrite mineralization is more abundant in D<sub>1L</sub>-type veinlet with minor chalcopyrite, and traces of pyrrhotite, and sphalerite (Tahoe Resources, unpub. files), implying an intermediate-sulfidation state (Seddorff et al., 2005).

#### 4.4.2 Calaorco high-sulfidation epithermal orebody

Calaorco high-sulfidation (HS) epithermal orebody is superimposed on the La Arena porphyry Cu-Au-(Mo) deposit as a result from telescoping (cf. Sillitoe, 1999), which strongly suggests certain uplift and erosion accompanied with hydrothermal activity (cf. Sillitoe, 1999; Masterman et al., 2005). The Calaorco orebody is slightly offset from the surface projection of the porphyry environment (Fig. 4.1); it extends ~ 1.2 km along strike at elevation between 3560 and 3250 m above sea level, and projected as a funnel ~0.6 km at depth along the unreactive Chimú quartz sandstone on porphyry's southwest shoulder (Figs. 5.2, 5.7). This relationship between HS epithermal and porphyry-type ore system was also recognized in the north parts of the La Arena porphyry (Ethel high-sulfidation system; Fig. 4.1; Garay et al., 2012), and had already been mined by Rio Alto Mining at the time of this study.

#### Depth of sulfidation-style mineralization at Calaorco orebody

The telescoped of HS epithermal system over porphyry-style mineralization is controlled by zones of maximum permeability, which was formed by syn-mineral faulting, such as Calaorco Fault System (CFS) and the intersection of this major fault system with transandean structures of strike NE (Fig. 4.7). Chimú bedding planes of steep dipping permeable quartz sandstone, and fracture network are as important as the mineralized faults at the Calaorco orebody.

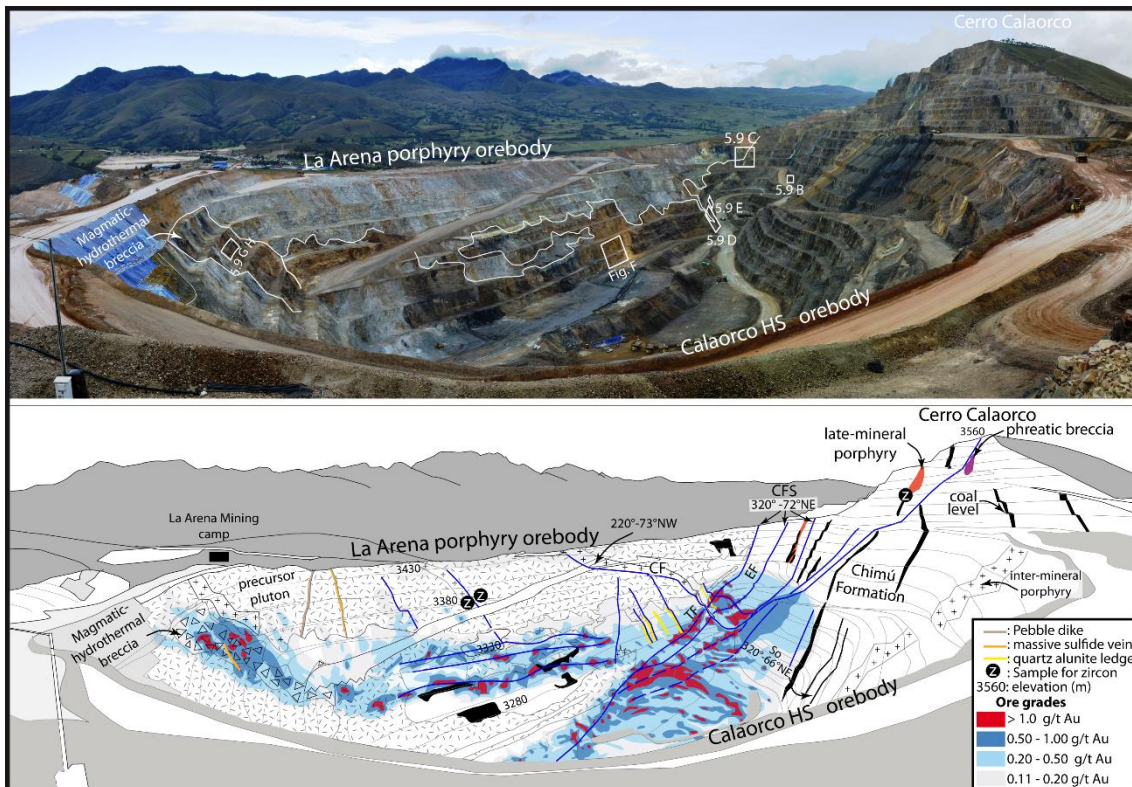


Figure 4.7. Photograph and interpretative sketch on field observation and gold distribution (based on blast holes data) of the open-pit in february 2019 of Calaorco high-sulfidation gold system on the La Arena porphyry shoulder (looking SE). The location of most samples selected for U-Pb geochronological dating are shown as letter referring to the mineral type (in black circles). Photographs from A to H show the different epithermal-style mineralization, photographs also are located in Calaorco open-pit photograph. Abbreviation, CF: Calaorco fault, TF: Tilza fault, EF: Esperanza fault, CFS: Calaorco fault system. Open-pit location are shown in figure 4.1

Chimú sediment rocks in the Calaorco open pit are composed of medium-to coarse grained quartz sandstone, as well as locally granoblastic quartzite varieties, grey to reddish in color. The sediments are dominated by mono- to polycrystalline quartz grains (> 95% vol) with disseminated grains of K-feldspar, rutile, zircon and variable amounts of disseminated high-sulfidation mineralization, such as pyrite – enargite and covellite, when these disseminated grains are leached, a pseudo-vuggy texture forms in the quartz sandstone in elevation from 3280- to 3450-m. The quartz sandstone associated with the silicic alteration is cut across by anhedral quartz veinlets, enargite-rich fractures (Fig. 4.8A), and thin (0.1 mm wide) breccias with wall-rock clasts and cemented mainly by quartz and goethite. The quartz sandstone hosts only trivial amounts of gold mineralization. However, the fracture network and oxidized bedding planes of steep dipping quartz sandstone (Fig. 4.8B) trend in NW-orientation within Calaorco Fault System, and are considered as major storage of gold with average grade of 1 g/t Au. This fault system appears to control the spatial distribution of gold mineralization at Calaorco deposit. The dominant orebody of Calaorco consists of massive quartz and mineralized zone along the Tilza reverse fault of Andean trending ( $320^{\circ}$ ) with  $70^{\circ}$ - $80^{\circ}$  NE-dipping, and is hosted on the subparallel Chimú quartz sandstone of steeply dipping overturned strata ( $65$ - $80^{\circ}$  NE) (Figs. 5.7, 5.8C). The vertical extend of ore is about 400 m in averages, although Tilza massive quartz root in some geologic section shows similar level with roof of the La Arena potassic alteration (Sangay et al., 2017). This feature implies that Tilza

mineralized fault may attain at least 800 m below of the original surface, with 0.1 to 1 m in wide. Tilza massive quartz is typically associated with hypogene advanced argillic alteration halo, which is characterized by well-zoned from quartz – pyrophyllite with minor dickite to quartz – kaolinite – dickite and local occurrences of alunite at elevations above about 3450 m (Sangay et al., 2017). This alteration is rooted by quartz-pyrophyllite occur lining ovoids in small areas (<25 m wide) as patchy texture (Sangay et al., 2017), and partially replaces silty beds of the Chimú Formation or infilling fractures and matrix of contact breccias. The patchy texture is interpreted to be formed through high-temperature outgassing of subjacent magma (Noble et al., 2011). The extension of this type of alteration is stratigraphically controlled (Sangay et al., 2017), and the coal levels appear to have controlled the lateral extent to the southwest of Calaorco orebody (Fig. 4.7). The Tilza mineralized fault occurs as the main structure controlling the gold mineralization, which assayed up to 653 g/t Au (Tahoe Resources, unpub. files). A series of other mineralized faults follow this primary trend, including the Esperanza mineralized fault (Fig. 4.7), which contains gold grades up to 77.61 g/t (Tahoe Resources, unpub. files), in oxidized mineralized faults (goethite > jarosite >> hematite) hosted by the Chimú quartz sandstone. Andean orientation structures and bedding are locally cut by NE-striking (transandean) faults and clay matrix breccia zones.

Transandean orientation structures are the second mineralized fault set, dominated by NE-striking, high-angle (220° to 235° and 70° to 85°NW) formed in the compressional direction with a slight offset of bedding planes. This normal dextral fault set controlled the emplacement of several dikes (e.g. Calaorco dike) and vuggy quartz replacement bodies (ledges; cf. Sillitoe, 1999, 2010; Muntean and Einaudi, 2000). The pre-existing fault Calaorco array on the development of Calaorco andesite dike (Fig. 4.8D), where downward into quartz sandstone in Calaorco open pit the dike gradually fade away (~3285 m a.s.l.). A weakly kaolinized andesite dike with fault gouge as argillic pseudo-envelopes cuts the Andean mineralized faults (Fig. 4.7), implying that the emplacement took place after the gold mineralization. Vuggy residual quartz is well developed between 3280 to 3350 m, and occurs in irregular ledges and in the roof of the porphyry stock within Chimú quartz sandstone at Calaorco open pit (Fig. 4.7). Residual vuggy quartz ledges, are laterally distributed to the southwest of a roof of the porphyry stock. Ledges range from a few centimeters to about 2 m wide, strike ~230° with dip steeply. The vuggy quartz ledges diminish in their size toward the precursor pluton contact with increasing elevation (up to 3350 m a.s.l), and finally fades away into the pluton. The ledge consists of vuggy quartz in the center-line zone, and quartz-alunite and kaolinite-dickite alteration zones are found on the periphery and outer edges, respectively (Fig. 4.9E). Hematite and trace pyrite are present in the voids filling or micro-veinlets together with anhedral quartz, and pyrite postdates the vuggy quartz formation. No gold appears in the sample used, but gold grades up to 10 g/t are reported on assays of blast holes. Some thin ledges (< 25 cm wide) located laterally adjacent to the roof of the cupola are brecciated and poorly cemented. These polymictic breccias contain angular to subrounded quartz sandstone and vuggy residual clasts, and the latter is cut by thin quartz veinlets (< 2 mm wide) and has a rock-flour matrix vuggy silica. The roof of the underlying andesitic porphyry is pervasively altered into vuggy quartz ± alunite, and coarse-grained (50 µm to 1 cm) alunite may occur as lining voids and fracture filling, and as disseminated fine grains in moderate alteration zones. The root alteration of the porphyry has a halo that extends outward and downward, with decreasing SiO<sub>2</sub> through the quartz – pyrophyllite – dickite – alunite, hematite – goethite to quartz – kaolinite – dickite ± alunite zones (Fig. 4.8F). Coarse- to



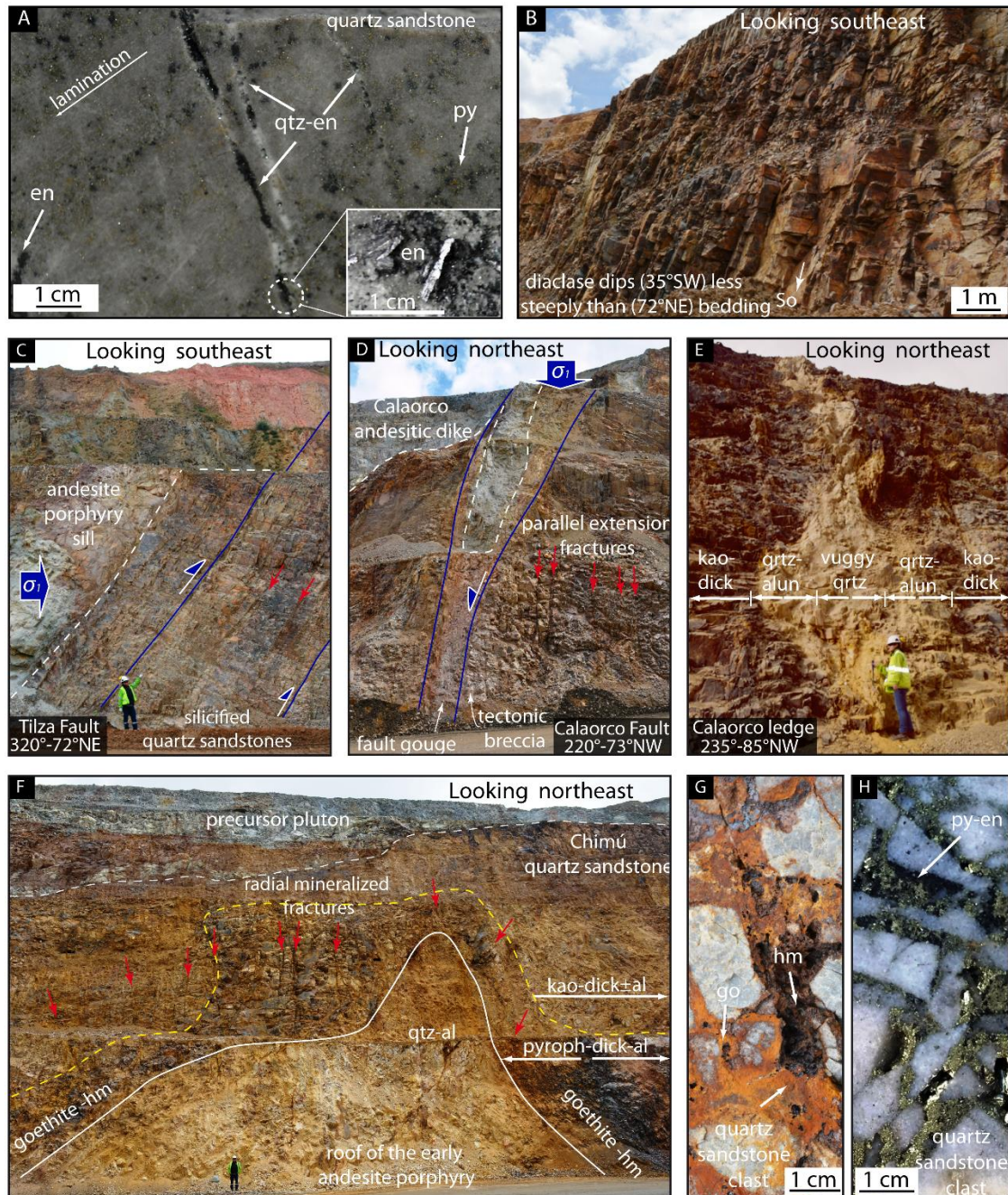


Figure 4.8. Different epithermal-style mineralization at Calaorco high-sulfidation gold system, photographs are located within of the Figure 4.8. **A.** Quartz-enge are presented in the fracture filling and pyrite plus enargite disseminates in Chimú quartz sandstone. Detail photo, longitudinal section of the plan fracture shows enargite crystals. **B.** Steep dipping overturned bedding quartz sandstone (determined by bedding/diabase relationship; McClay, 1991) with hematite-goethite on bedding planes. **C.** Northeast lateral tip of the Tilza thrust fault (320°-71°NE), where the gold-rich gouge is minor 1 cm wide and Chimú quartz sandstones footwall and hanging wall blocks show strong silicification. Photographs **D** and **E** are from transandean structures (230°-80° NW). This fault set controlled the emplacement of the several dike (image D), and quartz-alunite ledges (image E). **F.** Simplified alteration-mineralization zoning in and immediately above the early andesitic porphyry. Note the upward changes from quartz – alunite through quartz – pyrophyllite – dickite – alunite to quartz – kaolinite – dickite ± alunite, with oxide gold zones leached of copper. Magmatic-hydrothermal breccia cemented by hematite – goethite (**G**) after pyrite – enargite – luzonite ± chalcopyrite (**H**) and strongly silicified quartz sandstone. Abbreviated mineralogy according to Sedorff et al. (2005).

fine-grained alunite associated with the main mineralization and pervasive advance argillic alteration at Calaorco has  $\delta^{34}\text{S}$  values of 22.97–24.98 ‰ and  $\delta^{18}\text{O}_{\text{SO}_4}$  values of 9.9–13.0 ‰ (Montgomery, 2012). These values suggest that a  $\text{H}_2\text{S}$ -dominant magmatic fluid induced the mineralization under the condition of low pH (0–2) and  $\log f_{\text{O}_2}$  of –28 to –30, as shown in the Lagunas Norte deposit by Cerpa et al. (2013). The temperatures estimates from the alunite – pyrite sulfur isotope geothermometry are 214°, 229°, and 243 °C, and the alunite associated with pyrophyllite records the highest temperatures from 243° to 250 °C. The samples were collected from the top of the La Arena porphyry system at elevations of about 3500 m (Montgomery, 2012). These isotope results suggest that the deposition of the Calaorco high-sulfidation epithermal Au mineralization may occurred under low- to moderate temperature (~ 214° - 229°C) conditions.

### Shallow sulfidation-style mineralization at the Calaorco orebody

The mineralization of the shallow Calaorco HS orebody is related to a prominent style of structural control, together with magmatic-hydrothermal brecciation. Magmatic-hydrothermal, and phreatic breccias in the context of a genetic framework (cf. Sillitoe, 1985) are broadly observed in association with the multiphases porphyry complex of the La Arena deposit (Fig. 4.7). On the basis of matrix description we present a classification, which allowed us to subdivide the magmatic-hydrothermal breccias into the following two breccia subtypes common in the Calaorco orebody: (1) quartz-pyrophyllite breccias are located along the sub-vertical contact between porphyry bodies and sedimentary rocks, which contain subangular-rotated clasts of quartz sandstone and siltstone. They have a rock flour matrix and cement that consist of aggregates of quartz-pyrophyllite infilling fractures and partially replacing silty beds of Chimú formation. This type of breccia extends about to a depth of 1000 m below the current surface, where pyrophyllite predominates over quartz in the cement, and with gold grades about 0.789 g/t. (Fig. 4.2E). Quartz-pyrophyllite-brecciated fragments occur as xenoliths in the late inter-mineral porphyry, thus this relationship indicates that these breccias occurred prior to the emplacement of the third intrusive phase. (2) Silicified and oxide breccias (before Cu-Fe sulfides) range in horizontal dimensions from few meters to a maximum of 70 m, and are preserved in the northwest part of the Calaorco open-pit at elevations between 3,340 and 3,450 m above sea level (Fig. 4.7). This type of breccia is characterized by clast supported. Particularly toward the margins of the breccia pipe grading to moderate mineralized (up to 0.5 g/t Au), where clasts appear merely to have been slightly pulled apart (crackle breccia zone). In the central parts of these breccias have a jigsaw texture that consists of clasts sizes range from a few millimeters to 3 cm in diameter, and are subangular to angular in shape. The breccias are regarded to be derived from the Chimú quartz sandstone wall rock, suggesting limited vertical displacement of clasts (in situ hydraulic fragmentation) during the pipe emplacement (Fig. 4.8G). The cement consists of botryoidal hematite and goethite, together with gold mineralization. However, the magmatic-hydrothermal breccias cement is preserved as layers and/or lenses within the oxide gold zone leached of copper (leached cappings; cf. Sillitoe, 2005), consisting of dark-colored mixture of fine- to coarse-grained brass-yellow tetrahedral pyrite, dark-grey massive luzonite and greish-black enargite thick tabular to prismatic in habit, with minor covellite (Fig. 4.8H). Oxides and/or sulfides cement rarely exceed 20 vol%, and Au and Cu grades are up to 5.14 g/t and 0.25 wt%, respectively. Magmatic-hydrothermal breccias are cut by massive sulfide veins (D2L-type), where the gold grade increase up to 7 g/t, because these breccias underwent a second mineralization event.



Phreatic breccias also are identified in the Calaorco orebody, and are subdivided into two subtypes according to the geometric (cf. Sillitoe, 1985); (1) Pebble dikes (cf. Parsons, 1925) are preserved at elevations between 3,370 to 3,430 m above sea level, and are registered at the margins of an altered and wavy mineralized central diorite intrusion close to the northeast edge of the Calaorco orebody (Fig. 4.7). This subtype comprises mainly dikes, which are accompanied by sills-like bodies. Dikes and sills range in thickness from a few centimeters to ~1.2 m. These breccias contains subangular to rounded heterolithologic clasts in a dark-black sand- to silt-size rock flour matrix. (2) Isolate irregular phreatic breccia is observed at the top of the Calaorco orebody (Cerro Calaorco; 3530 m a.s.l.) within quartz sandstone with sharp contacts (Fig. 4.7). This breccia is structurally controlled by a transandean structure ( $210^{\circ}$ - $77^{\circ}$ NW), and occurs as an inverted cone structure of ~7 m wide in map view with their narrow part towards the depth. The angular to sub-angular fragments have dimensions range from a few centimeters to millimeter, and some of them are cut by hairline pyrite veinlets, which are inferred to be derived from the wall rock. The breccia fragments are separated by 35-45% volume open space, and are filled by a matrix dominantly of rock flour with trace pyrite and hematite. The two types of phreatic breccias are barren, corresponding to late- to post-mineralization products.

#### 4.5 Sulfide and metal zoning

In the Arena porphyry Cu, Au and Mo grades are concentrically changed around of the early andesite porphyry (Fig. 4.9), from the scale of the A<sub>3-5E</sub> and AB<sub>E</sub>, and D<sub>E</sub> veinlets, together with early pyrite veinlet generations (D<sub>E</sub>) to whole-rock volumes. Early andesite is generally altered and mineralized, and A<sub>3-5E</sub>, AB<sub>E</sub> and D<sub>E</sub>-type veinlets are highest in metal grades, containing up to 5.5% Cu and 6.5 g/t Au. Approximately 70 % of gold is associated with Cu-Fe sulfides, and 20 % of gold with gangue minerals rather than sulfides (Garcia et al., 2015; Cano, 2017) deposited during the magmatic stage. Late A<sub>1-2L</sub>, AB<sub>L</sub>, B<sub>L</sub>, D<sub>1-2L</sub>-type veinlets associated with inter-mineral porphyry bodies contain the remainder of the copper, gold, and molybdenum mineralization in conjunction with the small magmatic-hydrothermal breccias, and clearly give rise to the centers with the highest grade. Mineralized porphyry core is characterized by a steep, NE-plunging cylindrical body containing average grade of 0.35% Cu, and 0.24 g/t Au. Calaorco HS epithermal also plunge northeast at a similar angle (Fig. 4.9). Both deposits have similar Au grades (>0.5 g/t) and low concentrations of As and Sn. The distribution of molybdenum is confined to the southwest and northeast part of the central deposit within B<sub>E</sub> and B<sub>1-2T</sub> veinlets during the early to transitional stage, forming an irregular shell that contains <600 ppm Mo (Fig. 4.9). At the transitional stage, more Mo was precipitated relative to Cu.

Ore grades are lower in the precursor pluton, and contains up to 0.03-0.07 g/t Au and 0.007-0.05% Cu. The later hornblende-rich andesite porphyry has grades of <5 ppb Au and <0.003% Cu. The Cu, Au and Mo grades decrease together with the intensity of alteration from the intrusive contacts inward to the center of these early and later intrusive bodies. The lower grades of these early and later bodies are due to their intra-mineral timing of intrusion.

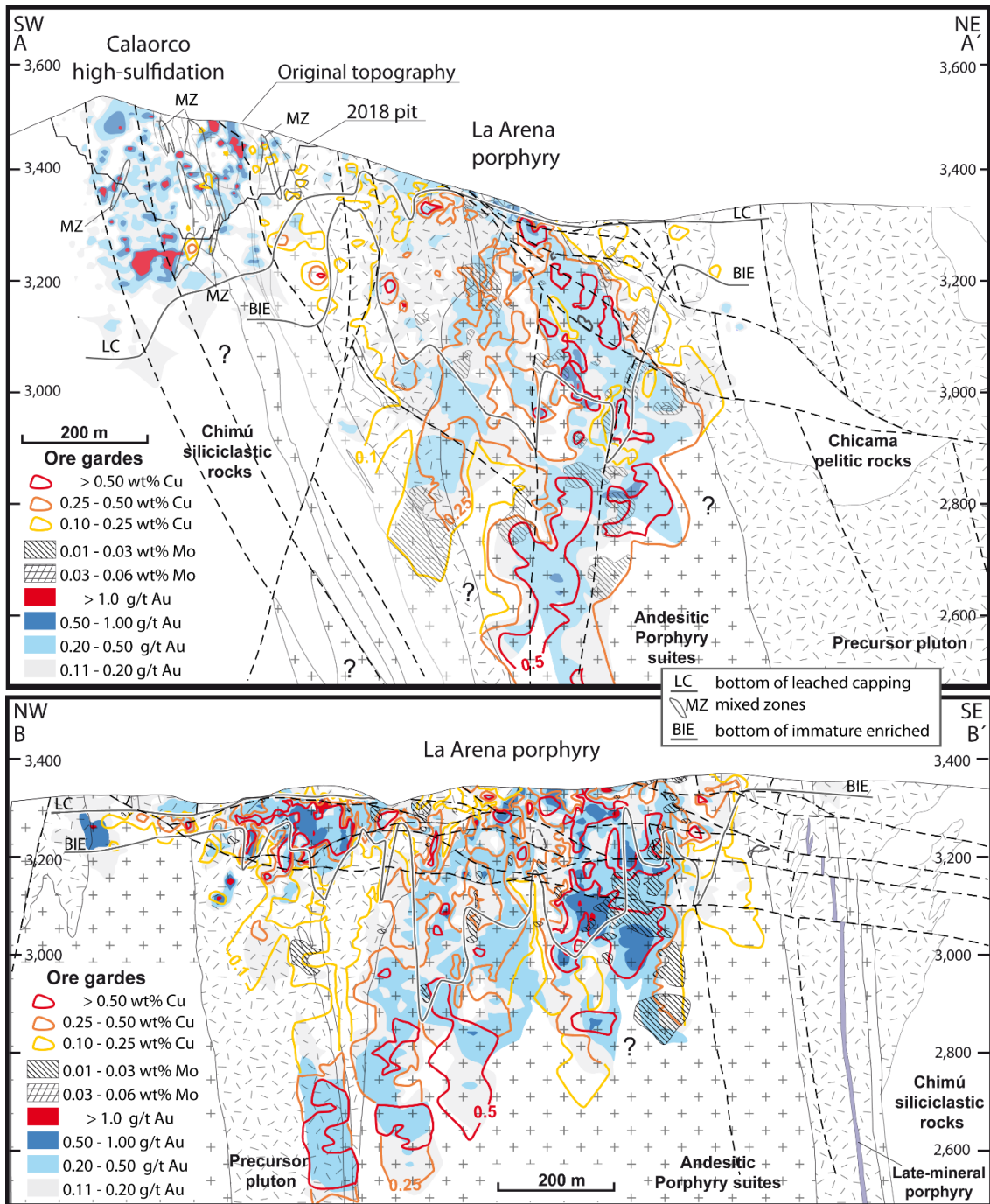


Figure 4.9. Two perpendicular cross section, illustrating copper, gold and molybdenum grade patterns. Cu, Au, and Mo grade data come from assay data from 168 and 374 drill holes for the AA' and BB' cross sections, respectively. Grades contours are based on continuous drill core assays (intervals of 2 m) of all drill holes shown on the section and taken from Tahoe Resources (unpub. files). Geologic unit are shown in different frames. Sections location are shown in figure 4.1.

### 4.6 Supergene alteration and mineralization

The principal supergene process in the La Arena porphyry is the contemporaneous leaching of sulfides and kaolinization – smectitization of plagioclase. The leach capping and pervasive kaolinite – smectite extends to a depth of about 50 m, but locally attains a maximum of 80 m at the top of the La Arena porphyry system. However, Calaorco

lithocap with advance argillic alteration developed on the Arena porphyry shoulder constitutes a dominant hematite – goethite leached capping that attain 400 m thick (Fig. 4.9), the formation of which was probably facilitated by microbial activity during supergene oxidation (e.g. Pierina; Bissig et al., 2015). Auriferous mineralization with sub-microscopic and locally coarsening of gold grain size mineralization of a now wholly or partially oxidized high-sulfidation epithermal system is mainly hosted mainly in a hematite – goethite dominated oxide assemblage on bedding planes of steep dipping quartz sandstone, mineralized faults, and ledges. Metal grades within leached capping range, from 0.11 up to 65.57 g/t Au (based on blast holes data 2018; Tahoe Resources, unpub. files), whereas copper grades are considerably low (<500 ppm Cu). Nonetheless, the grade increases up to 2,500 ppm Cu in the mixed zones, where pyrite and Cu-sulfides contents and leaching and oxidized Cu minerals are minimal, tend to occur as quartz sandstone lenses, from 10 to 70 m thick, and are preserved with the leached capping (Fig. 4.9).

The Cu-sulfides comprises chalcopyrite, enargite, luzonite, supergene chalcocite, and covellite with lesser bornite, in association with chalcantite as an oxidized Cu mineral. They are disseminated in the veinlets, fractures or matrix breccias. Leached capping is underlain by an immature supergene enrichment zone, which is developed within the uppermost 50 to 270 m of the sulfide zone. In the zone downward-projecting prongs of immature supergene enrichment minerals controlled by faults give rise to great irregularity into the hypogene ore (Fig. 4.9). The immature supergene enrichment zone is composed of pulverulent chalcocite, covellite, and minor bornite, occurring as secondary products on chalcopyrite and minor pyrite grains, with localized concentrations of massive chalcocite replacement coating on chalcopyrite. The copper grade within the supergene blanket ranges, from 0.2 to 0.8% Cu. These grades are generally similar to those of the hypogene mineralization zone with the range between 0.2 and 0.6% Cu. The gold grades in some areas within the supergene blanket are considerably higher (up to 1 g/t) than those related to the hypogene zone (up to 0.5 g/t; Fig. 4.9).

## **4.7 Other epithermal-porphyry transition prospects in the La Arena district**

### **4.7.1. Alizar-Vanessa porphyry and epithermal systems**

Alizar prospect is located approximately 2 km west of the La Arena village in northern Peru (Fig. 2.1), lies just northwest of the Calaorco open-pit at La Arena porphyry system. The Alizar is a partly explored prospect. Cambior and Tahoe Resources Inc. mining companies drilled the prospect in 2003-2005 and 2016, respectively, and tested the area for porphyry-style mineralization. Diamond drill hole and out crops were analyzed by Corbett (2014) and Hedenquist (2015) and identified a strong quartz-sericitic alteration and advanced argillic alterations at Vanessa prospect, suggesting that such alteration zones constitute laterally roots of a lithocap (Hedenquist, 2015). This hydrothermal alteration is preserved as short remnants, including pyrophyllite – alunite and dickite ± kaolinite associated with hematite – goethite. The advance argillic alteration is overprinted in late Oligocene Alizar Au-Cu porphyry system, which is centered on the La Arena precursor quartz diorite pluton. Porphyry-style mineralization in the upper levels occurs as a stockwork of quartz banded – pyrite veinlets, associated with illite-clay-chlorite, while quartz banded – magnetite – chalcopyrite with biotite alteration and disseminated chalcopyrite and magnetite are preserved below a depth of ~ 250 m.

#### 4.7.2 Agua Blanca porphyry and epithermal system

Agua Blanca prospect is situated approximately 3 km from the east of the La Arena mine (Fig. 2.1). This prospect contains epithermal- and porphyry-type mineralizations (Arias and Neglia, 2018), and is centered on a multiphase of andesite porphyry stocks emplaced into a precursor dacite pluton, which itself cuts quartz sandstone assigned to the Late Cretaceous Chimú Formation. The dacite pluton crops out along the Cerro El Coche and Quebrada Agua Blanca, and is a part of the dacitic Yamobamba Pluton. Andesite porphyry stock is composed of several discrete phases with medium- to fine-grained, equigranular characteristics, as well as porphyry varieties. Phenocrysts in the porphyry are composed of plagioclase, quartz, hornblende and biotite.

Potassic (quartz – biotite  $\pm$  K-feldspar) and argillic (quartz – illite - kaolinite) alterations are exposed in the surface area, where a potassic core is developed extensively throughout much of the andesite porphyry stock. The alteration zone is partially overprinted and completely surrounded by alteration assemblage of illite plus kaolinite, which is developed mainly in the dacite pluton. Locally, surface parts of the southwest limit of andesite porphyry contain quartz-illite-chlorite, minerals denoting the existence of intermediate argillic (cf. Meyer and Hemley, 1967). Dacite pluton namely a widespread precursor pluton in outcrops contains up to 0.05% Cu, 117 ppm Mo, and 0.016 ppm Au (Arias and Neglia, 2018), even though it displaying intense leaching of sulfides and kaolinization of silicates. The leached zone is mainly comprised of goethite and jarosite. Oxidized copper minerals are absent from the leached capping, however contained psilomelane close to contact between dacite pluton and quartz sandstone of the Chimú Formation. The andesite porphyry stock, includes typical disseminated fine-grained pyrite, chalcopyrite and supergene chalcocite. In addition, there are A-type chalcopyrite-pyrite and B-type chalcopyrite-pyrite-molybdenite quartz veinlets, which are cut by D-type pyrite-chalcopyrite veinlets with sericitic halos (cf. Gustafson and Hunt, 1975). The samples of the andesite porphyry from the outcrop contain up to 0.13% Cu, 77 ppm Mo, and 0.037 ppm Au (Arias and Neglia, 2018).

## Chapter 5

# Petrochemistry of the La Arena district

### 5.1 Introduction

Sampling at the La Arena District was done by chips, with about 1 to 2 kg of chip material and a hand specimen. The hand specimens served for preparation of thin and polished sections. The rock chips were crushed, divided and about 300 g of the split was pulverized in an agate mill.

Whole-rock geochemical analysis of 18 altered and unaltered samples were carried out using an Axois 4kw X-ray fluorescence spectrometer and AFS-2202a atomic fluorescence spectrometer (XRF), so as to determine major oxides. In addition, trace elements, including REE, were determined by means of Icap Q inductively coupled plasma mass spectrometer (iCAP Q ICP-MS) and AES-8000-type arc emission spectrometer at Nanjing Center, China Geological Survey/Nanjing Institute of Geology and Mineral Resources laboratory. The data are given in App. 1, Table A1. In the analyses of these geochemical data we must always consider the perturbations due to the effects of hydrothermal alteration. However, there are some elements (e.g. Ti, Zr, Y, and Nb) are regarded to be immobile during post-consolidation alteration and metamorphic processes, and may be used for petrochemistry characterization (Winchester and Floyd, 1977).

### 5.2 Bulk rock geochemistry

The locally-restricted La Arena, Alizar and Agua Blanca porphyry bodies associated with the copper, gold, and molybdenum mineralizations of the La Arena district (see below) are predominantly composed of andesite and lesser amounts of trachyandesite with Nb/Y ratios between 0.17 to 0.97 and 182 to 278 in Zr/TiO<sub>2</sub> ratios (Fig. 5.1, Table A1), according to the classification of altered rocks proposed by Winchester and Floyd (1977). These porphyry rocks together adapt to a calc-alkaline evolutionary line with a tendency to a high-K calc-alkaline fields (*sensu* Peccerillo and Taylor, 1976; Fig. 5.2A). While, latest-Early Miocene (~18 Ma) intrusive rocks from El Carmen and La Florida, which hosted polymetallic quartz veins are calc-alkaline diorite and granodiorite with SiO<sub>2</sub> contents between 57 and 66 % wt (Table A1), except the Carmen dike that presents high content of K<sub>2</sub>O (Fig. 5.2A, Table A1).

Mineralized and barren hypabyssal rocks from the La Arena district show steep rare earth element patterns, with lack of Eu anomalies (Fig. 5.2C), which may result from high

magmatic oxidation states and/or suppression of plagioclase fractionation (e.g. Frey et al., 1978; Lang and Tittley, 1998).

The distinctive Sr/Y, La/Yb, and Sm/Yb ratios of the mineralization-related porphyries occur along trends to slightly higher Sm/Yb, La/Yb, and Sm/Yb ratios in successively younger magmas and metal content in all three porphyry systems (Figs. 5.2B, D, E). The increasing Sm/Yb ratios of 2 to 6 for Alizar and La Arena porphyry bodies, and 9.7 for Agua Blanca porphyry prospect. Moreover, the increasing La/Yb ratios of 10 to 53, both are attributed to increasing crustal thicknesses (also increasing pressure) and cooling mantle source regions (e.g. Maricunga belt; Kay et al., 1994), which causes a change from pyroxene coexisting with amphibole (hornblende) to garnet in the mafic mineral residue in equilibrium with the magmas (Kay et al., 1999). These petrochemical features, together with increasing Sr/Y ratios (4-52), place the porphyry Au-Cu-, Cu-Au-(Mo)-, and Cu-Mo-related Alizar, La Arena, and Agua Blanca porphyry bodies, respectively, from normal to adakitic field with partial melting of a deep source containing clinopyroxene, amphibole and minor garnet. The petrochemical evolution and origin of the andesitic porphyry suites in the La Arena district, which bracket major Cu-Fe sulfides mineralization are similar to that other porphyry Cu-Au-(Mo) in northern Peru (e.g. Michiquillay, Galeno; Davies (2002). In contrast to other porphyry coppers in southern Peru (Valdivia et al., 2015) and central Chile (Kay and Mpodozis, 2002), where they strongly exhibit an association with strongly adakitic (Oyarzun, et al., 2001) and high Al tonalite-trondhjemite-granodiorite (TTG) magma series rocks are more common (Richards and Kerrich, 2007), emplaced during crustal thickening (Kay et al., 1999). In northern Peru, the initial crustal thickening recorded by the transition from normal calc-alkaline to adakitic magmatism was therefore apparently more critical for the genesis of high-sulfidation epithermal mineralization than for economically-significant porphyry deposits (Montgomery, 2012).

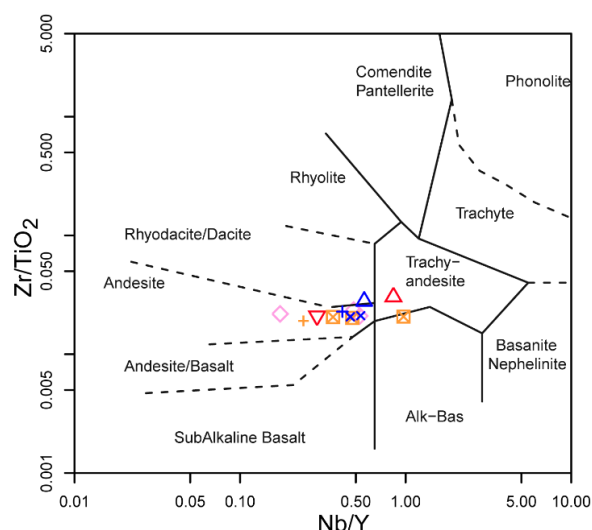


Figure 5.1. Zr/TiO<sub>2</sub>-Nb/ Y diagram showing the classification of altered porphyry bodies according to Winchester and Floyd (1977). Symbols as in Fig. 5.2.

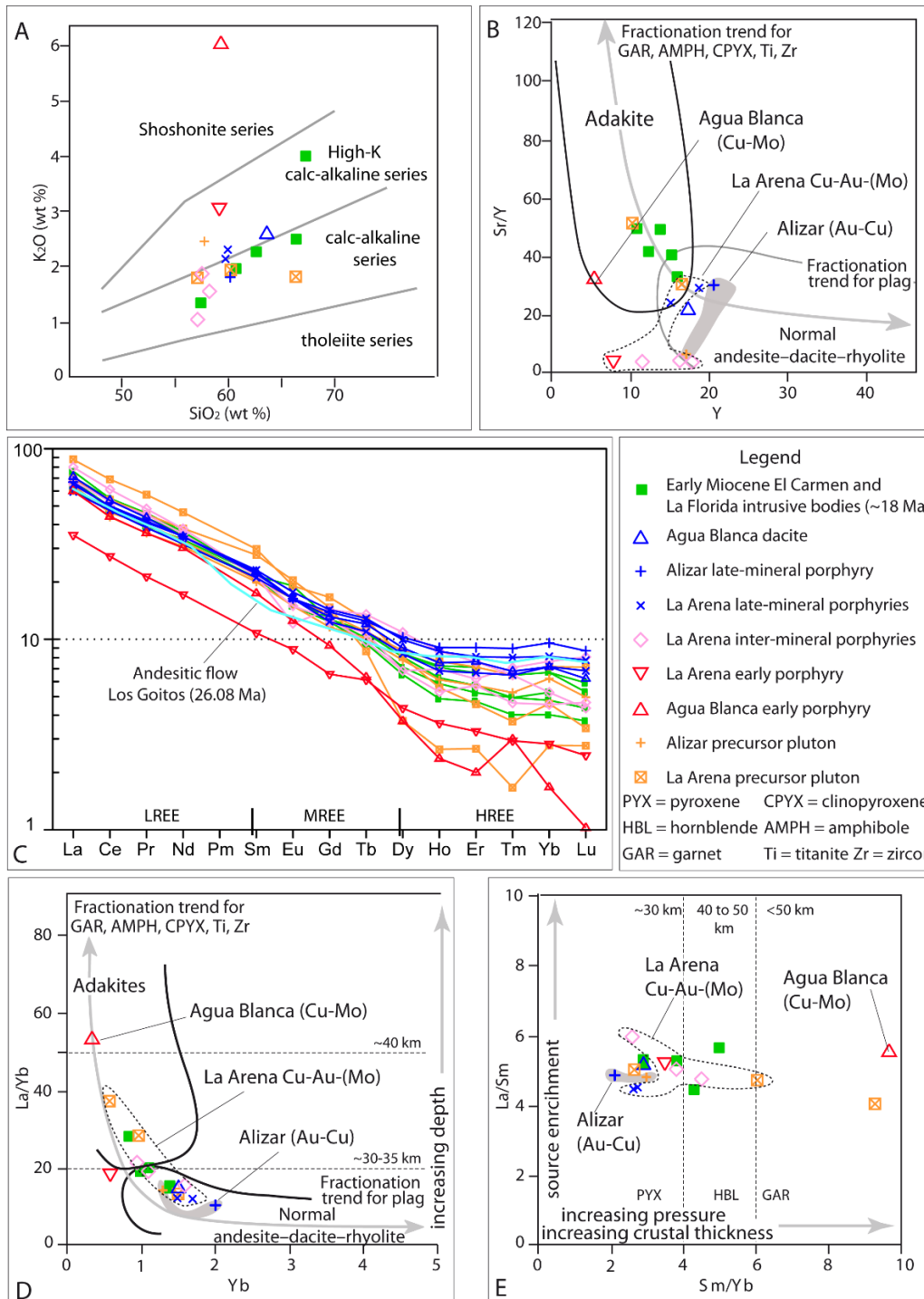


Figure 5.2. Petrochemical features of late Oligocene and early Miocene intrusive rocks from the La Arena district. A. Subdivision of subalkalic rocks using  $K_2O$  versus silica diagram. The lines between subalkalic series from Peccerillo and Taylor (1976). B.  $Sr/Y$  vs  $Y$  diagram show adakite and normal arc fields from Richards and Kerrich (2007) and Castillo et al. (1999), respectively. Moreover, diagram show fractionation trend for plagioclase and garnet, amphibole, clinopyroxene, titanite and zircon from Richards and Kerrich (2007). C. Chondrite-normalized rare earth elements, values from Boynton (1984). Line in cyan color represents coeval andesite flow with the La Arena porphyry from the Los Goitos (Lagunas Norte; data in Montgomery, 2012), shown for reference. D.  $La/Yb$  vs.  $Yb$  (Castillo et al., 1999), showing fields for adakite and normal arc. E. Plot of  $La/Sm$  vs.  $Sm/Yb$ . Ranges of  $Sm/Yb$  ratios and cortical thickness are from Kay et al. (1999).

## Chapter 6

# Geochronology

### 6.1 Introduction

We report the results of U-Pb zircon dating for the andesite porphyry bodies,  $^{40}\text{Ar}/^{39}\text{Ar}$  dating for hydrothermal biotite and alunite, and Re-Os dating for the molybdenite from A- and B-type veinlets. Coupled with unpublished in-house U-Pb and  $^{40}\text{Ar}/^{39}\text{Ar}$  geochronology data (Tahoe Resources, unpub. files) and available  $^{40}\text{Ar}/^{39}\text{Ar}$  geochronology data (Motgomery, 2012) on the Ethel HS epithermal systems and the La Arena porphyry Cu-Au-(Mo) deposit. The combinations of U-Pb,  $^{40}\text{Ar}/^{39}\text{Ar}$  and Re-Os ages are used to determine the timing of magmatism and associated Cu – Au  $\pm$  Mo mineralization and the lifespan of the ore-forming magmatic and hydrothermal system (cf. Richards, 2018).

### 6.2 Zircon U-Pb ages of porphyry bodies

This study is supported by 8 new and 10 unpublished LA-ICP-MS zircon U-Pb ages for the porphyry related to the copper, gold and molybdenum mineralization. Zircon crystals from all eight samples are clear and colorless crystals with tetragonal to subrounded shapes, and most of them commonly grows as doubly-terminated prismatic (less than 250  $\mu\text{m}$  in length) crystals with elongation (length-to-width) ratios ranging from 1 to 5. This combination of zircon shape and ratio suggests relatively rapid to moderate crystallization with a high-level emplacement (Corfu et al., 2003). The CL images reveal that the zircon grains have a strong oscillatory zoning and variations an irregular zoning towards the edges; many grains generally have planar fractured cores, with Th/U ratios from 0.4 to 1.2 (Fig. 6.1), which is indicative of an igneous origin (Hoskin and Schaltegger, 2003). All the analyses were carried out on the rim of individual zircon grains. U-Pb analytical data obtained are in App. 2, Tables A2 and App. 3, Table A3 (Tahoe Resources, unpub. files) and results are summarized in tables 6.1 and 6.2, and described below as show graphically in Figures 6.1 and A1 (annexes). Assigned ages are based on a weighted mean of  $^{206}\text{Pb}/^{238}\text{U}$  ages ( $2\sigma$ ) for twenty individual analyses from each sample, and the less concordant ( $\leq 90\%$ ) analyses, such as analytical spots that did not overlap the weighted mean age within their analytical uncertainty are excluded from final age calculation. The younger or older zircon  $^{206}\text{Pb}/^{238}\text{U}$  ages in all eight samples are interpreted as the lead-loss and inherited zircons, respectively.

The oldest intrusive suite, the precursor equigranular quartz diorite, forms an extensive body of medium- to fine-grained quartz diorite to diorite, semi-porphyrific in texture. Two altered samples characterized by hydrothermal white mica yielded a range of  $^{206}\text{Pb}/^{238}\text{U}$



ages from  $22.63 \pm 0.87$  to  $28.26 \pm 1.72$  Ma for seventeen zircons (CA-25; Fig. 6.1A; Table A2) and between  $22.92 \pm 1.07$  and  $27.39 \pm 0.93$  for nineteen zircons (LA-D15-003-A-68; Fig. 6.1B; Table A2), reinspectively, displaying a scatter in the analytical data. Regression of all the analyses yields a statistically invalid ages ( $24.97 \pm 0.82$  Ma; MSWD = 8.6 and  $26.00 \pm 0.46$  Ma; MSWD = 2.6). The distribution of individual zircon spot ages for both samples (App.2, Table 2A) and its distribution on the weighted mean  $^{206}\text{Pb}/^{238}\text{U}$  age histograms (Figs. 6.1A, B) suggest the presence of at least two populations of zircon for each sample. The sample CA-25 is represented for an older zircon population that has an age of  $26.64 \pm 0.71$  Ma for ten zircon crystals and younger zircon population that has an age of  $23.90 \pm 0.69$  Ma (Fig. 6.1A). While, the sample LA-D15-003-A-69 has an age of  $26.53 \pm 0.33$  Ma for an older population of twelve zircon grains and an age of  $25.00 \pm 0.45$  Ma for a younger population of five zircon crystals (Fig. 6.1B). In addition, two crystals are younger than 23.09 Ma (Fig. 6.1B). Other samples from precursor quartz diorite body display only weak developed propylitic alteration (LA-D14-008-CD-01), gives an age of  $26.50 \pm 0.28$  Ma (MSWD = 1.3) based on 17 of 20 analyses (Fig. 6.1C). Three zircons are younger than 24.42 Ma. Based upon field relation and statistically more robust calculated age by LA-D14-008-CD-01 sample, we interpret the  $26.64 \pm 0.71$  and  $26.53 \pm 0.33$  Ma ages to best represent the emplacement ages of the precursor pluton and, two younger zircon population ages and/or other younger crystals, may be results from different post-crystallization Pb-loss effects. Hence, these three zircon U-Pb ages show that the precursor pluton was emplaced between  $26.64 \pm 0.71$  and  $26.50 \pm 0.28$  Ma, defining an interval of  $0.14 \pm 0.76$  m.y. (calculated using the addition in quadrature method for estimating the error propagation).

An early andesite porphyry sample (LA-D11-001A-06), collected from the central part of the La Arena porphyry system. This sample show unambiguous field relations, which contains A1-4E- and AB<sub>E</sub>-type veinlets. These veinlets are truncated by the inter-mineral porphyry (Fig. 4.2D), but sampled 3 m away from the contact to exclude contamination. Based on ten spots of twenty grains analyzed, yielded a zircon U-P age of  $26.45 \pm 0.64$  Ma (Fig. 6.1D). Ten spots analyses were excluded from the calculated age, as gives discordant ages (App. 2, Table 2A). The partial temporal overlap between the age ranges for the precursor pluton and early porphyry is notable, bearing in mind that relationship with the precursor pluton is poorly defined. However, the abrupt increases in copper and gold contents on passing from precursor equigranular quartz diorite to early andesite porphyry are observed everywhere. Furthermore, the youngest zircon U-Pb age recorded in the precursor pluton (see above) suggests that it should be emplaced in a maximum of 0.75 m.y. ( $0.05 \pm 0.70$  m.y.) before the early porphyry, therefore implying a close relationship between precursor pluton emplacement and initiation of porphyry system development.

Three inter-mineral andesite porphyry samples were taken from the La Arena porphyry system. (1) Sample LA-D11-001A-07 is an andesite porphyry that truncate early stage quartz veinlets hosted in the early porphyry (Fig. 4.2D) from a zone of strong sericitic alteration in the central part of the porphyry system yielded an age of  $25.58 \pm 0.68$  Ma based on thirteen of fourteen (Fig. 6.1E; App.2, Table 2A). (2) An altered sample CA-24, collected from deeper open-pit surface exposure at northeast Calaorco orebody (on porphyry shoulder), where precursor pluton is cut by this inter-mineral andesite porphyry body of tabular geometry with hydrothermal kaolinite and illite alteration (Fig. 4.2F) yielded an age of  $25.58 \pm 0.51$  Ma (Fig. 6.1F; App. 2, Table 2A) based on twelve of sixteen zircons. (3) The sample LA-D15-003-A-009 from an andesite porphyry dike,

Table 6.1. U-Pb ages of intrusive stage from La Arena porphyry

Sample no.	UTM E	UTM N	Age (Ma $\pm$ $\sigma$ 2)	Depth (m)	Location**	Intrusion stage*	Primary minerals	Alteration minerals	
CA-25	815994	9126276	26.64 $\pm$ 0.71	0	CHS	PP	PXX: 60 GMS: 30	qtz, zr, ap plag?	ill, kao, qtz, rt qtz, kao, ill
LA-D15-003-A-068	816056	9126903	26.53 $\pm$ 0.33	142.5	LAPS	PP	PXX: 75 GMS: 25	qtz, plag? zr plag?	ser ser, qtz, ank
LA-D14-008-CD	816858	9126945	26.50 $\pm$ 0.28	50.50	LAPS	PP	PXX: 70 GMS: 20	plag, qtz, ksp, bio, hbd, zr plag, qtz	ca, ser, qtz ca, ser, chl
LA-D11-001A-06	816395	9126634	26.45 $\pm$ 0.64	365	LAPS	EAP	PXX: 70 GMS: 20	qtz, plag? plag?	qtz, ser qtz, ser, ca, ill
LA-D11-001A-07	816395	9126634	25.58 $\pm$ 0.68	369.5	LAPS	IAP	PXX: 75 GMS: 25	plag, qtz, ksp plag?	qtz qtz, ser, ank
CA-24	815995	9126276	25.58 $\pm$ 0.51	0	CHS	IAP	PXX: 70 GMS: 30	plag, qtz, hbd, ksp plag?	ill, kao, qtz qtz, kao, ill
LA-D15-003-A-009	816056	9126903	25.55 $\pm$ 0.27	158.2	LAPS	IAP	PXX: 60 GMS: 40	qtz, zr plag?	ser, ank ser, qtz
CA-13	815937	9125675	24.81 $\pm$ 0.48	0	CHS	LAP	PXX: 65 GMS: 35	plag, hbd, bio, ksp, qtz, zr plag	qtz, chl, ser, rt, ap ca

Notes: UTM datum for all samples is WGS 84, Zone 17 South

\*Magmatic phase according to Sillitoe (2000). PP=precursor pluton, EAP=early andesite porphyry, IAP=inter-mineral andesite porphyry, LAP=late-mineral andesite porphyry

\*\*CHS= Calarco high-sulfidation, LAPS= La Arena porphyry system

PXX=phenocrysts, GMS= groundmass. Mineral abbreviation according to Seedorff et al., 2005

All samples were dated at the Wuhan SampleSolution Analytical Technology Co., Ltd, China

Table 6.2. U-Pb ages of intrusive stage from La Arena porphyry and Calaorco HS.

Sample no.	UTM E	UTM N	Age (Ma $\pm$ $\sigma$ 2)	Depth (m)	Locatio n**	Intrusion stage*	Comments
07D-LA-324-161	816045	9126131	25.47 $\pm$ 0.52	161	LAPS	EIAP	Andesite porphyry with strong developed sericitic alteration.
MD-03	815894	9125882	25.47 $\pm$ 0.29	0	CHS	EIAP	Andesite porphyry shows moderate developed of advance argillic alteration together with goethite, quartz veining.
05D-LA-216-99	815854	9126930	25.44 $\pm$ 0.30	99.5	LAPS	EIAP	Pyrite disseminated in andesite porphyry matrix (2-3% vol) and trace enargite. While plagioclase is replaced by sericite.
MD-02	816076	9125967	25.24 $\pm$ 0.46	0	CHS	LIAP	Andesite porphyry shows strong developed of advance argillic alteration together with hematite.
LA-D11-004-799	816197	9126794	25.22 $\pm$ 0.27	799	LAPS	LIAP	Potassic alteration with hydrothermal biotite – magnetite $\pm$ k-feldspar, chalcopyrite and pyrite dissemination.
MD-01	815987	9125938	25.21 $\pm$ 0.27	0	CHS	LIAP	Andesite porphyry display weak developed of propylitic and argillic alteration, pyrite dissemination (<1% vol).
LA-D11-004-686	816239	9126793	24.95 $\pm$ 0.29	686	LAPS	LIAP	Sericitic alteration, developed extensively throughout much of the andesite porphyry, and contain disseminate pyrite and chalcopyrite.
LA-D11-004-518	816303	9126791	24.75 $\pm$ 0.32	518	LAPS	LAP	Andesite porphyry display weak developed of sericitic alteration with illite, pyrite veining and dissemination.
07D-LA-324-126	816056	9126132	24.44 $\pm$ 0.32	126	LAPS	LAP	Chlorite replace hornblende and magmatic biotite, while calcite and epidote appear replacing plagioclase in andesite porphyry.
MD-05	815572	9126233	24.40 $\pm$ 0.34	0	CHS	LAP	Andesite porphyry dike with weak silicic and argillic alteration, and hematite.

Notes: UTM datum for all samples is WGS 84, Zone 17 South

\*Magmatic phase according to Sillitoe (2000). EIAP= early inter-mineral andesite porphyry, LIAP=late inter-mineral andesite porphyry, and LAP=late-mineral andesite porphyry

\*\*CHS= Calaorco high-sulfidation, LAPS= La Arena porphyry system

All samples were dated at the University of Tasmania (Tahoe Resources, unpub. files)

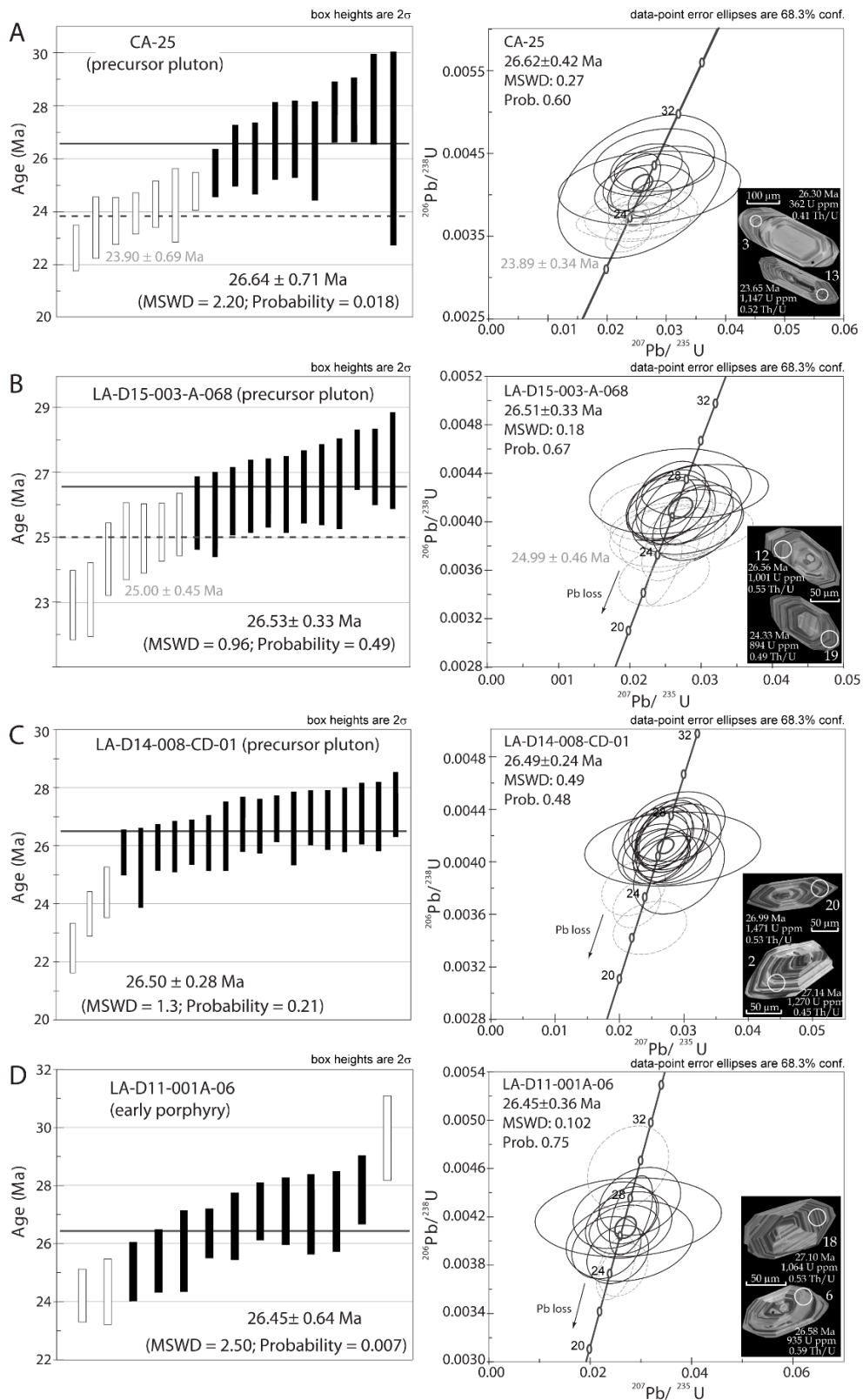


Figure 6.1. U-Pb dates for precursor pluton, early, inter-mineral, and late mineral from the La Arena porphyry system. Ages are calculated based on the weighted means  $^{206}\text{Pb}/^{238}\text{U}$  age histograms and Concordia diagrams. The white circles in the CL images represent the spots of the LA-ICP-MS analyses in representative zircon crystals. The white bars show the distribution for Pb loss (under weighted mean age) and inheritance (over weighted mean age) in some of the analyzed zircon grains.

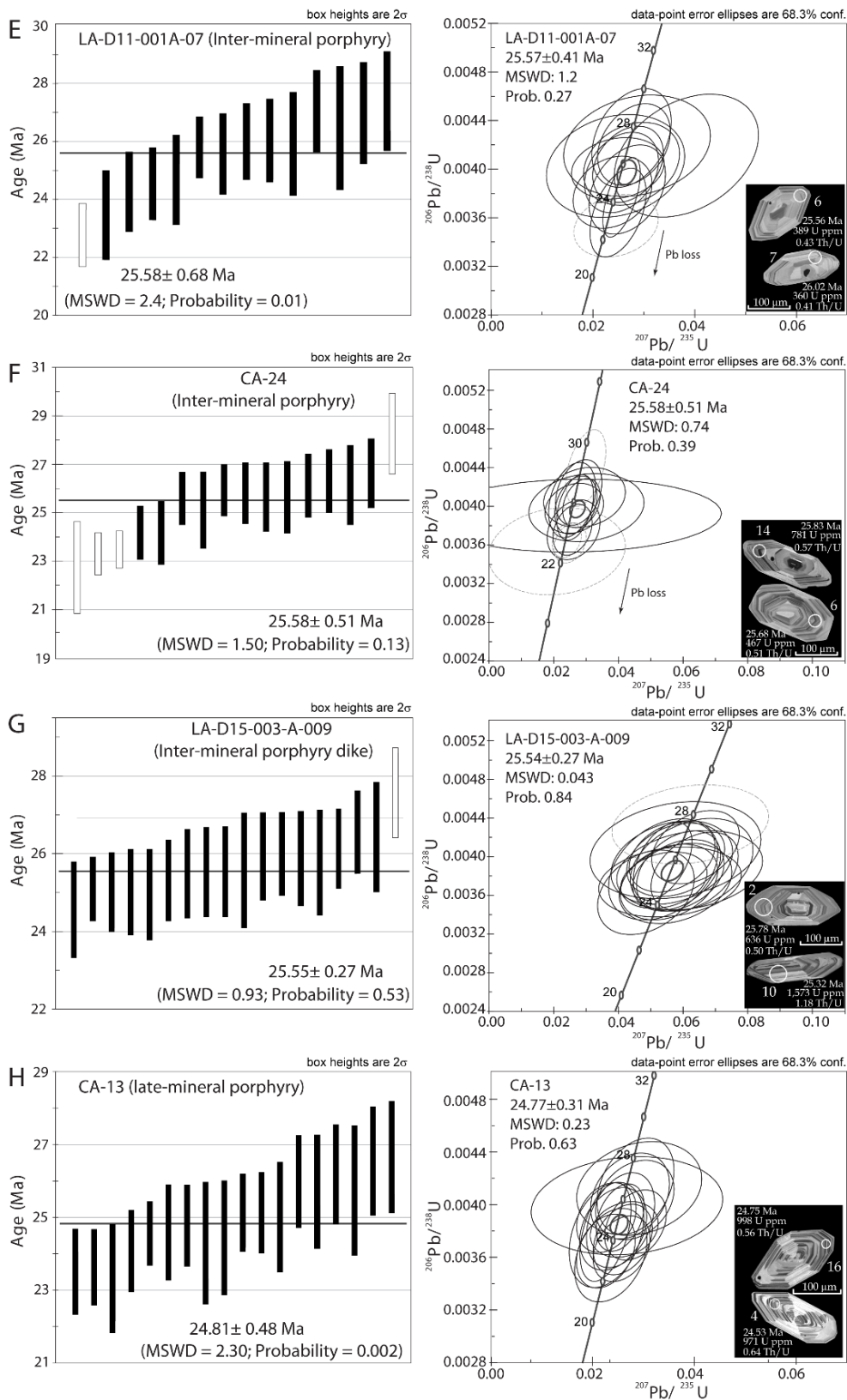


Fig. 6.1. (Cont.)

which intrude the precursor quartz diorite body (Fig. 4.2C) gives an age of  $25.55 \pm 0.27$  Ma, based on seventeen of eighteen zircons (Fig. 6.1G). These inter-mineral ages are,

within error limits ( $2\sigma$ ), basically the same as the three youngest ages obtained for the early inter-mineral porphyry by Tahoe Resources (unpub. files), which ranging from  $25.47 \pm 0.29$  to  $25.44 \pm 0.30$  Ma (Tables 6.2; App. 3, Figs. A3A, B, C). Furthermore, a group of three samples from the late inter-mineral porphyry reported by Tahoe Resources (unpub. data) bracket within their individual uncertainties ( $25.24 \pm 0.46$ ,  $25.22 \pm 0.27$ , and  $25.21 \pm 0.27$  Ma; Tables 6.2; App. 3, Figs. A3D, E, F), and an additional sample, a discernably different U-Pb age of  $24.95 \pm 0.29$  Ma is given by Tahoe Resources (unpub. files) between this magmatic stage (Tables 6.2; App. 3, Fig. A3G). The single age for the late mineral andesite porphyry from Cerro Calaorco, based on eighteen zircon crystals (Tables 6.2; App. 3, Fig. 6.1H), gives an age of  $24.81 \pm 0.48$  Ma. This age is highly compatible with a previously reported zircon U-Pb ages of  $24.75 \pm 0.32$  Ma (Tables 6.2; App. 3, Fig. A3H; Tahoe Resources, unpub. files) within the error limits ( $2\sigma$ ). In contrast, other two samples are significantly younger than late-mineral porphyries ( $24.44 \pm 0.32$  and  $24.40 \pm 0.34$  Ma; Tahoe Resources, unpub. files), but together they represent the last recorded magmatic event at the La Arena porphyry (Tables 6.2; App. 3, Figs. A3I, J). Therefore, a time interval of  $0.41 \pm 0.59$  m.y. is detected between the late mineral porphyry ages.

### 6.3 Re-Os ages of molybdenite-bearing quartz veinlets

Molybdenum mineralization age at La Arena porphyry system was determined by Re-Os analysis of five single molybdenite-bearing quartz veinlets included in the early andesite porphyry of moderate to pervasive sericitic alteration zone at  $>570$  m deep. The concentration of total Re,  $^{187}\text{Re}$ ,  $^{187}\text{Os}$  and Re-Os calculated model ages with  $2\sigma$  uncertainties for these analyses, are given in Table 6.3. The five accurate and reproducible Re-Os molybdenite age determinations give a restricted time interval of  $0.75 \pm 0.60$  m.y. from  $26.61 \pm 0.41$  to  $25.86 \pm 0.44$  Ma. The molybdenite from a granular quartz veinlet (A3<sub>E</sub>-type, Fig. 6.2A), has a Re-Os age of  $26.61 \pm 0.41$  Ma, which is similar to the molybdenite age ( $26.51 \pm 0.46$  Ma) from a quartz – pyrite ± bornite B<sub>E</sub>-type veinlet with an irregular white sericitic selvage (Fig. 6.2B). These quartz veinlets with very minor molybdenite have relatively high Re contents that vary from 175 – 283 ppm (Table 6.3).

The B1<sub>T</sub> veinlet molybdenite occurring as fracturing infillings (Fig. 6.2C) yields a model age of  $26.05 \pm 0.39$  Ma, and is appreciably younger than the Re-Os molybdenite age from A3<sub>E</sub>-type quartz veinlet. Discontinue molybdenite-quartz veinlets (B1<sub>T</sub>-type) with a white sericitic halos (Fig. 6.2D), have a Re-Os age of  $25.93 \pm 0.41$  Ma, which is indistinguishable from the molybdenite age ( $25.86 \pm 0.44$  Ma, Fig. 6.2E) for the fracture-infilled molybdenite in the B2<sub>T</sub> veinlet. The molybdenite-rich B1<sub>T</sub>- and B2<sub>T</sub>-type veinlet samples contains very high Re concentrations from 917 to 1,787 ppm, and such high Re contents are typically observed in subduction-related porphyry deposits (Stein et al., 2006, and references therein). Re is highly compatible in molybdenite rather than Cu-Fe sulfides (Stein et al., 2001), and it is thus probable to form minor amounts of Re-rich molybdenite in Cu-Fe sulfides-abundant precipitates (Stein et al., 2001; Spencer et al., 2015). At the La Arena Cu-Au-(Mo) porphyry systems, however, high Re concentration molybdenites occur in early quartz veinlets (A3<sub>E</sub> and B<sub>E</sub>). These are directly associated with Cu-Fe sulfides as inclusions within few molybdenite grains, suggesting that molybdenite and Cu-Fe sulfides formed in a nearly same period. In contrast, very high Re concentrations is found in later molybdenite-bearing B1<sub>L</sub> and B2<sub>L</sub> veinlets with little or no deposition of copper (Fig. 6.3). This suggests that the reduction of  $\text{Re}^{6+}$  to  $\text{Re}^{4+}$  (from incompatible to compatible; Sun et al., 2015) and the subsequent Re concentrations may increase, and



then decrease gradually during the final stage of hydrothermal activity linked to the early andesite porphyry.

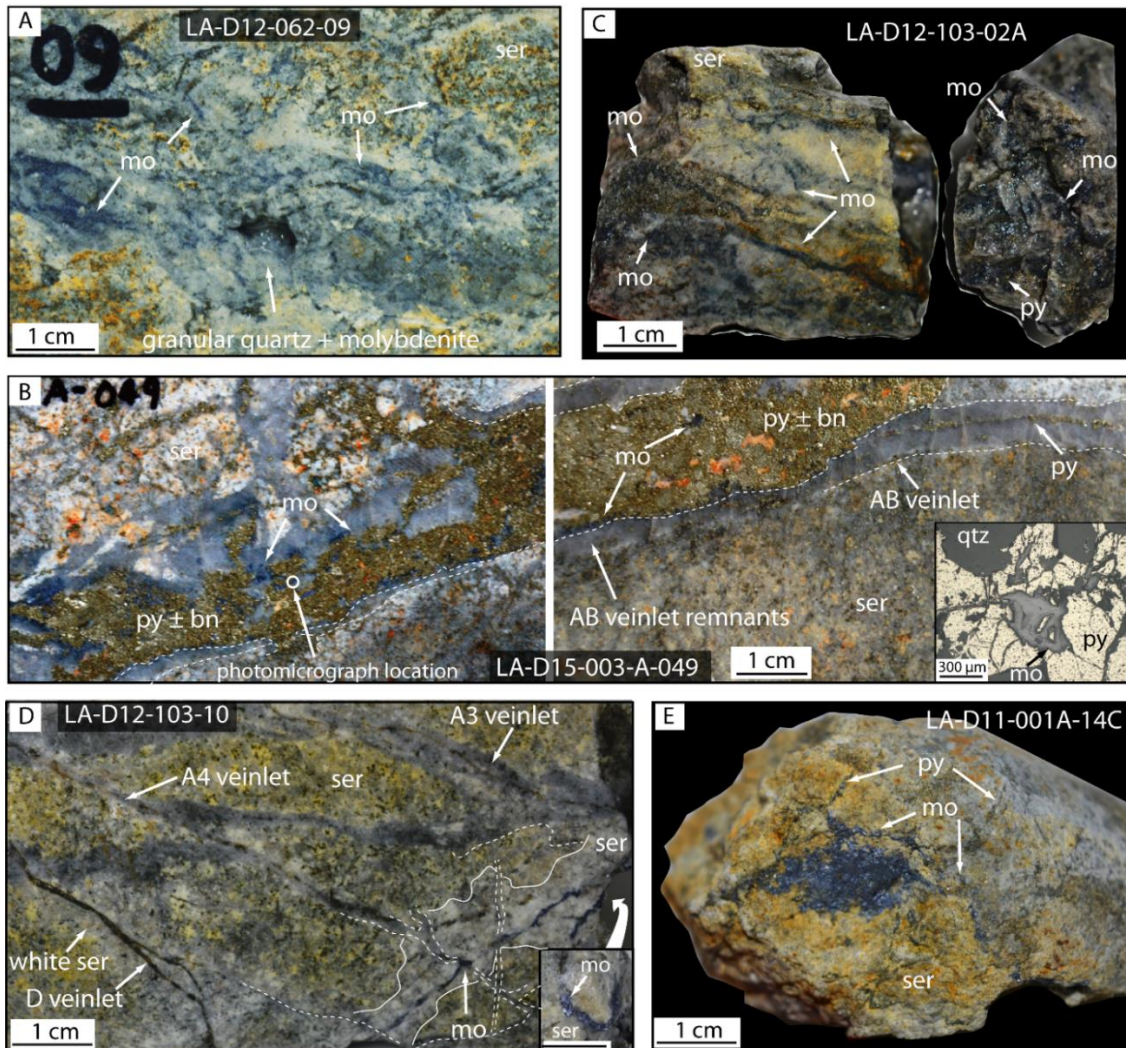


Figure 6.2. Early porphyry with moderate to pervasive quartz – sericitic alteration cut by molybdenite-bearing quartz veinlets. A. A<sub>3E</sub>-type granular quartz veinlet with irregular veinlet walls and lack internal symmetry. This veinlet has irregular arrays of molybdenite. B. Two slightly parallel AB<sub>E</sub>-type quartz ± pyrite veinlets are cut by B<sub>E</sub>-type pyrite – molybdenite ± bornite veinlet with irregular sericitic selvage. C. Molybdenite ± pyrite B<sub>1T</sub> veinlet as short fracture coatings into early porphyry with pervasive quartz-sericite alteration. D. Swarm of quartz – molybdenite ± pyrite B<sub>1T</sub> veinlets white sericite selvage. E. Thin (<2 mm) and short (< 2 cm) molybdenite fracture infillings (B<sub>2T</sub>-type) within pervasive quartz-sericite alteration.

Table 6.3. Re-Os (molybdenite) ages from La Arena porphyry.

Sample no.	UTM E	UTM N	Depth (m)	Sample weight (g)	Re (ppm)	<sup>187</sup> Re (ppm)	<sup>187</sup> Os (ppb)	Model age (Ma ± σ <sub>2</sub> )	Description
LA-D12-062-09	816223	9126716	758	0.00225	283.23 ± 1.95	178.01 ± 1.22	78.93 ± 0.75	26.61 ± 0.41	Sericitic alteration, qtz-mo±cp, A <sub>3E</sub> -type veinlet
LA-D15-003-A-049	816056	9126903	683	0.00213	175.95 ± 1.27	110.59 ± 0.80	48.85 ± 0.61	26.51 ± 0.46	Sericitic alteration, qtz-py-mo±bn, B <sub>E</sub> -type veinlet with sericitic halos
LA-D12-103-02A	816722	9126692	732	0.00217	917.40 ± 7.74	576.60 ± 4.86	250.30 ± 1.87	26.05 ± 0.39	Sericitic alteration, mo±qtz, fracture-infilling of the B <sub>1T</sub> veinlet
LA-D12-103-10	816722	9126692	772	0.00212	1,413.40 ± 13.83	888.35 ± 8.69	383.85 ± 2.82	25.93 ± 0.41	Sericitic alteration, mo±qtz, B <sub>1T</sub> -type veinlet with sericitic halos.
LA-D11-001A-14C	816395	9126634	574	0.00219	1,787.26 ± 20.36	1123.33 ± 12.79	484.14 ± 3.80	25.86 ± 0.44	Sericitic alteration, mo, molybdenite in the B <sub>2T</sub> veinlet occurs as fracture infillings
<u>Control sample</u>									
GBW04435 (HLP)				0.01015	273.448 ± 2.88		630.7 ± 4.2	219.9 ± 3.5	Molybdenite reference material

Notes: UTM datum for all samples is WGS 84, Zone 17 South

All samples were dated at the Re-Os Laboratory of the National Research Center of Geoanalysis, Chinese Academy of Geological Sciences, Beijing

#### 6.4 K-Ar ages for whole-rock and $^{40}\text{Ar}/^{39}\text{Ar}$ ages for silicate minerals

Three K-Ar ages of  $25.7 \pm 0.9$ ,  $24.8 \pm 0.8$ , and  $24.6 \pm 0.8$  Ma for whole-rocks from the La Arena porphyry complex (?) were reported by Gauthier et al. (1999), and are younger than the ages reported for  $^{40}\text{Ar}/^{39}\text{Ar}$  dating for mineral separates (see below). The hornblende sample from the precursor pluton yielded  $^{40}\text{Ar}/^{39}\text{Ar}$  age of  $26.59 \pm 0.29$  Ma (Montgomery, 2012).  $^{40}\text{Ar}/^{39}\text{Ar}$  dating carried out by Tahoe Resources (unpub. files, Table 6.4) for two hydrothermal biotite samples from a deep (<620 m elevation) level of early potassic alteration zone with high-grades (<0.76% Cu and 0.50 g/t Au) yielded plateau ages of  $26.40 \pm 0.29$  and  $26.35 \pm 0.14$  Ma ( $2\sigma$ ).

The biotite from the pale-green sericite-chlorite alteration zone (LA-D15-003-A-041), located on the northern side of the Calarco open pit at 592 m deep, yields an undisturbed age spectrum with a plateau at  $25.96 \pm 0.16$  Ma (Fig. 6.3A) and a concordant  $26.00 \pm 0.16$  Ma inverse isochron age (Table 6.5). This value is relatively similar to a previously reported  $^{40}\text{Ar}/^{39}\text{Ar}$  plateau age for hydrothermal phenocrystic biotites of  $26.08 \pm 0.13$  Ma, dated in shallow parts (250 m) of the La Arena porphyry (Montgomery, 2012).

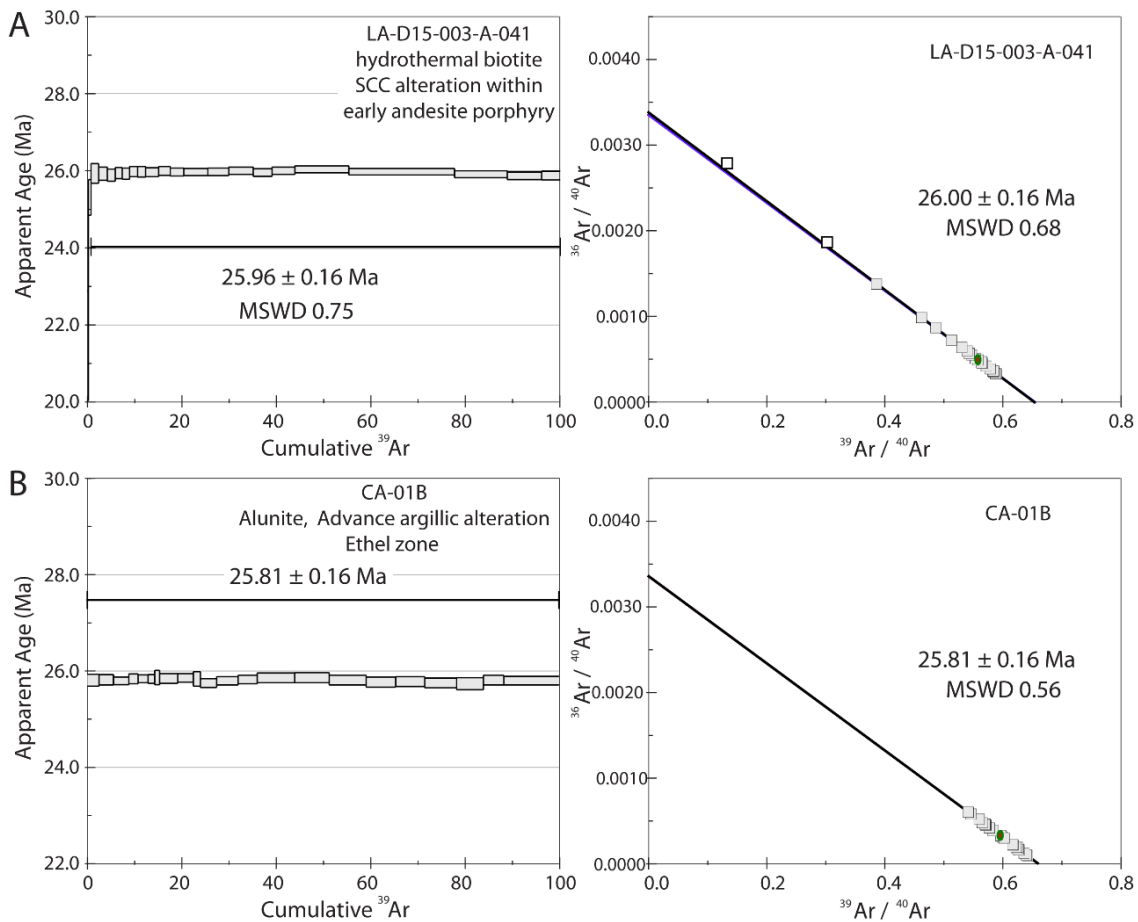


Figure 6.3. Apparent  $^{40}\text{Ar}/^{39}\text{Ar}$  age spectra ( $\pm 2\sigma$ ) and inverse isochrons of hydrothermal biotite from sericite-clays-chlorite alteration within early andesite porphyry (A) and hypogene alunite from advance argillic alteration close to Ethel HS deposit (B).

A muscovite-bearing sample collected at a similar depth as the potassic biotites (601.8 m) and one sericite-bearing samples at depth of 416.2 m from the main sericitic hydrothermal alteration zone cut by quartz veinlet stockworks with copper-gold

Table 6.4.  $^{40}\text{Ar}/^{39}\text{Ar}$  ages of magmatic-hydrothermal events from La Arena porphyry and Calaorco HS.

Sample no.	UTM E	UTM N	Mineral	Age (Ma $\pm$ $\sigma$ 2)	Depth (m)	Location**	Intrusion stage*	Comments
MD-07	815697	9126096	alunite	25.51 $\pm$ 0.10	0	CHS	EAP	Pink alunite is replacing plagioclase within andesite porphyry dike
MD-10	815954	9126043	alunite	25.51 $\pm$ 0.17	0	CHS	EAP	Pinkish alunite is present as fine-grained dissemination within andesite porphyry dike
MD-09	815611	9126190	alunite	25.57 $\pm$ 0.16	0	CHS	EAP	Andesite porphyry dike with vuggy texture, where plumose crystallized alunite filling vugs
05D-LA-209-331	816011	9126738	sericite	26.02 $\pm$ 0.07	331.7	LAPS	EAP	Pervasive to moderate stockwork veining cutting EAP with sericitic alteration.
LA-D11-025-416	816400	9126439	sericite	26.38 $\pm$ 0.24	416.2	LAPS	EAP	Sericitic alteration overprinting the EAP cut by quartz veinlet stockwork.
LA-D11-034-601	816429	9126539	muscovite	26.41 $\pm$ 0.52	601.8	LAPS	EAP	EAP sericitized cut by molybdenite-rich quartz veinlet.
LA-D11-004-809	816182	9126794	biotite	26.35 $\pm$ 0.14	809.2	LAPS	EAP	Hydrothermal biotite with magnetite within EAP
LA-D11-016-621	816280	9126737	biotite	26.40 $\pm$ 0.29	621.8	LAPS	EAP	EAP strong biotitized.

Notes: UTM datum for all samples is WGS 84, Zone 17 South

\*Magmatic phase according to Sillitoe (2000). EAP=early andesite porphyry

\*\*CHS= Calaorco high-sulfidation, LAPS= La Arena porphyry system

All samples were dated at the University of Tasmania (Tahoe Resources, unpub. files)

Table 6.5.  $^{40}\text{Ar}/^{39}\text{Ar}$  ages of magmatic-hydrothermal events from La Arena porphyry and Calaorco HS.

Sample no.	UTM E	UTM N	Mineral	Plateau age (Ma $\pm$ $\sigma$ 2)	Total fusion age (Ma $\pm$ $\sigma$ 2)	Normal isochron age (Ma $\pm$ $\sigma$ 2)	Inverse isochron Age (Ma $\pm$ $\sigma$ 2)	Comments
CA-01B	815746	9127322	alunite	25.81 $\pm$ 0.16	25.81 $\pm$ 0.16	25.82 $\pm$ 0.16	25.81 $\pm$ 0.16	Medium- to fine grained alunite filling fractures within early andesite porphyry with vuggy texture.
LA-D15-003-A-041	816056	9126903	biotite	25.96 $\pm$ 0.16	25.94 $\pm$ 0.16	26.00 $\pm$ 0.16	26.00 $\pm$ 0.16	Sericite-clay-chlorite alteration overprinting early andesite porphyry.

Notes: UTM datum for all samples is WGS 84, Zone 17 South

All samples were dated at the China University of Geosciences (Wuhan).

mineralization (<1.29% Cu and 0.93 g/t Au) yielded  $^{40}\text{Ar}/^{39}\text{Ar}$  ages of  $26.41 \pm 0.52$  and  $26.38 \pm 0.24$ , respectively. In contrast, one sericite sample (05D-LA-209-331), located on the northwestern margin of the porphyry deposit at 331.7 m, yield a younger age of  $26.02 \pm 0.07$  Ma ( $2\sigma$ ) (Tahoe Resources, unpub. files; Table 6.4).

All pinkish hypogene alunite samples from the Calaorco HS open-pit are related to the roofs of early porphyry body with advanced argillic (MD-09, MD-10, and MD-07). The alunite from sample MD-09 yields a plateau age of  $25.57 \pm 0.16$  Ma, sample MD-10 gives an age of  $25.51 \pm 0.17$  Ma, and sample MD-07 gives an age of  $25.51 \pm 0.10$  Ma (Tahoe Resources, unpub. files; Table 6.4). Alunite crystals from northern part of the Calaorco open-pit close to Ethel HS deposit is also relate to early porphyry (CA-01B) shows a plateau at  $25.81 \pm 0.16$  Ma (Fig. 6.3B, Table 6.5) and appears to be undisturbed. This age is similar to plateau age of  $25.81 \pm 0.16$  Ma (Montgomery, 2012) for hypogene alunite in quartz-alunite - altered clasts in polymictic hydrothermal breccia from Ethel HS system.

The  $^{40}\text{Ar}/^{39}\text{Ar}$  ages indicate that the hydrothermal biotite from the potassic core and muscovite/sericitic minerals at deep levels (>416 m) produced similar older ages. In contrast, hydrothermal biotite from SCC alteration and sericite in shallow-level porphyry system (up to 331 m deep) produced similar younger ages, but in both cases in agreement with crosscutting relations, where sericite alteration overprints potassic biotite and SCC alteration zones shows that the hydrothermal biotite is older than the sericite/muscovite.

## Chapter 7

# Discussion

### 7.1 District-scale controls and rapid uplift

The La Arena-Calaorco porphyry and related epithermal deposits are located at a regional-scale overthrust anticline folded axis of axial trace NW-striking and NE-vergent within Marañón fold-trust belt. The Marañón fold-trust belt in central Peru is the product of early folding and east-vergent thin-skinned tectonics at ~80-20 Ma, followed by west-vergent thick-skinned deformation at ~20-0 Ma (Scherrenberg et al., 2016) and consequent uplift between ~20-4 Ma in north central Peru Andes (Garver et al., 2005). The west-vergent thick-skinned deformation style is coincident with the formation of the mineral deposits in the Marañón fold-trust belt during the early Miocene, and in the mid-Miocene (Scherrenberg et al., 2016). However, the onset of sub-andean fold-thrust belt developed in northern Peru (~30-24 Ma; Eude et al., 2015) and emplacement of the La Arena-Calaorco porphyry and epithermal deposits (26.64-24.81 Ma) coincide with break-up between the Cocos and Nazca plate of the original Farallón Plate (from ~26 Ma; Pardo-Casas and Molnar, 1987; Lonsdale, 2005) and the ensuing fast subduction of the Nazca Ridge underneath the leading edge of the South America plate (Pardo-Casas and Molnar, 1987; Somoza, 1998), which accelerated the shortening and uplift of the Andes from 28-26 Ma (Sebríer et al., 1988; Jaillard et al., 2000).

The very large (*sensu* Clark, 1993) La Arena porphyry Au-Cu-(Mo) deposit was formed from normal arc magmas prior to the evolution to adakitic magmatism (Montgomery, 2012). Nevertheless, the porphyry copper-related intrusions at the La Arena were uninterrupted during the tectonic shortening, as described earlier. However, the chemical signatures of the porphyry intrusive rocks changed from a normal arc to adakitic signatures (*sensu* Richards, 2011) with increase of Sr/Y (4-354) and La/Yb (12-37) ratios, and weak or absent Eu anomalies on normalized REE diagrams indicative of hornblende fractionation in high magmatic water content and oxidized (cf. Richards, 2011, and references therein). Furthermore, the aforementioned chemical changes of the pyroxene- to amphibole-dominated residual mineralogy of the magma source support the interpretation that the crustal thickening of northern Peru began contemporaneously with the La Arena porphyry formation in the study area (cf. Kay et al., 1999, 2005), and thus a tectonic relaxation of subduction-related SW-NE compression has provided a trigger for the rapid rise of ore fluids within northwest feeder structures (Calaorco fault systems) and into Chimú steep dipping bedding planes in the late Oligocene (Corbett, 2014).

Late Oligocene exhumation rates in the northern Peru ( $\geq 110 \pm 8$  mm/y) reflect uplift and erosion caused by the crustal thickening during the Aymará orogenic event (Sebríer



et al., 1988), together with tectonic relaxation that could have caused partial gravitational collapse of the orogenic belt (e.g. Rosario; Masterman et al., 2005). These may be the main factors that accelerated partial exhumation of the La Arena-Calaorco hydrothermal systems during the late Oligocene, and may have caused the telescoping of the high-sulfidation epithermal mineralization superimposed on the nearly coeval formed porphyry-style mineral assemblages.

## 7.2 Timing formation of porphyry- and epithermal-style mineralization

Metal introduction at the La Arena porphyry Cu-Au-(Mo) deposit spans at least four main phases of intermediate composition (precursor, early, inter-mineral, and late-mineral) that have unambiguous relative temporal relationships, based on crosscutting field relations in a continuous open-pit outcrop and in drill cores (Fig. 4.2). Each of the four magmatic phases resulted in variable changes in the alteration, veinlet formation, and mineralization. However, drastic changes in mineralization style are observed with decreasing temperature in shallow depths, where the Calaorco high-sulfidation Au mineralization developed within non-reactive, permeable Chimú quartz sandstone sediment rocks (Fig. 7.1). The cooling history of early andesite porphyry event provides an estimate of the minimum lifespan of the La Arena – Calaorco porphyry-epithermal systems. Nevertheless, the maximum duration of the magmatic-hydrothermal events associated with all metal introduction at the La Arena – Calaorco orebodies are bracketed temporally by a precursor quartz diorite pluton and late-mineral andesitic porphyry dikes depleted in metals, and sulfur by earlier and inter-mineral andesitic porphyry events.

The hydrothermal altered barren quartz diorite stocks are emplaced between  $26.64 \pm 0.71$  and  $26.50 \pm 0.28$  Ma (Fig. 7.1), and intrusion of the early andesite porphyry commenced at  $26.45 \pm 0.64$  Ma (Fig. 7.1). These zircon U-Pb dates are indistinguishable within corresponding  $2\sigma$  errors, and may well indicate that both intrusion stages were emplaced in the same time or coeval. However, assay data and field relationship have recorded the abrupt increases in ore minerals from precursor pluton to early porphyry (e.g., Sillitoe, 2000; Fig. 4.3). Thus, the early porphyry was emplaced immediately after of the precursor pluton at a time gap of up to  $0.05 \pm 0.70$  m.y. The very short time gap is also in accordance with previous studies which concluded that the emplacement of a precursor pluton and the subsequent mineralized magmatic phase is likely to occur on a time scale of 1 m.y. or less (e.g., Dilles and Wright, 1988; Marsh et al., 1997; Deckart et al., 2005; Campbell et al., 2006; Sillitoe and Mortensen, 2010; Barra et al., 2013). Therefore, the quartz diorite pluton is clearly a large-scale precursor intrusion spatially, temporally and genetically related to the La Arena porphyry Cu-Au-(Mo) deposit and Calarco epithermal high-sulfidation gold system formation.

The deep potassic alteration core with vertically fracture networks is formed after the early andesite porphyry, which is interpreted to have acted as the focus of emergence of at least two fluid flow paths as separated pulses of hydrothermal activity during the main ore-formation time. The first generation of voluminous fluid fluxes ascended along structure networks, recorded by sequential formation of  $M_E$ ,  $A1-5_E$ , and  $AB_E$  veinlets and an upward gradual fading of potassic alteration. The low-pressure fluid ascent continued its advance outward up to reach groundwater table, where the high-temperature lithocap was generated (cf. Sillitoe, 2010; Fig. 7.1). In depth of  $\sim 758$  m, the reproducible Re-Os age of molybdenite in the oldest  $A3_E$  veinlet ( $26.61 \pm 0.41$  Ma) and zircon U-Pb age of the early andesite porphyry ( $26.45 \pm 0.64$  Ma) are indistinguishable within uncertainty ( $2\sigma$ ), indicating that the crystallization of the early porphyry was nearly coeval with early

molybdenum ore deposition, probably at a higher temperature than ~500° C estimated by Suzuki et al. (1996). The magmatic fluids continue to rise predominantly through preexisting quartz veinlets stockworks. This is contrasted in deep parts of the porphyry system, where hydrothermal quartz veinlets are cut along their edges by B<sub>E</sub> veinlets. The molybdenite Re-Os age of one B<sub>E</sub>-type with irregular white sericitic envelopes is 26.51 ± 0.46 Ma. Compared to the weighted mean <sup>40</sup>Ar/<sup>39</sup>Ar muscovite/sericite ages of 26.41 ± 0.52 and 26.38 ± 0.24 Ma, and hydrothermal biotite ages of 26.40 ± 0.29 and 26.35 ± 0.14 Ma, this ages are similar, taking their error brackets. This overlap between Re-Os and <sup>40</sup>Ar/<sup>39</sup>Ar ages would appear to reflect the initial path cooling of the system below the argon blocking temperature (Fig. 7.1). In shallow depth, the fluids intersected unreactive permeable quartz sandstone sequence, allowed lateral flow to develop the Calaorco advance argillic lithocap near the surface into volcanic base rocks. This deposit architecture suggests a limited volcanic eruption, as in flow-dome complexes, but shows no evidences of fairly deep origin (cf. Sillitoe, 1999), in the light of the low-temperature sulfide mineralization of luzonite – enargite (cf. Einaudi et al., 2003; Corbett, 2008). The second generation of hydrothermal activity is Mo-rich fluids that may be attributed to the late preferential extraction of Mo from the underlying magma chamber, but without the evidence of an associated porphyry stock for metal-bearing volatiles transport (Fig. 7.1) as discussed in detail by Li et al. (2017). This is suggested by the reproducible Re-Os ages of 26.05 ± 0.39 to 25.86 ± 0.44 Ma for three molybdenites in the B1<sub>T</sub>- and B2<sub>T</sub>-type veinlet samples, which are nominally younger than the host early andesite porphyry zircon U-Pb age (see above), and are older than the inter-mineral andesite porphyry (see below), in agreement with clear field crosscutting relation. This set of Re-Os molybdenite ages overlap with the hydrothermal biotite <sup>40</sup>Ar/<sup>39</sup>Ar ages of 26.08 ± 0.13 Ma (Montgomery, 2012) and 25.96 ± 0.16 Ma from the SCC alteration zone and a sericite <sup>40</sup>Ar/<sup>39</sup>Ar age of 26.02 ± 0.07 Ma (Tahoe Resources, unpub. files). The ages would appear to reflect a second fluid flow path of hydrothermal activity during the transition veinlet stage of the La Arena system (Fig. 7.1).

The rapid uplift and progressive paleosurface degradation accompanied with hydrothermal activity supported the overprinting of Calaorco lithocap on the shoulder of the causative andesite porphyry stock as at the Rosario Cu-Mo porphyry and superimposed high-sulfidation style mineralization in the Collahuasi district, Chile (Masterman et al., 2005). The Calaorco lithocap is offset from the deep central fluid plume (Fig. 7.1), similar to the distribution of advance argillic alteration at Lepanto epithermal system, Philippines, which occurs up to 3 km from the causative Far Southeast porphyry (Hedenquist et al., 1998; Chang et al., 2011). Alunite from Calaorco HS deposit that is topographically above and ~250 m southwest of La Arena have ages of 25.57 ± 0.16, 25.51 ± 0.10, and 25.51 ± 0.17 Ma, and alunite samples from Ethel HS deposit ~600 m northwest of La Arena has an age of 25.81 ± 0.16 Ma; 0.89 ± 0.34 and 0.59 ± 0.33 m.y. younger than the porphyry-style potassic biotite alteration at La Arena, respectively. However, porphyry-style hydrothermal biotite is documented to have occurred at approximately at the same time with alunite of the advance argillic alteration in the porphyry-epithermal transition systems (Arribas et al., 1995; Longo et al., 2010). Otherwise, biotite <sup>40</sup>Ar/<sup>39</sup>Ar ages from SCC alteration zone in the La Arena porphyry is statistically similar within a 2σ error (0.15 ± 0.16) to the hypogene alunites from Ethel HS and 0.39 ± 0.16 m.y. older than the alunites from the Calaorco. This supports that the hydrothermal alteration at La Arena and Calaorco-Ethel deposits, evolved along two fluid flow paths as separate pulses of hydrothermal activity during the main ore-forming

process (Fig. 7.1), as have been also reported in other porphyry-epithermal transition systems (e.g. Muntean and Einaudi, 2001; Longo et al., 2010).

The short lifespan intervals that provided the  $^{40}\text{Ar}/^{39}\text{Ar}$  method does not date the early high-temperature history of porphyry systems (von Quadt et al., 2002). This method only records the later stages of porphyry copper formation (cf. Sillitoe and Mortensen, 2010) at lower temperatures (250°–400°C; Richards and Noble, 1998), after system cooling below the closure temperatures of the commonly dated minerals (Chiaradia et al., 2013, 2014, and references therein). Whereby, this suggests that later hydrothermal activity from the La Arena porphyry to Calaorco epithermal high-sulfidation environment cooled within  $0.89 \pm 0.34$  m.y. from potassic biotite argon- closure temperature as indicative of cooling time of the hydrothermal systems at  $\sim 320^\circ\text{C}$  to below the argon closure temperature of alunite at  $280^\circ \pm 20^\circ\text{C}$  (Lovera et al., 1997). In contrast, the entire lifespan of the intensely mineralized early porphyry was recorded by zircon grain ages ( $26.45 \pm 0.64$  Ma) and alunite crystals ( $25.51 \pm 0.17$  Ma), suggest that this early porphyry and its hydrothermal activity cooled below the alunite argon closure temperature (ca.  $280^\circ\text{C}$ ) within a time interval no less than 0.28 and no longer than 1.60 m.y. ( $0.94 \pm 0.66$  m.y.; Fig. 7.1). The minimum duration estimate appear to be similar to the lifespan of hydrothermal systems at the Far Southeast-Lepanto porphyry and epithermal systems, Philippines ( $\sim 0.30$  m.y., Arribas et al., 1995), Potrerillos district, Chile (0.033-0.65 m.y., Marsh et al., 1997), Elatsite, Bulgaria (1.2 m.y., von Quadt et al., 2002), Bingham Canyon, Utah and Bajo de la Alumbrera, Argentina (0.32 and 0.09 m.y., respectively, von Quadt et al., 2011), Tibetan Qulong, China ( $\sim 0.84$  m.y., Li et al., 2017), Butte, Montana ( $\sim 0.60$  m.y., Mercer et al., 2015) and Haquira, Peru (0.17 m.y., Cernuschi et al., 2018), and also numerical simulations on fluid flow accompanied by a single-magma cooling event which provides porphyry hydrothermal system lifespans of 0.05 to 0.80 m.y. (Norton and Cathles, 1979; Cathles, 1997; Driesner and Geiger, 2007; Weis et al., 2012).

After the earliest and most intensely mineralized early andesite porphyry, inter-mineral andesite porphyry bodies and dikes intruded along irregular subvertical contacts (Fig. 4.2D) between  $25.58 \pm 0.68$  and  $25.55 \pm 0.27$  Ma (25.47 to 25.44 Ma; Tahoe Resources, unpub. files),  $0.90 \pm 0.69$  m.y. after the main mineralized event (Fig. 7.1). The inter-mineral porphyry stage was followed by waning generation of magmatic-hydrothermal fluids and, under the conditions a lower veinlet density (A1-2<sub>L</sub>, AB<sub>L</sub>, B<sub>L</sub>, D1<sub>L</sub>) associated with weaker mineralization within pervasive sericitic-illite alteration were formed. The inter-mineral porphyry in the southwest shoulder of the La Arena porphyry orebody, where is cut by D2<sub>L</sub>-type veins tend to be younger than those within the central part of the deposit, is consistency with the southwestward younging of the zircon U-Pb ages of  $25.24 \pm 0.46$  and  $25.21 \pm 0.27$  Ma (Tahoe Resources, unpub. files). In contrast, the other two zircon U-Pb ages of  $25.22 \pm 0.27$  and  $24.95 \pm 0.29$  Ma, which are significantly younger than the aforementioned ages, are obtained using one drill core of the northwest part of the deposit with potassic and sericitic alterations, respectively (Tahoe Resources, unpub. files). We thus interpret that these ages may represent a late inter-mineral magmatic event. Therefore, at least two successive individual magmatic events within the inter-mineral porphyry are associated with the latest stage of copper and gold ores introduction at the La Arena porphyry (Fig. 7.1).

The U-Pb age of  $24.81 \pm 0.48$  Ma and three unpublished zircon U-Pb ages of  $24.75 \pm 0.32$ ,  $24.44 \pm 0.32$ , and  $24.40 \pm 0.48$  for late-mineral andesite porphyry bodies and dikes emplaced into the Calaoroco open-pit that are within a time span of  $\sim 0.41$  m.y. The high-

sulfidation mineralized veins at Calarco are cut by these late mineral porphyries, which mark the end of magmatic-hydrothermal activity in the porphyry-epithermal systems.

In summary, the magmatic-hydrothermal activity at the La Arena porphyry Cu-Au-(Mo) systems, from the precursor pluton to late mineral porphyry, developed over an interval of  $2.24 \pm 0.79$  m.y. according with U-Pb ages from  $26.64 \pm 0.71$  to  $24.40 \pm 0.34$  Ma. However, the most veinlets development and the main copper-gold-molybdenum introduction (up to 90 vol%) was linked a two fluid flow paths as separate pulses of hydrothermal activity centered in the early andesite porphyry magmatic event from La Arena porphyry environment to Calaorco-Ethel high-sulfidation systems for a maximum time interval of  $0.94 \pm 0.66$  m.y. The remaining introduction of ore mineral was related to inter-mineral porphyries formation, which must have been completed in a time interval of  $0.63 \pm 0.83$  m.y. in base to U-Pb ages from  $25.58 \pm 0.68$  to  $24.95 \pm 0.29$  Ma. Late-mineral porphyry finally postdated essentially all copper, gold, and molybdenum introduction within of an estimate time range of  $0.41 \pm 0.59$  m.y. from  $24.75 \pm 0.32$  to  $24.40 \pm 0.34$  Ma.

### 7.3 Exploration Implications

The mineral exploration boom in the Huamachuco-Cajabamba belt of Oligocene-Miocene age was followed after the discovery of disseminated high sulfidation-style Au epithermal mineralization at Ethe-Calaorco, La Virgen (Gauthier et al., 1999; Quirita and Gauthier, 2000), El Toro (Noble and McKee, 1999), Lagunas Norte (Araneda et al., 2003; Montgomery, 2012; Cerpa et al., 2013), as the main oreshoot hosted in the quartz sandstone sedimentary sequence of the early Cretaceous Chimú Formation. The quartz sandstones is characterized by a limited- to non-reactive chemistry in interaction with hydrothermal fluids, resulting in important challenges in the alteration mapping (Araneda et al., 2003), despite the fact that it is well exposed in the surface area (Cerpa et al., 2013). However, the supergene alteration-mineralization is a key to promote discovery of this deposit type developed within the Chimú quartz sandstone. In the Huamachuco-Cajabamba belt, the lithocaps are superimposed on porphyry shoulders, offset from the causative porphyry intrusions and show different grade of erosion. The lithocaps contains dominant hematite-goethite leached cappings, together with oxidized Au mineralization and variable occurrences of advanced argillic alteration. The lithocaps between La Arena and Lagunas Norte districts are formed mainly in the quartz sandstone sediment rocks, but some of them are hosted in the volcanic sequences. Examples include lithocaps on porphyry shoulders at Calaorco-Ethel (Aquino et al., 2006) and Milagros-Lagunas Norte (Garcia, 2009), which in base to close spatial relationship, suggests a porphyry-epithermal transition analogous to the Far Southeast in the Philippines (Arribas et al., 1995), Kupfertal (Longo, 2005), and Tantahuatay (Noble, 1991; Tostal, 1996; Gustafson et al., 2004, Noble et al., 2011), northern Peru.

At least 5 porphyry prospects overprinted by roots of lithocaps in quartz sandstone, which are extensively eroded (Hedenquist, 2015), were recently discovered at Alizar, Agua Blanca, and Belen. In the preserved lithocaps in quartz sandstone, the high-sulfidation epithermal gold mineralization at Lagunas Norte (13.1-Moz Au; Cerpa et al., 2013), La Virgen, and El Toro (Noble and McKee, 1999) and deeper porphyry orebodies were the major objective of extensive drilling campaign by Minera Barrick Misquichilca and Cambior in the early 2000s. Several deep holes at the La Arena and Lagunas Norte districts, show pyrophyllite-diaspore alteration assemblages with patchy replacement textures, which may be consistent with the roots of the epithermal environment, near the

transition to the top of the porphyry environment (Garcia, 2009). Unfortunately, no economically potential porphyry systems were recognized at the Lagunas Norte district (Montgomery, 2012). However, the absence of epithermal mineralization in the Miocene porphyry copper belt at El Galeno, Michiquillay, Chailhuagón, and Cerro Corona porphyry deposits is possibly related to grade of erosion (Gustafson et al., 2004). Therefore, the lithocaps identified in the Chimú quartz sandstone and/or volcanic rocks (e.g. Yanacocha district; Longo et al., 2010; Tantauatay; Noble et al., 2011) have significance for exploration strategies, and are important key to explore porphyry-related Cu-Au-(Mo) systems as suggested in the Huamachuco-Cajabamba metallogenic belt.

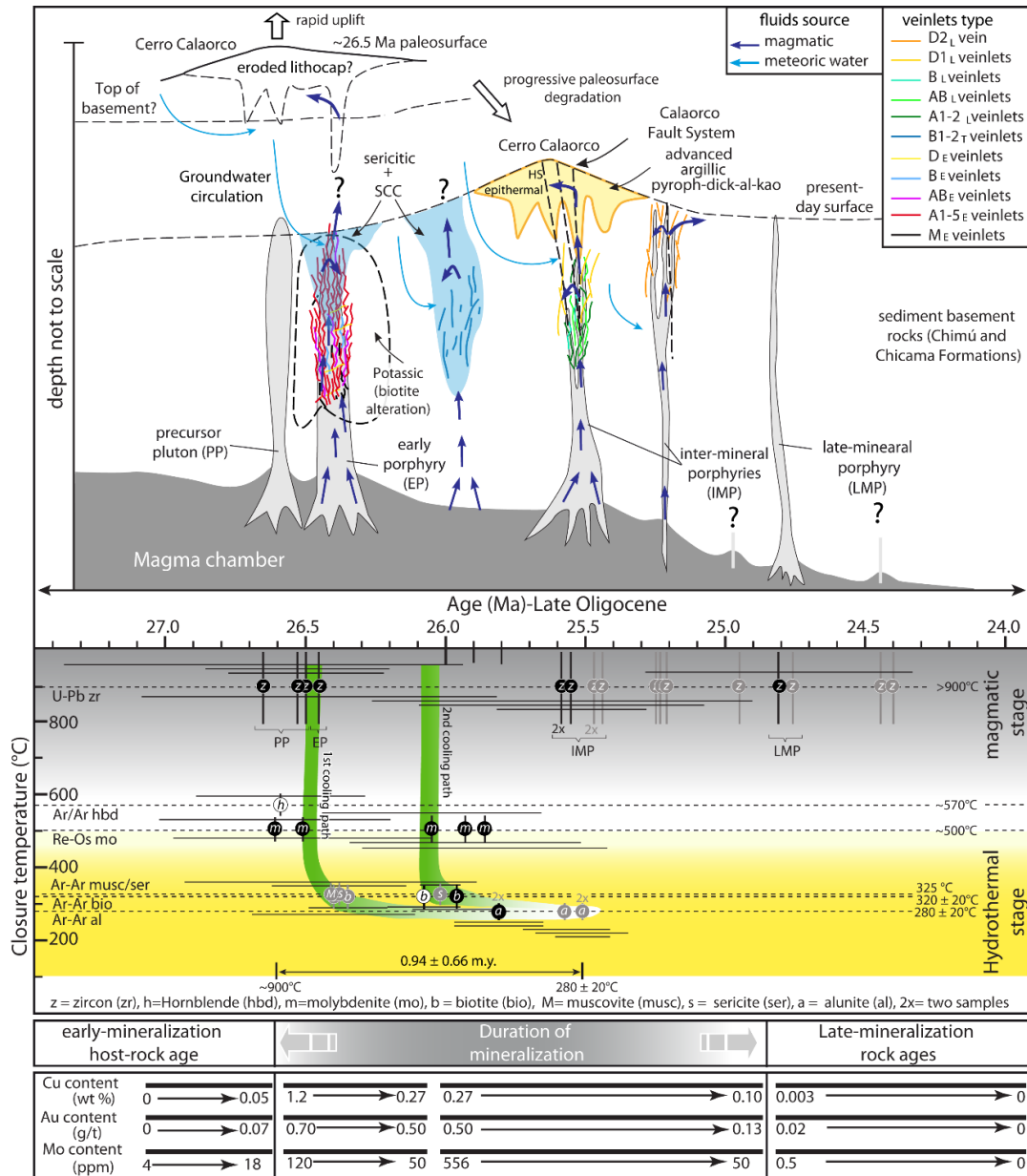


Figure 7.1. Schematic time-space sequence and Cu, Au, and Mo mineralization of the telescoped La Arena porphyry Cu-Au-(Mo) system. Diagram show the veinlet formation, hydrothermal alteration types in concert with consecutive magmatic and fluid injections, rapid uplift, and paleosurface degradation. The previous age data (white circles, Montgomery, 2012; gray circles, Tahoe Resources, unpub. files) and new radiometric (black circles) U-Pb, Re-Os, and <sup>40</sup>Ar/<sup>39</sup>Ar ages (±2σ) for mineral separates (see text) provide

a timeframe for the magmatic – hydrothermal evolution system of about  $2.24 \pm 0.79$  Ma from the precursor pluton (PP) to late mineral porphyry (LMP). Diagram also show two cooling path for the magmatic-hydrothermal into the early andesite porphyry, through a thermal ranges that goes from high-closure temperature for zircon ( $>900$  °C, Cherniak and Watson, 2000, and references therein), hornblende (570 °C, Dobson, 1973; Harrison, 1981), and molybdenite ( $\sim 500$  °C, Suzuki et al., 1996) to low-closure temperature for sericite/muscovite ( $\sim 325$  °C; Snee et al., 1988), biotite ( $320 \pm 20$  °C; Dobson, 1973; Harrison et al., 1985; McDougall and Harrison, 1999), and alunite ( $280 \pm 20$  °C; Lovera et al., 1997). Black bars represent the different magmatic events associated with Cu, Au, and Mo mineralization.

## Chapter 8

# Conclusion

### 8.1 Conclusive remarks

At La Area-Calaorco porphyry and epithermal deposits, unambiguous field relationship suggests at least four intrusive porphyry phases from precursor pluton, through generation of early and inter-mineral porphyries to late-mineral porphyry bodies related to copper, gold, and molybdenum mineralization. This multiphase of andesite porphyry intruded into Mesozoic sediment rocks during the late Oligocene, and was localized by the preexisting, regional-scale overthrust anticline folded axis of axial trace NW-orientation and NE-vergent under compressional tectonic regime. Alternatively, the Calaorco orebody was formed in the southwest flank of the fold. The formation of the porphyry and epithermal systems marks the beginning of magmatic-hydrothermal activity in northern Peru, just after break-up subduction Farallón plate between the Cocos and Nazca plate and the subsequent thickening of the continental crust.

Hydrothermal alteration at the La Arena porphyry conforms to the gold-rich porphyry zonal pattern, in which early potassic core is widely overprinted by SCC hydrothermal alteration, both grades laterally to an annular sericitic zone surrounded by a propylitic halo. The extensive advanced argillic alteration forms the Calaorco lithocap in the shoulder of the La Arena shallow porphyry, when the ore-forming fluids cool to  $250\text{-}214$ °C that is inferred to be developed by hydrothermal fluids exsolved from offset the porphyry system. The metal resources at the La Arena are hosted in the early and inter-mineral porphyry intrusions as multiple veinlets of early, transitional and late stages. The  $M_E$  and  $A1\text{-}2_E$  are associated with potassic and SCC alteration zones. The  $A3\text{-}5_E$ ,  $AB_E$ ,  $B_E$ ,  $D_E$  types are voluminous, and thus are economically more important ( $>90\%$ , Cu and Au inventory), and display a spatial correlation with the SCC and sericitic alterations. The  $B1\text{-}2_T$  veinlets are the principal contributor of molybdenite mineralization within pervasive sericitic alteration. The  $A1\text{-}2_L$ ,  $AB_L$ ,  $B_L$ ,  $D1\text{-}2_L$  types are irregularly distributed throughout the sericitic alteration overprinting inter-mineral porphyry intrusives. Whereas, the Calaorco advanced argillic zone with oxidized high-sulfidation style contains a hematite-goethite-



dominant leached capping. The disseminated HS gold zone is hosted in permeable, non-reactive Chimú quartz sandstone, bedding planes, fracture network, and multiple stages of brecciation and silicification controlled by a series of northwest- and northeast-trending faults.

The timing of the magmatic-hydrothermal activity is constrained by U-Pb, Re-Os,  $^{40}\text{Ar}/^{39}\text{Ar}$  dating on zircon grains, molybdenite-bearing quartz veinlets, and silicate mineral, respectively, in the La Arena-Calaorco deposits. U-Pb age determinations on zircon grains indicates four successive magmatic events of intermediate composition within the La Arena-Calaorco orebodies: (1) precursor quartz-diorite pluton crystallized between of  $26.64 \pm 0.71$  to  $26.50 \pm 0.28$  Ma; (2) early andesite porphyry age of  $26.45 \pm 0.64$  Ma for an early porphyry at the central part of the La Arena orebody; (3) inter-mineral andesite porphyry intrusions have ages from  $25.58 \pm 0.68$  to  $24.95 \pm 0.29$  Ma; and (4) late mineral porphyry dikes and small bodies yielded ages between  $24.81 \pm 0.48$  to  $24.40 \pm 0.34$  Ma. The U-Pb ages suggests that the magmatic-hydrothermal activity in the La Arena-Calaorco deposits were produced during a maximum period time of  $2.24 \pm 0.79$  m.y. The Re-Os analyses yield ore-formation ages of  $26.61 \pm 0.41$  and  $26.51 \pm 0.46$  for two early molybdenite-bearing quartz veinlets,  $26.05 \pm 0.39$ ,  $25.93 \pm 0.44$ , and  $25.86 \pm 0.44$  Ma for three molybdenite-rich transitional veinlets in the La Arena porphyry that are within a time span of  $0.75 \pm 0.60$  m.y. The earliest directly related to the early andesite porphyry emplacement, but the latter formed without the association of a nearly coeval porphyry plug, based on zircon U-Pb ages of the early and inter-mineral porphyries, a similar feature to that recognized at the Tibetan Qulong porphyry Cu-Mo deposit (Li et al., 2017). This implies that the molybdenum were deposited in two separated mineralization stages into the early andesite porphyry. The cooling  $^{40}\text{Ar}/^{39}\text{Ar}$  ages have been determined on biotite, muscovite/sericite, and alunite. The deep potassic biotites have ages of  $26.40 \pm 0.29$  and  $26.35 \pm 0.14$  Ma, biotite in paleo-green SCC alteration zone yielded an age of  $25.96 \pm 0.16$  Ma, muscovite/sericite in sericitic zones dating ages of  $26.41 \pm 0.52$ ,  $26.38 \pm 0.24$ , and  $26.02 \pm 0.07$  Ma. Alunite crystals related to advanced argillic altered roofs of the early andesite porphyry from the Calaorco open-pit yielded ages of  $25.57 \pm 0.16$ ,  $25.51 \pm 0.10$ , and  $25.51 \pm 0.17$  Ma and  $25.81 \pm 0.16$  Ma from the Ethel area. The deep porphyry-style hydrothermal biotites are  $\sim 0.89$  and  $\sim 0.59$  m.y. older than the overlying advanced argillic alteration at Calaorco and Ethel, respectively, but biotite from SCC alteration zone have the same range as those of alunite from Calaorco-Ethel deposits. This supported that the hydrothermal alteration centered in the early andesite porphyry from porphyry to epithermal environment evolved along two fluid flow paths as separate pulses of hydrothermal activity linked to early and transitional veinlet stages within a time span of  $0.89 \pm 0.34$  m.y.

Based on all the field features and a combined isotopic dating, we conclude that there is a clear spatial-temporal genetic connection between these two styles of mineralization, as well as the tectonic uplift and erosion accompanied of magmatic-hydrothermal activity as separate pulses during late Oligocene. The magmatic-hydrothermal activity has a lifespan of at least  $2.24 \pm 0.79$  m.y. ranging in  $26.64 \pm 0.71$  to  $24.40 \pm 0.34$  Ma, but about 90 % of copper, gold and molybdenum reserves were deposited within a short time-interval between 0.28 and 1.60 m.y. ( $0.94 \pm 0.66$  m.y.) at the La Arena and Calaorco-Ethel orebodies.



### **Acknowledgments**

This manuscript results from a MSc. dissertation completed at China University of Geosciences (Wuhan). We wish to express our gratitude to Geological survey project of China Geological Survey (project No. DD20201157) and Minera Tahoe Resources Inc. for their support in the logistics of obtaining the La Arena district samples and information generated during their exploration stages. We wish to acknowledge the many La Arena mining exploration geologists, particularly Raúl Jiménez, Wilder Garcia, Ricardo Gordillo, Jhuleyssa Sánchez, Saúl Arias, and Isaac Barboza, who guided to the lithocaps generation in quartz sandstone rocks in the La Arena district. The authors also wish to thank Sandra Choquehuanca, Guo Weimin, and Liu Junan for their help in samples selection for geochronological studies. Jay and Lin provided some of the U-Pb and  $^{40}\text{Ar}/^{39}\text{Ar}$  geochronology reported here. We give special thanks to Luis Cerpa and Enrique Garay for their critical reviews and valuable comments to greatly improve this manuscript.

## References

- Allmendinger, R. W., Jordan, T. E., Kay, S. M., and Isacks, B. L., 1997, The evolution of the Altiplano-Puna plateau of the Central Andes: *Annual Review of Earth and Planetary Sciences*, v. 25, p. 139-174.
- Andrew, B., and Warren, P., 2005, El proyecto de Cu-Mo Rio Blanco Segundo Congreso Internacional de Prospectores y Exploradores, Lima 2005, Instituto de Ingeniero de Minas del Perú., p. 59.
- Aquino, A., Quirita, V., and Garipey, L., 2006, El pórfido de Cu-Au La Arena, [ext. abs.]: *Sociedad Geológica del Perú, XIII Congreso Peruano de Geología, Volumen de Resúmenes Extendidos*, p. 692-695.
- Araneda, R., Guerra, R., Gaboury, F., McEwan, C., Soto, R., Davidson, A. J., and Hodgson, J., 2003, Proyecto del Alto Chicama, Distrito de Quiruvilca, Departamento de La Libertad, Perú, Tercer Congreso Internacional de Prospectores y Exploradores, Lima 2003, Instituto de Ingeniero de Minas del Perú, CD-ROM.
- Arias, S., and Neglia, O., 2018, Reporte geológico proyecto Agua Blanca: Tahoe Peru internal report, Huamachuco, Peru, 20 p.
- Arribas, A., Hedenquist, J. W., Itaya, T., Okada, T., Concepcion, R. A., and Garcia, J. S., 1995, Contemporaneous Formation of Adjacent Porphyry and Epithermal Cu-Au Deposits over 300 Ka in Northern Luzon, Philippines: *Geology*, v. 23, no. 4, p. 337-340.
- Arribas, A., 1995, Characteristics of high-sulfidation epithermal deposits, and their relation to magmatic fluid, in *Magmas, Fluids, and Ore Deposits*, in Thompson, J. F. H., ed., *Mineralogical Association of Canada, Short Course Series, Volume 23*, p. 419-454.
- Asami, N., and Britten, R. M., 1980, The porphyry copper deposits of the Frieda River prospect, Papua New Guinea: *Mining Geology Special Issue*, v. 8, p. 117-139.
- Atherton, M. P., Warden, V., and Sanderson, L. M., 1985, The Mesozoic marginal basin of central Peru: A geochemical study of within plate-edge volcanism, in Pitcher, W. S., Atherton, M. P., Cobbing, E. J., and Beckinsale, R. D., eds., *Magmatism at a plate edge: The Peruvian Andes*, Blackie Hasted, London, p. 47-58.
- Bai, X. J., Qiu, H. N., Liu, W. G., and Mei, L. F., 2018, Automatic  $^{40}\text{Ar}/^{39}\text{Ar}$  dating techniques using multicollector ARGUS VI noble gas mass spectrometer with self-made peripheral apparatus: *Journal of Earth Science*, v. 29, no. 2, p. 408-415.
- Bai, X. J., Hu, R. G., Jiang, Y. D., Liu, X., Tang, B., and Qiu, H. N., 2019, Refined insight into  $^{40}\text{Ar}/^{39}\text{Ar}$  progressive crushing technique from K–Cl–Ar correlations in fluid inclusions: *Chemical Geology*, v. 515, p. 37-49.
- Baker, J., Peate, D., Waight, T., and Meyzen, C., 2004, Pb isotopic analysis of standards and samples using a  $^{207}\text{Pb}$ – $^{204}\text{Pb}$  double spike and thallium to correct for mass bias with a double-focusing MC-ICP-MS: *Chemical Geology*, v. 211, no. 3, p. 275-303.
- Barboza, I., 2017, Análisis textural-mineralógico de las venillas en el pórfido de Au "El Alizar", Sánchez Carrión-La Libertad [Geologist Engineer thesis]: Universidad Nacional de Ingeniería, Lima, 225 p.
- Barra, F., Alcota, H., Rivera, S., Valencia, V., Munizaga, F., and MaksaeV, V., 2013, Timing and formation of porphyry Cu–Mo mineralization in the Chuquicamata district, northern Chile: new constraints from the Toki cluster: *Mineralium Deposita*, v. 48, no. 5, p. 629-651.
- Barton, P. B., and Skinner, B. J., 1967, Sulfide mineral stabilities, in Barnes, H. L., ed., *Geochemistry of hydrothermal ore deposits*: New York, Holt, Rinehart & Winston, p. 236–333.
- Benavides-Cáceres, V. E., 1956, Cretaceous system in northern Peru. *Bulletin of the American Museum of Natural History*, v. 108, p. 352–494.
- Benavides-Cáceres, V. E., 1999, Orogenic evolution of the Peruvian Andes: the Andean cycle: *Geology and ore deposits of the Central Andes*, v. 7, p. 61-107.
- Berger, B. R., Ayuso, R. A., Wynn, J. C., and Seal, R. R., 2008, Preliminary model of porphyry copper deposits: US geological survey open-file report, v. 1321, p. 65.
- Bertrand, G., Guillou-Frottier, L., and Loiselet, C., 2014, Distribution of porphyry copper deposits along the western Tethyan and Andean subduction zones: Insights from a paleotectonic approach: *Ore Geology Reviews*, v. 60, p. 174-190.
- Bissig, T., Clark, A. H., Rainbow, A., and Montgomery, A., 2015, Physiographic and tectonic settings of high-sulfidation epithermal gold–silver deposits of the Andes and their controls on mineralizing processes: *Ore Geology Reviews*, v. 65, p. 327-364.
- Black, L. P., and Gulson, B. L., 1978, The age of the Mud tank Carbonatite, Strangways Range, Northern Territory: *BMR Journal of Australian Geology and Geophysics*, v. 3, p. 227-232.

- Black, L. P., Kamos, L., Allen, C. M., Aleinikoff, J. N., Davis, D. W., Korsch, R. J., and Foudoulis, C., 2003, TEMORA 1: a new zircon standard for Phanerozoic U–Pb geochronology: *Chemical Geology*, v. 200, p. 155–170.
- Black, L. P., Kamo, S. L., Allen, C. M., Davis, D. W., Aleninikoff, J. N., Valley, J. W., Mundil, R., Campbell, I. H., Korsch, R. J., Williams, I. S., and Foudoulis, C., 2004, Improved  $^{206}\text{Pb}/^{238}\text{U}$  microprobe geochronology by the monitoring of a trace-element related matrix effect; SHRIMP, ID-TIMS, ELA-ICP-MS, and oxygen isotope documentation for a series of zircon standards: *Chemical Geology*, v. 205, p. 115-140.
- Bodnar, R. J., and Beane, R. E., 1980, Temporal and spatial variations in hydrothermal fluid characteristics during vein filling in preore cover overlying deeply buried porphyry copper-type mineralization at Red Mountain, Arizona: *Economic Geology*, v. 75, no. 6, p. 876–893.
- Boynton, W. V., 1984, Cosmochemistry of the rare earth elements: Meteorite studies, in Henderson, P., ed., *Rare earth element geochemistry*: Amsterdam, Elsevier, ed., p. 63-114.
- Brimhall, G. H., 1979, Lithologic determination of mass transfer mechanisms of multiple-stage porphyry copper mineralization at Butte, Montana: Vein formation by hypogene leaching and enrichment of hypogene protore: *Economic Geology*, v. 74, p. 556–589.
- Burke, K. C. A., and Kidd, W. S. F., 1980, *Volcanism on Earth through time*: Geological Association of Canada Special Paper 20, p. 503–522.
- Burnham, C. W., and Ohmoto, H., 1980, Late-stage processes of felsic magmatism: *Mining Geology Special Issue* 8, p. 1-11.
- Burnham, C. W., 1979, Magmas and hydrothermal fluids, in Barnes, H.L., ed., *Geochemistry of hydrothermal ore deposits*, 2nd ed.: New York, John Wiley and Sons, p. 71-136.
- Burnham, C. W., 1985, Energy-Release in Subvolcanic Environments - Implications for Breccia Formation: *Economic Geology*, v. 80, no. 6, p. 1515-1522.
- Bussey, S., and Nelson, E., 2011, Geological analysis of the Shahuindo district, Cajabamba Province, Peru: Unpublished report: Prepared by Western Mining Servicess LLC for Sulliden Gold Corporation.
- Campbell, I. H., Ballard, J. R., Palin, J. M., Allen, C., and Faunes, A., 2006, U-Pb zircon geochronology of granitic rocks from the Chuquicamata-El Abra porphyry copper belt of northern Chile: Excimer laser ablation ICP-MS analysis: *Economic Geology*, v. 101, no. 7, p. 1327-1344.
- Campos, E., 2002, Metal origin and fluid evolution in the Zaldivar porphyry copper deposit, Chile an orthomagmatic model [Unpublished Ph.D. dissertation]: Vrije Universiteit, Amsterdam, 166 p.
- Candente Copper Corp. Annual Report (2019), <https://candentecopper.com/corporate/overview/>. Accessed 15 August 2020
- Cano, O., 2017, Geología y geometalurgia del pórfido La Arena (Cu, Au), La Libertad-Perú [MSc Thesis]: Universidad Nacional de Ingeniería, 123 p.
- Castillo, P. R., 2012, Adakite petrogenesis: *Lithos*, v. 134-135, p. 304-316.
- Cathles, L. M., Erendi, A., and Barrie, T., 1997, How long can a hydrothermal system be sustained by a single intrusive event?: *Economic Geology*, v. 92, no. 7-8, p. 766-771.
- Cernuschi, F., Dilles, J. H., Grocke, S. B., Valley, J. W., Kitajima, K., and Tepley, F. J., 2018, Rapid formation of porphyry copper deposits evidenced by diffusion of oxygen and titanium in quartz: *Geology*, v. 46, no. 7, p. 611-614.
- Cerpa, L. M., Bissig, T., Kyser, K., McEwan, C., Macassi, A., and Rios, H. W., 2013, Lithologic controls on mineralization at the Lagunas Norte high-sulfidation epithermal gold deposit, northern Peru: *Mineralium Deposita*, v. 48, no. 5, p. 653-673.
- Chang, Z. S., Hedenquist, J. W., White, N. C., Cooke, D. R., Roach, M., Deyell, C. L., Garcia, J., Gemmill, J. B., McKnight, S., and Cuison, A. L., 2011, Exploration Tools for Linked Porphyry and Epithermal Deposits: Example from the Mankayan Intrusion-Centered Cu-Au District, Luzon, Philippines: *Economic Geology*, v. 106, no. 8, p. 1365-1398.
- Chang, J., Li, J.-W., Selby, D., Liu, J.-C., and Deng, X.-D., 2017, Geological and chronological constraints on the long-lived Eocene Yulong porphyry Cu-Mo deposit, eastern Tibet: implications for the lifespan of giant porphyry Cu deposits: *Economic Geology*, v. 112, no. 7, p. 1719-1746.
- Chelle-Michou, C., and Chiaradia, M., 2017, Amphibole and apatite insights into the evolution and mass balance of Cl and S in magmas associated with porphyry copper deposits: *Contributions to Mineralogy and Petrology*, v. 172, no. 11-12.
- Cherniak, D. J., and Watson, E. B., 2000, Pb diffusion in zircon: *Chemical Geology*, v. 172, no. 1, p. 5-24.

- Chiaradia, M., Schaltegger, U., Spikings, R., Wotzlav, J.-F., and Ovtcharova, M., 2013, How accurately can we date the duration of magmatic-hydrothermal events in porphyry systems?—an invited paper: *Economic Geology*, v. 108, no. 4, p. 565-584.
- Chiaradia, M., Schaltegger, U., and Spikings, R. A., 2014, Time scales of mineral systems—advances in understanding over the past decade: *Society of Economic Geologists, Special Publication 18*, p. 37–58.
- Clark, A. H., 1993, Are outsize porphyry copper deposits either anatomically or environmentally distinctive?: *Society of Economic Geology Special Publication*, v. 2, p. 213-283.
- Clark, A. H., 1990, The Slump Breccias of the Toquepala Porphyry Cu(-Mo) Deposit, Peru - Implications for Fragment Rounding in Hydrothermal Breccias: *Economic Geology and the Bulletin of the Society of Economic Geologists*, v. 85, no. 7, p. 1677-1685.
- Cline, J. S., and Bodnar, R. J., 1991, Can Economic Porphyry Copper Mineralization Be Generated by a Typical Calc-Alkaline Melt: *Journal of Geophysical Research-Solid Earth and Planets*, v. 96, no. B5, p. 8113-8126.
- Clode, C., Proffett, J., Mitchell, P., and Munajat, I., 1999, Relationships of intrusion, wall-rock alteration and mineralisation in the Batu Hijau copper-gold porphyry deposit: *Pacrim'99: International Congress on Earth Science, Exploration and Mining around the Pacific Rim, Proceedings*, v. 99, no. 4, p. 485-498.
- Cloos, M., 2001, Bubbling magma chambers, cupolas, and porphyry copper deposits: *International Geology Review*, v. 43, no. 4, p. 285-311.
- Coira, B., Davidson, J., Mpodozis, C., and Ramos, V., 1982, Tectonic and Magmatic Evolution of the Andes of Northern Argentina and Chile: *Earth-Science Reviews*, v. 18, no. 3-4, p. 303-332.
- Cooke, D. R., and Simmons, S. F., 2000, Characteristics and genesis of epithermal gold deposits: *Reviews in Economic Geology*, v. 13, p. 221–244.
- Cooke, D. R., Wilkinson, J. J., Baker, M., Agnew, P., Wilkinson, C. C., Martin, H., Chang, Z., Chen, H., Gemmill, J. B., and Inglis, S., Using mineral chemistry to detect the location of concealed porphyry deposits—an example from Resolution, Arizona, in *Proceedings 27th International Applied Geochemistry Symposium 2015/2015*, p. 1-6.
- Corbett, G., and Leach, T., 1998, Southwest Pacific Rim gold-copper systems: structure, alteration, and mineralization, *Society of Economic Geologists Special Publication 6*, 234 p.
- Corbett, G., 2008, Influence of magmatic arc geothermal systems on porphyry-epithermal Au-Cu-Ag exploration models, Paper presented at the Terry Leach Symposium, Volume 17.
- Corbett, G., 2014, Comments on the exploration potential of projects in the vicinity of the La Arena Mine, Peru: Unpublished report: Prepared by Corbett Geological Services Pty. Ltd. for Rio Alto Mining Limited. 33 p.
- Córdova, R. J., and Hoyos, J. D., 2000, Geología del pórfido de Cu-(Au-Mo) El Galeno, Cajamarca, Perú, [ext. abs.]: *Sociedad Geológica del Perú, X Congreso Peruano de Geología, Volumen de Resúmenes Extendidos*, tomo 3, p. 1158-1177
- Corfu, F., Hanchar, J. M., Hoskin, P. W., and Kinny, P., 2003, Atlas of zircon textures: *Reviews in mineralogy and geochemistry*, v. 53, no. 1, p. 469-500.
- Cossio, A., and Jaén, H., 1967, Geología de los cuadrángulos de Puémape, Chocope, Otuzco, Trujillo, Salaverry y Santa, Instituto Geológico Minero y Metalúrgico. Lima, Perú: *Boletín Serie A: Carta Geológica Nacional*, no. 17, 141 p.
- Cossio, A., 1964, Geología de los cuadrángulos de Santiago de Chuco y Santa Rosa, Comisión Carta Geológica Nacional, *Boletín no. 8*, 69 p.
- Davies, R. C. I., and Williams, P. J., 2005, The El Galeno and Michiquillay porphyry Cu–Au–Mo deposits: geological descriptions and comparison of Miocene porphyry systems in the Cajamarca district, northern Peru: *Mineralium Deposita*, v. 40, no. 5, p. 598-616.
- Davies, R. C. I., 2002, Tectonic, magmatic and metallogenic evolution of the Cajamarca mining district, Northern Peru [PhD thesis]: James Cook University, 323 p.
- Deckart, K., Clark, A. H., Celso, A. A., Ricardo, V. R., Bertens, A. N., Mortensen, J. K., and Fanning, M., 2005, Magmatic and Hydrothermal Chronology of the Giant Río Blanco Porphyry Copper Deposit, Central Chile: Implications of an Integrated U-Pb and <sup>40</sup>Ar/<sup>39</sup>Ar Database: *Economic Geology*, v. 100, no. 5, p. 905-934.
- Deckart, K., Clark, A. H., Cuadra, P., and Fanning, M., 2013, Refinement of the time-space evolution of the giant Mio-Pliocene Río Blanco-Los Bronces porphyry Cu–Mo cluster, Central Chile: new U–Pb (SHRIMP II) and Re–Os geochronology and <sup>40</sup>Ar/<sup>39</sup>Ar thermochronology data: *Mineralium Deposita*, v. 48, no. 1, p. 57-79.



- Díaz, N., Jiménez, C., and Alva, C., 1997, Estudio geoquímico de orientación del depósito de cobre La Granja [ext. abs.]: Sociedad Geológica del Perú, IX Congreso Peruano de Geología, Volumen de Resúmenes Extendidos, p. 25-30.
- Dilles, J. H., and Einaudi, M. T., 1992, Wall-Rock Alteration and Hydrothermal Flow Paths About the Ann-Mason Porphyry Copper-Deposit, Nevada - a 6-Km Vertical Reconstruction: *Economic Geology*, v. 87, no. 8, p. 1963-2001.
- Dilles, J., Einaudi, M., Proffett, J., and Barton, M., 2000, Overview of the Yerington porphyry copper district: Magmatic to nonmagmatic sources of hydrothermal fluids: Their flow paths and alteration effects on rocks and Cu-Mo-Fe-Au ores: *Society of Economic Geologists Guidebook Series*, v. 32, no. Part 1, p. 55-66.
- Dilles, J. H., Halley, S., Tosdal, R. M., and Cernuschi, F., 2014, The geochemical and mineralogic footprint of hydrothermal alteration at Butte, Montana 2014 GSA Annual Meeting in Vancouver, British Columbia.
- Dilles, J. H., and Wright, J. E., 1988, The chronology of early Mesozoic arc magmatism in the Yerington district of western Nevada and its regional implications: *Geological Society of America Bulletin*, v. 100, no. 5, p. 644-652.
- Dilles, J. H., 1987, Petrology of the Yerington Batholith, Nevada; evidence for evolution of porphyry copper ore fluids: *Economic Geology*, v. 82, no. 7, p. 1750-1789.
- Dodson, M. H., 1973, Closure temperature in cooling geochronological and petrological systems: *Contributions to Mineralogy and Petrology*, v. 40, no. 3, p. 259-274.
- Driesner, T., and Geiger, S., 2007, Numerical Simulation of Multiphase Fluid Flow in Hydrothermal Systems: *Reviews in Mineralogy and Geochemistry*, v. 65, no. 1, p. 187-212.
- Du, A. D., Wu, S. Q., Sun, D. Z., Wang, S. X., Qu, W. J., Markey, R., Stein, H., Morgan, J., and Malinovskiy, D., 2004, Preparation and certification of Re-Os dating reference materials: Molybdenite HLP and JDC: *Geostandards and Geoanalytical Research*, v. 28, p. 41-52.
- Einaudi, M. T., Hedenquist, J. W., and Inan, E. E., 2003, Sulfidation state of fluids in active and extinct hydrothermal systems: Transitions from porphyry to epithermal environments: *Special Publication-Society of Economic Geologists*, v. 10, p. 285-314.
- Einaudi, M., 1977, Environment of ore deposition at Cerro de Pasco, Peru: *Economic Geology*, v. 72, no. 6, p. 893-924.
- Emmons, W., 1927, Relations of the Disseminated Copper Ores in Prophyry to Igneous Intrusives, American Institute of Mining and Metallurgical Engineers.
- Eude, A., Roddaz, M., Bricchau, S., Brusset, S., Calderon, Y., Baby, P., and Soula, J. C., 2015, Controls on timing of exhumation and deformation in the northern Peruvian eastern Andean wedge as inferred from low-temperature thermochronology and balanced cross section: *Tectonics*, v. 34, no. 4, p. 715-730.
- Farrar, E., and Noble, D., 1976, Timing of late Tertiary Deformation in the Andes of Peru: *Geology Society of America Bulletin*, v. 87, no. 9, p. 1247 - 1250.
- Frey, F. A., Chappell, B. W., and Roy, S. D., 1978, Fractionation of rare-earth elements in the Tuolumne Intrusive Series, Sierra Nevada batholith, California: *Geology*, v. 6, p. 239-242.
- Fournier, R. O., 1999, Hydrothermal processes related to movement of fluid from plastic into brittle rock in the magmatic-epithermal environment: *Economic Geology*, v. 94, no. 8, p. 1193-1211.
- Garay, E., Valdivia, J., Rivera, J., Corbett, G., and Sangay, I., 2012, Spatial and Genetic Relationship between Epithermal Sediment-Hosted Au and Porphyry Cu-Au-(Mo) Deposits: La Arena – La Libertad, Peru, [ext. abs.]: Sociedad Geológica del Perú, XVI Congreso Peruano de Geología & SEG, Volumen de Resúmenes Extendidos, CD-ROM, 2 p.
- García, W., Cano, O., Cabrera, O., Gordillo, R., and Garay, E., 2015, Geometalurgia del pórfido La Arena, [abs.]: Noveno Congreso Internacional de Prospectores y Exploradores, Lima 2015, Instituto de Ingeniero de Minas del Perú.
- García, W. V., 2009, Geology of the Milagros Project, Alto Chicama district, La Libertad, Peru: [Unpublished MSc thesis]: Colorado School of Mines, Colorado, USA, 145 p.
- Garver, J. I., Montario, M., Perry, S. E., Reiners, P. W., and Ramage, J. R., 2005, Uplift and exhumation of the northern Peruvian Andes, [ext. abs.]: VI International Symposium on Andean Geodynamics (ISAG 2005, Barcelona), Extended Abstracts, p. 305 – 307.
- Gauthier, A., Díaz, N., and Quirita, V., 1999, Yacimientos La Arena-Virgen, [abs.]: Primero Congreso Internacional de Prospectores y Exploradores, Lima 1999, Instituto de Ingeniero de Minas del Perú, p. 73-91.

- Geggenbach, W. F., 1997, The origin and evolution of fluids in magmatic-hydrothermal systems, in Barnes, H.L., ed., *Geochemistry of Hydrothermal ore deposits*, 3rd ed.: New York, Wiley Interscience, p. 737-796.
- Gow, P., and Walshe, J., 2005, The role of preexisting geologic architecture in the formation of giant porphyry-related Cu±Au deposits: Examples from New Guinea and Chile: *Economic Geology*, v. 100, no. 5, p. 819-833.
- Gray, J. E., and Coolbaugh, M. F., 1994, Geology and geochemistry of Summitville, Colorado: An epithermal acid sulfate deposit in a volcanic dome: *Economic Geology*, v. 89, p. 1906-1923.
- Gustafson, L. B., and Hunt, J. P., 1975, The porphyry copper deposit at El Salvador, Chile: *Economic Geology*, v. 70, no. 5, p. 857-912.
- Gustafson, L. B., and Titley, S. R., 1978, Porphyry copper deposits of the southwestern Pacific Islands and Australia: *Economic Geology*, v. 73, p. 597-599.
- Gustafson, L. B., Vidal, C., Pinto, R., and Noble, D., 2004, Porphyry-epithermal transition, Cajamarca region, northern Peru: *Society of Economic Geologists*, v. 11, p. 279-299.
- Gustafson, L. B., 1978, Some major factors of porphyry copper genesis: *Economic Geology*, v. 73, p. 600-607.
- Halley, S., Dilles, J., and Tosdal, R., 2015, Footprints: Hydrothermal alteration and geochemical dispersion around porphyry copper deposits: *Society of Economic Geologists Newsletter*, v. 100, no. 1, p. 12-17.
- Hamilton, W., and Myers, W. B., 1967, The nature of batholiths: U.S. Geology Survey Prof. Paper 554-C, p. 1-30.
- Hamilton, W., 1969, Mesozoic California and the underflow of Pacific mantle: *Geological Society of America Bulletin*, v. 80, no. 12, p. 2409-2430.
- Harris, A. C., Dunlap, W. J., Reiners, P. W., Allen, C. M., Cooke, D. R., White, N. C., Campbell, I. H., and Golding, S. D., 2008, Multimillion year thermal history of a porphyry copper deposit: application of U–Pb, 40 Ar/39 Ar and (U–Th)/He chronometers, Bajo de la Alumbrera copper–gold deposit, Argentina: *Mineralium Deposita*, v. 43, no. 3, p. 295-314.
- Harrison, T.M., Duncan, I., and McDougall, I., 1985, Diffusion of <sup>40</sup>Ar in biotite: temperature, pressure and compositional effects: *Geochimica et Cosmochimica Acta*, v. 49, no. 11, p. 2461-2468.
- Harrison, T. M., 1981, Diffusion of <sup>40</sup>Ar in hornblende: *Contributions to Mineralogy and Petrology*, v. 78, no. 3, p. 324-331.
- Heald, P., Foley, N. K., and Hayba, D. O., 1987, Comparative Anatomy of Volcanic-Hosted Epithermal Deposits - Acid-Sulfate and Adularia-Sericite Types: *Economic Geology*, v. 82, no. 1, p. 1-26.
- Hedenquist, J. W., and Lowenstern, J. B., 1994, The role of magmas in the formation of hydrothermal ore deposits: *Nature*, v. 370, no. 6490, p. 519-527.
- Hedenquist, J. W., and Taran, Y. A., 2013, Modeling the formation of advanced argillic lithocaps: volcanic vapor condensation above porphyry intrusions: *Economic Geology*, v. 108, no. 7, p. 1523-1540.
- Hedenquist, J. W., Aoki, M., and Shinohara, H., 1994, Flux of volatiles and ore-forming metals from the magmatic-hydrothermal system of Satsuma Iwojima volcano: *Geology*, v. 22, no. 7, p. 585-588.
- Hedenquist, J. W., Arribas, A., and Reynolds, T. J., 1998, Evolution of an intrusion-centered hydrothermal system; Far Southeast-Lepanto porphyry and epithermal Cu-Au deposits, Philippines: *Economic Geology*, v. 93, no. 4, p. 373-404.
- Hedenquist, J. W., 2015, Observations on the Shahuindo Au development, Cajamarca, and Alizar Au-(Cu) and La Florida Au-Ag prospects, La Libertad, Peru: Unpublished report: Prepared by Hedenquist Consulting, Inc. for Rio Alto Mining Limited. 23 p.
- Hemley, J. J., and Hunt, J. P., 1992, Hydrothermal ore-forming processes in the light of studies in rock-buffered systems: II. Some general geologic applications: *Economic Geology*, v. 87, p. 23-43.
- Hemley, J. J., Montoya, J. W., Marinenko, J. W., and Luce, R. W., 1980, Equilibria in the system Al<sub>2</sub>O<sub>3</sub>-SiO<sub>2</sub>-H<sub>2</sub>O and some general implications for alteration mineralization processes: *Economic Geology*, v. 75, p. 210-228.
- Holliday, J. R., and Cooke, D. R., 2007, Advances in geological models and exploration methods for copper ± gold porphyry deposits: in Milkereit, B., ed., *Proceedings of Exploration 07: Fifth Decennial International Conference on Mineral Exploration*: Toronto, Prospectors and Developers Association of Canada, p. 791-809.
- Hollister, V., 1977, Kinematics and regional tectonic interpretation of the east-trending fold belt of Peru: *Geological Society of America Bulletin*, v. 88, p. 1749-1755.
- Hoskin, P. W., and Schaltegger, U., 2003, The composition of zircon and igneous and metamorphic petrogenesis: *Reviews in mineralogy and geochemistry*, v. 53, no. 1, p. 27-62.

- Hou, Z. Q., Ma, H. W., Khin, Z., Zhang, Y. Q., Wang, M. J., Wang, Z., Pan, G. T., and Tang, R. L., 2003, The Himalayan Yulong porphyry copper belt: Product of large-scale strike-slip faulting in eastern Tibet: *Economic Geology*, v. 98, no. 1, p. 125-145.
- Hunt, J. P., 1991, Porphyry copper deposits: *Economic Geology Monograph* 8, p. 192–206.
- Jannas, R. R., Beane, R. E., Ahler, B. A., and Brosnahan, D. R., 1990, Gold and copper mineralization at the El Indio deposit, Chile, in *Epithermal Gold Mineralization of the Circum-Pacific*; *Geology*, in J. W. Hedenquist, N. C. W. a. G. S., *Journal of Geochemical Exploration*, ed., *Geochemistry, Origin and Exploration*, Volume 2, p. 233-266.
- Jackson, S. E., Pearson, N. J., Griffin, W. L., and Belousova, E. A., 2004, The application of laser ablation-inductively coupled plasma-mass spectrometry to in situ U-Pb zircon geochronology: *Chemical Geology*, v. 211, p. 47–69.
- Jaillard, E., Hérail, G., Monfret, T., Díaz-Martínez, E., Baby, P., Lavenu, A., and Dumont, J. F., 2000 Tectonic evolution of the Andes of Ecuador, Peru, Bolivia and Northernmost Chile. , In: U. G. Cordani, E. J. Milani, A. Thomaz Filho, D. A. Campos (eds) *Tectonic Evolution of South America*, 31st Int. Geol. Congress. Brazil p. 481–559.
- Jaillard, E., and Soler, P., 1995, Cretaceous to early Paleogene tectonic evolution of the northern Central Andes (0–18 S) and its relations to geodynamics: *Tectonophysics*, v. 259, no. 1-3, p. 41-53.
- Jaillard, E., 1987, Sedimentary evolution of an active margin during middle and upper Cretaceous times: the North Peruvian margin from Late Aptian up to Senonian: *Geologische Rundschau*, v. 76, no. 3, p. 677-697.
- Jones, B. K., 1992, Application of Metal Zoning to Gold Exploration in Porphyry Copper Systems: *Journal of Geochemical Exploration*, v. 43, no. 2, p. 127-155.
- Kay, S. M., and Mpodozis, C., 2002, Magmatism as a probe to the Neogene shallowing of the Nazca plate beneath the modern Chilean flat-slab: *Journal of South American Earth Sciences*, v. 15, no. 1, p. 39-57.
- Kay, S. M., Mpodozis, C., Tittler, A., and Cornejo, P., 1994, Tertiary Magmatic Evolution of the Maricunga Mineral Belt in Chile: *International Geology Review*, v. 36, no. 12, p. 1079-1112.
- Kay, S. M., Mpodozis, C., and Coira, B., 1999, Neogene magmatism, tectonism, and mineral deposits of the Central Andes (22 to 33 S latitude): *Geology and ore deposits of the Central Andes*, v. 7, p. 27-59.
- Kay, S. M., Godoy, E., and Kurtz, A., 2005, Episodic arc migration, crustal thickening, subduction erosion, and magmatism in the south-central Andes: *Geological Society of America Bulletin*, v. 117, no. 1-2, p. 67-88.
- Kesler, S. E., Chryssoulis, S. L., and Simon, G., 2002, Gold in porphyry copper deposits: its abundance and fate: *Ore Geology Reviews*, v. 21, no. 1-2, p. 103-124.
- Kesler, S. E., 1973, Copper, molybdenum and gold abundances in porphyry copper deposits: *Economic Geology*, v. 68, no. 1, p. 106-112.
- Kirkham, B., and Sinclair, W., 1995, Porphyry copper, gold, molybdenum, tungsten, tin, silver, in Eckstrand, O. R., Sinclair, W. D., and Thorpe, R. I., eds., *Geology of Canadian Mineral Deposit Types*, Volume 8, Geological Survey of Canada Geology of Canada, p. 421-446.
- KMC (Kirk Mining Consultants Pty. Ltd.), 2012, La Arena Project, Peru: Unpublished report: Rio Alto Mining Limited. 174 p.
- Koppers, A. A. P., 2002, ArArCALC — software for  $^{40}\text{Ar}/^{39}\text{Ar}$  age calculations: *Comput. Geosci*, v. 28, no. 5, p. 605–619.
- Kosler, J., 2001, Laser-ablation ICPMS study of metamorphic minerals and processes, in Sylvester, P. J., ed., *Laser-ablation-ICPMS in the earth sciences; principles and applications* Mineralogical Association of Canada Short Course Handbook, Volume 29, p. 185-202.
- Lang, J. R., Stanley, C. R., Thompson, J. F. H., and Dunne, K. P. E., 1995, Na-K-Ca magmatic-hydrothermal alteration in alkalic porphyry Cu-Au deposits: *British Columbia: Mineralogical Association of Canada Short Course*, v. 23, p. 339–366.
- Lang, J. R., and Titley, S. R., 1998, Isotopic and geochemical characteristics of Laramide magmatic system in Arizona and implication for the genesis of porphyry copper deposits: *Economic Geology*, v. 93, p. 138–170.
- Laughlin, A., Damon, P. E., and Watson, B., 1968, Potassium-argon dates from Toquepala and Michiquillay, Peru: *Economic Geology*, v. 63, no. 2, p. 166-168.
- Li, Y., Selby, D., Condon, D., and Tapster, S., 2017, Cyclic magmatic-hydrothermal evolution in porphyry systems: high-precision U-Pb and Re-Os geochronology constraints on the Tibetan Qulong porphyry Cu-Mo deposit: *Economic Geology*, v. 112, no. 6, p. 1419-1440.

- Lindsay, D. D., Zentilli, M., and Rojas de la Rivera, J., 1995, Evolution of an active ductile to brittle shear system controlling mineralization at the Chuquicamata porphyry copper deposit, northern Chile: *International Geology Review*, v. 37, p. 945–958.
- Liu, Y. S., Hu, Z. C., Zong, K. Q., Gao, C. G., Gao, S. X., and Chen, J. H., 2010, Reappraisal and refinement of zircon U–Pb isotope and trace element analyses by LA-ICP-MS: *Chinese Science Bulletin*, v. 55, p. 1535-1546.
- Llosa, F., and Veliz, J., 2000, Geología, alteración y mineralización de los pórfidos de Au-Cu de Minas Conga, norte del Perú (Cajamarca), [ext. abs.]: Sociedad Geológica del Perú, X Congreso Peruano de Geología, Volumen de Resúmenes Extendidos, tomo 3, p. 1178-1194.
- Llosa, F., Lescuyer, J. L., and Milesi, J. P., 1996, Minas Conga: descubrimiento, exploración y marco geológico de los pórfidos Au-Cu en la región de Cajamarca: Segundo Simposio Internacional del Oro, Comité Aurífero, Sociedad Nacional de Minería y Petróleo, Lima, p. 275-283.
- Longo, A. A., Dilles, J. H., Grunder, A. L., and Duncan, R., 2010, Evolution of calc-alkaline volcanism and associated hydrothermal gold deposits at Yanacocha, Peru: *Economic Geology*, v. 105, no. 7, p. 1191-1241.
- Longo, A. A., 2005, Evolution of volcanism and hydrothermal activity in the Yanacocha mining district, northern Perú [Unpublished Ph.D. dissertation]: Corvallis, Oregon State University, 469 p.
- Longridge, J., 2016, Evolution of hydrothermal alteration facies at the Cerro Corona Cu-Au porphyry deposit, Northern Peru [PhD thesis]: Imperial College London, London, 329 p.
- Lonsdale, P., 2005, Creation of the Cocos and Nazca plates by fission of the Farallon plate: *Tectonophysics*, v. 404, no. 3, p. 237-264.
- Losada-Calderdn, A. J., and McPhail, D. C., 1996, Porphyry and high-sulfidation epithermal mineralization in the Nevados de Famatina mining district, Argentina, in F. Camus, R. H. S. a. R. P., Society of Economic Geologists, Special Publication, 5, ed., Andean Copper Deposits: New Discoveries Mineralization Styles and Metallogeny, p. 91-117.
- Lovera, O. M., Grove, M., Mark Harrison, T., and Mahon, K. I., 1997, Systematic analysis of K-feldspar  $^{40}\text{Ar}/^{39}\text{Ar}$  step heating results: I. Significance of activation energy determinations: *Geochimica et Cosmochimica Acta*, v. 61, no. 15, p. 3171-3192.
- Lowell, J. D., and Guilbert, J. M., 1970, Lateral and vertical alteration-mineralization zoning in porphyry ore deposits: *Economic Geology*, v. 65, no. 4, p. 373-408.
- Ludwig, K. R., 2001, User's manual for Isoplot/ex Version 2.49. A Geochronological Toolkit for Microsoft Excel: Berkeley Geochronological Center: Special Publication 1a, Berkeley, USA.
- Macfarlane, A. W., Prol-Ledesma, R.-M., and Conrad, M. E., 1994, Isotope and fluid inclusion studies of geological and hydrothermal processes, northern Peru: *International Geology Review*, v. 36, p. 645-677.
- Madera, A., and Rohrlach, B., 1998, Geology and resource potential of the Tampakan copper deposit, southern Mindanao: in 11th Annual GSP Geological Convention (Geological Society of the Philippines: Manila), v. Manuscripts, p. 220-231.
- Maksaev, V., Munizaga, F., McWilliams, M., Fanning, M., Mathur, R., Ruiz, J., and Zentilli, M., 2004, New chronology for El Teniente, Chilean Andes, from U-Pb,  $^{40}\text{Ar}/^{39}\text{Ar}$ , Re-Os, and fission track dating: Implications for the evolution of a supergiant porphyry Cu-Mo deposit: *Society of Economic Geologists Special Publication 11*, p. 15–54.
- Marsh, T. M., Einaudi, M. T., and McWilliams, M., 1997,  $^{40}\text{Ar}/^{39}\text{Ar}$  geochronology of Cu-Au and Au-Ag mineralization in the Potrerillos District, Chile: *Economic Geology*, v. 92, no. 7-8, p. 784-806.
- Masterman, G. J., Cooke, D. R., Berry, R. F., Walshe, J. L., Lee, A. W., and Clark, A. H., 2005, Fluid chemistry, structural setting, and emplacement history of the Rosario Cu-Mo porphyry and Cu-Ag-Au epithermal veins, Collahuasi district, northern Chile: *Economic Geology*, v. 100, no. 5, p. 835-862.
- McClay, K., 1991, *The Mapping of Geological Structures*, J. Wiley and Sons Ltd., England, 168 p.
- McDougall, I., and Harrison, T.M., 1999, *Geochronology and Thermochronology by the  $^{40}\text{Ar}/^{39}\text{Ar}$  Method*, Oxford University Press, New York, 269 p.:
- Meffre, S., Large, R. R., Scott, R., Woodhead, J., Chang, Z., Gilbert, S. E., Danyushevsky, L. V., Maslennikov, V., and Hergt, J. M., 2008, Age and pyrite Pb-isotopic composition of the giant Sukhoi Log sediment-hosted gold deposit, Russia: *Geochimica et Cosmochimica Acta*, v. 72, p. 2377-2391.
- Mégard, F., 1984, The Andean orogenic period and its major structures in central and northern Peru: *Journal of the Geological Society*, v. 141, no. 5, p. 893-900.
- Mercer, C. N., Reed, M. H., and Mercer, C. M., 2015, Time scales of porphyry Cu deposit formation: Insights from titanium diffusion in quartz: *Economic Geology*, v. 110, no. 3, p. 587-602.

- Meyer, C., and Hemley, J. J., 1967, Wall rock alteration, *in* Barnes, H. L., ed., *Geochemistry of hydrothermal ore deposits*, New York, Holt, Rinehart, and Winston, p. 166–123.
- Meyer, C., 1981, Ore-forming processes in geologic history: *Economic Geology 75th Anniversary Volume*, p. 6-41.
- Montgomery, A. T., 2012, Metallogenetic controls on Miocene high sulphidation epithermal gold mineralization, Alto Chicama district, La Libertad, Northern Peru. [Unpublished Ph.D. dissertation]: Queen's University, Kingston, 382 p.
- Montoya, J. W., and Hemley, J. J., 1975, Activity relations and stabilities in alkali feldspar and mica alteration reactions: *Economic Geology*, v. 70, p. 577–583.
- Montoya, D. E., Noble, D. C., Eyzaguirre, V. R., and DesRosiers, D. F., 1995, Sandstone-hosted gold deposits: A new exploration target is recognized in Peru: *Engineering and Mining Journal*, v. 196, no. 6, p. 34-41.
- Montoya, D., 1999, Yacimiento aurífero Santa Rosa, [abs.]: *Primer Congreso Internacional de Prospectores y Exploradores, Lima 1999*, Instituto de Ingeniero de Minas del Perú, p. 93-99.
- Mpodozis, C., Cornejo, P., Kay, S. M., and Tittler, A., 1995, La Franja de Maricunga: Síntesis de la evolución del Frente Volcánico Oligoceno-Mioceno de la zona sur de los Andes Centrales: *Andean Geology*, v. 22, no. 2, p. 273-313.
- Muntean, J. L., and Einaudi, M. T., 2000, Porphyry gold deposits of the Refugio district, Maricunga belt, northern Chile: *Economic Geology* v. 95, no. 7, p. 1445-1472.
- Muntean, J. L., and Einaudi, M. T., 2001, Porphyry-epithermal transition: Maricunga belt, northern Chile: *Economic Geology*, v. 96, no. 4, p. 743-772.
- Murakami, H., Seo, J. H., and Heinrich, C. A., 2010, The relation between Cu/Au ratio and formation depth of porphyry-style Cu–Au±Mo deposits: *Mineralium Deposita*, v. 45, no. 1, p. 11-21.
- Navarro, J.P., Bodin, S., Heimhofer, U., and Immenhauser, A., 2015, Record of Albian to early Cenomanian environmental perturbation in the eastern sub-equatorial Pacific: *Palaeogeography, Palaeoclimatology, Palaeoecology*, v. 423, p. 122-137.
- Navarro, P. A., 2007, Características metalogénicas de los yacimientos asociados al Grupo Calipuy en el norte del Perú, departamentos de la Libertad y Ancash: *Boletín de la Sociedad Geológica del Perú*, v. 102, p. 1-29.
- Noble, D., and McKee, E., 1999, The Miocene metallogenic belt of central and northern Peru: *Geology and ore deposits of the central Andes*, v. 7, p. 155-193.
- Noble, D. C., McKEE, E. H., Mourier, T., and Mégard, F., 1990, Cenozoic stratigraphy, magmatic activity, compressive deformation, and uplift in northern Peru: *Geological Society of America Bulletin*, v. 102, no. 8, p. 1105-1113.
- Noble, D., Vidal, C., Perelló, J., and Rodríguez, O., 2004, Space-time relationships of some porphyry Cu–Au, epithermal Au, and other magmatic-related mineral deposits in northern Perú: *Society of Economic Geology*, p. 313-318.
- Noble, D., Vidal, C. E., Miranda, M., Amaya, W., and McCormack, J. K., 2011, Ovoidal- and mottled-textured rock and associated silica veinlets and their formation by high-temperature outgassing of subjacent magma: *in* Steininger, R., and Pennell, B., eds., *Proceedings, Geological Society of Nevada 2010 Symposium Great Basin Evolution and Metallogeny*, p. 795-811.
- Noble, D., 1991, Reconnaissance observations on the geology and gold potential of the Sinchao-Tantahuatay area, Hualgayoc district, northern Peru: Unpublished report: Prepared for Compañía Buenaventura S.A., 6 p.
- Norton, D., and Cathles, L. M., 1979, Thermal Aspects of Ore Deposition, *in* Barnes, H. L., ed., *Geochemistry of hydrothermal ore deposits, Volume 2*: New York, Holt, Rinehart, and Winston, p. 611-631.
- Oyarzun, R., Márquez, A., Lillo, J., López, I., and Rivera, S., 2001, Giant versus small porphyry copper deposits of Cenozoic age in northern Chile: adakitic versus normal calc-alkaline magmatism: *Mineralium deposita*, v. 36, no. 8, p. 794-798.
- Pardo-Casas, F., and Molnar, P., 1987, Relative motion of the Nazca (Farallon) and South American plates since Late Cretaceous time: *Tectonics*, v. 6, no. 3, p. 233-248.
- Parsons, A. B., 1925, The Tintic Standard mine: *New York: Engineering and Mining Journal-Press*, v. 120, no. 17, p. 645-652.
- Paton, C., Woodhead, J. D., Hellstrom, J. C., Hergt, J. M., Greig, A., and Maas, R., 2010, Improved laser ablation U-Pb zircon geochronology through robust down-hole fractionation correction: *Geochemistry, Geophysics, Geosystems*, v. 11, p. 1525-2027.

- Peccerillo, A., and Taylor, S. R., 1976, Geochemistry of Eocene calc-alkaline volcanic rocks from the Kastamonu area, Northern Turkey: *Contributions to Mineralogy and Petrology*, v. 58, no. 1, p. 63-81.
- Perelló, J., Posso, H., Zárate, A., Neyra, C., Caballero, A., and Stein, H., 2003, Syntectonic Ag-rich Porphyry Copper Mineralization at Pachagón, Northern Peru, [abst.]: Universidad de Concepción, X Congreso Geológico Chileno, CD-ROM, 1 p.
- Perelló, J., Cox, D., Garamjav, D., Sanjdorj, S., Diakov, S., Schissel, D., Munkhbat, T.-O., and Oyun, G., 2001, Oyu Tolgoi, Mongolia: siluro-devonian porphyry Cu-Au-(Mo) and high-sulfidation Cu mineralization with a cretaceous chalcocite blanket: *Economic Geology*, v. 96, no. 6, p. 1407-1428.
- Phillips, W. J., 1973, Mechanical effects of retrograde boiling and its probable importance in the formation of some porphyry ore deposits: *Transactions of the Institute of Mining and Metallurgy*, v. 82, p. B90-98.
- Pinto, R., 2002, Transición de un sistema de alta sulfuración a un sistema porfírico de alto nivel en Kupfertal Distrito Minero de Yanacocha, Cajamarca, Perú [Unpublished Geologist Engineer. dissertation]: Universidad Nacional Mayor de San Marcos, Lima, 89 p.
- Quirita, V., and Gauthier, A., 2000, Yacimientos de Oro en la "Región Huamachuco", Norte del Perú, Sociedad Nacional de Minería, Petróleo y Energía, Perú, IV Simposio Internacional del Oro, 9 p.
- Ramos, V. A., and Aleman, A., 2000, Tectonic evolution of the Andes, (Cordani, U.G.; Milani, E.J.; Thomaz Filho, A.; Campos, D.A; editors). *In Tectonic Evolution of South America. International Geological Congress, No. 31, Special Publication: 635-685. Rio de Janeiro.*
- Redwood, S. D., Heather, K. B., Gamarra, H. B., and Mamani, C., 2017, The AntaKori Cu-Au-Ag Skarn Project, Cajamarca, Northern Peru, [abs.]: Décimo Congreso Internacional de Prospectores y Exploradores, Lima 2017, Instituto de Ingeniero de Minas del Perú. 4 p.
- Reyes, L., 1980, Geología de los Cuadrángulos de Cajamarca, San Marcos y Cajabamba (Hojas 15-f, 15-g, 15-h), Instituto Geológico Minero y Metalúrgico. Lima, Perú: Boletín Serie A: Carta Geologica Nacional, no. 31.
- Richards, J. P., and Kerrich, R., 2007, Special paper: adakite-like rocks: their diverse origins and questionable role in metallogenesis: *Economic geology*, v. 102, no. 4, p. 537-576.
- Richards, J., and Noble, S. R., 1998, Application of radiogenic isotope systems to the timing and origin of hydrothermal systems: *Reviews in Economic Geology*, v. 10, p. 195-233.
- Richards, J. P., Wilkinson, D., and Ullrich, T., 2006, Geology of the Sari Gunay epithermal gold deposit, northwest Iran: *Economic Geology*, v. 101, no. 8, p. 1455-1496.
- Richards, J., 2003, Tectono-magmatic precursors for porphyry Cu-(Mo-Au) deposit formation: *Economic Geology*, v. 98, no. 8, p. 1515-1533.
- 2009, Postsubduction porphyry Cu-Au and epithermal Au deposits: Products of remelting of subduction-modified lithosphere: *Geology*, v. 37, no. 3, p. 247-250.
- 2011, High Sr/Y arc magmas and porphyry Cu±Mo±Au deposits: just add water: *Economic Geology*, v. 106, no. 7, p. 1075-1081.
- 2013, Giant ore deposits formed by optimal alignments and combinations of geological processes: *Nature geoscience*, v. 6, no. 11, p. 911.
- 2018, A shake-up in the porphyry world?: *Economic Geology*, v. 113, no. 6, p. 1225-1233.
- Rivera, M., Monge, R., and Navarro, P. A., 2005, Nuevos datos sobre el Volcanismo Cenozoico (Grupo Calipuy) en el Norte del Perú: Departamentos de La Libertad y Ancash: *Boletín Sociedad Geológica del Perú*, v. 99, p. 7-21.
- Robert, E., and Bulot, L. G., 2004, Origin, phylogeny, faunal composition, and stratigraphical significance of the Albian engonoceratidae (pulchelliaceae, ammonitina) of Peru: *Journal of South American Earth Sciences* v. 17, no. 1, p. 11–23.
- Robert, E., Latil, J. L., and Bulot, L. G., 2009, Albian ammonite faunas from South America: the genus *Tegoceras hyatt*, 1903 *Revue de Paleobiologie*, v. 28, no. 1, p. 43–51.
- Rolim, D. R., 2005, Estudo geocronológico das rochas vulcânicas do Grupo Calipuy, Região Noroeste do Peru. [Unpublished MSc dissertation]: Instituto de Geociências da Universidade de São Paulo, 40 p.
- Rye, R. O., 1993, The Evolution of Magmatic Fluids in the Epithermal Environment - the Stable Isotope Perspective: *Economic Geology and the Bulletin of the Society of Economic Geologists*, v. 88, no. 3, p. 733-753.
- Sandeman, H. A., Clark, A. H., and Farrar, E., 1995, An integrated tectono-magmatic model for the evolution of the southern Peruvian Andes (13-20 S) since 55 Ma: *International Geology Review*, v. 37, no. 12, p. 1039-1073.



- Sangay, I., Vivas, J., Pérez, J., Gordillo, R., and García, W., 2017, La Arena, ¿transición o sobreimposición entre el pórfido Cu-Au(Mo) y el epitermal alta sulfuración Au?, correlación estructural con otros Yacimientos hospedados en rocas sedimentarias, norte del Perú, [abs.]: Décimo Congreso Internacional de Prospectores y Exploradores, Lima 2017, Instituto de Ingeniero de Minas del Perú, p. 74-78.
- Sawkins, F. J., 1984, Metal deposits in relation to Plate Tectonics, Berlin, Springer-Verlag.
- Scherrenberg, A. F., Kohn, B. P., Holcombe, R. J., and Rosenbaum, G., 2016, Thermotectonic history of the Marañon Fold-Thrust Belt, Peru: Insights into mineralisation in an evolving orogen: *Tectonophysics*, v. 667, p. 16-36.
- Sévrier, M., and Soler, P., 1991, Tectonics and magmatism in the Peruvian Andes from late Oligocene time to the present: *Geological Society of America Special Papers*, v. 265, p. 259-278.
- Sévrier, M., Mercier, J. L., Macharé, J., Bonnot, D., Cabrera, J., and Blanc, J. L., 1988, The state of stress in an overriding plate situated above a flat slab: The Andes of central Peru: *Tectonics*, v. 7, no. 4, p. 895-928.
- Seedorf, E., Dilles, J. H., Proffett, J. M., Einaudi, M. T., Zurcher, L., Stavast, W. J. A., Johnson, D. A., and Barton, M. D., 2005, Porphyry deposits: Characteristics and origin of hypogene features: *Economic Geology 100th Anniversary Volume*, p. 251-298.
- Shinohara, H., and Hedenquist, J., 1997, Constraints on magma degassing beneath the Far Southeast porphyry Cu-Au deposit, Philippines: *Journal of Petrology*, v. 38, no. 12, p. 1741-1752.
- Shirey, S. B., and Walker, R. J., 1995, Carius tube digestion for low-blank rhenium-osmium analysis: *Analytical Chemistry*, v. 67, p. 2136-2141.
- Sillitoe, R. H., and Gappe, I. M., Jr., 1984, Philippine porphyry copper deposits: Geologic setting and characteristics, United Nations Economic Social Commission Asia-Pacific, Committee for Coordination of Joint Prospecting for Mineral Resources in Asian Offshore Areas, Technical Publication 14, p. 89.
- Sillitoe, R. H., Marquardt, J. C., Ramírez, F., Becerra, H., and Gómez, M., 1996, Geology of the concealed MM porphyry copper deposit, Chuquicamata district, northern Chile: *Society of Economic Geologists Special Publication 5*, p. 59-70.
- Sillitoe, R. H., Steele, G. B., Thompson, J. F. H., and Lang, J. R., 1998, Advanced argillic lithocaps in the Bolivian tin-silver belt: *Mineralium Deposita*, v. 33, no. 6, p. 539-546.
- Sillitoe, R. H., and Hedenquist, J. W., 2003, Linkages between volcanotectonic settings, ore-fluid compositions, and epithermal precious metal deposits: *Special Publication-Society of Economic Geologists*, v. 10, p. 315-343.
- Sillitoe, R. H., and Mortensen, J. K., 2010, Longevity of porphyry copper formation at Quellaveco, Peru: *Economic Geology*, v. 105, no. 6, p. 1157-1162.
- Sillitoe, R. H., and Perelló, J., 2005, Andean copper province: Tectonomagmatic settings, deposit types, metallogeny, exploration, and discovery: *Economic Geology 100th Anniversary Volume*, p. 845-890.
- Sillitoe, R. H., Tolman, J., and Van Kerkvoort, G., 2013, Geology of the Caspiche porphyry gold-copper deposit, Maricunga belt, northern Chile: *Economic Geology*, v. 108, no. 4, p. 585-604.
- 1972, A plate tectonic model for the origin of porphyry copper deposits: *Economic geology*, v. 67, no. 2, p. 184-197.
- 1973, The tops and bottoms of porphyry copper deposits: *Economic Geology*, v. 68, no. 6, p. 799-815.
- 1979, Some thoughts on gold-rich porphyry copper deposits: *Mineralium Deposita*, v. 14, no. 2, p. 161-174.
- 1983, Enargite-bearing massive sulfide deposits high in porphyry copper systems: *Economic Geology*, v. 78, no. 2, p. 348-352.
- 1985, Ore-related breccias in volcanoplutonic arcs: *Economic Geology*, v. 80, no. 6, p. 1467-1514.
- 1988, Epochs of intrusion-related copper mineralization in the Andes: *Journal of South American Earth Sciences*, v. 1, no. 1, p. 89-108.
- 1989, Gold deposits in Western Pacific island arcs: The magmatic connection: *Economic Geology Monograph 6*, p. 274-291.
- 1994, Erosion and collapse of volcanoes: Causes of telescoping in intrusion-centered ore deposits: *Geology*, v. 22, no. 10, p. 945-948.
- 1995, Exploration and discovery of base- and precious-metal deposits in the Circum-Pacific region during the last 25 years: *Resource Geology Special*, no. 19, p. 119.
- 1997, Characteristics and controls of the largest porphyry copper-gold and epithermal gold deposits in the circum-Pacific region: *Australian Journal of Earth Sciences*, v. 44, no. 3, p. 373-388.

- 1998, Major regional factors favouring large size, high hypogene grade, elevated gold content and supergene oxidation and enrichment of porphyry copper deposits: *Porphyry and Hydrothermal Copper and Gold Deposits—a global perspective*: Perth, p. 49-60.
- 1999, Styles of high-sulphidation gold, silver and copper mineralisation in porphyry and epithermal environments, in *PACRIM '99*, A. I. o. M. a. M. C., Bali, Indonesia, 10–13 October 1999, Proceedings, ed., p. 29–44.
- 2000, Gold-rich porphyry deposits: descriptive and genetic models and their role in exploration and discovery: *Reviews in Economic Geology*, v. 13, p. 315-345.
- 2002, Some metallogenic features of gold and copper deposits related to alkaline rocks and consequences for exploration: *Mineralium Deposita*, v. 37, no. 1, p. 4-13.
- 2003, Iron oxide-copper-gold deposits: an Andean view: *Mineralium Deposita*, v. 38, no. 7, p. 787-812.
- 2005, Supergene oxidized and enriched porphyry copper and related deposits: *Econ. Geol.*, v. 100, p. 723-768.
- 2008, Special paper: major gold deposits and belts of the North and South American Cordillera: distribution, tectonomagmatic settings, and metallogenic considerations: *Economic Geology*, v. 103, no. 4, p. 663-687.
- 2010, Porphyry copper systems: *Economic geology*, v. 105, no. 1, p. 3-41.
- Simmons, A. T., Tosdal, R. M., Wooden, J. L., Mattos, R., Concha, O., McCracken, S., and Beale, T., 2013, Punctuated magmatism associated with porphyry Cu-Mo formation in the Paleocene to Eocene of southern Peru: *Economic Geology*, v. 108, no. 4, p. 625-639.
- Skarmeta, J., McKlay, K., and Bertens, A., Structural controls on porphyry Copper deposits in northern Chile: new models and implications for Cu-Mo mineralization on subduction orogens, in *Proceedings Congreso Geológico Chileno 2003*.
- Smoliar, M. I., Walker, R. J., and Morgan, J. W., 1996, Re-Os ages of group IIA, IIIA, IVA, and IVB iron meteorites: *Science*, v. 271, p. 1099-1102.
- Snee, L. W., Sutter, J. F., and Kelly, W. C., 1988, Thermochronology of economic mineral deposits; dating the stages of mineralization at Panasqueira, Portugal, by high-precision  $^{40}Ar / ^{39}Ar$  age spectrum techniques on muscovite: *Economic Geology*, v. 83, no. 2, p. 335-354.
- Somoza, R., 1998, Updated Nazca (Farallon)—South America relative motions during the last 40 My: implications for mountain building in the central Andean region: *Journal of South American Earth Sciences*, v. 11, no. 3, p. 211-215.
- Spencer, E. T., Wilkinson, J. J., Creaser, R. A., and Seguel, J., 2015, The Distribution and Timing of Molybdenite Mineralization at the El Teniente Cu-Mo Porphyry Deposit, Chile: *Economic Geology*, v. 110, no. 2, p. 387-421.
- Stappenbeck, R., 1929, *Geologie des Chicamatales in Nordperu und seiner Anthrazitlagenstaetten: Geologie und Palaeontologie Abhandl. N. F. 16, H. 14.*
- Stein, H. J., Markey, R. J., Morgan, J. W., Hannah, J. L., and Scherstén, A., 2001, The remarkable Re–Os chronometer in molybdenite: how and why it works: *Terra Nova*, v. 13, no. 6, p. 479-486.
- Stein, H., Sundblad, K., Markey, R., Morgan, J., and Motuza, G., 1998, Re-Os ages for Archean molybdenite and pyrite, Kuittila-Kivisuo, Finland and Proterozoic molybdenite, Kabeliai, Lithuania: Testing the chronometer in a metamorphic and metasomatic setting: *Mineralium Deposita*, v. 33, no. 4, p. 329-345.
- Stein, H. J., 2006, Low-rhenium molybdenite by metamorphism in northern Sweden: Recognition, genesis, and global implications: *Lithos*, v. 87, no. 3, p. 300-327.
- Stein, H., 2014, *13.4 Dating and Tracing the History of Ore Formation: Treatise on Geochemistry (second edition)*. Oxford, Elsevier, p. 87-118.
- Steinmann, G., 1929, *Geologie von Perú: Heidelberg, Carl Winterss Universitats Buch Handlung*, p. 448.
- Stern, C. R., and Skewes, M. A., 2005, Origin of giant Miocene and Pliocene Cu-Mo deposits in central Chile: Role of ridge subduction, decreased subduction angle, subduction erosion, crustal thickening and long-lived, batholith sized, open-system magma chambers: *Porter Geoconsultancy Publishing, de Adelaide, Australia*, v. 1, p. 65-82.
- Stoffregen, R., 1987, Genesis of acid-sulfate alteration and Au-Cu-Ag mineralization at Summitville, Colorado: *Economic Geology*, v. 82, p. 1575-1591.
- Streckeisen, A., 1974, Classification and nomenclature of plutonic rocks recommendations of the IUGS subcommission on the systematics of igneous rocks: *Geologische Rundschau*, v. 63, no. 2, p. 773-786.

- Sun, W., Huang, R. F., Li, H., Hu, Y. B., Zhang, C. C., Sun, S. J., Zhang, L. P., Ding, X., Li, C. Y., and Zartman, R. E., 2015, Porphyry deposits and oxidized magmas: *Ore Geology Reviews*, v. 65, p. 97-131.
- Suzuki, K., Shimizu, H., and Masuda, A., 1996, Re-Os dating of molybdenites from ore deposits in Japan: Implication for the closure temperature of the Re-Os system for molybdenite and the cooling history of molybdenum ore deposits *Geochimica et Cosmochimica Acta*, v. 60, p. 3151-3159.
- Tahoe Resources Inc. Annual Report, 2018, <https://www.tahoeresources.com>. Accessed 20 February 2019
- Tera, F., and Wasserburg, G. J., 1972, U-Th-Pb systematics in three Apollo 14 basalts and the problem of initial Pb in lunar rocks: *Earth and Planetary Science Letters*, v. 14, no. 3, p. 281-304.
- Thorpe, R. S., and Francis, P. W., 1979, Petrogenetic relationships of volcanic and intrusive rocks of the Andes: in Atherton, M., and Tarney, J., eds., *Origin of granite Batholiths Geochemical evidence: British Library Cataloguing*, p. 65-75.
- Thorpe, R., 1984, The tectonic setting of active Andean volcanism, in R.S. Hamon, et al., (eds) *Andean magmatism*. London, Wiley, p. 4-8.
- Titley, S. R., and Beane, R. E., 1981, Porphyry copper deposits: *Economic Geology 75th Anniversary Volume*, p. 214-269.
- Titley, S. R., 1993, Characteristics of porphyry copper occurrence in the American Southwest: *Geological Association of Canada Special Paper 40*, p. 433-464.
- Titley, S. R., 1966, *Geology of the porphyry copper deposits: southwestern North America*: Tucson, University of Arizona Press, 287 p.
- Tosdal, R. M., and Richards, J. P., 2001, Magmatic and Structural Controls on the Development of Porphyry Cu ± Mo ± Au Deposits, in Richards, J. P., and Tosdal, R. M., eds., *Structural Controls on Ore Genesis, Volume 14, Society of Economic Geologists*, p. 157-181.
- Tosdal, R., 1996, Geologic and structural setting of the Tantauatay volcanic field and associated high-sulfidation Cu-Au mineralization, Northern Peru: Unpublished report: Prepared for Cía. Minas Buenaventura S.A. 56 p.
- Tsang, D. P. W., Wallis, S. R., Yamamoto, K., Takeuchi, M., Hidaka, H., Hori, K., and Tattitch, B. C., 2018, Zircon U-Pb geochronology and geochemistry of the Cerro Colorado porphyry copper deposit, northern Chile: *Ore Geology Reviews*, v. 93, p. 114-140.
- Ulrich, T., and Heinrich, C. A., 2001, Geology and alteration geochemistry of the porphyry Cu-Au deposit at Bajo de la Alumbrera, Argentina: *Economic Geology*, v. 96, no. 8, p. 1719-1742.
- Uyeda, S., and Nishiwaki, C., 1980, Stress field, metallogenesis, and mode of subduction in Strangway, D.W., ed., *The continental crust and its mineral deposits: Geological Society of Canada Special Publication 20*, p. 323-340.
- Valdivia, V., Toro, J. C., Mamani, M., and Terán, J. C., 2014, Chipispaya: Pórfido Cu-Au del Mioceno Inferior en el sur de Perú, [ext. abs.]: *Sociedad Geológica del Perú, XVII Congreso Peruano de Geología, Volumen de Resúmenes Extendidos, CD-ROM*, 4 p.
- Valdivia, V., Mamani, M., Toro, J. C., and Terán, J. C., 2015, Aplicación de la geocronología y litogeoquímica a la exploración de pórfidos en el Paleoceno, [abs.]: *Noveno Congreso Internacional de Prospectores y Exploradores, Lima 2015, Instituto de Ingeniero de Minas del Perú*.
- Vallance, J., Balboa, M., Berna, B., Cabrera, O., Baya, C., Baby, P., and Pokrovski, G. S., 2018, Oro y material orgánico en el depósito de Shahuindo (Cajamarca, Peru), [ext. abs.]: *Sociedad Geológica del Perú, XIX Congreso Peruano de Geología, Volumen de Resúmenes Extendidos, CD-ROM*, 4 p.
- Vila, T., and Sillitoe, R. H., 1991, Gold-rich porphyry systems in the Maricunga belt, northern Chile: *Economic Geology*, v. 86, no. 6, p. 1238-1260.
- Vila, T., Sillitoe, R. H., Betzhold, J., and Viteri, E., 1991, The porphyry gold deposit at Marte, northern Chile: *Economic Geology*, v. 86, no. 6, p. 1271-1286.
- von Quadt, A., Peytcheva, I., Kamenov, B., Fanger, L., Heinrich, C. A., and Frank, M., 2002, The Elatsite porphyry copper deposit in the Panagyurishte ore district, Srednagorie zone, Bulgaria: U-Pb zircon geochronology and isotope-geochemical investigations of magmatism and ore genesis, 119-135 p.:
- von Quadt, A., Erni, M., Martinek, K., Moll, M., Peytcheva, I., and Heinrich, C. A., 2011, Zircon crystallization and the lifetimes of ore-forming magmatic-hydrothermal systems: *Geology*, v. 39, no. 8, p. 731-734.
- Wallace, A. B., 1979, Possible signatures of buried porphyrycopper deposits in middle to late Tertiary volcanic rocks of western Nevada, in Ridge, J. D., ed., ed., *Papers on mineral deposits of western North-Amrica-proceedings the fifth quadrennial symposium of the International Association of the Genesis of Ore Deposits: Nevada Bureau of Mines, Report 33*, p. 69-76.

- Wang, S. S., 1983, Age determinations of  $^{40}\text{Ar}/^{40}\text{K}$ ,  $^{40}\text{Ar}/^{39}\text{Ar}$  and radiogenic  $^{40}\text{Ar}$  released characteristics on K–Ar geostandards of China: *Scientia Geologica Sinica*, v. 4, p. 315–323 (in Chinese, with English abstract).
- Weis, P., Driesner, T., and Heinrich, C. A., 2012, Porphyry-Copper Ore Shells Form at Stable Pressure-Temperature Fronts Within Dynamic Fluid Plumes: *Science*, v. 338, no. 6114, p. 1613.
- Wiedenbeck, M., Alle, P., Corfu, F., Griffin, W. L., Meier, M., Oberli, F., Quadt, A. V., Roddick, J. C., and Spiegel, W., 1995, Three natural zircon standards for U-Th-Pb, Lu-Hf, trace element and REE analyses: *Geostandards Newsletter*, v. 19, p. 1-23.
- Wilkinson, J. J., 2013, Triggers for the formation of porphyry ore deposits in magmatic arcs: *Nature Geoscience*, v. 6, no. 11, p. 917.
- Wilson, J. W. J., Kesler, S. E., Cloke, P. L., and Kelly, W. C., 1980, Fluid inclusion geochemistry of the Granisle and Bell porphyry copper deposits, British Columbia: *Economic Geology*, v. 75, p. 45-61.
- Wilson, P. A., 1975, Potassium-argon age studies in Peru with special reference to the emplacement of the Coastal Batholith [Unpublished Ph.D. dissertation]: Liverpool, England, University of Liverpool, 299 p.
- Winchester, J. A., and Floyd, P. A., 1977, Geochemical discrimination of different magma series and their differentiation products using immobile elements: *Chemical geology*, v. 20, p. 325-343.
- Xie, G., Mao, J., Richards, J. P., Han, Y., and Fu, B., 2019, Distal Au Deposits Associated with Cu-Au Skarn Mineralization in the Fengshan Area, Eastern China: *Economic Geology*, v. 114, no. 1, p. 127-142.
- Zentilli, M., Maksaev, V., Boric, R., and Wilson, J., 2018, Spatial coincidence and similar geochemistry of Late Triassic and Eocene-Oligocene magmatism in the Andes of northern Chile: evidence from the MMH porphyry type Cu-Mo deposit, Chuquicamata District: *International Journal of Earth Sciences*, v. 107, no. 3, p. 1097–1126.

# APPENDIX

APPENDIX 1. Table A1. Chemical Composition of Selected rock Types Related to the La Arena district

Sample no.	Precursor plutons				early porphyries		inter-mineral porphyries		
	La Arena-Calaorco			Alizar	La Arena	Agua Blanca	La Arena-Calaorco		
	LA-D14-008-CD-01 (50.50 m) (1)	CA-10 (2)	CA-25 (3)	AL-01 (4)	LA-D11-001A-07 (369.50 m) (5)	AB-04 (6)	CA-12 (7)	CA-24 (8)	LA-D15-003-A-068 (142.50 m) (9)
<b>SiO<sub>2</sub></b> (wt %)	57	60.17	66.2	57.77	59.11	59.16	57.04	57.06	58.18
<b>Al<sub>2</sub>O<sub>3</sub></b>	17.24	15.35	17.93	17.13	14.74	14.79	17.68	19.66	17.71
<b>Fe<sub>2</sub>O<sub>3</sub></b>	3.56	6.76	6.48	4.67	6.16	3.02	5.59	4.9	6.13
<b>FeO</b>	2.28	0.24	0.12	0.88	1.26	2.86	0.3	0.24	0.26
<b>CaO</b>	6.12	0.2	0.21	0.24	0.069	1.29	0.1	0.082	0.37
<b>MgO</b>	2.29	0.28	0.18	2.92	0.77	1.01	3.09	0.44	0.35
<b>K<sub>2</sub>O</b>	1.81	1.88	1.84	2.46	3.05	6.01	1.07	1.84	1.55
<b>Na<sub>2</sub>O</b>	3.42	0.94	0.86	1.95	0.13	1.53	0.32	0.24	0.37
<b>TiO<sub>2</sub></b>	0.61	0.68	0.66	0.62	0.48	0.41	0.62	0.62	0.58
<b>P<sub>2</sub>O<sub>5</sub></b>	0.23	0.16	0.41	0.11	0.042	0.17	0.027	0.19	0.23
<b>MnO</b>	0.14	0.002	0.003	0.052	0.06	0.006	0.016	0.024	0.011
<b>LOI</b>	5.07	7.27	4.28	6.57	7.76	4.36	9.11	9.53	9.28
<b>Sum</b>	99.77	93.932	99.173	95.372	93.631	94.616	94.963	94.826	95.021
<b>Cu</b> (ppm)	29.1	2160	53.9	120	2070	976	163	252	44.1
<b>Pb</b>	7.1	8.2	187	12.9	11	6.6	5.1	480	17.7
<b>Zn</b>	68.7	8.9	8.8	121	153	17.2	120	4720	195
<b>Cr</b>	6	4.8	3.9	8	4.9	4	6	8.6	3.5
<b>Ni</b>	5.1	6.2	1.1	9.4	5.9	10.6	7.8	5.8	5.1
<b>Co</b>	12.3	16.1	0.08	10.3	22.2	34	14.9	14.8	13.5
<b>Cd</b>	0.038	0.054	0.033	0.54	0.32	0.09	0.43	15	1.3
<b>Li</b>	24	10.5	3	28.8	9.5	12.4	20.2	34.4	18.8
<b>Rb</b>	69.5	67.8	64.4	91.5	90.6	211	57.2	83	73.2
<b>Cs</b>	3.4	2	2.5	3.2	5.2	5.2	5.1	17.5	5.3
<b>W</b>	1	1.2	1.1	0.46	2.3	22.3	0.55	1.2	1.3
<b>Mo</b>	0.97	1.9	2.8	5	25.2	3.5	0.72	1.2	7
<b>As</b>	0.44	5.2	60.31	3.73	12.8	0.98	2.84	36.2	3.14
<b>Sb</b>	0.14	1	9.42	0.99	2.16	0.97	2.32	5.8	1.39
<b>Bi</b>	0.068	1.9	5.85	0.786	0.218	0.57	0.817	3.8	0.244
<b>Sr</b>	504	526	1310	102	29	165	71.3	75.8	45.3
<b>Ba</b>	597	524	613	595	346	807	278	668	332
<b>V</b>	101	78.2	92.1	72.1	62	60.7	84.2	110	62.1
<b>Sc</b>	12.6	13.6	14.5	13.7	8.9	6.5	14.6	16.2	10.1
<b>Nb</b>	7.8	3.7	3.6	4.1	2.3	4.4	3.1	8.6	5.5
<b>Ta</b>	0.44	0.22	0.24	0.26	0.13	0.27	0.19	0.54	0.35
<b>Zr</b>	124.1	140	136.2	118.5	100.6	124.4	135.2	130	136.8
<b>Hf</b>	4.2	4.8	6.2	3.2	2.6	3.3	4	3.5	3.2
<b>Be</b>	0.98	1.4	0.45	0.81	1	0.84	0.9	1.4	1.3
<b>Ga</b>	20.3	19.2	35.3	21.6	11.4	18.4	22.1	28.6	23.6
<b>Sn</b>	1.2	4.8	6.5	2.3	3.4	1.6	3.2	1.4	6.3
<b>In</b>	0.03	0.16	0.18	0.22	0.075	0.014	0.24	3	0.017
<b>Tl</b>	0.23	0.85	1	0.92	0.73	0.72	0.75	1.4	0.62
<b>U</b>	1.3	1.8	1.9	1.4	0.44	1.4	2	2.7	1.7
<b>Th</b>	5.1	6.5	6.5	4.5	4.2	4	5.8	6.3	5.7

APPENDIX 1. Table A1 (cont.)

Sample no.	late-mineral				Early Miocene intrusive bodies				
	La Arena- Calaorco	Yamobamba	Alizar	Agua Blanca	El Carmen			La Florida	
	CA-13 (10)	YA-01 (11)	AL-07 (12)	AB-11 (13)	AB-09 (14)	CAR-09 (15)	CAR-08 dike (16)	CAR-01 (17)	FO-04 (18)
<b>SiO<sub>2</sub></b> (wt %)	59.79	59.69	60.17	63.6	57.27	61.45	67.17	66.22	60.35
<b>Al<sub>2</sub>O<sub>3</sub></b>	17.14	17.61	17.41	17.39	17.64	17.09	15.93	16.32	17.52
<b>Fe<sub>2</sub>O<sub>3</sub></b>	3.14	3.05	3.66	0.79	1.04	0.29	0.71	0.66	0.68
<b>FeO</b>	2.17	2.92	2.06	3.22	4.85	4.51	1.17	1.86	4.68
<b>CaO</b>	3.3	4.99	5.73	5.24	6.82	4.59	2.7	4.13	5.88
<b>MgO</b>	2.81	2.08	2.14	1.39	3.72	1.96	1.26	0.96	2.25
<b>K<sub>2</sub>O</b>	2.33	2.17	1.84	2.59	1.36	2.25	3.99	2.47	1.97
<b>Na<sub>2</sub>O</b>	2.36	4.14	3.69	2.38	3.42	3.07	2.91	3.48	3.28
<b>TiO<sub>2</sub></b>	0.56	0.61	0.6	0.49	0.68	0.5	0.45	0.46	0.57
<b>P<sub>2</sub>O<sub>5</sub></b>	0.22	0.22	0.23	0.2	0.2	0.19	0.16	0.17	0.19
<b>MnO</b>	0.13	0.14	0.14	0.14	0.13	0.25	0.031	0.027	0.12
<b>LOI</b>	5.78	2.18	2.05	2.15	1.7	1.84	2.12	1.59	1.82
<b>Sum</b>	99.73	99.8	99.72	99.58	98.83	97.99	98.601	98.347	99.31
<b>Cu</b> (ppm)	26.4	25.3	23.2	28.5	26.3	20.5	148	169	39.8
<b>Pb</b>	39.4	6.6	6.6	9	6.1	7.5	11	6.8	5
<b>Zn</b>	190	60.7	73.2	108	113	122	239	37.8	82.6
<b>Cr</b>	4.8	4.6	5.3	4.7	53.1	9	4.8	7.2	11.8
<b>Ni</b>	5	5.1	5.1	4.6	21.3	6.6	6.5	5	9.8
<b>Co</b>	10.9	12.3	11.3	8.3	17.6	9.9	12.6	16.6	12.4
<b>Cd</b>	0.92	0.043	0.051	0.059	0.091	0.064	3.7	0.29	0.034
<b>Li</b>	46.5	51.2	12.2	9.6	10.3	13	16.7	12.1	20
<b>Rb</b>	121	84.5	69.6	125	69	125	163	94.7	70.5
<b>Cs</b>	64.1	3.9	1.2	4.9	6.4	14.7	8.7	4.2	4.2
<b>W</b>	0.68	0.54	0.42	1.8	0.77	1.9	1.5	0.7	0.38
<b>Mo</b>	0.4	0.22	0.69	0.42	0.48	1.2	28.4	55.3	1.8
<b>As</b>	0.69	2.68	0.95	2.8	5.2	1.29	2.65	1.12	0.96
<b>Sb</b>	0.2	0.81	0.26	0.5	0.55	0.29	0.52	0.22	0.63
<b>Bi</b>	0.072	0.121	0.062	0.324	0.2	1.08	1.589	0.33	0.073
<b>Sr</b>	374	545	617	366	675	621	514	536	532
<b>Ba</b>	762	741	573	804	611	764	1050	703	699
<b>V</b>	86.8	101	88.5	71.6	148	81.9	71.8	68.8	107
<b>Sc</b>	11.1	11.9	11.7	8.6	18.7	10.2	6.3	5.5	12.1
<b>Nb</b>	8	8.6	8.5	9.7	9.1	9	10	10.3	7.9
<b>Ta</b>	0.5	0.53	0.52	0.66	0.52	0.62	0.66	0.68	0.54
<b>Zr</b>	118	126.4	136.1	137.1	113	129.4	117.3	143.9	129.8
<b>Hf</b>	3.7	4	4.2	3.8	3.6	3.8	4.3	5.1	4.1
<b>Be</b>	1.1	1.1	1.1	1.2	0.96	1.2	1.2	1.5	1.1
<b>Ga</b>	20.4	21.2	20.4	21.1	21.2	20	20.4	22.2	20.7
<b>Sn</b>	1.1	1.9	1.2	3	2.2	4.6	2.4	0.5	1.8
<b>In</b>	0.024	0.029	0.033	0.14	0.082	0.14	0.036	0.0025	0.095
<b>Tl</b>	0.53	0.26	0.19	0.85	0.54	0.9	0.78	0.42	0.36
<b>U</b>	1.7	1.7	1.6	1.6	0.66	1.9	2.6	2.2	2
<b>Th</b>	5.2	5.8	5.3	6.7	3	5.8	4.9	7.2	7.1

APPENDIX2. TABLE A2. LA-ICP-MS Zircon U-Pb Data of Porphyry Intrusions from the La Arena porphyry Cu-Au-(Mo) deposit

Spot Name	ppm Total Pb	ppm 232Th	ppm 238U	232Th /238U	207Pb /206Pb	% ±1σ	207Pb /235U	% ±1σ	206Pb /238U	% ±1σ	rho	aparent ages						
												207Pb /206Pb	Ma ±1σ	207Pb /235U	Ma ±1σ	206Pb /238U	Ma ±1σ	% conc.
<b>Sample LA-D11-001A-06-01 (early porphyry)</b>																		
LA-D11-001A-06-01	13.69	498.56	964.16	0.52	0.140	0.020	0.074	0.010	0.004	0.000	0.281	2,233.03	249.53	72.34	9.91	27.71	1.10	10
LA-D11-001A-06-02	20.53	728.32	1,196.67	0.61	0.114	0.018	0.072	0.013	0.004	0.000	0.233	1,861.12	291.97	70.22	12.63	26.90	1.17	10
LA-D11-001A-06-03	6.65	392.41	653.43	0.60	0.082	0.015	0.033	0.006	0.003	0.000	0.334	1,257.40	351.86	33.05	6.01	21.71	1.34	58
LA-D11-001A-06-04	14.91	1,029.56	1,526.68	0.67	0.065	0.016	0.025	0.004	0.004	0.000	0.258	764.82	531.44	25.55	3.98	25.02	1.02	97
LA-D11-001A-06-05	6.58	404.72	775.84	0.52	0.048	0.011	0.023	0.005	0.004	0.000	0.222	87.13	488.83	23.32	4.47	25.39	1.09	91
LA-D11-001A-06-06	8.82	556.08	935.17	0.59	0.060	0.014	0.028	0.006	0.004	0.000	0.215	616.69	511.99	27.71	5.57	26.58	1.17	95
LA-D11-001A-06-07	7.88	309.69	1,244.85	0.25	0.059	0.010	0.027	0.003	0.004	0.000	0.314	553.74	368.48	26.61	3.17	24.19	0.92	90
LA-D11-001A-06-08	7.84	511.01	985.55	0.52	0.047	0.011	0.025	0.005	0.004	0.000	0.197	57.50	496.24	25.00	5.39	27.10	1.16	91
LA-D11-001A-06-09	16.35	382.91	762.74	0.50	0.199	0.029	0.123	0.018	0.005	0.000	0.325	2,813.89	238.90	117.86	16.45	30.34	1.46	-19
LA-D11-001A-06-10	63.53	515.78	917.12	0.56	0.341	0.035	0.460	0.058	0.008	0.001	0.594	3,666.35	156.48	383.93	40.59	49.31	3.71	-55
LA-D11-001A-06-11	5.27	347.70	694.58	0.50	0.053	0.011	0.025	0.003	0.004	0.000	0.463	338.95	429.58	25.17	2.49	24.32	1.13	96
LA-D11-001A-06-12	14.36	954.24	1,224.31	0.78	0.051	0.008	0.027	0.005	0.004	0.000	0.191	227.85	344.41	26.84	4.53	26.34	0.86	98
LA-D11-001A-06-13	9.36	582.53	890.92	0.65	0.054	0.009	0.028	0.003	0.004	0.000	0.512	366.72	327.74	28.14	2.78	27.09	1.39	96
LA-D11-001A-06-14	8.52	403.89	721.20	0.56	0.061	0.015	0.028	0.005	0.005	0.000	0.256	633.35	466.65	27.57	5.24	29.63	1.46	92
LA-D11-001A-06-15	4.04	186.84	398.24	0.47	0.063	0.021	0.028	0.012	0.004	0.000	0.116	694.46	600.92	27.62	12.02	26.99	1.38	97
LA-D11-001A-06-16	10.21	564.29	1,144.98	0.49	0.062	0.012	0.030	0.005	0.004	0.000	0.240	672.24	414.78	29.87	5.24	27.84	1.19	92
LA-D11-001A-06-17	49.06	312.09	657.75	0.47	0.422	0.044	0.539	0.053	0.008	0.000	0.542	3,987.97	155.99	437.69	34.68	50.83	2.67	-59
LA-D11-001A-06-18	10.29	559.90	1,063.86	0.53	0.051	0.009	0.027	0.004	0.004	0.000	0.254	233.40	364.77	27.54	3.95	27.10	1.00	98
LA-D11-001A-06-19	36.15	361.83	747.44	0.48	0.255	0.031	0.370	0.056	0.007	0.001	0.488	3,216.97	194.45	319.31	41.26	46.19	3.38	-50
LA-D11-001A-06-20	7.18	205.00	451.28	0.45	0.069	0.026	0.028	0.008	0.004	0.000	0.184	922.22	624.08	27.88	8.20	25.73	1.41	91
<b>Sample LA-D14-008-CD-01 (precursor pluton)</b>																		
LA-D14-008-CD-01-01	21.34	1,344.92	2,255.01	0.60	0.057	0.009	0.028	0.004	0.004	0.000	0.216	501.89	347.18	28.24	3.97	25.79	0.79	90
LA-D14-008-CD-01-02	9.57	572.89	1,269.65	0.45	0.049	0.009	0.027	0.004	0.004	0.000	0.295	138.98	370.33	27.48	3.61	27.14	1.06	98
LA-D14-008-CD-01-03	9.12	566.29	1,089.22	0.52	0.054	0.010	0.029	0.005	0.004	0.000	0.239	372.28	359.22	28.87	4.89	27.45	1.13	94
LA-D14-008-CD-01-04	9.90	556.26	1,040.91	0.53	0.055	0.010	0.029	0.004	0.004	0.000	0.316	466.71	322.18	29.09	4.35	26.63	1.28	91
LA-D14-008-CD-01-05	13.03	963.77	1,561.76	0.62	0.056	0.011	0.025	0.004	0.004	0.000	0.255	435.23	398.10	25.31	3.64	26.12	0.97	96
LA-D14-008-CD-01-06	11.52	726.76	1,217.24	0.60	0.053	0.009	0.028	0.004	0.004	0.000	0.278	342.65	336.99	27.94	3.52	26.77	0.95	95
LA-D14-008-CD-01-07	7.14	448.38	908.21	0.49	0.050	0.012	0.028	0.009	0.004	0.000	0.142	209.33	488.83	28.28	8.93	26.35	1.20	92
LA-D14-008-CD-01-08	4.41	240.35	571.05	0.42	0.051	0.013	0.029	0.005	0.004	0.000	0.343	238.96	485.13	29.24	4.61	25.26	1.38	85
LA-D14-008-CD-01-09	21.47	1,572.78	2,488.64	0.63	0.057	0.009	0.027	0.003	0.004	0.000	0.270	475.97	343.48	27.40	3.08	25.97	0.80	94
LA-D14-008-CD-01-10	7.68	482.59	1,054.13	0.46	0.059	0.012	0.028	0.004	0.004	0.000	0.348	583.36	431.28	28.22	3.57	27.04	1.21	95
LA-D14-008-CD-01-11	10.41	677.08	1,479.35	0.46	0.047	0.008	0.022	0.003	0.004	0.000	0.243	42.69	390.69	22.26	3.27	24.42	0.88	90
LA-D14-008-CD-01-12	16.40	1,057.17	1,845.01	0.57	0.050	0.007	0.027	0.003	0.004	0.000	0.299	187.12	312.92	26.61	2.63	26.96	0.80	98
LA-D14-008-CD-01-13	10.85	652.43	1,121.13	0.58	0.047	0.009	0.025	0.004	0.004	0.000	0.221	33.43	409.21	25.01	3.95	26.70	0.94	93
LA-D14-008-CD-01-14	10.35	837.73	1,638.29	0.51	0.061	0.010	0.025	0.004	0.003	0.000	0.251	633.35	370.33	24.77	3.74	22.50	0.86	90
LA-D14-008-CD-01-15	10.07	666.34	1,267.76	0.53	0.051	0.009	0.027	0.003	0.004	0.000	0.378	255.62	342.55	27.16	2.72	26.92	1.03	99
LA-D14-008-CD-01-16	15.65	1,260.26	1,830.07	0.69	0.047	0.008	0.023	0.002	0.004	0.000	0.301	33.43	342.55	22.74	2.43	23.67	0.77	96
LA-D14-008-CD-01-17	10.20	619.14	1,368.80	0.45	0.050	0.009	0.026	0.003	0.004	0.000	0.253	213.04	359.22	25.75	3.44	26.00	0.89	99
LA-D14-008-CD-01-18	12.52	891.57	1,456.62	0.61	0.051	0.008	0.026	0.003	0.004	0.000	0.274	233.40	316.64	26.36	2.83	26.15	0.78	99
LA-D14-008-CD-01-19	10.06	657.76	1,280.38	0.51	0.057	0.010	0.028	0.004	0.004	0.000	0.307	487.08	411.06	28.15	3.76	26.92	1.12	95
LA-D14-008-CD-01-20	13.75	784.38	1,471.37	0.53	0.046	0.008	0.026	0.004	0.004	0.000	0.257	13.06	359.22	26.16	3.53	26.99	0.95	96



APPENDIX2. TABLE A2. (cont.)

Spot Name	ppm Total Pb	ppm 232Th	ppm 238U	232Th /238U	207Pb /206Pb	% ±1σ	207Pb /235U	% ±1σ	206Pb /238U	% ±1σ	rho	aparent ages						
												207Pb /206Pb	Ma ±1σ	207Pb /235U	Ma ±1σ	206Pb /238U	Ma ±1σ	% conc.
<b>Sample LA-D11-003-A-009 (inter-mineral porphyry dike)</b>																		
LA-D15-003-A-009-01	4.79	307.26	615.08	0.500	0.047	0.012	0.023	0.004	0.004	0.000	0.318	31.58	540.68	22.72	3.55	24.56	1.23	92
LA-D15-003-A-009-02	8.31	321.31	636.32	0.505	0.061	0.014	0.028	0.005	0.004	0.000	0.321	638.91	521.10	27.81	4.49	25.78	1.35	92
LA-D15-003-A-009-03	9.43	636.32	1,013.12	0.628	0.059	0.012	0.028	0.003	0.004	0.000	0.351	572.26	462.91	28.23	3.20	26.56	1.07	93
LA-D15-003-A-009-04	9.35	566.58	860.58	0.658	0.053	0.010	0.026	0.003	0.004	0.000	0.316	338.95	388.84	25.64	3.15	26.13	1.02	98
LA-D15-003-A-009-05	6.51	385.00	882.32	0.436	0.077	0.015	0.032	0.004	0.004	0.000	0.345	1,131.49	418.67	32.29	3.85	23.36	0.97	67
LA-D15-003-A-009-06	6.73	386.94	825.26	0.469	0.048	0.009	0.025	0.004	0.004	0.000	0.309	76.02	424.02	25.30	3.57	25.02	1.10	98
LA-D15-003-A-009-07	7.34	486.11	845.00	0.575	0.053	0.011	0.026	0.004	0.004	0.000	0.295	346.35	422.17	26.05	3.59	26.00	1.07	99
LA-D15-003-A-009-08	3.45	206.35	485.80	0.425	0.072	0.023	0.025	0.004	0.004	0.000	0.351	988.89	699.96	24.65	4.01	25.57	1.48	96
LA-D15-003-A-009-09	4.75	300.27	634.56	0.473	0.059	0.016	0.026	0.005	0.004	0.000	0.267	566.70	483.31	25.60	4.46	25.88	1.22	98
LA-D15-003-A-009-10	20.73	1,858.03	1,573.21	1.181	0.060	0.010	0.026	0.003	0.004	0.000	0.321	587.07	387.77	26.35	3.35	25.32	1.04	96
LA-D15-003-A-009-11	7.75	289.24	766.95	0.377	0.057	0.013	0.025	0.005	0.004	0.000	0.196	475.97	442.24	25.41	5.23	25.02	1.02	98
LA-D15-003-A-009-12	6.62	433.62	803.30	0.540	0.050	0.012	0.026	0.004	0.004	0.000	0.291	190.82	485.12	26.02	4.13	24.95	1.17	95
LA-D15-003-A-009-13	5.71	334.12	798.02	0.419	0.072	0.018	0.028	0.003	0.004	0.000	0.391	994.45	537.01	28.14	3.19	25.49	1.14	90
LA-D15-003-A-009-14	7.26	507.94	863.38	0.588	0.059	0.013	0.028	0.005	0.004	0.000	0.232	553.74	435.15	27.59	5.34	25.54	1.16	92
LA-D15-003-A-009-15	5.86	332.96	730.67	0.456	0.059	0.014	0.028	0.006	0.004	0.000	0.199	553.74	451.82	27.65	5.73	27.56	1.15	99
LA-D15-003-A-009-16	17.34	1,434.77	1,633.61	0.878	0.046	0.008	0.025	0.003	0.004	0.000	0.253	20.47	362.92	24.72	3.17	25.10	0.82	98
LA-D15-003-A-009-17	5.02	251.30	648.20	0.388	0.085	0.020	0.033	0.006	0.004	0.000	0.272	1,306.48	471.76	32.88	5.78	23.17	1.13	65
LA-D15-003-A-009-18	7.51	434.10	836.08	0.519	0.064	0.017	0.026	0.003	0.004	0.000	0.382	750.01	578.66	26.36	3.08	25.53	1.15	96
LA-D15-003-A-009-19	6.57	400.58	829.47	0.483	0.052	0.011	0.025	0.002	0.004	0.000	0.491	294.51	433.28	24.58	2.16	25.93	1.13	94
LA-D15-003-A-009-20	3.88	240.72	478.34	0.503	0.052	0.015	0.026	0.006	0.004	0.000	0.220	275.99	555.49	26.03	6.27	26.43	1.41	98
<b>Sample LA-D15-003-A-068 (precursor pluton)</b>																		
LA-D15-003-A-068-01	9.79	731.99	1,212.35	0.604	0.054	0.009	0.028	0.004	0.004	0.000	0.264	368.57	351.81	27.92	3.71	25.16	0.89	89
LA-D15-003-A-068-02	11.66	951.35	1,091.05	0.872	0.051	0.012	0.024	0.005	0.004	0.000	0.185	261.18	466.61	23.91	5.13	26.37	1.06	90
LA-D15-003-A-068-03	5.93	332.69	731.95	0.455	0.059	0.012	0.028	0.003	0.004	0.000	0.446	561.15	448.10	28.19	2.51	26.11	1.05	92
LA-D15-003-A-068-04	11.27	674.69	1,073.03	0.629	0.049	0.011	0.027	0.007	0.004	0.000	0.157	131.57	474.01	27.32	6.52	25.40	0.96	92
LA-D15-003-A-068-05	9.30	546.31	1,109.48	0.492	0.054	0.012	0.025	0.005	0.004	0.000	0.200	372.28	440.69	25.46	5.34	24.97	1.06	98
LA-D15-003-A-068-06	5.38	314.85	592.76	0.531	0.055	0.014	0.029	0.004	0.004	0.000	0.366	394.50	488.84	29.52	4.06	25.70	1.31	86
LA-D15-003-A-068-07	5.78	354.91	718.72	0.494	0.053	0.012	0.028	0.004	0.004	0.000	0.328	342.65	431.12	27.64	4.35	26.65	1.39	96
LA-D15-003-A-068-08	6.82	299.65	631.33	0.475	0.060	0.016	0.026	0.003	0.004	0.000	0.349	611.13	490.72	25.85	3.18	27.17	1.18	95
LA-D15-003-A-068-09	3.72	174.13	486.60	0.358	0.067	0.022	0.026	0.007	0.004	0.000	0.188	833.33	577.78	25.81	7.40	27.36	1.49	94
LA-D15-003-A-068-10	6.02	372.88	822.51	0.453	0.047	0.012	0.025	0.004	0.004	0.000	0.274	57.50	507.35	25.35	4.35	24.89	1.18	98
LA-D15-003-A-068-11	4.77	275.89	631.24	0.437	0.059	0.013	0.025	0.002	0.004	0.000	0.733	588.92	480.51	24.92	1.66	23.09	1.14	92
LA-D15-003-A-068-12	8.55	553.41	1,001.15	0.553	0.049	0.010	0.025	0.004	0.004	0.000	0.279	131.57	440.69	25.46	3.82	26.56	1.12	95
LA-D15-003-A-068-13	9.51	404.50	814.15	0.497	0.132	0.017	0.072	0.008	0.004	0.000	0.393	2,131.48	221.92	70.83	7.11	26.93	1.10	10
LA-D15-003-A-068-14	8.48	620.77	944.09	0.658	0.050	0.010	0.028	0.005	0.004	0.000	0.240	194.53	425.87	28.21	5.07	25.75	1.13	90
LA-D15-003-A-068-15	6.45	307.79	680.90	0.452	0.061	0.015	0.027	0.005	0.004	0.000	0.235	653.72	526.34	27.10	4.88	26.27	1.12	96
LA-D15-003-A-068-16	7.24	360.76	698.75	0.516	0.057	0.013	0.025	0.004	0.004	0.000	0.278	479.67	440.70	24.94	4.14	22.92	1.07	91
LA-D15-003-A-068-17	4.73	291.70	700.08	0.417	0.053	0.014	0.026	0.004	0.004	0.000	0.315	338.95	516.61	25.61	3.75	26.62	1.24	96
LA-D15-003-A-068-18	8.27	406.59	807.26	0.504	0.060	0.012	0.026	0.003	0.004	0.000	0.447	590.77	442.55	25.60	2.54	26.31	1.18	97
LA-D15-003-A-068-19	6.82	435.33	893.59	0.487	0.059	0.011	0.026	0.003	0.004	0.000	0.443	550.04	409.99	25.86	2.65	24.33	1.12	93
LA-D15-003-A-068-20	11.87	695.57	1,272.55	0.547	0.057	0.013	0.031	0.006	0.004	0.000	0.177	479.67	437.00	30.58	5.77	27.39	0.93	88

APPENDIX2. TABLE A2. (cont.)

Spot Name	ppm Total Pb	ppm 232Th	ppm 238U	232Th /238U	207Pb /206Pb	% ±1σ	207Pb /235U	% ±1σ	206Pb /238U	% ±1σ	rho	apparent ages						
												207Pb /206Pb	Ma ±1σ	207Pb /235U	Ma ±1σ	206Pb /238U	Ma ±1σ	% conc.
<b>Sample LA-D11-001A-07 (inter-mineral porphyry)</b>																		
LA-D11-001A-07-01	12.86	108.86	252.55	0.431	0.071	0.023	0.046	0.005	0.004	0.000	0.615	970.06	698.57	45.32	4.88	28.54	1.93	54
LA-D11-001A-07-02	12.26	290.99	622.82	0.467	0.047	0.013	0.022	0.007	0.004	0.000	0.164	53.80	579.55	21.95	6.88	24.74	1.28	88
LA-D11-001A-07-03	16.35	141.21	393.14	0.359	0.053	0.018	0.028	0.005	0.004	0.000	0.337	344.50	616.61	27.64	5.09	27.39	1.72	99
LA-D11-001A-07-04	4.61	259.17	517.93	0.500	0.048	0.014	0.027	0.005	0.004	0.000	0.341	105.65	594.37	26.80	4.91	24.66	1.56	91
LA-D11-001A-07-05	3.40	201.04	382.21	0.526	0.106	0.029	0.042	0.008	0.004	0.000	0.294	1,740.43	512.81	41.57	8.24	24.80	1.47	49
LA-D11-001A-07-06	3.07	168.47	389.20	0.433	0.055	0.013	0.026	0.005	0.004	0.000	0.294	409.31	462.91	25.69	4.76	25.56	1.40	99
LA-D11-001A-07-07	2.94	146.94	360.01	0.408	0.059	0.017	0.028	0.006	0.004	0.000	0.246	588.92	509.24	27.65	6.16	26.02	1.44	93
LA-D11-001A-07-08	3.47	174.92	458.86	0.381	0.064	0.017	0.027	0.005	0.004	0.000	0.301	738.90	605.51	26.94	4.53	25.99	1.33	96
LA-D11-001A-07-09	13.56	346.88	693.76	0.500	0.050	0.012	0.024	0.005	0.004	0.000	0.239	183.42	470.31	23.94	5.08	24.52	1.26	97
LA-D11-001A-07-10	2.48	124.41	320.83	0.388	0.072	0.033	0.029	0.010	0.004	0.000	0.198	988.89	720.37	28.70	9.40	26.97	1.77	93
LA-D11-001A-07-11	13.02	156.21	367.47	0.425	0.063	0.023	0.024	0.009	0.004	0.000	0.189	724.08	622.21	24.52	8.90	25.90	1.79	94
LA-D11-001A-07-12	6.07	461.29	845.75	0.545	0.054	0.014	0.025	0.006	0.004	0.000	0.172	350.06	494.08	24.95	5.95	25.78	1.07	96
LA-D11-001A-07-13	4.30	258.47	643.65	0.402	0.070	0.019	0.025	0.005	0.004	0.000	0.216	931.48	568.95	24.62	5.43	22.75	1.09	92
LA-D11-001A-07-14	6.22	244.63	529.46	0.462	0.079	0.025	0.030	0.007	0.004	0.000	0.226	1,183.34	653.83	30.20	6.65	24.96	1.26	80
LA-D11-001A-07-15	13.21	223.26	401.04	0.557	0.066	0.022	0.026	0.002	0.004	0.000	0.606	795.99	574.07	25.71	2.40	24.24	1.39	94
LA-D11-001A-07-16	12.02	238.97	467.32	0.511	0.061	0.018	0.025	0.004	0.004	0.000	0.454	631.50	529.62	25.01	3.60	23.44	1.55	93
LA-D11-001A-07-17	2.34	96.43	295.12	0.327	0.048	0.017	0.028	0.004	0.004	0.000	0.488	98.24	690.34	28.39	4.15	24.47	1.77	85
LA-D11-001A-07-18	9.85	171.71	384.87	0.446	0.047	0.015	0.036	0.009	0.005	0.000	0.201	42.69	633.25	35.43	9.23	29.07	1.54	80
LA-D11-001A-07-19	4.89	290.91	637.27	0.457	0.063	0.015	0.028	0.005	0.004	0.000	0.314	698.16	513.70	28.11	4.67	27.03	1.42	96
LA-D11-001A-07-20	2.46	119.62	327.73	0.365	0.087	0.024	0.038	0.009	0.004	0.000	0.333	1,365.74	549.23	38.23	9.15	26.45	2.14	63
<b>Sample CA-25 (precursor pluton)</b>																		
CA-25-01	7.44	511.62	882.91	0.579	0.066	0.018	0.027	0.004	0.004	0.000	0.292	816.67	601.81	26.72	3.96	27.85	1.22	95
CA-25-02	12.66	662.63	1,352.27	0.490	0.057	0.009	0.027	0.002	0.004	0.000	0.405	500.04	353.66	27.29	2.38	25.46	0.91	93
CA-25-03	3.60	149.99	361.71	0.415	0.060	0.024	0.027	0.010	0.004	0.000	0.191	605.58	692.58	27.25	10.04	26.30	1.87	96
CA-25-04	11.81	505.93	1,064.77	0.475	0.069	0.015	0.030	0.006	0.004	0.000	0.222	903.39	461.09	29.73	5.50	27.78	1.16	93
CA-25-05	7.10	373.63	768.57	0.486	0.060	0.013	0.025	0.003	0.004	0.000	0.486	620.39	490.70	24.90	2.77	26.74	1.46	92
CA-25-06	24.38	212.01	495.28	0.428	0.070	0.021	0.028	0.007	0.004	0.000	0.253	924.07	635.61	28.00	6.64	28.26	1.72	99
CA-25-07	13.61	815.49	2,116.39	0.385	0.049	0.007	0.026	0.003	0.004	0.000	0.214	138.98	314.78	25.65	3.46	24.77	0.72	96
CA-25-08	14.87	401.97	954.59	0.421	0.078	0.018	0.031	0.003	0.004	0.000	0.389	1,138.90	462.96	31.35	3.41	23.76	1.02	72
CA-25-09	17.92	258.35	649.44	0.398	2.288	2.242	1.078	2.378	0.004	0.000	0.023	error	error	742.87	1,161.83	26.20	1.34	-87
CA-25-10	5.38	335.66	784.57	0.428	0.050	0.012	0.027	0.005	0.004	0.000	0.306	209.33	466.61	26.68	4.75	26.68	1.47	99
CA-25-11	13.34	546.06	1,100.43	0.496	0.053	0.010	0.026	0.004	0.004	0.000	0.242	322.28	364.77	26.28	3.89	24.29	0.88	92
CA-25-12	12.59	313.92	664.36	0.473	0.064	0.020	0.026	0.006	0.004	0.000	0.234	766.67	542.59	25.85	6.23	24.25	1.39	93
CA-25-13	8.75	596.31	1,146.80	0.520	0.047	0.010	0.024	0.006	0.004	0.000	0.145	38.99	440.69	24.51	6.31	23.65	0.89	96
CA-25-14	10.31	351.25	835.50	0.420	0.047	0.010	0.024	0.002	0.004	0.000	0.448	50.10	459.21	23.74	2.32	26.12	1.15	90
CA-25-15	9.75	412.89	1,088.09	0.379	0.046	0.008	0.024	0.002	0.004	0.000	0.335	400.05	-35.18	23.80	2.30	23.93	0.78	99
CA-25-16	7.05	508.22	1,142.25	0.445	0.058	0.011	0.024	0.003	0.004	0.000	0.356	538.93	408.29	23.66	2.53	22.63	0.87	95
CA-25-17	9.22	276.88	626.21	0.442	0.069	0.028	0.026	0.005	0.004	0.000	0.250	887.04	674.08	26.29	5.43	26.01	1.36	98
CA-25-18	15.59	442.90	897.19	0.494	0.062	0.013	0.025	0.002	0.004	0.000	0.527	657.42	456.44	25.41	2.36	23.40	1.16	91
CA-25-19	2.59	136.05	368.96	0.369	0.071	0.025	0.026	0.009	0.004	0.001	0.384	950.00	597.23	25.93	9.27	26.39	3.66	98
CA-25-20	2.17	113.92	296.04	0.385	0.165	0.044	0.058	0.011	0.004	0.000	0.372	2,510.80	465.58	57.12	10.33	25.98	1.79	25

APPENDIX 2. TABLE A2. (cont.)

Spot Name	ppm Total Pb	ppm 232Th	ppm 238U	232Th /238U	207Pb /206Pb	% ±1σ	207Pb /235U	% ±1σ	206Pb /238U	% ±1σ	rho	aparent ages						
												207Pb /206Pb	Ma ±1σ	207Pb /235U	Ma ±1σ	206Pb /238U	Ma ±1σ	% conc.
<b>Sample CA-24 (inter-mineral porphyry)</b>																		
CA-24-01	4.07	185.16	447.67	0.414	0.069	0.025	0.025	0.005	0.004	0.000	0.334	894.45	604.63	25.56	4.77	26.17	1.64	97
CA-24-02	6.62	216.20	401.90	0.538	0.048	0.012	0.030	0.004	0.004	0.000	0.431	98.24	514.74	29.76	4.03	28.30	1.67	94
CA-24-03	11.70	815.30	1,717.69	0.475	0.053	0.008	0.024	0.003	0.004	0.000	0.261	324.13	307.37	23.92	2.95	23.50	0.76	98
CA-24-04	7.81	485.76	977.44	0.497	0.065	0.015	0.026	0.005	0.004	0.000	0.260	761.12	524.03	26.02	5.36	24.19	1.31	92
CA-24-05	3.49	221.64	475.94	0.466	0.107	0.083	0.027	0.030	0.004	0.000	0.057	1,742.59	992.91	26.85	29.37	25.13	1.60	93
CA-24-06	6.06	240.11	467.43	0.514	0.056	0.017	0.026	0.004	0.004	0.000	0.395	442.64	551.81	26.48	3.71	25.68	1.44	96
CA-24-07	4.56	304.15	514.14	0.592	0.088	0.021	0.040	0.005	0.004	0.000	0.478	1,375.93	478.71	39.67	4.75	27.52	1.61	63
CA-24-08	5.75	189.34	412.14	0.459	0.046	0.016	0.030	0.011	0.004	0.000	0.182	9.36	662.88	30.39	10.42	24.13	1.52	77
CA-24-09	6.95	379.65	829.78	0.458	0.072	0.021	0.029	0.008	0.004	0.000	0.175	976.86	608.77	29.35	8.26	26.34	1.31	89
CA-24-10	9.46	547.49	1,106.64	0.495	0.050	0.009	0.028	0.004	0.004	0.000	0.306	213.04	377.74	28.41	3.80	25.95	1.08	90
CA-24-11	2.09	96.00	269.99	0.356	0.050	0.029	0.021	0.014	0.004	0.000	0.124	213.04	975.86	20.86	13.95	22.76	1.91	91
CA-24-12	7.78	417.13	1,130.81	0.369	0.062	0.013	0.026	0.004	0.004	0.000	0.296	679.64	461.07	25.68	3.96	24.20	1.12	94
CA-24-13	6.19	409.82	752.87	0.544	0.082	0.019	0.038	0.004	0.004	0.000	0.465	1,242.59	458.17	37.69	4.12	26.21	1.36	64
CA-24-14	7.22	449.02	781.49	0.575	0.063	0.018	0.027	0.004	0.004	0.000	0.305	694.46	572.21	26.70	4.27	25.83	1.27	96
CA-24-15	5.66	233.69	524.60	0.445	0.108	0.026	0.045	0.005	0.004	0.000	0.565	1,768.83	455.56	44.60	4.38	25.63	1.45	45
CA-24-16	7.99	416.09	1,008.31	0.413	0.047	0.010	0.026	0.006	0.004	0.000	0.187	42.69	429.58	26.21	5.94	25.62	1.10	97
CA-24-17	6.43	367.98	726.42	0.507	0.067	0.027	0.028	0.005	0.004	0.000	0.313	833.33	672.23	27.58	4.68	26.66	1.43	96
CA-24-18	5.16	231.25	491.64	0.470	0.076	0.025	0.030	0.012	0.004	0.000	0.148	1,092.28	700.12	29.93	11.62	25.66	1.49	84
CA-24-19	12.03	942.67	1,378.98	0.684	0.060	0.010	0.025	0.003	0.004	0.000	0.283	590.77	367.55	24.92	3.27	23.32	0.88	93
CA-24-20	6.67	314.21	618.36	0.508	0.062	0.015	0.024	0.001	0.004	0.000	1.263	661.13	524.95	24.50	0.96	26.15	1.31	93
<b>Sample CA-13 (late-mineral porphyry)</b>																		
CA-13-01	3.79	195.20	466.18	0.419	0.074	0.030	0.025	0.004	0.004	0.000	0.351	1,051.55	655.55	25.51	4.38	24.98	1.52	97
CA-13-02	5.01	194.25	462.38	0.420	0.051	0.019	0.023	0.005	0.004	0.000	0.327	261.18	666.60	22.76	4.80	24.27	1.69	93
CA-13-03	5.82	272.27	752.00	0.362	0.063	0.015	0.024	0.004	0.004	0.000	0.298	724.08	531.44	24.07	4.31	24.56	1.32	97
CA-13-04	8.73	623.99	971.20	0.642	0.052	0.010	0.026	0.004	0.004	0.000	0.216	275.99	407.36	26.24	4.36	24.53	0.89	93
CA-13-05	8.85	375.60	815.32	0.461	0.070	0.017	0.026	0.004	0.004	0.000	0.318	940.43	499.05	25.95	3.80	24.04	1.13	92
CA-13-06	6.96	348.03	638.15	0.545	0.078	0.030	0.029	0.008	0.004	0.000	0.203	1,147.84	844.86	29.14	8.01	26.52	1.50	90
CA-13-07	4.30	196.90	504.91	0.390	0.067	0.019	0.027	0.005	0.004	0.000	0.282	850.00	632.36	27.37	5.06	26.16	1.38	95
CA-13-08	8.47	246.54	512.44	0.481	0.050	0.015	0.028	0.005	0.004	0.000	0.331	194.53	577.70	28.43	4.93	26.64	1.54	93
CA-13-09	10.29	830.37	1,042.07	0.797	0.077	0.014	0.041	0.006	0.004	0.000	0.298	1,127.79	365.74	40.60	5.82	25.17	1.09	53
CA-13-10	8.03	570.31	928.44	0.614	0.048	0.009	0.025	0.003	0.004	0.000	0.351	76.02	424.02	25.43	3.08	25.11	1.08	98
CA-13-11	5.31	187.61	468.83	0.400	0.063	0.021	0.028	0.002	0.004	0.000	1.038	709.27	588.88	27.74	1.84	25.72	1.80	92
CA-13-12	46.84	376.94	807.82	0.467	0.404	0.038	0.396	0.032	0.007	0.000	0.620	3,923.16	140.64	338.62	23.22	47.53	2.37	-51
CA-13-13	5.39	420.98	660.96	0.637	0.065	0.022	0.023	0.004	0.004	0.000	0.299	787.04	575.61	22.64	3.79	23.48	1.18	96
CA-13-14	4.26	250.40	545.76	0.459	0.047	0.016	0.024	0.005	0.004	0.000	0.324	31.58	668.43	23.62	4.66	23.28	1.50	98
CA-13-15	7.81	428.91	798.41	0.537	0.072	0.018	0.028	0.005	0.004	0.000	0.273	988.58	519.42	28.29	5.03	25.97	1.28	91
CA-13-16	8.69	559.22	998.01	0.560	0.059	0.013	0.028	0.004	0.004	0.000	0.322	575.96	476.81	28.43	3.96	24.75	1.12	86
CA-13-17	6.00	466.81	833.63	0.560	0.058	0.013	0.026	0.004	0.004	0.000	0.311	522.26	477.74	25.72	3.65	23.60	1.05	91
CA-13-18	5.85	319.48	626.72	0.510	0.057	0.015	0.022	0.003	0.004	0.000	0.442	494.49	492.56	22.57	3.28	24.41	1.58	92
CA-13-19	7.01	208.44	586.14	0.356	0.050	0.017	0.027	0.012	0.004	0.000	0.132	172.31	644.36	26.76	12.29	25.69	1.57	95
CA-13-20	9.93	522.32	736.05	0.710	0.047	0.012	0.023	0.004	0.004	0.000	0.262	50.10	514.76	22.76	3.83	25.11	1.12	90

## APPENDIX 3

### Method

Zircon U-Pb dating (unpub. data): LA-ICPMS zircon geochronology at the University of Tasmania

Approximately 100 g of rock was repeatedly sieved and crushed in a Cr-steel ring mill to a grain size <400 micron. Non-magnetic heavy minerals were then separated using a gold pan and a Fe-B-Nd hand magnet. The zircons were hand-picked from the heavy mineral concentrate under the microscope in cross-polarized transmitted light. The selected crystals were placed on double sided sticky tape and epoxy glue was then poured into a 2.5 cm diameter mould on top of the zircons. The mount was dried for 12 hours and polished using clean sandpaper and a clean polishing lap. The samples were then washed in distilled water in an ultrasonic bath.

The analyses in this study were performed on an Agilent 7500cs quadrupole ICPMS with a 193 nm Coherent Ar-F gas laser and the Resonetics M50 ablation cell at the University of Tasmania in Hobart. The downhole fractionation, instrument drift and mass bias correction factors for Pb/U ratios on zircons were calculated using 2 analyses on the primary (91500 standard of Wiendenbeck et al. 1995) and 1 analysis on each of the secondary standard zircons (Temora standard of Black et al. 2003 and JG1 of Jackson et al. 2004) analyzed at the beginning of the session and every 12 unknown zircons (roughly every 1/2 hour) using the same spot size and conditions as used on the samples. Additional secondary standards (The Mud Tank Zircon of Black and Gulson 1978) were also analyzed. The correction factor for the  $^{207}\text{Pb}/^{206}\text{Pb}$  ratio was calculated using 3 large spot of NIST610 analyzed at the beginning and end of the day and corrected using the values recommended by Baker et al. (2004).

Each analysis on the zircons began with a 30 second blank gas measurement followed by a further 30 seconds of analysis time when the laser was switched on. Zircons were sampled on 32 micron spots using the laser at 5 Hz and a density of approximately 1.5 J/cm<sup>2</sup>. A flow of He carrier gas at a rate of 0.6 litres/minute carried particles ablated by the laser out of the chamber to be mixed with Ar gas and carried to the plasma torch. Isotopes measured were  $^{49}\text{Ti}$ ,  $^{56}\text{Fe}$ ,  $^{90}\text{Zr}$ ,  $^{178}\text{Hf}$ ,  $^{202}\text{Hg}$ ,  $^{204}\text{Pb}$ ,  $^{206}\text{Pb}$ ,  $^{207}\text{Pb}$ ,  $^{208}\text{Pb}$ ,  $^{232}\text{Th}$  and  $^{238}\text{U}$  with each element being measured every 0.16 s with longer counting time on the Pb isotopes compared to the other elements. The data reduction used was based on the method outlined in detail in Meffre et al. (2008) similar to that outlined in Black et al. (2004) and Paton et al. (2010).

Element abundances on zircons were calculated using the method outlined by Kosler (2001) using Zr as the internal standard element, assuming stoichiometric proportions and using the 91500 to standard correct for mass bias.

APPENDIX 3. Table A3. U/Pb zircon analytical data obtained using the LA-ICP-MS Method

Spot name	comm Pb	238U ppm	232Th ppm	232Th/238U	<sup>207</sup> Pb corrected			<sup>204</sup> Pb corrected				
					<sup>206</sup> Pb/ <sup>U</sup> <sup>238</sup> age (Ma)	±1σ	<sup>206</sup> Pb/ <sup>238</sup> U	% ±1σ	<sup>238</sup> U/ <sup>206</sup> Pb	±1σ	<sup>207</sup> Pb/ <sup>206</sup> Pb	±1σ
<b>MD-03</b>												
M03-01	0.8372	292.8	146.1	0.499	23.86	0.82	0.0037	0.034	266.9538	9.020	0.0545	0.006
M03-02	0.8372	491.7	165.9	0.337	23.98	0.64	0.0037	0.026	267.4833	7.020	0.0491	0.005
M03-03	0.8372	224.5	115.3	0.513	24.52	1.07	0.0039	0.042	259.6353	10.999	0.0550	0.008
M03-04	0.8372	400.5	199.9	0.499	24.98	0.70	0.0039	0.027	254.9230	6.988	0.0545	0.005
M03-05	0.8372	479.8	290.6	0.606	25.01	0.78	0.0039	0.031	254.6143	7.767	0.0548	0.005
M03-06	0.8372	410.6	362.4	0.883	25.18	0.70	0.0039	0.027	253.4788	6.891	0.0529	0.005
M03-07	0.8372	466.1	292.7	0.628	25.27	0.79	0.0039	0.031	255.9823	7.911	0.0423	0.004
M03-08	0.8373	600.7	362.2	0.603	25.45	0.68	0.0040	0.026	252.2960	6.581	0.0481	0.004
M03-09	0.8373	542.1	355.8	0.656	25.48	0.68	0.0040	0.026	252.1077	6.579	0.0478	0.004
M03-10	0.8373	374.0	142.1	0.380	25.61	0.89	0.0040	0.034	248.4970	8.480	0.0552	0.005
M03-11	0.8373	316.0	147.3	0.466	25.65	0.82	0.0040	0.031	250.1517	7.854	0.0486	0.005
M03-12	0.8373	565.6	348.4	0.616	25.72	0.70	0.0040	0.027	249.8482	6.642	0.0474	0.004
M03-13	0.8373	298.5	106.9	0.358	25.79	0.95	0.0040	0.036	248.4016	9.013	0.0499	0.006
M03-14	0.8373	427.8	240.7	0.563	26.16	0.82	0.0040	0.031	247.5216	7.636	0.0414	0.004
M03-15	0.8374	187.5	68.3	0.364	26.73	1.03	0.0042	0.037	236.4927	8.808	0.0602	0.008
<b>07D-LA-324-161</b>												
D161-01	0.8371	128.7	47.0	0.365	22.71	1.44	0.0037	0.056	271.4271	15.235	0.0797	0.023
D161-02	0.8374	140.1	34.2	0.244	22.88	1.61	0.0042	0.061	235.8100	14.311	0.1742	0.024
D161-03	0.8372	557.3	323.3	0.580	23.37	0.61	0.0037	0.025	267.8982	6.795	0.0679	0.005
D161-04	0.8372	292.3	175.6	0.601	23.75	1.37	0.0038	0.055	264.6501	14.654	0.0648	0.013
D161-05	0.8372	432.8	257.2	0.594	24.59	0.81	0.0038	0.032	264.0781	8.521	0.0391	0.005
D161-06	0.8372	312.5	146.9	0.470	24.62	1.12	0.0038	0.044	261.9464	11.552	0.0447	0.008
D161-07	0.8372	231.0	76.0	0.329	24.84	1.19	0.0039	0.046	258.5547	11.942	0.0479	0.010
D161-08	0.8372	530.1	487.9	0.921	24.94	1.02	0.0039	0.040	253.1666	10.001	0.0613	0.008
D161-09	0.8372	246.5	122.4	0.497	25.26	0.94	0.0039	0.035	254.8577	8.992	0.0461	0.010
D161-10	0.8373	436.0	260.6	0.598	26.08	0.73	0.0041	0.027	243.9710	6.665	0.0552	0.005
D161-11	0.8373	244.0	103.1	0.423	26.13	1.03	0.0042	0.037	240.4634	8.995	0.0649	0.009
D161-12	0.8373	333.7	173.7	0.520	26.17	1.02	0.0040	0.038	251.1638	9.588	0.0293	0.006
D161-13	0.8374	131.1	45.8	0.350	26.30	1.61	0.0042	0.058	235.9061	13.603	0.0746	0.016
D161-14	0.8373	155.9	52.4	0.336	26.35	1.41	0.0041	0.052	245.1914	12.629	0.0432	0.011
D161-15	0.8446	137.5	70.4	0.512	137.80	3.86	0.0217	0.028	46.1239	1.273	0.0515	0.005
<b>05D-LA-216-99</b>												
D99-01	0.8372	404.3	187.7	0.464	23.93	0.69	0.0038	0.028	265.2745	7.502	0.0570	0.005
D99-02	0.8372	216.1	71.0	0.328	24.29	1.02	0.0037	0.041	267.9340	11.005	0.0373	0.007
D99-03	0.8372	319.9	135.6	0.424	24.78	1.47	0.0039	0.058	258.7246	14.980	0.0493	0.011
D99-04	0.8372	203.7	78.3	0.384	24.81	0.98	0.0039	0.038	257.2735	9.800	0.0529	0.008
D99-05	0.8372	280.5	147.0	0.524	24.90	0.84	0.0039	0.033	258.7825	8.573	0.0455	0.006
D99-06	0.8372	147.8	65.6	0.444	25.29	1.17	0.0039	0.044	254.0887	11.160	0.0476	0.012
D99-07	0.8372	298.1	103.1	0.346	25.34	0.81	0.0039	0.031	254.8811	7.950	0.0435	0.006
D99-08	0.8373	338.4	293.1	0.866	25.59	1.00	0.0040	0.038	252.0976	9.474	0.0444	0.008
D99-09	0.8373	203.1	83.6	0.412	25.69	1.15	0.0040	0.043	248.8262	10.788	0.0515	0.009
D99-10	0.8373	212.9	71.2	0.334	25.82	0.96	0.0041	0.036	246.3292	8.880	0.0554	0.007
D99-11	0.8373	346.6	174.3	0.503	25.83	0.83	0.0040	0.031	249.6200	7.850	0.0447	0.005
D99-12	0.8373	139.0	47.0	0.338	25.97	1.43	0.0041	0.053	245.4618	12.935	0.0537	0.013
D99-13	0.8373	152.7	51.4	0.337	26.03	1.19	0.0041	0.044	245.9879	10.890	0.0503	0.009
D99-14	0.8379	277.3	50.8	0.183	34.73	1.99	0.0055	0.055	183.0418	10.081	0.0555	0.012
D99-15	0.8457	173.2	69.0	0.398	153.72	4.01	0.0243	0.026	41.2213	1.064	0.0533	0.004
<b>MD-02</b>												
M2-01	0.8371	357.9	152.4	0.426	23.06	0.79	0.0036	0.033	274.6454	9.193	0.0590	0.006
M2-02	0.8371	284.2	179.6	0.632	23.63	0.90	0.0037	0.037	271.0544	10.107	0.0501	0.007
M2-03	0.8372	188.4	70.8	0.376	24.35	1.12	0.0038	0.045	263.5084	11.887	0.0487	0.008
M2-04	0.8372	206.0	77.4	0.376	24.47	1.21	0.0039	0.048	255.6812	12.352	0.0683	0.009
M2-05	0.8372	459.4	280.8	0.611	24.88	0.74	0.0038	0.029	259.9564	7.628	0.0422	0.004
M2-06	0.8373	266.5	135.1	0.507	25.08	1.12	0.0040	0.043	248.0730	10.588	0.0726	0.010
M2-07	0.8372	310.6	153.3	0.494	25.11	0.79	0.0039	0.031	254.5977	7.802	0.0516	0.006
M2-08	0.8372	147.5	65.1	0.441	25.19	1.42	0.0039	0.055	255.2748	14.102	0.0469	0.010
M2-09	0.8372	176.0	64.2	0.365	25.25	1.28	0.0039	0.049	254.4786	12.528	0.0476	0.010
M2-10	0.8373	306.9	150.3	0.490	25.96	0.89	0.0040	0.034	247.6183	8.334	0.0472	0.005
M2-11	0.8373	291.8	125.5	0.430	26.15	0.96	0.0041	0.036	244.7897	8.789	0.0506	0.006
M2-12	0.8373	201.1	80.7	0.401	27.03	2.41	0.0041	0.088	245.1361	21.548	0.0227	0.013
M2-13	0.8374	264.4	98.5	0.372	27.35	1.40	0.0042	0.050	235.4383	11.779	0.0457	0.009
M2-14	0.8387	217.6	62.0	0.285	47.58	1.77	0.0075	0.036	132.7439	4.838	0.0601	0.006
M2-15	0.8426	179.0	87.9	0.491	107.35	2.91	0.0170	0.027	58.9423	1.577	0.0563	0.004

APPENDIX 3. Table A3. (cont.)

Spot name	comm Pb	238U ppm	232Th h ppm	232Th /238U	<sup>207</sup> Pb corrected			<sup>204</sup> Pb corrected			<sup>207</sup> Pb/ <sup>206</sup> Pb b	±1σ
					<sup>206</sup> Pb/ <sup>U</sup> <sup>238</sup> age (Ma)	±1σ	<sup>206</sup> Pb/ <sup>238</sup> U	% ±1σ	<sup>238</sup> U/ <sup>206</sup> Pb	±1σ		
<b>LA-D11-004-799</b>												
L799-01	0.8373	138.9	52.4	0.377	24.40	2.06	0.0041	0.074	241.1084	17.860	0.1144	0.029
L799-02	0.8372	127.8	42.2	0.330	24.50	1.33	0.0038	0.051	261.1607	13.353	0.0510	0.014
L799-03	0.8372	502.5	187.2	0.372	24.85	0.68	0.0039	0.027	257.3382	6.909	0.0515	0.005
L799-04	0.8372	319.0	156.5	0.491	24.99	0.83	0.0039	0.032	257.8361	8.335	0.0454	0.007
L799-05	0.8373	165.6	68.5	0.414	25.02	1.32	0.0040	0.050	250.9826	12.667	0.0654	0.013
L799-06	0.8372	374.3	208.8	0.558	25.17	0.83	0.0039	0.032	254.0590	8.170	0.0512	0.005
L799-07	0.8375	372.0	163.7	0.440	25.26	1.06	0.0046	0.038	218.1043	8.183	0.1603	0.013
L799-08	0.8373	174.5	92.4	0.529	25.45	1.50	0.0041	0.055	246.5304	13.572	0.0660	0.017
L799-09	0.8372	427.0	176.9	0.414	25.47	0.80	0.0039	0.031	254.6052	7.833	0.0402	0.004
L799-10	0.8373	275.5	119.8	0.435	25.51	0.98	0.0041	0.037	246.8497	9.121	0.0634	0.008
L799-11	0.8372	129.1	48.7	0.377	25.52	1.47	0.0039	0.053	253.5850	13.416	0.0420	0.018
L799-12	0.8373	262.2	112.0	0.427	25.53	1.02	0.0040	0.039	250.5288	9.770	0.0512	0.007
L799-13	0.8373	201.6	75.0	0.372	25.65	1.20	0.0041	0.045	246.5070	11.030	0.0602	0.011
L799-14	0.8372	231.4	102.8	0.444	25.73	1.16	0.0039	0.044	253.2584	11.056	0.0362	0.010
<b>MD-01</b>												
M1-01	0.8371	142.5	56.7	0.398	22.72	1.18	0.0035	0.050	284.4798	14.213	0.0429	0.011
M1-02	0.8372	294.4	164.0	0.557	22.79	1.09	0.0038	0.045	259.7433	11.753	0.1098	0.011
M1-03	0.8371	262.4	125.2	0.477	23.53	0.91	0.0037	0.038	270.2408	10.147	0.0557	0.007
M1-04	0.8372	352.9	176.7	0.501	24.82	0.89	0.0040	0.035	253.0057	8.836	0.0656	0.006
M1-05	0.8372	393.3	122.5	0.311	24.98	0.71	0.0039	0.028	258.3214	7.241	0.0441	0.004
M1-06	0.8372	480.2	280.2	0.583	25.02	0.73	0.0039	0.029	258.2862	7.388	0.0432	0.004
M1-07	0.8372	259.9	100.1	0.385	25.07	0.98	0.0039	0.038	256.8896	9.842	0.0456	0.006
M1-08	0.8373	371.0	199.3	0.537	25.22	1.05	0.0040	0.040	251.2807	10.146	0.0584	0.008
M1-09	0.8372	235.7	100.2	0.425	25.25	0.93	0.0040	0.036	253.1628	8.992	0.0515	0.008
M1-10	0.8372	284.6	112.6	0.396	25.27	0.94	0.0039	0.036	254.3756	9.031	0.0473	0.009
M1-11	0.8372	382.2	239.9	0.628	25.29	0.74	0.0040	0.029	253.1158	7.301	0.0507	0.004
M1-12	0.8373	263.2	134.9	0.513	25.59	0.97	0.0041	0.037	246.5650	9.039	0.0618	0.007
M1-13	0.8373	254.2	123.8	0.487	25.94	0.93	0.0040	0.035	247.4253	8.652	0.0485	0.007
M1-14	0.8461	347.8	254.2	0.731	159.82	2.40	0.0251	0.015	39.7755	0.594	0.0505	0.002
M1-15	0.8489	286.9	93.7	0.327	196.64	4.92	0.0318	0.025	31.4150	0.773	0.0716	0.004
<b>LA-D11-004-686</b>												
L686-01	0.8372	186.0	82.2	0.442	24.14	0.95	0.0038	0.038	264.3125	10.093	0.0532	0.007
L686-02	0.8372	220.4	84.6	0.384	24.35	0.96	0.0038	0.038	263.7849	10.078	0.0477	0.008
L686-03	0.8372	167.5	70.6	0.422	24.41	1.24	0.0038	0.048	263.7204	12.730	0.0462	0.013
L686-04	0.8372	191.0	98.4	0.515	24.68	1.16	0.0038	0.046	261.4623	11.990	0.0443	0.009
L686-05	0.8372	199.4	94.2	0.472	24.86	1.12	0.0038	0.044	259.8799	11.378	0.0432	0.009
L686-06	0.8372	260.2	96.8	0.372	24.86	0.98	0.0039	0.039	258.4703	9.957	0.0475	0.007
L686-07	0.8372	163.7	61.0	0.373	24.98	1.27	0.0039	0.050	257.5834	12.805	0.0466	0.009
L686-08	0.8372	211.5	97.1	0.459	25.01	1.07	0.0039	0.041	255.4332	10.592	0.0521	0.009
L686-09	0.8372	195.1	47.2	0.242	25.01	1.04	0.0039	0.040	257.9225	10.424	0.0444	0.008
L686-10	0.8372	220.7	95.0	0.430	25.04	1.04	0.0039	0.040	256.3838	10.362	0.0482	0.007
L686-11	0.8372	177.0	61.4	0.347	25.45	1.01	0.0039	0.038	254.4465	9.764	0.0413	0.008
L686-12	0.8373	360.4	129.9	0.360	25.67	0.88	0.0040	0.034	251.2223	8.447	0.0447	0.005
L686-13	0.8373	136.8	53.1	0.388	26.13	1.36	0.0041	0.050	243.4508	12.241	0.0554	0.011
L686-14	0.8373	248.0	101.7	0.410	26.71	0.96	0.0042	0.035	238.7395	8.378	0.0536	0.006
L686-15	0.8457	241.5	150.1	0.622	152.29	4.63	0.0242	0.030	41.3086	1.231	0.0591	0.006
<b>LA-D11-004-518</b>												
L518-01	0.8372	231.4	96.1	0.415	23.42	0.95	0.0037	0.039	267.4160	10.443	0.0676	0.009
L518-02	0.8372	373.0	215.1	0.577	24.00	0.73	0.0038	0.030	265.5916	7.905	0.0540	0.005
L518-03	0.8372	270.5	111.1	0.411	24.45	0.93	0.0038	0.037	262.7320	9.654	0.0477	0.007
L518-04	0.8372	156.0	51.4	0.329	24.51	1.25	0.0038	0.049	260.4620	12.788	0.0526	0.011
L518-05	0.8372	220.6	94.4	0.428	24.68	1.10	0.0038	0.044	260.0984	11.357	0.0482	0.008
L518-06	0.8372	206.1	79.6	0.386	24.95	1.11	0.0038	0.043	261.8437	11.295	0.0343	0.008
L518-07	0.8372	272.9	97.6	0.358	24.96	1.00	0.0039	0.039	258.1385	10.058	0.0454	0.008
L518-08	0.8372	351.0	203.8	0.580	25.06	0.88	0.0039	0.034	253.5424	8.722	0.0565	0.005
L518-09	0.8373	286.7	121.2	0.423	25.25	0.92	0.0040	0.036	252.3096	9.044	0.0542	0.006
L518-10	0.8372	77.6	25.1	0.323	25.29	1.77	0.0039	0.067	255.1373	17.029	0.0443	0.017
L518-11	0.8372	113.3	42.0	0.371	25.62	1.48	0.0039	0.056	256.7206	14.435	0.0290	0.011
L518-12	0.8374	207.8	98.2	0.472	27.76	1.03	0.0043	0.037	234.4479	8.578	0.0371	0.005
L518-13	0.8398	132.3	60.5	0.457	65.11	2.42	0.0102	0.036	98.4249	3.588	0.0480	0.006
L518-14	0.8449	264.8	143.4	0.541	141.00	4.32	0.0225	0.030	44.4842	1.344	0.0618	0.005
L518-15	0.8404	235.8	80.3	0.341	72.35	3.16	0.0115	0.043	86.9687	3.779	0.0621	0.004

APPENDIX 3. Table A3. (cont.)

Spot name	comm Pb	238U ppm	232Th ppm	232Th/238U	<sup>207</sup> Pb corrected			<sup>204</sup> Pb corrected				
					<sup>206</sup> Pb/ <sup>238</sup> U age (Ma)	±1σ	<sup>206</sup> Pb/ <sup>238</sup> U	% ±1σ	<sup>238</sup> U/ <sup>206</sup> Pb	±1σ	<sup>207</sup> Pb/ <sup>206</sup> Pb	±1σ
<b>07D-LA-324-126</b>												
D126-01	0.8372	367.0	132.3	0.360	23.57	0.82	0.0037	0.034	268.7890	9.138	0.0586	0.007
D126-02	0.8372	234.5	104.2	0.444	24.05	1.07	0.0038	0.043	261.9667	11.169	0.0630	0.009
D126-03	0.8372	252.4	98.6	0.391	24.12	0.95	0.0039	0.038	258.7184	9.839	0.0704	0.009
D126-04	0.8372	187.5	73.5	0.392	24.13	1.11	0.0039	0.044	258.2899	11.368	0.0714	0.010
D126-05	0.8372	455.4	259.4	0.570	24.22	0.93	0.0038	0.038	261.5255	9.841	0.0590	0.006
D126-06	0.8372	315.6	145.1	0.460	24.25	0.86	0.0039	0.034	259.4271	8.905	0.0642	0.006
D126-07	0.8372	454.0	242.5	0.534	24.32	0.71	0.0038	0.029	263.5589	7.591	0.0494	0.004
D126-08	0.8372	255.2	124.2	0.487	24.50	1.12	0.0039	0.045	259.4186	11.692	0.0562	0.007
D126-09	0.8372	468.2	219.7	0.469	24.60	1.39	0.0039	0.055	255.3171	14.106	0.0654	0.009
D126-10	0.8372	247.1	138.8	0.562	24.64	1.11	0.0038	0.044	260.3124	11.372	0.0488	0.008
D126-11	0.8373	314.7	133.2	0.423	24.94	0.88	0.0040	0.034	251.8477	8.640	0.0653	0.007
D126-12	0.8373	320.6	171.1	0.534	25.05	0.84	0.0040	0.032	247.3585	8.032	0.0756	0.006
D126-13	0.8372	230.9	87.0	0.377	25.51	0.94	0.0039	0.036	253.8840	9.117	0.0412	0.007
D126-14	0.8373	261.8	117.3	0.448	26.99	0.99	0.0042	0.036	240.1456	8.681	0.0406	0.006
D126-15	0.8395	504.5	491.0	0.973	59.63	1.90	0.0093	0.032	107.0630	3.389	0.0512	0.003
<b>MD-05</b>												
M5-01	0.8371	305.4	170.2	0.557	23.24	0.83	0.0036	0.034	276.0848	9.523	0.0489	0.007
M5-02	0.8372	173.9	70.8	0.407	23.64	1.19	0.0037	0.049	268.3693	13.025	0.0577	0.010
M5-03	0.8372	480.2	294.0	0.612	23.89	0.73	0.0037	0.030	267.3914	8.018	0.0522	0.004
M5-04	0.8372	335.1	135.4	0.404	24.04	0.77	0.0037	0.031	267.8220	8.353	0.0461	0.006
M5-05	0.8372	437.3	324.4	0.742	24.15	0.69	0.0037	0.028	266.8374	7.451	0.0453	0.004
M5-06	0.8372	371.4	182.8	0.492	24.18	0.74	0.0038	0.030	263.8651	7.879	0.0530	0.006
M5-07	0.8372	201.3	91.3	0.454	24.26	1.11	0.0039	0.044	255.0491	11.325	0.0769	0.009
M5-08	0.8372	423.2	189.8	0.448	24.33	0.79	0.0038	0.032	262.9489	8.301	0.0509	0.006
M5-09	0.8372	276.1	120.1	0.435	24.78	1.11	0.0039	0.044	259.4471	11.402	0.0471	0.007
M5-10	0.8372	284.7	201.8	0.709	24.88	0.98	0.0039	0.038	258.9623	9.832	0.0453	0.008
M5-11	0.8373	415.3	178.0	0.429	25.08	0.81	0.0041	0.030	242.7773	7.371	0.0889	0.009
M5-12	0.8372	410.5	199.9	0.487	25.21	0.75	0.0039	0.029	253.5493	7.327	0.0517	0.005
M5-13	0.8373	414.8	213.2	0.514	25.66	0.70	0.0040	0.027	250.5872	6.684	0.0471	0.005
M5-14	0.8373	269.3	109.5	0.406	25.69	0.97	0.0040	0.037	249.6725	9.166	0.0488	0.007
M5-15	0.8397	324.5	241.0	0.743	63.22	1.74	0.0099	0.027	101.1390	2.724	0.0499	0.005



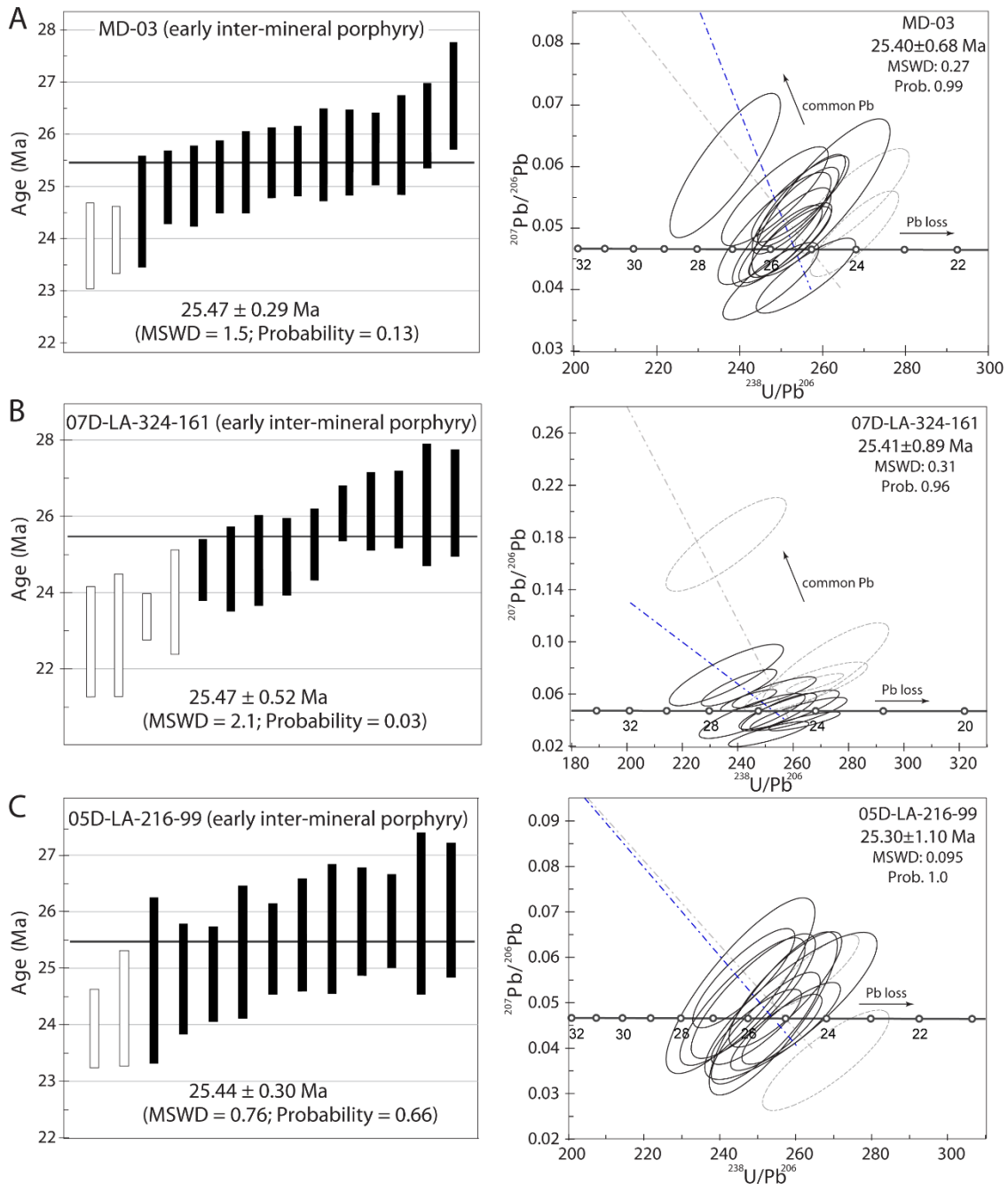


**Figure A3.** U-Pb ages for rock samples from La Arena porphyry system, northern Peru. Ages are calculated based on the weighted mean  $^{207}\text{Pb}$ -corrected  $^{206}\text{Pb}/^{238}\text{U}$  histograms. Histogram diagrams also show the distribution for Pb loss (A, B, C, and F) and inheritance (G and I) or both (D, H, and J) in some of the analyzed zircons (white bars). U-Pb age are also calculated based on the Tera and Wasserburg (1972) concordia diagrams, where shown for each samples demonstrate the presence of common Pb, Pb loss, and inheritance zircons in some of the analyzed zircons. A, B, and C early inter-mineral andesite porphyry. D, E, F, and G late inter-mineral andesite porphyry. H, I, and J late-mineral andesite porphyry.

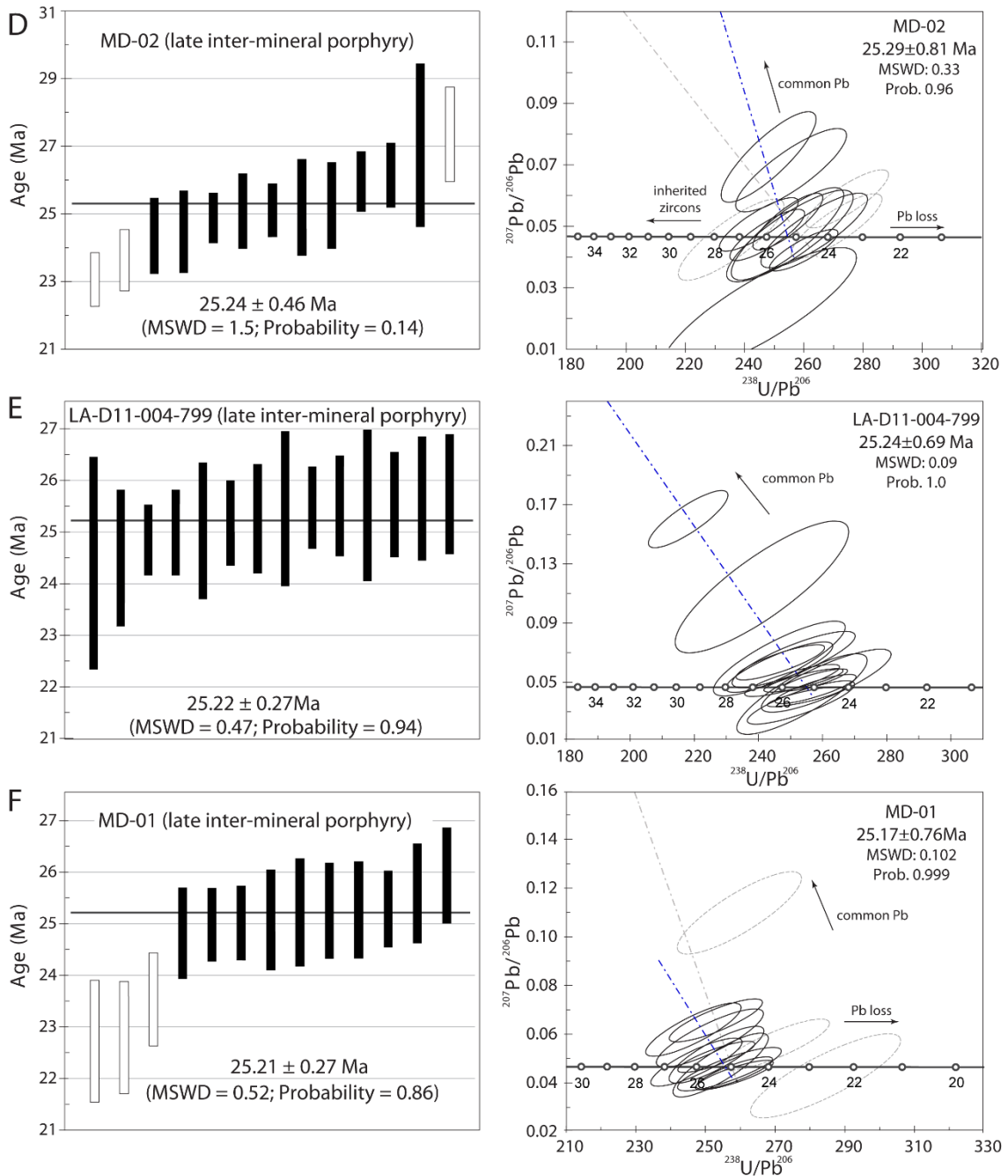


Fig. A3 (Cont)

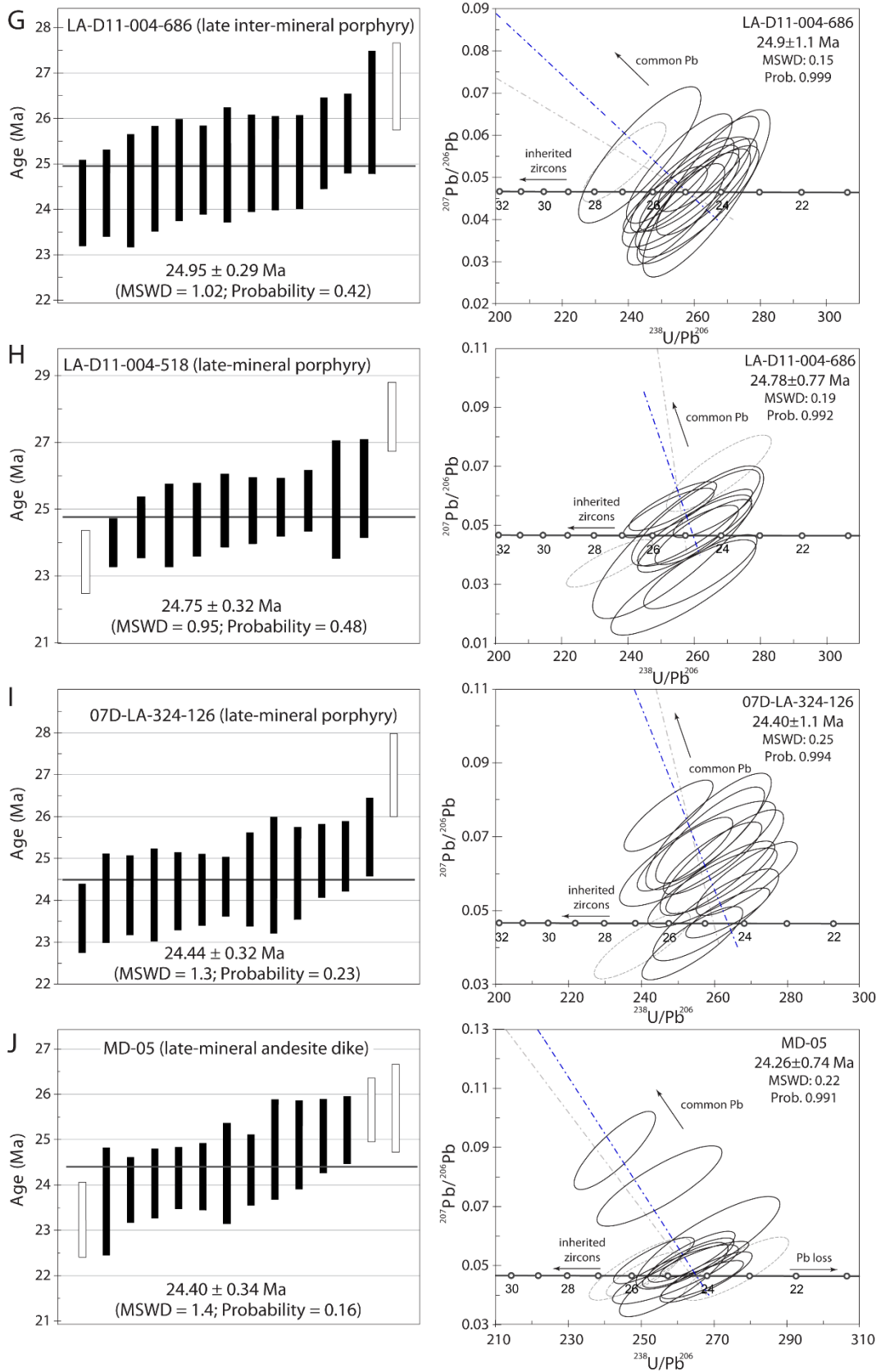


Fig. A3 (Cont)

APPENDIX 4. Table A4. Analytical data for  $^{40}\text{Ar}/^{39}\text{Ar}$  age determinations

Relative Abundances	$^{36}\text{Ar}$	$\pm 1\sigma$ %	$^{37}\text{Ar}$	$\pm 1\sigma$ %	$^{38}\text{Ar}$	$\pm 1\sigma$ %	$^{39}\text{Ar}$	$\pm 1\sigma$ %	$^{40}\text{Ar}$	$\pm 1\sigma$ %	$^{40}(\text{r})/^{39}(\text{k})$	$\pm 2\sigma$	Age (Ma)	$\pm 2\sigma$	$^{40}\text{Ar}(\text{r})$ %	$^{39}\text{Ar}(\text{k})$ %	K/Ca	$\pm 2\sigma$	
<b>CA-01B, hypogene alunite, Ethel deposit; J= 0.00947140 ± 0.00002841</b>																			
0105-004	5.00	1.336	0.798	-1.018	56.580	12.616	0.311	1,270.677	0.151	2,330.375	0.073	1.5177	0.007	25.81	0.123	82.753	2.495		
0105-005	5.80	1.709	0.682	2.127	29.543	15.444	0.306	1,548.534	0.150	2,864.418	0.014	1.5181	0.006	25.82	0.108	82.070	3.041	281.80	166.51
0105-006	6.60	0.230	1.311	1.690	34.434	16.395	0.307	1,673.643	0.150	2,610.794	0.010	1.5168	0.005	25.79	0.079	97.232	3.287	383.21	263.91
0105-007	7.20	0.178	3.740	1.244	41.037	9.812	0.329	1,002.780	0.150	1,579.151	0.031	1.5194	0.006	25.84	0.104	96.486	1.969	311.94	256.02
0105-009	8.00	0.155	1.666	1.439	33.292	10.491	0.319	1,074.148	0.150	1,680.527	0.019	1.5193	0.005	25.84	0.082	97.109	2.109	288.90	192.36
0105-010	9.00	0.184	1.759	0.517	74.952	6.969	0.331	714.484	0.151	1,142.136	0.023	1.5193	0.005	25.84	0.091	95.043	1.403	534.90	801.83
0105-011	10.00	0.439	1.462	1.317	50.833	5.192	0.358	524.541	0.150	929.875	0.042	1.5208	0.009	25.86	0.148	85.790	1.030	154.16	156.73
0105-012	11.50	1.522	0.851	2.052	29.968	19.524	0.306	1,957.648	0.150	3,433.860	0.014	1.5197	0.006	25.84	0.102	86.641	3.844	369.12	221.24
0105-013	13.00	0.410	1.691	1.531	29.535	16.533	0.313	1,683.686	0.150	2,686.523	0.017	1.5206	0.005	25.86	0.088	95.300	3.306	425.58	251.39
0105-014	15.00	0.212	3.583	1.076	50.763	7.663	0.337	769.669	0.226	1,234.309	0.028	1.5192	0.009	25.83	0.154	94.730	1.511	276.83	281.06
0105-016	18.00	0.516	1.717	2.158	43.876	17.202	0.308	1,744.562	0.150	2,799.259	0.012	1.5141	0.005	25.75	0.092	94.360	3.426	312.89	274.57
0105-017	21.00	0.691	1.117	3.364	12.867	22.972	0.308	2,317.339	0.152	3,726.589	0.010	1.5169	0.005	25.80	0.085	94.328	4.551	266.55	68.60
0105-018	24.00	0.708	1.102	6.015	8.319	20.632	0.309	2,076.162	0.154	3,368.338	0.033	1.5186	0.005	25.82	0.090	93.600	4.077	133.59	22.23
0105-019	27.00	2.617	0.721	6.279	5.986	40.222	0.306	4,038.062	0.155	6,930.416	0.065	1.5206	0.006	25.86	0.100	88.599	7.930	248.88	29.81
0105-020	30.00	2.650	0.670	8.244	4.839	37.080	0.307	3,717.134	0.157	6,451.560	0.073	1.5207	0.006	25.86	0.103	87.615	7.300	174.49	16.90
0105-021	34.00	3.171	0.670	10.463	8.933	40.011	0.305	3,997.018	0.155	7,021.938	0.066	1.5179	0.006	25.81	0.104	86.399	7.849	147.84	26.42
0105-023	38.00	1.724	0.874	7.135	8.258	31.793	0.306	3,184.108	0.157	5,346.328	0.084	1.5153	0.006	25.77	0.105	90.249	6.253	172.71	28.53
0105-024	42.00	1.594	0.803	8.047	5.484	31.260	0.305	3,147.013	0.157	5,252.751	0.087	1.5158	0.006	25.78	0.103	90.812	6.180	151.34	16.60
0105-025	46.00	1.687	0.791	7.481	7.849	34.188	0.307	3,449.965	0.156	5,735.270	0.080	1.5143	0.006	25.75	0.100	91.092	6.775	178.47	28.02
0105-026	50.00	2.638	0.879	9.019	6.510	28.824	0.307	2,881.485	0.156	5,154.537	0.088	1.5134	0.007	25.74	0.125	84.604	5.659	123.64	16.10
0105-028	55.00	1.171	0.796	5.321	7.584	22.060	0.308	2,207.683	0.159	3,705.397	0.080	1.5179	0.006	25.81	0.103	90.436	4.335	160.57	24.36
0105-029	60.00	2.088	0.675	15.137	3.624	58.855	0.304	5,941.186	0.153	9,648.937	0.055	1.5170	0.005	25.80	0.087	93.409	11.667	151.89	11.02

Plateau age:  $25.81 \pm 0.16$  Ma ( $2\sigma$ ); Total fusion age:  $25.81 \pm 0.16$  Ma ( $2\sigma$ ); Normal Isochron age:  $25.82 \pm 0.16$  Ma ( $2\sigma$ ); Inverse Isochron age:  $25.81 \pm 0.16$  Ma ( $2\sigma$ )

APPENDIX 4. Table A4. (cont.)

Relative Abundances	<sup>36</sup> Ar	±1σ	%	<sup>37</sup> Ar	±1σ	%	<sup>38</sup> Ar	±1σ	%	<sup>39</sup> Ar	±1σ	%	<sup>40</sup> Ar	±1σ	%	<sup>40</sup> (r)/ <sup>39</sup> (k)	±2σ	Age (Ma)	±2σ	<sup>40</sup> Ar(r) %	<sup>39</sup> Ar(k) %	K/Ca	±2σ
<b>LA-D15-003-A-041, hydrothermal biotite, La Arenal deposit; J = 0.00946324 ± 0.00002839</b>																							
0101-002	3.50	3.553	0.669	25.346	0.978	3.091	0.465	169.516	0.151	1,273.025	0.016	1.2614	0.084	21.46	1.418	16.795	0.287	2.59	0.05				
0101-003	4.20	2.038	0.728	28.582	1.120	5.117	0.422	329.294	0.153	1,097.471	0.013	1.4895	0.027	25.31	0.460	44.690	0.557	4.46	0.10				
0101-004	5.00	3.383	0.673	32.423	1.087	14.359	0.321	946.639	0.150	2,454.404	0.017	1.5263	0.015	25.93	0.255	58.866	1.603	11.30	0.25				
0101-005	5.80	2.308	0.686	22.937	2.658	16.018	0.312	1,080.010	0.151	2,337.305	0.016	1.5258	0.010	25.92	0.167	70.502	1.828	18.22	0.97				
0101-006	6.60	1.793	0.756	17.380	2.267	14.846	0.313	1,004.896	0.151	2,066.912	0.015	1.5236	0.009	25.89	0.157	74.075	1.701	22.38	1.02				
0101-007	7.20	1.221	0.856	15.132	2.702	12.654	0.316	861.886	0.151	1,680.996	0.015	1.5270	0.009	25.94	0.145	78.292	1.459	22.04	1.19				
0101-009	8.00	1.112	1.020	13.396	3.401	13.535	0.315	922.017	0.151	1,739.419	0.014	1.5258	0.009	25.92	0.146	80.877	1.561	26.64	1.81				
0101-010	9.00	0.999	1.064	14.291	3.462	14.502	0.309	990.451	0.150	1,813.399	0.014	1.5291	0.008	25.98	0.133	83.515	1.677	26.82	1.86				
0101-011	10.00	1.054	1.064	12.180	4.466	14.672	0.313	1,004.047	0.150	1,850.855	0.016	1.5290	0.008	25.98	0.137	82.942	1.700	31.90	2.85				
0101-012	11.50	1.441	0.912	16.121	2.538	23.754	0.306	1,625.583	0.150	2,916.223	0.016	1.5283	0.007	25.97	0.113	85.190	2.752	39.02	1.98				
0101-013	13.00	1.340	0.904	17.145	2.752	21.119	0.308	1,445.498	0.151	2,613.702	0.013	1.5303	0.007	26.00	0.115	84.634	2.447	32.63	1.80				
0101-014	15.00	1.388	0.852	17.381	3.271	24.735	0.307	1,697.603	0.151	3,010.816	0.014	1.5284	0.006	25.97	0.105	86.177	2.874	37.80	2.48				
0101-016	18.00	2.225	0.698	28.803	2.334	43.950	0.304	3,014.521	0.151	5,274.605	0.016	1.5282	0.006	25.96	0.094	87.341	5.103	40.50	1.89				
0101-017	21.00	2.111	0.697	26.175	2.954	38.143	0.304	2,614.362	0.151	4,629.162	0.017	1.5285	0.006	25.97	0.097	86.323	4.426	38.65	2.29				
0101-018	24.00	1.885	0.764	24.525	2.931	44.406	0.303	3,050.767	0.151	5,235.377	0.018	1.5304	0.005	26.00	0.092	89.178	5.165	48.14	2.83				
0101-019	27.00	1.576	0.882	24.026	3.257	34.048	0.303	2,338.106	0.151	4,045.125	0.005	1.5277	0.006	25.96	0.098	88.303	3.958	37.66	2.46				
0101-020	30.00	1.733	0.691	25.273	1.697	41.534	0.303	2,853.779	0.151	4,888.204	0.029	1.5304	0.005	26.00	0.090	89.344	4.831	43.70	1.49				
0101-021	34.00	3.805	0.659	54.416	1.105	97.886	0.302	6,728.518	0.151	11,457.052	0.015	1.5327	0.005	26.04	0.087	90.013	11.391	47.85	1.07				
0101-023	38.00	7.404	0.617	117.179	0.844	191.757	0.302	13,191.951	0.151	22,397.252	0.015	1.5291	0.005	25.98	0.086	90.061	22.332	43.57	0.75				
0101-024	42.00	4.128	0.630	58.825	1.023	96.012	0.303	6,594.993	0.151	11,297.947	0.015	1.5251	0.005	25.91	0.088	89.022	11.165	43.39	0.90				
0101-025	46.00	3.585	0.654	48.625	1.390	62.418	0.303	4,281.752	0.151	7,593.670	0.016	1.5225	0.006	25.87	0.096	85.847	7.249	34.08	0.95				
0101-026	50.00	2.576	0.729	23.908	1.888	33.980	0.306	2,324.541	0.151	4,312.245	0.017	1.5232	0.007	25.88	0.113	82.108	3.935	37.63	1.42				

Plateau age: 25.96 ± 0.16 Ma (2σ); Total fusion age: 25.94 ± 0.16 Ma (2σ); Normal Isochron age: 26.00 ± 0.16 Ma (2σ); Inverse Isochron age: 26.00 ± 0.16 Ma (2σ)